Long Term Implantable Pressure Sensors

Thesis by
Aubrey Michael Shapero

In Partial Fulfillment of the Requirements for the
Degree of
Doctor of Philosophy in Electrical Engineering

CALIFORNIA INSTITUTE OF TECHNOLOGY
Pasadena, California

2019
Defended May 24, 2019

Aubrey Michael Shapero
ORCID: 0000-0002-8036-3623

ACKNOWLEDGEMENTS

My thesis would not be possible at all without the tremendous support of my PhD advisor, Professor Yu-Chong Tai. He has given me an incredible opportunity to learn from him over the past six years, not just on technical subjects, but also about what it takes to be a leader in all aspects. I felt that from the beginning Prof. Tai had trust in me and made himself available when I needed to discuss recent findings or ideas with him. He has shown me what it means to be a sophisticated, methodical engineer, and a general problem solver. From the first day I met him I knew I would be joining his lab.

I also thank Professors Azita Emami, Mark Humayun, Juan-Carlos Martinez, and Damien Rodger for their support in a fruitful collaboration between three components, the MEMS, the circuitry, and medical perspective. I also thank Professors Changhuei Yang and Hyuck Choo for their time and insights as members on my candidacy and defense committees.

I also thank my current and former lab mates and post-docs, Drs. Jun Park, Jay Chang, Monty Nandra, Joy Zhao, Clark Kang, Shell Zhang, Yang Liu, Colin Cook, Yuan Luo, Nicholas Scianmarello, and Jake Chou, May Yu, Allen Shang, and Shane Shahrestani. I have had many enlightening conversations about research and other topics. I am very proud to know such a talented and diverse group of people. Also thank Caltech student Siva Gangavarapu for building a multi-DOF motorized stage for characterizing wireless performance of devices. I also thank Cameron Sylber and Maya Ordoñez for their long hours helping me gather weekly soaking and parylene thickness data respectively.

Christine Garske provided unimaginable help with ordering parts and taking care of administrative tasks so I could focus on the work, and Trevor Roper provided tireless support for maintaining the parylene machine and other equipment.

Abhinav Agarwal became my closest friend of all from my time at Caltech, and my social life and research work would be fundamentally different if we did not become friends, and then roommates, and then collaborators. He is the hardest working person I have ever met, and always been a supporting pillar when times were tough. And I'd like to thank all my friends from early days to undergrad and grad school.

I thank Vanessa Klotzman for the encouragement to finish in the last months.

I have had great teachers and professors throughout my life, too many to name them all, from early on all the way to high school with Mr. Maine, and to Stanford and Caltech, where Professor Roger Howe and Professor Tai are the reason I got into MEMS and medical devices.

Above all else, I thank my family, for I have been blessed by their unwavering love and support since I was born. Since I was a child, I wanted to be an inventor, and I distinctly remember my disappointment when I mistakenly concluded that 'inventor' was an extinct profession based on my observation that the term 'inventor' seemed to be only used for people from history books and not anyone contemporary. I assumed that everything worthwhile must have already been invented. It was not until I was around 14 years old that I realized the reason is that 'inventors' are nowadays called 'engineers'!

I remember my Grandpa, Ezra Mintz, an electrical engineer, sharing his love of music, card games, fishing, and baseball. I wish had the chance to ask him more about engineering, but his inspiration drives me every day to be a better electrical engineer and scientist. Like the rest of my family, he would be just equally proud had I gone into any other field, but I can only imagine the conversations we could have had if he were here today.

I also remember my grandmother, Ray Shapero, or "Baubie." She was fun, caring, and insightful. She predicted I would love systems, even before I knew.

During my PhD years I had the privilege to live near my parents, Sharon Mintz and Steve Shapero, and both Grandma Natalie Mintz and Zeyde Martin Shapero, and have been able to see them more often than most PhD students get to see their families. I have cherished this time with my loving and supportive grandparents, who always enjoy hearing about my projects and life.

To Ben, my older brother and oldest friend, you forged the path in our early years, and I wouldn't be where I am today without you.

Lastly, to Mom and Dad, you always have and always will be there for me. I could not have had more loving parents.

ABSTRACT

One of the ways to describe the human body is as a fluidic system, with pressure and flow being the fundamental parameters. To date, there has been no proven general strategy for long term reliable, continuous, and precise measurements of either quantity. Knowing the pressure or flow in various organs could be extremely valuable to maintaining health and monitoring for diseases like heart disease, glaucoma, hydrocephalus, and more. This thesis aims to present a generic pressure sensor packaging scheme to make them reliable for long lifetimes while inside the body, while also being compatible with active microelectronics.

This thesis discusses the failure mechanisms and sources of inaccuracy over time, or drift, of standard microelectronic pressure sensors inside the body, and proposes and analyses a new encapsulation scheme in order to protect against these factors, such as an electrolytic environment, and biofouling, while being biocompatible and space-efficient. In other words, rather than the performance immediately after implantation, the bottleneck has been long term reliability of sensors past the 1-3 month range within the clinical accuracy tolerance, much less than a practical lifetime of at least 1-2 years.

The novel packaging scheme is called parylene-oil-encapsulation, where a pressure sensor membrane is submerged in biocompatible silicone oil, and then encapsulated *in situ* with chemically vapor deposited parylene, which is also biocompatible. The advantages of this packaging scheme, over the contemporary attempts, such as silicone gel and/or pure parylene coatings are discussed theoretically and confirmed with benchtop experiments.

To prove the viability of this packaging scheme, we built a wireless intraocular pressure sensor implant for monitoring glaucoma, and we conducted *ex vivo* and *in vivo* tests in rabbits. Glaucoma is a disease in which the optic nerve gets damaged, leading to gradual but irreversible vision loss. Although the mechanisms that cause glaucoma are varied, the most typical cause of optic nerve damage is excessive intraocular pressure, or IOP. IOP is a crucial metric to monitor the health of eyes for patients with or at risk of having glaucoma.

For those with severe glaucoma, the state of care is to go to the doctor's office for a single measurement to get a single data point per visit using an instrument such as a tonometer. This procedure is inconvenient, but even worse, provides an

incomplete assessment of IOP. It is known that IOP fluctuates throughout the day, and is often higher at night, when patients would not be at the doctor's office. Also, the IOP waveform can fluctuate day to day. So unlucky patients may lose eyesight because the outpatient monitoring method may miss brief periods of elevated IOP, which can still damage the optic nerve. So doctors have identified that an IOP sensing implant which can be read at home easily and on demand can prevent vision loss by giving an accurate assessment of IOP and reduce the burden of time-consuming outpatient measurements.

In summary, this thesis presents the first practical approach towards a solution to the problem of general implantable pressure sensors having insufficient lifetimes, with a specific example to show its compatibility with standard electronics to meet an actual clinical need.

PUBLISHED CONTENT AND CONTRIBUTIONS

[1] A. Shapero, A. Agarwal, J. C. Martinez, A. Emami, M. Humayun, and Y.-C. Tai, "Wireless implantable intraocular pressure sensor with parylene-oil-encapsulation and forward-angled rf coil," in *2019 IEEE Micro Electro Mechanical Systems (MEMS)*, Seoul: IEEE, Jan. 2019, pp. 21–24,
A.M.S. carried out every experiment and fabricated every device, and analyzed the results beyond the that already included in the CICC 2018 paper.

[2] A. Agarwal, A. Shapero, D. Rodger, M. Humayun, Y.-C. Tai, and A. Emami, "A wireless, low-drift, implantable intraocular pressure sensor with parylene-on-oil encapsulation," in *2018 IEEE Custom Integrated Circuits Conference (CICC)*, San Diego, CA: IEEE, Apr. 2018, pp. 1–4, ISBN: 978-1-5386-2483-8. DOI: 10.1109/CICC.2018.8357049. [Online]. Available: https://ieeexplore.ieee.org/document/8357049/ (visited on 03/20/2019),
A.M.S. was co-first author with A.A. A.M.S was the lead system and packaging architect, and assembled and fabricated the device. A.M.S. also worked with A.A. on the high-level decisions for the ASIC and did bench top verification and wrote the Verilog code on the ASIC. A.M.S. also carried out every experiment. A.A. led and designed the ASIC with input from A.M.S.

[3] A. Shapero and Y.-C. Tai, "Parylene-oil-encapsulated low-drift implantable pressure sensors," in *2018 IEEE Micro Electro Mechanical Systems (MEMS)*, Belfast: IEEE, Jan. 2018, pp. 47–50, ISBN: 978-1-5386-4782-0. DOI: 10.1109/MEMSYS.2018.8346478. [Online]. Available: https://ieeexplore.ieee.org/document/8346478/ (visited on 10/04/2018),
A.M.S. carried out every experiment and fabricated every device, and analyzed the results.

[4] A. M. Shapero, Y. Liu, and Y.-C. Tai, "Parylene-on-oil packaging for long-term implantable pressure sensors," *Biomedical Microdevices*, vol. 18, no. 4, Aug. 2016, ISSN: 1387-2176, 1572-8781. DOI: 10.1007/s10544-016-0089-4. [Online]. Available: http://link.springer.com/10.1007/s10544-016-0089-4 (visited on 02/22/2018),
A.M.S. carried out every experiment and fabricated every device, and analyzed the results.

[5] A. Shapero, Y. Liu, and Y.-C. Tai, "Parylene-on-oil packaging for implantable pressure sensors," presented at the MEMS, IEEE, Jan. 2016, pp. 403–406, ISBN: 978-1-5090-1973-1. DOI: 10.1109/MEMSYS.2016.7421646. [Online]. Available: http://ieeexplore.ieee.org/document/7421646/ (visited on 02/22/2018),
A.M.S. carried out every experiment and fabricated every device, and analyzed the results.

TABLE OF CONTENTS

LIST OF ILLUSTRATIONS

LIST OF TABLES

NOMENCLATURE

Acetone. An organic solvent, $(CH_3)_2CO$.

ADC. Analog-to-digital conversion.

ASIC. Application Specific Integrated Circuit.

CSF. Cerebrospinal fluid.

CVD. Chemical Vapor Deposition. A method of depositing films on samples.

DI. De-ionized water.

DUT. Device under test.

ENIG. Electroless Nickel Immersion Gold. A type of surface plating in PCBs.

ESD. Electrostatic discharge. A phenomenon that can cause permanent damage to semiconductor devices.

ESL. Equivalent series inductance, here in the context of parasitic capacitor characteristics.

ESR. Equivalent series resistance, here in the context of parasitic capacitor characteristics.

GDD. Glaucoma Drainage Device.

Glass transition temperature. For polymers, the temperature below which the polymer material is brittle more like glass, or above which, is soft more like rubber.

Glaucoma. A disease of the eye where the optic nerve gets damaged leading to irreversible vision loss. The most common cause of optic nerve damage is hypertension in the eye, i.e., IOP in excess of ~22 mmHg (for humans). However, there are cases where the optic nerve gets damaged when IOP would be considered within the normal range.

I2C. Inter-integrated Circuit. Alternatively written as I^2C. A two-wire communication bus/protocol where multiple masters and multiple slaves talk over a serial bus using pull-down or pull-up resistors. One wire is clock, the other is data.

IC. Integrated Circuit.

ICP. Intracranial Pressure, the gage pressure inside the cranium, in other words, the pressure inside the cranium minus the atmospheric pressure. Usually quoted in mmHg.

ID. Inner diameter.

IID. Identical and independently distributed random variables.

IOP. Intraocular Pressure, the gage pressure inside the eyeball, in other words, the pressure inside the eyeball minus the atmospheric pressure. Usually quoted in mmHg.

IPA. Isopropyl alcohol. An organic solvent.

IR. Internal resistance, here in the context of parasitic capacitor characteristics.

ISM Band. Industrial, Scientific, and Medical Radio Band. A designated frequency band in the radio frequency range in which is legally permissible for devices to cause interference.

LED. Light-emitting diode.

LSB. Least significant bit first.

MSB. Most significant bit first.

OD. Outer diameter.

PA-C. Parylene species equivalent to PA-N with an additional Chlorine atom on its unit cell.

PA-D. Parylene species equivalent to PA-N with two additional Chlorine atoms on its unit cell, (or PA-C plus one more additional Chlorine atom).

PA-HT. High temperature parylene species equivalent to PA-N except the CH2 chains are replaced by CF2 chains.

PA-N. Basic parylene species with a benzene center and a CH2 chain.

Parylene. A trade name for poly(para-xylylene). A family of biocompatible polymers which is typically deposited as films onto samples using CVD process.

PCB. Printed Circuit Board.

PLT. Porous Layer Thickness (of parylene). The repeatable thickness of a porous layer of parylene deposited on oil or other liquids even when the parylene dimer weight changes.

Polyimide. A biocompatible polymer that is sometimes used for flexible PCBs.

Potting. A process of filling a complete electronic assembly with a solid or gelatinous compound for resistance to shock and vibration, and for exclusion of moisture and corrosive agents.

RF. Radio Frequency. The electromagnetic spectrum covering 20 kHz to 300 GHz.

SEM. Scanning electron microscope/microscopy.

SMA. SubMiniature version A. A type of co-axial RF cable.

SPI. Serial Peripheral Interface. A single master and multiple slave communication bus/protocol. There is a clock, MISO (master-in, slave-out), MOSI (master-out, slave-in) lines, as well as a slave-select line for each slave.

Tonovet. A handheld measurement device for measuring IOP in animals.

WVTR. Water Vapor Transmission Rate.

Chapter 1

INTRODUCTION

Pressure is defined as force per area. A conversion table for many different common units of pressure relevant in this thesis is provided in table 1.1.

Table 1.1: Pressure conversion ratios pertinent here. Data compiled from [1].

To Convert	Into	Multiply By
atmosphere	bar	1.01295
atmosphere	in. Hg	29.9213
atmosphere	mbar or mb	1012.95
atmosphere	Pa or N/m^2	1.01295×10^5
atmosphere	torr or mmHg	760
bar	atmosphere	0.9872
bar	mbar	1000
bar	Pa	1×10^5
bar	kPa	100
bar	psi or lb/in^2	14.508
bar	mmHg	750.2838
mbar	atmosphere	9.872×10^{-4}
mbar	bar	0.001
mbar	Pa	100
mbar	mmHg	0.75028
mbar	cm. water	1.0206
kPa	Pa	1000
kPa	mbar	10
mmHg	mbar	1.3328
mmHg	Pa	133.28

1.1 MEMS Pressure Sensors

There are many types of MEMS (microelectromechanical systems) pressure sensors. Most MEMS pressure sensors are based on the phenomenon of a deflecting membrane, but there are other ways to measure the pressure as well, such as piezoelectric sensors. But within the scope of this thesis, only membrane-based MEMS pressure sensors are considered.

Nearly all MEMS pressure sensors based off deflecting membranes function with one of these two principles. The first principle is to use piezoresistance, where for piezoresistors are placed as shown in Figure 1.1 on a deflecting membrane and

connected in a Wheatstone bridge circuit to maximize sensitivity. There are analog and digital circuit techniques to compensate for temperature (not shown). The orientation of the resistors changes the sign of resistance change with stress.

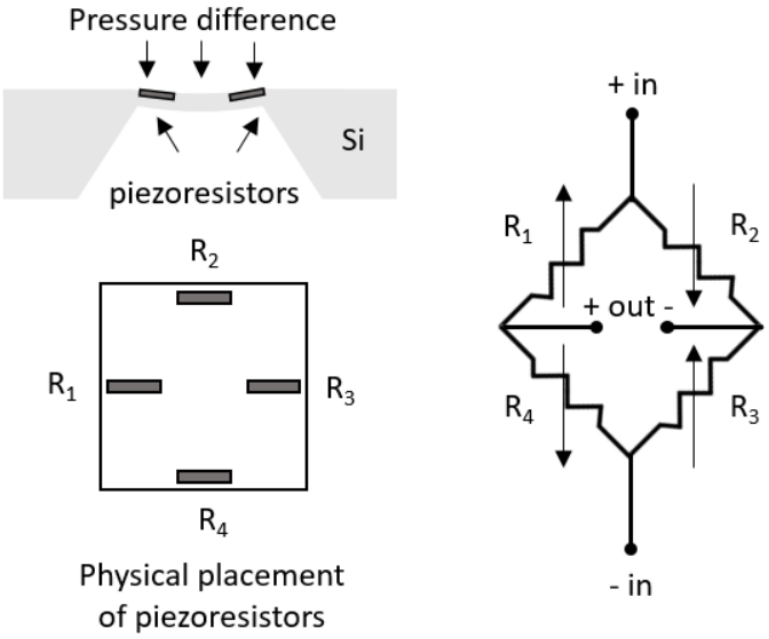

Figure 1.1: Piezoresistive MEMS pressure sensor. Adapted from [2].

The second principle is measuring the capacitance of a parallel plate capacitor with at least one deflecting plate. Depending on the geometry, a capacitive pressure sensor operation can be thought of changing the effective area or distance, or a a combination of both with pressure. The pressure could be interpreted by a change in oscillation frequency, time, charge, or voltages.

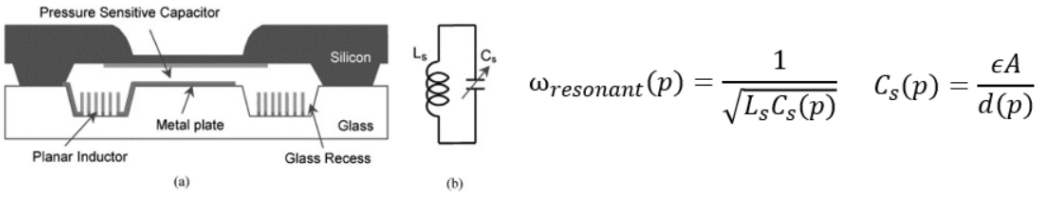

Figure 1.2: Capacitive MEMS pressure sensor. Reprinted from [3].

There are different categories of pressure sensing. Absolute pressure literally means the pressure above vacuum. Gauge (or gage) pressure refers to the pressure relative to atmosphere. Gauge vacuum likewise refers to pressure below atmosphere.

Differential pressure usually refers to the pressure difference between two inputs (both non-atmosphere). Differential pressure sensors can act as a gauge sensor if one of the ports is left open to air. In analog terms, an absolute pressure sensor has a vacuum sealed chamber so that the pressure across the membrane is proportional to absolute pressure. A sealed gauge sensor is like an absolute pressure sensor, except there is a nonzero reference pressure inside the sealed chamber. Once the signal is digitized, it is simple to add the reference pressure in digital calculation such that a sealed gauge sensor reports a value in terms of absolute pressure. For this reason, digital-output commercial chips with an internal sealed gauge analog pressure sensing diaphragm can be referred to as absolute pressure sensors, if that is how the bits are interpreted. Commercial MEMS barometers are typically sealed gauge type, since that would bias a neutral point (i.e. zero deflection) within a range that is on the order of 1 atm. See Figure 1.3.

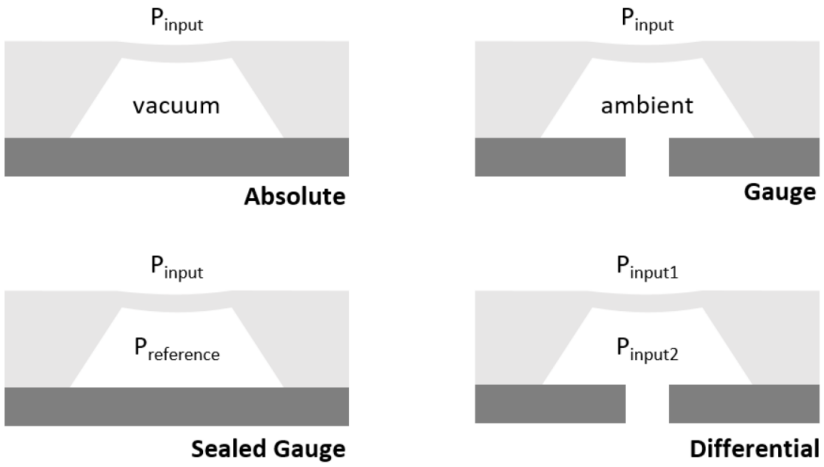

Figure 1.3: Types of pressure sensors or measurements. Adapted from [2].

Another way to categorize MEMS pressure sensors is whether they are active or passive, meaning whether or not they require an energy source, other than the pressure difference across the membrane itself, to operate.[1] Most, but not all, MEMS pressure sensors are active. Indeed, the more common of the two types, piezoresistive sensors, are all active, and capacitive sensors can be either active or passive. Active sensors are convenient because they could measure on their own, given a battery source, and potentially store those measurements for later inspection. However, all active sensors are based on silicon microelectronics, and thus may be

[1] This applies to all pressure sensors as well. For example, the common dial-type pressure gauges often seen in labs or homes are passive spring-based sensors.

susceptible to corrosion, whereas passive sensors are not restricted to using silicon. This is a significant point. Fundamentally, pressure sensors are transducers which convert pressure into information. In the modern world, information is stored as digital bits in the form of voltage, and active sensors can be easily integrated with digital circuits to store the information as bits and transmit that data wirelessly, in the case of a medical implant, but passive sensors are trickier. They require remote sensing to infer the capacitance, and ultimately, the pressure. See Figure 1.2 right.

The most common way of remotely sensing the capacitance is to incorporate the pressure-dependent capacitor with an inductor to make an LC tank, and remotely infer the resonant frequency given a known inductance, as $\omega = \frac{1}{\sqrt{LC}}$. Unsurprisingly, this remote measurement has much smaller signal to noise ratio than measuring and digitizing the signal at or near the sensor itself. The low signal to noise ratio of passive pressure in implanted settings vastly limits the number applications in which they can be used relative to the potential diseases whose treatment may benefit from pressure sensing.

1.2 Organs Pertinent to Long Term Active Pressure Sensing

The human body is a fluidic system, in addition to being an electrical system, chemical system, mechanical system, etc. In a fluidic system, pressure and flow are fundamental quantities just as voltage and current are fundamental quantities of electrical systems. It is no surprise that many diseases and organ health states could be quantified by pressure and/or flow, just as the electrical signature is one of the ways used to diagnose the state of cardiovascular health. In this section, several diseases, each related to a different organ, are discussed to show the breadth of applicability once a long term active implantable pressure sensor can be achieved in the clinic.

Summary figures are presented here for overall target pressure ranges and sampling frequencies depending on the organ of interest (see Figures 1.4 and 1.5).

1.2.1 Eye

The human eye produces an intraocular fluid called aqueous humor, which is 99.1% water [5]. The intraocular fluid is produced at a rate of 2-3 µL/min with a turnover rate of 1.5-2 hours [5]. It is produced in the posterior chamber, which is naturally filled with vitreous tissue, and diffuses to the anterior chamber, which is not filled with vitreous tissue [5]. It then exits the eye through the trabecular network into the Schlemm's canal, and then through the sclera into the venous system. If

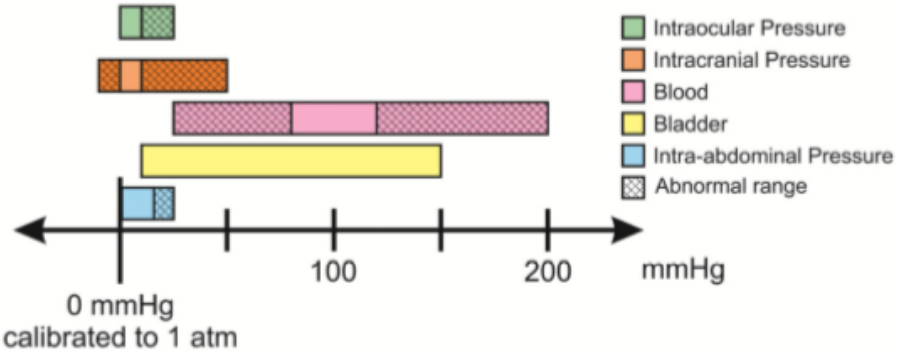

Figure 1.4: Relevant pressure ranges for *in vivo* pressure monitoring for diagnostic applications. Reprinted from [4].

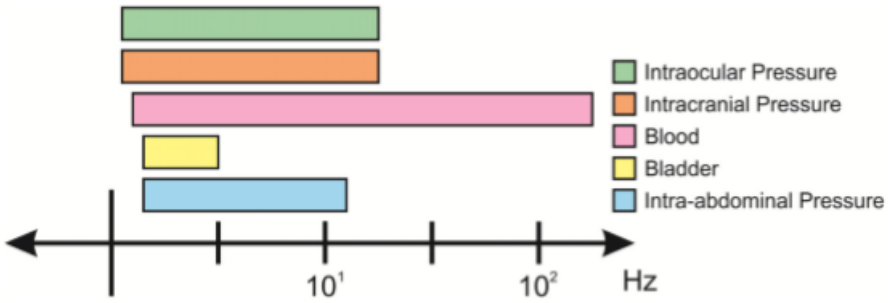

Figure 1.5: Relevant frequency bandwidths for varying pressure signals *in vivo*. Reprinted from [4].

the pathway is blocked, or the production is too high, than the intraocular pressure becomes hypertensive [5]. This excessive pressure is felt by the ends of the optic nerve, and if untreated can cause irreversible vision loss and even blindness over time [6]. See Figure 1.6.

Figure 1.6: Glaucoma related vision impairment. Reprinted from [7].

This phenomenon is called primary open angle glaucoma, and is by far the most common type of glaucoma, although there are other types in which the optic nerve gets damaged despite regular IOP [8]. There was about 60 million people worldwide with glaucoma, and estimated that number will be 80 million by 2020 [8]. This thesis focuses on the large group in which IOP readings may be relevant. Typical IOP is around 16 mmHg (gauge) and IOP above 21 mmHg (gauge) is considered excessive [5]. It is also known that IOP can fluctuate throughout the day, and is often higher at night, when the doctor's office is typically closed [9], [10]. See Figure 1.7. Even brief periods of excessive IOP can damage the optic nerve over long periods of time [9].

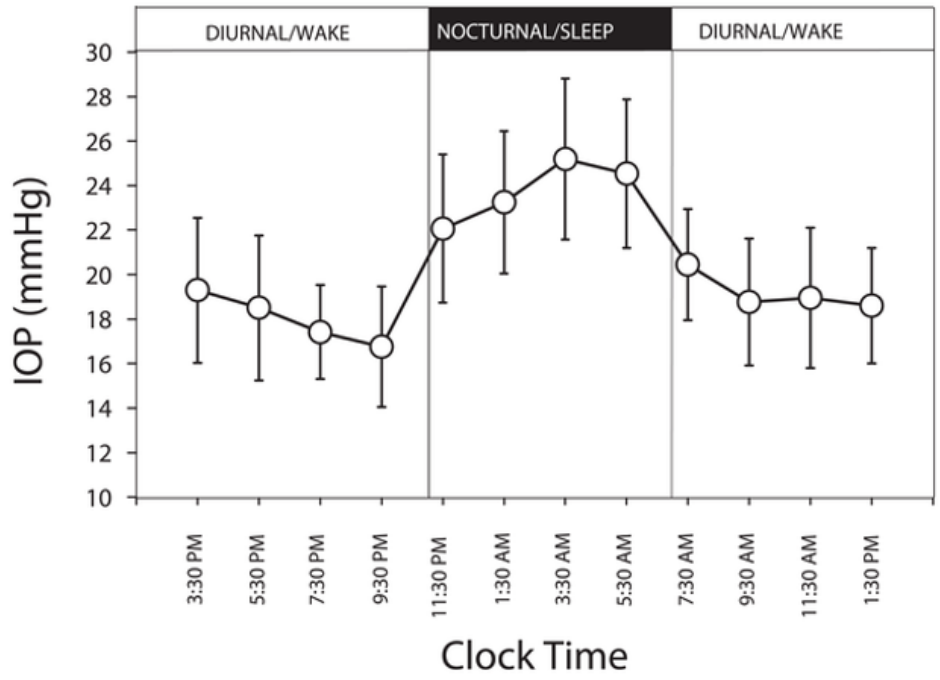

Figure 1.7: Twenty-four-hour intraocular pressure (IOP) pattern in the contralateral eye. Reprinted from [10].

The most common types of treatment for primary open angle glaucoma includes eye drops or oral medication to treat the excessive fluid production and/or insufficient natural draining [11]. If those do not reduce IOP sufficiently, or the medicines lose effectiveness over time, the glaucoma is called refractory glaucoma [5], [12]. At this point, patients typically get a trabeculectomy, which makes a hole in the trabecular mesh or get a glaucoma drainage device (GDD) implanted to increase drainage [5], [13]. There are studies about the success and complication rate for the various surgeries and implants [13]. Drawbacks exist for both approaches. An

ablated hole without and implanted tube can heal and seal again, or drain too much, leading to hypotony [11], which is associated with other risks, and a tube may clog over a longer time scale, but is also more intrusive [13].

For those with severe glaucoma, their IOP needs to be monitored very carefully to ensure that the therapy is successful, because every day excessive IOP is not treated contributes to irreversible vision loss [9]. One cannot feel that that the IOP is excessive, and the loss of vision begins at the periphery, making it difficult to notice day-to-day changes until the visual impairment is substantial. The current method to measure IOP in humans requires a visit to the doctor's office because it requires a tonometer and special training to operate correctly to get an IOP reading which meets the clinical accuracy tolerance of 2 mmHg [5], [14], [15]. This also involves the use of topical anesthetic for humans [16]. Interestingly, even though humans need anesthetic, animals such as rabbits and dogs can tolerate the IOP readings without anesthetic [17]. For this reason also, it is inconvenient for patients to get IOP readings every week or two, but there is no better alternative in the clinic [18].

Goldmann Applanation Tonometry for IOP measurement

Tonopen

Figure 1.8: Goldmann applanation Tonometry and Tonopen. Reprinted from [19], [20].

Thus, an intraocular pressure sensor which could be operated at home, and would give accurate readings over the long term, could give an incredible improvement in quality of life in terms of vision retained by catching the status of excessive IOP sooner than later, and in time saved by avoiding doctor's visits, especially given the fact that many glaucoma patients are older than the general population.

Another fact to consider is that an IOP sensor has to be small in volume, since there is not much available space. Either the device needs to go inside the eye, where

it must be deliverable by a needle of 1 mm diameter at maximum, or it must exist outside and somehow interface with the intraocular fluid with a tube, and not be more than 2-3 mm thick [4]. The small size constraint and tight accuracy tolerance makes the use of passive pressure sensors difficult for measuring IOP. Ideally, the sensor could also measure on its own and record the data for upload later, but a sensor that yields accurate data long term would be a step forward in the field.

1.2.2 Brain

Hydrocephalus is a condition where too much cerebrospinal fluid (CSF) is created in the brain relative to the rate it can drain out, causing excess intracranial pressure (ICP) on the brain. ICP is also quoted in mmHg and is a gauge pressure quantity. Those with hydrocephalus often get drainage shunts, which solves the problem, until they get clogged up much like GDDs can get clogged [4]. If the drains get clogged, it can result in migraines and even death if not addressed quickly. In hydrocephalus, ICP above 15 mmHg is considered dangerous [21]. Similarly, there are other conditions in which knowing the ICP would be useful, such as traumatic brain injury, brain tumors, or strokes to name a few [4], [21].

1.2.3 Heart and Cardiovasculature

Measuring the blood pressure at various spots over long time periods is the state-of-care for treating many diseases. One application is to watch for repaired aneurysms [4]. In fact, the only FDA-approved implantable pressure sensor is for predicting heart failure within the pulmonary artery, called the CardioMEMS Heart Failure System (Acquired by St. Jude, then Abbott). Pulmonary hypertension means that the heart has to work harder than normal, and a rising pulmonary artery pressure may be indicative of the onset of cardiac arrest [22]. The CardioMEMS HF system uses a passive device, so it takes multiple readings to reach confidence that the pressure value is accurate. More will be discussed in a later section.

1.2.4 Bladder

Paraplegics are paralyzed below the waist, and do not have sensation in the lower half of their bodies. This can include lack of bladder sensation. Often times, a catheter is used to empty the bladder and is left there for up to two weeks [4]. If there is clogging, or the bag gets full, there is excessive pressure in the bladder, which can lead to kidney damage [23]. An implanted or semi-implanted sensor could alert the patient that the bladder pressure is too high.

1.3 Implantable Pressure Sensors

There is a long history of implantable pressure sensors in academia, but a rather brief one in the clinic, so far. This section will discuss various reasons for failure for long term stability in implanted pressure sensors, as well as contemporary attempts for context.

1.3.1 Challenges Preventing Long Term Use

The two typical issues that cause pressure sensors to become inaccurate are corrosion, and biofouling.

1.3.1.1 Corrosion

Corrosion is a redox process. There are two kinds of corrosion: galvanic corrosion and electrolytic corrosion. Galvanic corrosion is also called bimetal corrosion, because it is when two metals of differing electric potentials are in contact with each other through the presence of an electrolytic solution. A small current will flow from the metal acting as the anode and flow into the metal acting as the cathode. As the anode oxidizes, it will corrode away. This can be alleviated with a technique using a sacrificial metal in contact with the rest of the metal, so the sacrificial metal will corrode away instead of the functional metal. Zinc anodes are commonly used as sacrificial anodes, though not necessarily in biomedical settings.

Electrolytic corrosion is a similar process as galvanic corrosion where the anode will corrode, except there is also the presence of an active current, which speeds up the corrosion. The key to protecting from electrolytic corrosion is to keep the solvents far away from the currents, as the solvents are necessary for the mass transport of ions and electrons [24]. Silicone oil with higher viscosity has slower mobility for ions as well [25].

1.3.1.2 Biofouling

Part of the body's immune response is to identify foreign objects of all kinds, and eliminate them or at least isolate them, in the case of non-degradable materials. This also known as the foreign body response, and while it keeps us healthy, it poses a challenge for medical implant longevity. Specifically, proteins or cells may coat or accumulate on the surface of objects [26]. Cells may even encapsulate and apply stress [27]. For example, a study on fibrous capsules around breast implants found that fibrous capsules which caused minor irritation had a Young's modulus 10 MPa,

while the fibrous capsules of the most severe and painful type had Young's modulus of almost 30 MPa [27]. This material accumulation can affect the mechanical performance of pressure sensors. In general, all else equal, the larger the implant, the thicker the biofilm accumulation will be by the time it saturates [28], [29]. Also, different organs have different foreign body responses. For example, the eye is immunoprivileged, meaning that the foreign body response is lighter than average, which is an evolutionary result that prevents us from going blind for every foreign particle that happens to be seen inside the eye [30]. However, the foreign body response inside the bloodstream will include cells and proteins [26].

1.3.2 Contemporary Attempts

Here are some recent work in literature on implantable pressure sensors, categorized by important aspects towards practical clinical use.

1.3.2.1 Passive LC tanks

In 2010, a passive LC tank flexible pressure sensor was made for measuring IOP [31]. It had a flexible coil, so that it was injectable with a needle and demonstrated to change its resonant frequency with pressure. However, other factors such as the medium in between the tissue, temperature uncertainty and misalignment issues in real cases make it unlikely that this could be used to retrieve an absolute IOP value within a 2 mmHg precision. In fact, the authors could not present an in vivo absolute IOP value, either acute or long term. Additionally, the device was unanchored in the eye, and the authors acknowledge this could be a problem in the long term. There were no electronics inside this device.

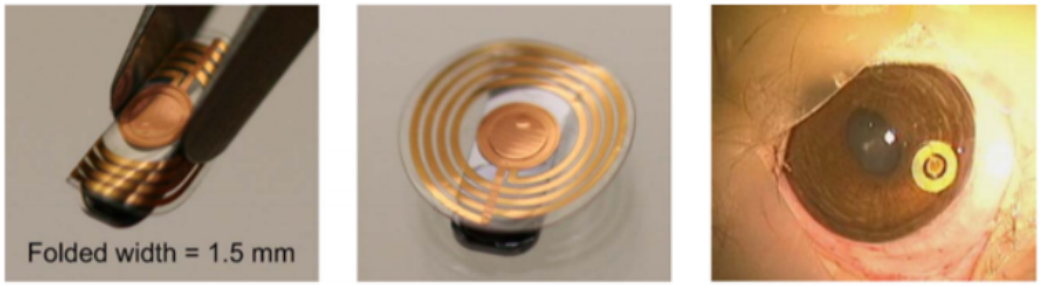

Figure 1.9: Wireless IOP sensing Using Flexible LC Sensing. Reprinted from [31].

The first and only FDA approved implantable pressure sensor remains to be the CardioMEMS Heart Failure pressure sensor [4]. It is a custom designed, passive resonant frequency device. It may be modelled as an LC tank with variable

capacitance, but more accurately it is made of two independent traces, placed in parallel so the two wires give it both inductance and capacitance, and both parameters are modelled versus the deflection to get the best possible accuracy. The device is enclosed in glass and is rather stiff, but large in area (see Figure 1.10). The use of glass with high stiffness is how the low drift is achieved. Despite the accumulation of biofouling in the pulmonary artery, the overall stiffness of the deflecting membrane is not changed by a significant fraction, so stable pressure sensing is achieved. However, the passive nature of the device means that fundamental changes would be required to make this device record pressure on its own, which could jeopardize the longevity due to corrosion or even make the manufacturing incompatible with the current method. Thus, the custom pillow with a large antenna coil is needed to investigate the pressure, and multiple recordings with precise alignment is needed to give confidence the pressure reading is accurate. The daily monitoring of these values is time consuming. In other words, while it is the only proven low-drift implantable pressure sensor, its approach is not generally applicable to other organs due to space limitations, and there is room for improvement in the pulmonary artery pressure monitoring as well.

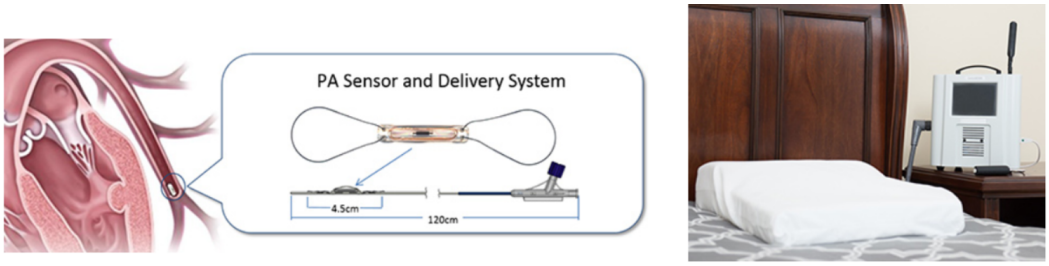

Figure 1.10: CardioMEMS Heart Failure System. Reprinted from [32].

1.3.2.2 Optical Measurement

An interesting device for measuring IOP uses a miniature pressure dependent chamber and an artificial neural network to analyze the Raman spectroscopy response with a nanoengineered black silicon surface (see Figure 1.11 [33]–[35]. They could achieve precise IOP measurements, with the ability to get a reading after it was implanted 9 months in an animal, and seemed to meet the accuracy of ±2 mmHg over 4.5 months, which is impressive [34]. However, this optical approach requires careful alignment to overcome inaccuracy, which is future work for the authors. The cite that ±10 degrees misalignment will cause an additional ±2 mmHg error [35]. However, this implant is tiny and so it suffers the same anchoring requirement as

the Chen, et al. device. Also, this device requires the eye to be open and using a sophisticated laser source, so this seems challenging for potential use at night or while asleep by humans. However, there is a lot of fundamental research that can be done with this 100 Hz sampling rate, wireless real time IOP sensor.

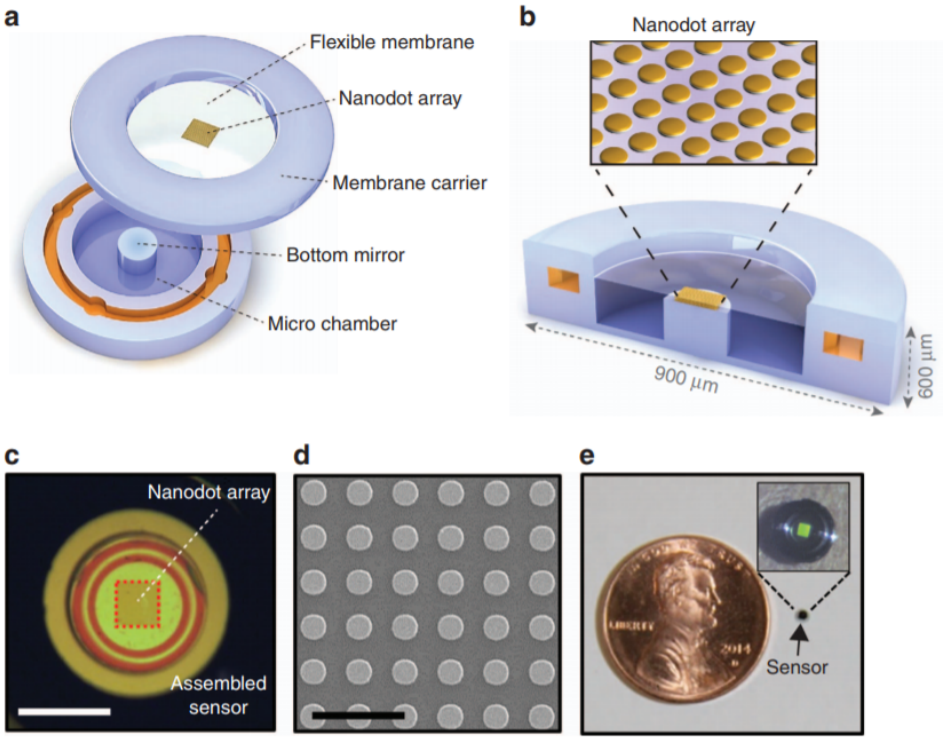

Figure 1.11: Black silicon optical IOP sensor. Reprinted from [34].

1.3.2.3 Commercial IOP efforts

The Argos-IO (formerly Eyemate-IO) (Implandata Ophthalmic Products GmbH, Hanover, Germany) implantable pressure sensor is a capacitive, active pressure sensor, which is powered by an external reader. Like the approach taken in this thesis, the reader powers the implant, collects a reading, and sends digitized pressure reading back to the reader module. However, this device is different in that there is no specific scheme to address the drift problem. In their own publications, they mention that frequent recalibrations are necessary [36]. In fact, in one paper, the mean bias from a sample was calibrated out every measurement event for long term drift analysis [37]. In addition, it was found that "YAG membranotomy to treat retroprosthetic membrane formation can lead to a malfunctioning of the telemetric systems. After completion of the laser procedure, telemetric values were measured

out of range" [36]. However, they note that the device is safe for up to one year, but that since the device takes a lot of space in the posterior chamber, the onset of glaucoma because of the device may be possible [36]. We believe that the constant recalibrations are impractical for patients, and is not a general solution to the drift problem in implantable pressure sensors.

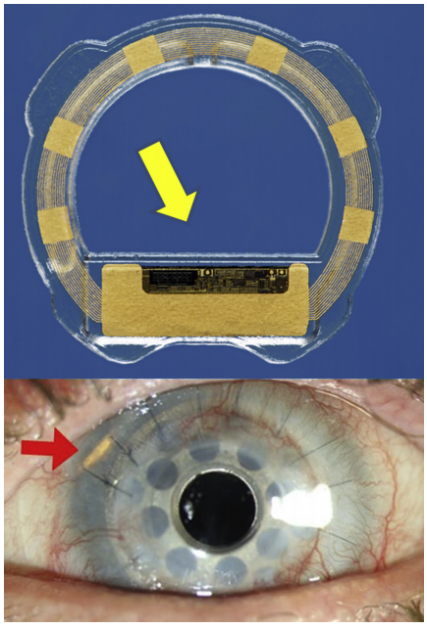

Figure 1.12: Argos-IO IOP sensor. Reprinted from [38].

Although it is not an implant, it is worth mentioning the Triggerfish contact lens IOP monitor, by Sensimed, since it was FDA approved anbd CE marked by 2018 (see Figure 1.13). Much like the Argos-IO, it is wirelessly powered. However, this device requires a coil to be worn on the face, and is intended to catalog 24 hours of continuous IOP data. However, it cannot guarantee absolute accuracy of IOP, since it infers the IOP due to corneal stretching, which suffers from too high of variability in the population to guarantee an absolute measurement. Rather, it can only provide relative IOP throughout the day, so that it can suggest a time of day to measure the IOP with a method that is absolutely accurate. While it is definitely a progress in the field, we believe this approach is not a final general solution in the long term either, as it relies on another device altogether, and assumes that the time of day for peak IOP is absolutely stable [39].

Figure 1.13: Sensimed Triggerfish. Reprinted from [39].

1.3.2.4 Other General Packaging Efforts

Another group has a similar approach to ours, where a pressure sensor is encapsulated by silicone oil, but instead it is in a prefabricated balloon (see Figure 1.14) [40]. The balloon is rather large compared to our pressure sensor packaging scheme, as will be shown, and the stability data is at room temperature, rather than body temperature. Since the bag is prefabricated, putting the sensor and other components inside and sealing with another material is critical, which is another potential failure point.

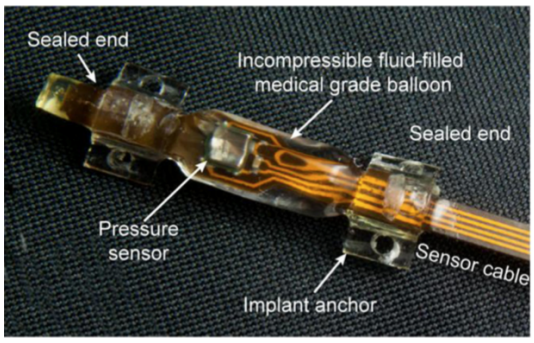

Figure 1.14: Balloon with oil pressure sensor packaging. Reprinted from [40].

Yet another paper packaged a pressure sensor with parylene on silicone gel [41] (see Figure 1.15). As can be seen, the drift data shows nearly immediate sensitivity drift up to 2% or more, and the package dramatically increases the size of the pressure sensor portion. The sensitivity and offset drift in part due to silicone swelling, possibly exacerbated by the fact that it is encapsulated by the parylene, which may cause stress.

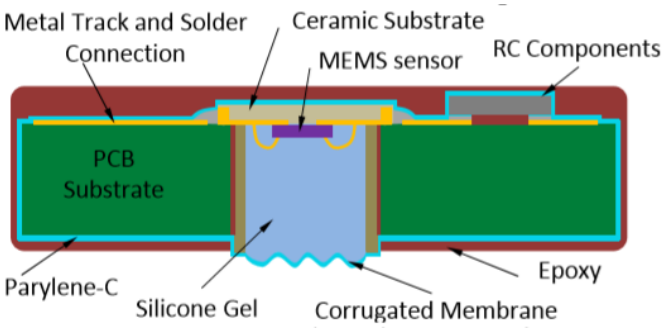

Figure 1.15: Parylene on silicone gel. Reprinted from [41].

1.3.2.5 Temperature Sensing and Calibration

Nearly all sensors have some sensitivity to temperature, and pressure sensors are no exception. In fact, assuming that the body temperature is fixed inside the body leads to more error than necessary, especially for implants that may be near the surface of the body, such as an intraocular pressure sensor. In fact, an impressive, energy-autonomous, cubic-millimeter IOP implant with advanced electronics got hampered by the oversight that it did not measure temperature in addition to pressure, despite the familiarity and capability of building integrated circuit temperature sensors by that same group [42]. The outer surface of the eye can fluctuate in temperature up to 10 °C [43]. It should be standard practice to incorporate a temperature sensor in all implanted sensors to calibrate for temperature dependence, as this anecdote demonstrates the error that arises when assuming the temperature is constant. In a IC, a temperature sensor is very small and not energy demanding compared to the rest of the system, so it could have been incorporated essentially without a drawback. No long term in vivo data could be found for this implant.

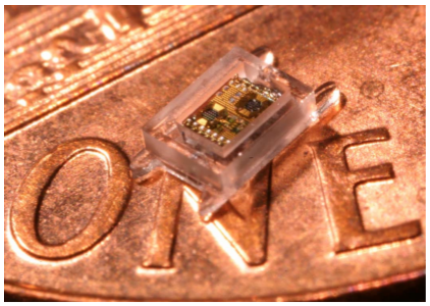

Figure 1.16: Cubic-millimeter IOP sensor implant. Reprinted from [42].

1.4 Parylene

Parylene is the common name for a family of polymers widely used in the medical and electronic industries. The scientific name is poly-(para-xylylene). The base unit consists of a benzene ring. The four most common types of parylene are parylene-N (PA-N), parylene-C (PA-C), parylene-D (PA-D), and parylene-HT (PA-HT).

Parylene-N is the basic version, where PA-C and PA-D replace one or two aromatic hydrogen atoms for chlorine respectively. Parylene-HT has CF_2 instead of ethylene chains (see Figure 1.17).

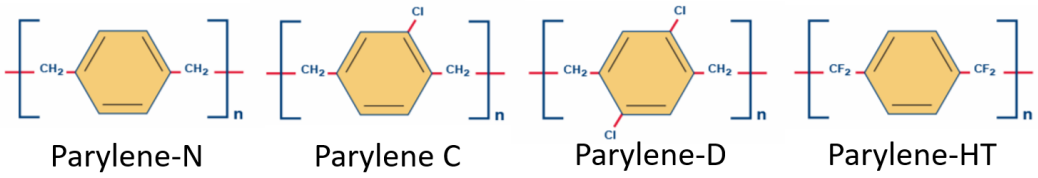

Figure 1.17: Molecular structures of common parylene types, reprinted from [44].

Parylene is an excellent insulator, and is biocompatible material. PA-N, PA-C and PA-HT are rated ISO 10993 biocompatible [44]. It is deposited by chemical vapor deposition, also known as the Gorham process [45], [46]. (See Figure 1.18). Dimer powder is loaded into a vaporizer chamber, which vaporizes the dimer, which then goes through a pyrolizer to split the gaseous dimer into monomers. Then the monomer reaches the deposition chamber, typically at room temperature, and the gas solidifies due to the relatively cool surface. The temperature of the substrate and and the mass of the parylene molecule affects deposition rates [47]. The sticking coefficient may depend on the substrate and temperature, but once the substrate is coated, the sticking surface is that of the parylene itself [46]. The low sticking coefficient makes the coating more conformal, because the first point of contact is not much more likely to retain a parylene unit than the later points of contact. The deposition pressure, which is under 100 mTorr, gives the parylene monomer a mean free path of about 1 mm, which influences how conformal is the coating [48]. Parylene's high surface mobility also plays a factor in how conformal is the coating [49]. In general, if surface mobility is low, then material deposition can be described by a nucleation site model, rather than an overall equal coating as is the case with parylene.

PA-C is the most common type of parylene, as it easy to access, and is biocompatible. Additionally, there is literature on the adhesion of it to various surfaces. On the other hand, PA-HT has a much higher temperature tolerance than PA-C (hence the acronym), but is harder to access, yet it is also biocompatible. The benzene rings in the parylene is why the parylene is very chemically inert. The fluorine atoms in PA-HT give it high temperature tolerance, but also much poorer adhesion qualities. However, the ethylene-like chains make parylene extremely flexible [48].

There are excellent treatises about parylene in the literature and on the web for many properties and summaries of the characterization and uses for parylene [48].

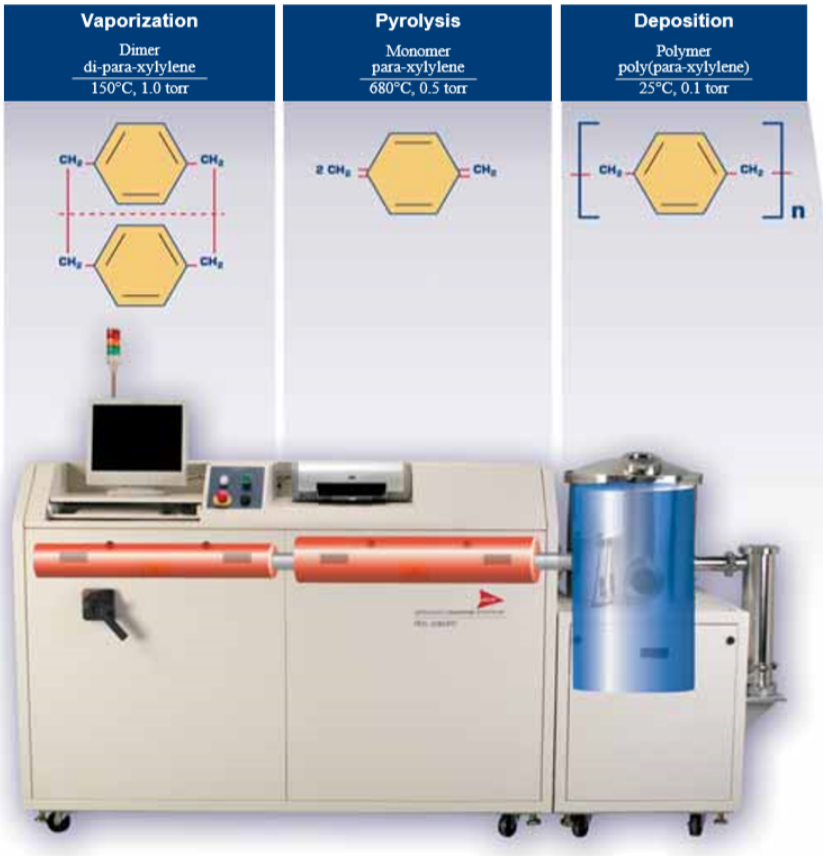

Figure 1.18: Parylene deposition process (Parylene-N shown). Reprinted from [44].

Further, parylene has been shown to be an excellent MEMS material itself, not just as an encapsulate [5], [48], but also as a substrate and a bulk material [50]. For example, its thickness can be selected depending on the amount of dimer wished, which can effect the stiffness of the piece, and plasma etching techniques allow for

the patterned removal of material. Plasma techniques can also modify the surface hydrophobicity/hydrophilicity [51]. Other techniques such as chemical treatment or annealing may also modify the adhesion [52], [53].

As parylene deposition grows, the density grows and porosity lessens, and other properties saturate at about 0.5 to 1 μm, as more and more particles enter the matrix of polymer [54]. The physics of the deposition also accounts for the typical compressive stress for its deposition on solids (20 MPa) [55].

Parylene is less permeable to gases than silicone by orders of magnitude, but it is nonzero [44]. See table 1.3. The permeability of parylene grows according to the Arrhenius relationship at a rate of doubling roughly every 10 °C [56].

1.5 Glass Transition Temperature

As a plastic, parylene can undergo various plastic deformations. One of the properties that can itself change is the glass transition temperature. The glass transition temperature is a way of characterizing the material.

Plastic materials can undergo a change with temperature where they are more crystalline at lower temperature, and more rubbery at higher temperature. The transition is not instantaneous with temperature, but rather a temperature range. Nonetheless, it is common to quote a single value as a shorthand for the boundary between these states, and this is called the glass transition temperature [5], [57].

Plastic polymers like parylene, can undergo permanent change, hence the name. Even though Figure 1.19 may imply an indifference to time or history effects, those do occur. Specifically, flexible, freshly deposited parylene at room temperature may exist in the glassy region initially, but if the temperature exceeds even the glass transition temperature and cooled down again, it can become brittle and more glass-like. The mechanics of this are studied in depth in literature [5], [57], [58]. Fresh PA-C has a glass transition temperature T_g of around 42 °C, but PA-D has a T_g of around 82 °C, while PA-HT has a T_g in excess of 200 °C, much higher temperature than any process involved in this project [5], [44]. As explained in the later chapters, avoiding exceeding the glass transition temperature of the parylene as deposited on oil is critical to maintaining the mechanical properties and avoiding unpredictable behavior such as plastic shrinking. For example, this can greatly change the pressure offset in the film and make the sensor inaccurate.

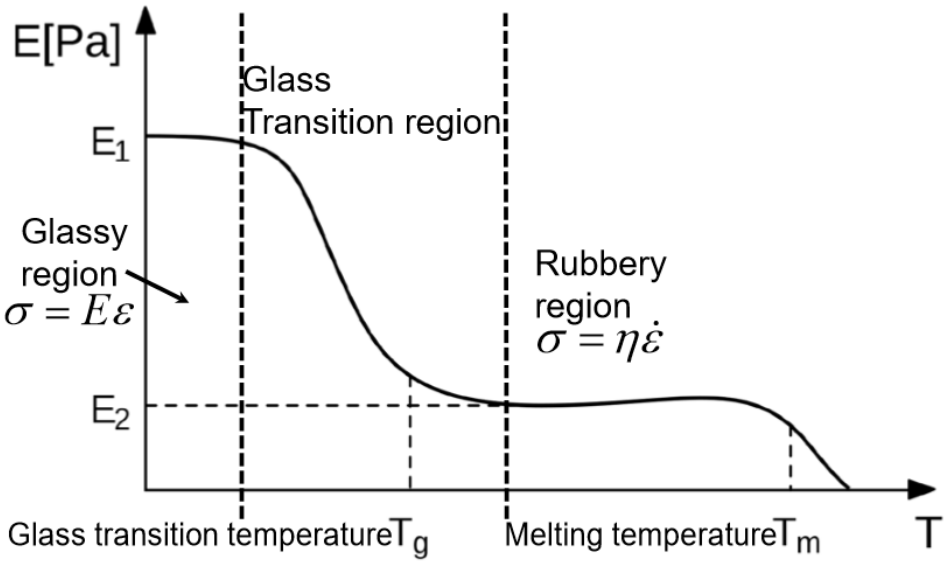

Figure 1.19: Elastic modulus response versus temperature change. Reprinted from [5].

1.6 Solubility and Permeability

Water diffusion follows Fick's law.

$$\frac{\partial C}{\partial t} = D\nabla^2 C \tag{1.1}$$

If there is a liquid in contact with a gas, then the concentration C is related to the the pressure of the gas p by Henry's Law.

$$C = Sp \tag{1.2}$$

where S is the solubility constant. This linear relationship holds at small concentrations until the saturation concentration is reached, where it can be written

$$C_{sat} = Sp_{sat} \tag{1.3}$$

Relative humidity R_H is defined as

$$R_H = \frac{C_{sat}}{C} \tag{1.4}$$

Within the context of saline soaking tests and in the context of medical implants, we simply assume R_H to be 100%. The form of the equation for the water saturation limit versus temperature is

$$M_\infty = A \exp \frac{-E_a}{RT} \tag{1.5}$$

Silicone oil is available in a variety of viscosities. In Figure 1.20, two viscosities of silicone oil (100 cSt and 10k cSt) were each examined for their water saturation limit by two different methods, the Karl Fischer method and the Freeze Dry method [59]. As seen in the figure, the water saturation limit of silicone oil is around 300 ±100 ppm at body temperature.

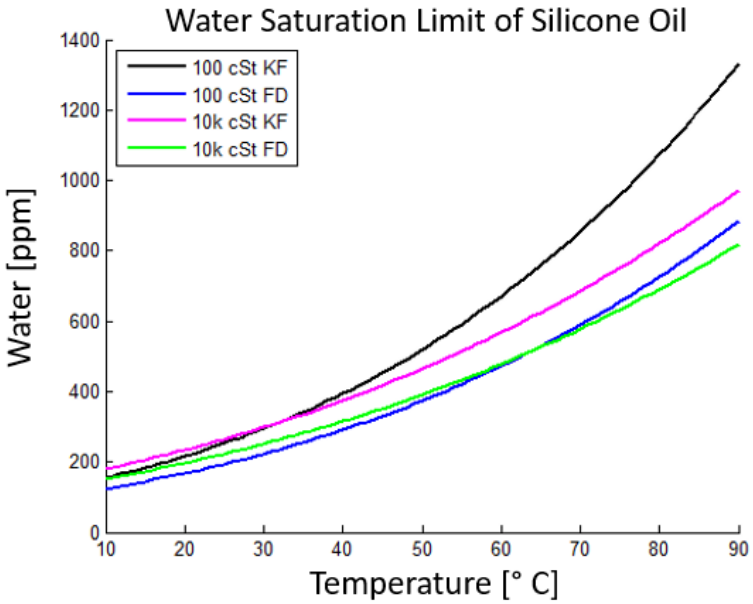

Figure 1.20: Water saturation limit for silicone oil versus temperature. Parameters and equation taken from [59].

The low saturation limit of the oil is key to limiting the electrolytic corrosion in the long term more than the permeation. Unless the permeability of the encapsulating material is low enough to be on the order of glass or hermetic metals, which parylene and other organic polymers are not, then the saturation limit of water at the interface or surface of metal or electronics is the determining factor, not the barrier properties [60]. In other words, since equilibrium will be reached, Fick's law is moot. See Tables 1.2 and 1.3 and Figure 1.21.

Also notice the much larger value of water vapor saturation limit for polyimide than for parylene or oil [63]. This is a significant bottleneck for the use of polyimide for very long term implants, although polyimide is admittedly easier to obtain/make since the technology is more mature. There are additional requirements for hermetic materials and packages, as is well documented [64].

Table 1.2: Water Vapor Saturation Limit. Temperatures provided when known.

Material	Water Sat. Limit	Comments
Silicone oil	300 ppm	At 37 °C [59]
Silicone gel	0.1%	At 23 °C [44], [61]
Parylene-N	<0.1%	After 24 hours [44]
Parylene-C	<0.1%	After 24 hours [44]
Parylene-D	<0.1%	After 24 hours [44]
Parylene-HT	<0.01%	After 24 hours [44]
Acrylic	0.3%	[44]
Polyimide	1.2-2.5%	At 23 °C [62]

Table 1.3: Water Vapor Transmission Rate (WVTR). Temperatures provided when known.

Material	WVTR mm g/(m^2 24h)	Comments
Silicone gel	1.7-47.5	At 23 °C [44], [61]
Parylene-N	0.59	After 24 hours [44]
Parylene-C	0.08	After 24 hours [44]
Parylene-D	0.09	After 24 hours [44]
Parylene-HT	0.22	After 24 hours [44]
Acrylic	13.9	[44]
Polyimide	88-1,350	At 23 °C [62]
Glass	10^{-6}	[65]
Metal	10^{-10}	[65]

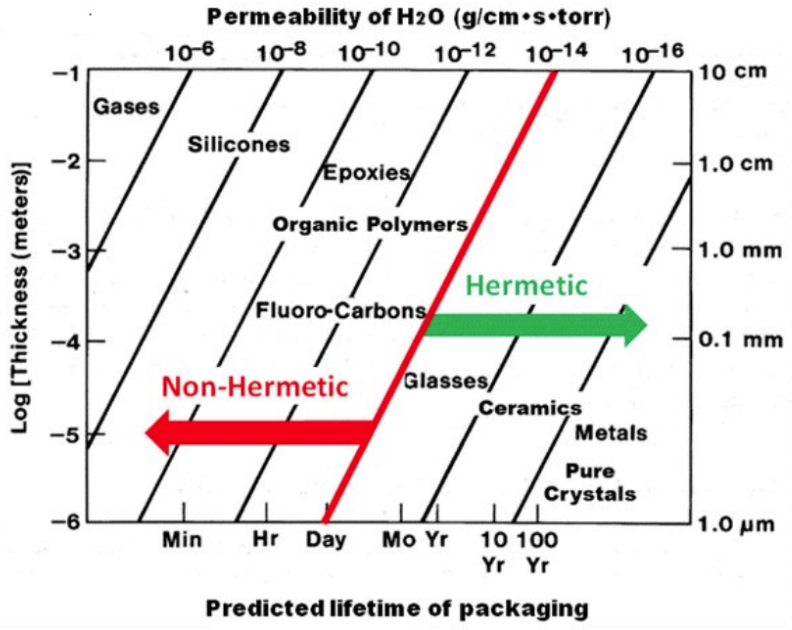

Figure 1.21: Water vapor permeability of various materials. Reprinted from [66].

1.7 Layout of Thesis

Chapter 1 provides context for this work. The main topic research content of the thesis is grouped into the two following chapters. Chapter 2 is on the pressure sensor packaging method, including the fundamentals of the theory and benchtop experiments pertaining solely to the pressure sensor packaging. Chapter 3 includes all discussions of the wireless implant, including some benchtop tests of components which exist on the implant, but not directly considered part of the pressure sensor packaging method itself. However, the purpose of the implant is towards proving the feasibility of the pressure sensor packaging method *in vivo* for long term. Overall conclusions are presented in Chapter 4.

There are two short chapters in the appendix on ancillary topics. Appendix A is on a preliminary experiment of packaging a battery with the same technique as for packaging the pressure sensors, and Appendix B is on preliminary work on constructing a glaucoma drainage tube that could be integrated with the implant discussed in Chapter 3.

1.8 Summary

This chapter introduced the fundamentals of MEMS pressure sensors in general, and described the context for how implantable pressure sensors might improve the treatment and monitoring of various diseases. Typical challenges preventing long term use because of drift or extraneous sources of inaccuracy, such as no temperature sensing, and various case studies of the failure point being long term use are shown. Next, the material parylene is introduced and important concepts of glass transition temperature and water solubility are discussed. More specific background about packaging implantable pressure sensors is discussed in the next chapter.

Chapter 2

PARYLENE-OIL-ENCAPSULATION FOR IMPLANTABLE PRESSURE SENSORS

Continuous internal body fluid pressure monitoring, rather than snapshot measurements taken in the clinic, in organs such as the heart, eye, brain, and bladder, is important to indicate health or progression of disease [4],[67]. Some examples of these diseases and symptoms to be monitored are restenosis, hypertension, heart failure, glaucoma, intracranial hypertension, and urinary incontinence. Although telemetric techniques exist for some applications, none provide adequate precision and accuracy, and catheterization is very invasive and can increase risk of infection. For example, no piezoresistive pressure sensor has lasted more than 1 month inside the body due to a variety of reasons ranging from electronics failure to sensitivity and offset drift. Note that both the sensitivity and offset drifts are the two most common failure modes and are often caused by the accumulation of biological material on the surface of the device (i.e., biofouling) which changes the mechanical properties of the membrane. Capacitive membrane-based implantable pressure sensors have had some success such as the FDA-approved CardioMEMS® sensor, and preliminary clinical trials of an intraocular pressure sensor with recalibrations for continued use up to 1 year. [68],[4]. This chapter then aims at packaging a commercially available pressure sensor device and maintaining its sensor accuracy for long term application (e.g., >12 months) in the body.

This packaging method is suitable for any sensor based on membrane deflection, namely piezoresistive or capacitive sensors. Piezoresistive sensors are prioritized in this paper because commercial piezoresistive pressure sensors are more popular in use due to their greater linearity than capacitive pressure sensors, which can suffer from parasitic capacitances [67]. Because the sensor's silicon membrane needs to be protected from the environment, the deflecting membrane is never in direct contact with body fluids just like the circuitry of any medical implant. However, the deflecting membrane needs to mechanically sense the environmental pressure.

The traditional way to protect pressure sensors is to use oil in a bulky, hermetic metal can, which attenuates power and transmission signals [69], [4],

[64]. Previous work involving oil without metal to transduce pressure from an ideally compliant outer membrane to the sensor membrane injects the oil into a bag structure [70],[71]. In contrast, this packaging technique encapsulates the entire sensor in oil before coating a layer of flexible parylene onto the oil. Parylene-on-oil chemical vapor deposition (CVD) has been investigated for making optical lenses out of oil [45], [72],[73] or to make isolated parylene films by separating the parylene after deposition [74],[75]. In general, it is possible to deposit parylene using CVD when the vapor pressure of the oil is low (<5 Pa) [76].

2.1 Packaging Concept

For long term implantation of a pressure sensor, the packaging must protect the functionality of the circuitry and the accuracy of the reported pressure. Circuit functionality degrades due to corrosion from water, water vapor, or ions exposed to the circuit. Thus stopping or minimizing water or ions from reaching the sensor is critical. Our approach is to change the chemical environment that the sensor stays in, rather than solely relying on a barrier. This is achieved by housing the electronics in a hydrophobic liquid, such as silicone oil, to reduce the concentration limit of water vapor in the sensor's environment. In silicone oil, the saturation limit of water vapor is around 350 ppm at 37 °C [59]. Here, silicone oil is a better choice over cured silicone, because even though both repel liquid water, only the silicone oil repels water vapor, while water vapor is drawn towards inevitable defects in the silicone [61]. One purpose of the parylene is to encapsulate the oil *in situ* without bubbles so the oil remains where it needs to be. Swelling of silicone gel is also possible and leads to inaccuracies, which are also lessened by the use of oil. The oil also reduces shear forces on submerged parts because it is a liquid. So in summary, compared to a sensor packaged with silicone gel, we switch the gel to oil for better water vapor rejection. But now since the oil is a liquid, we need to trap the oil where we intend to keep the oil. We trap the oil with parylene, which is also biocompatible. (See Figure 2.1).

In theory, one could also make a bag first, and place a sensor inside, but it complicates the removal of all bubbles. In contrast, the oil is placed over the sensor first, and then it is encapsulated *in situ*, bubble-free, because the CVD process happens in vacuum anyway. The bag-first approach needs an encapsulate or sealant anyways, whereas the parylene-oil-encapsulation (or parylene-on-oil deposition) encapsulates and forms the membrane simultaneously.

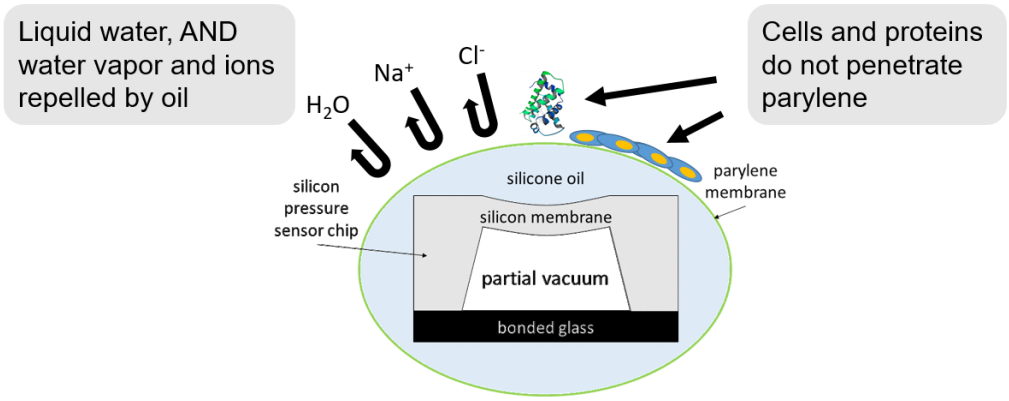

Figure 2.1: Concept for parylene-oil-encapsulation of implantable pressure sensors.

2.2 Failure Modes for Implanted Pressure Sensors and Additional Constraints Towards Practical Use in the Clinic

Since the bottleneck for achieving implantable pressure sensors in the clinic is to achieve long lifetimes with accurate measurements, considerations that affect lifetime and accuracy are important to discuss. They are grouped in two main categories, the chemical corrosion by nature of the sensor existing in an electrolytic environment, and mechanical loading or swelling effects.

Every factor needs to be addressed simultaneously. First, for each organ pressure, there will be a limited volume available to house an implant. So any packaging method must be space-efficient.

An example of a packaging method that is not space efficient is a hermetic metal can (Figure 2.2). The surrounding metal blocks wireless communication, so metal feedthroughs are needed to get signal out. These metal feedthroughs are large in order to be hermetically sealed while still passing current. But since the metal is rigid, the pressure sensing membrane cannot exist inside the metal can while measuring the small biological pressure sources.

Another factor to consider, even after assuming electrical corrosion is prevented entirely, is how to retain pressure sensing accuracy despite possible material buildup, also known as biofouling. There have been efforts in literature to prevent or mitigate the biofouling amount using ablation techniques or specially functionalized coatings [4], but they would run out before the full lifetime of a long lifetime device. We feel that if a packaging scheme could retain accuracy despite buildup, all of these difficulties are avoided. Luckily, since the parylene-oil-encapsulation

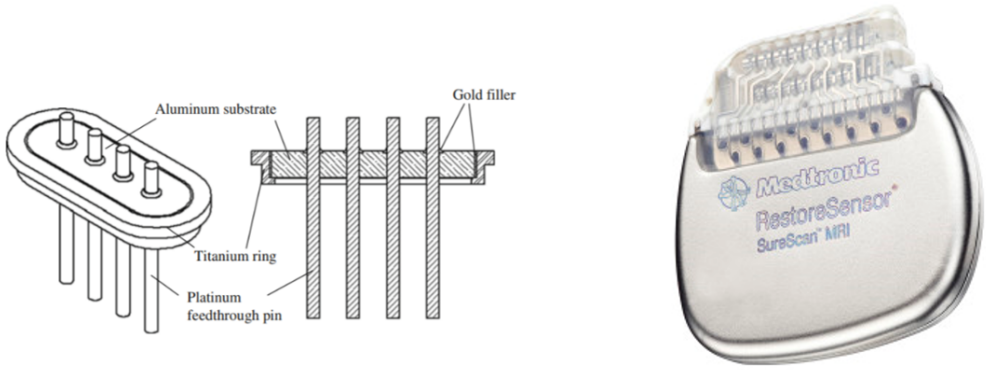

Figure 2.2: Hermetic metal cans require bulky feedthroughs to get the signal outside of the can. Reprinted from [64], [77].

scheme has an exterior membrane, it will be shown that the effect of sensitivity drift will be drastically suppressed. We do not make any mathematical claims about the effect of offset drift due to material buildup. However, since implantable pressure sensors are necessarily absolute pressure sensors (since there is no direct access to atmosphere), a small relative sensitivity error may appear like a large constant offset error. Previous literature may have reported offset errors that were indeed caused by sensitivity drifts if only one-point comparisons were done.

Most commercial pressure sensors have a layer of gel on top of the membrane, which is sufficiently protective for use in air. Coating parylene directly on gel has been investigated for implanted applications, but the gel absorbs gases, including water vapor, and can swell [4]. If the gel is directly coated with parylene, the swelling of the gel can cause sensitivity drift of up to 5% [41]. This work also coated parylene directly on commercial sensors with gel without oil for comparison, and measurement drift and delamination problems were observed in saline soaking tests. Thus, gel is not a viable substitute for oil in pressure sensor packaging for long term implantation.

Last, of course all the materials used in implants must be biocompatible, so only a limited selection of materials is available for use. By choice, silicone oil, and parylene-C and -HT are all class VI rated biocompatible by the FDA.

2.3 Thickness of Deposition on Oil versus Solids

Binh-Khiem, et al. showed that parylene can deposit on low-vapor pressure liquids as a porous layer, relatively rapidly; then after parylene saturates, further parylene accumulation grows at a rate equal to that on solids [75]. This is because at

the beginning of deposition, parylene monomer can reach the surface of the liquid, and get submerged, which is not possible for non-porous solids. This is especially true for hydrophobic liquids like silicone oil. Then, submerged parylene re-exposes the liquid surface again, explaining how the oil can saturate with porous parylene effectively instantly. Once a solid film of parylene is established, it coats as standard parylene, and grows in thickness identical to film growth on any other surface. The saturation process happens so quickly, it is practical to model the total thickness as the nominal deposition thickness as would be on a non-porous solid, plus a consistent porous layer thickness (PLT) which is depended on liquid substrate and parylene dimer type, but not the amount of dimer. This process is explained in Figure 2.3.

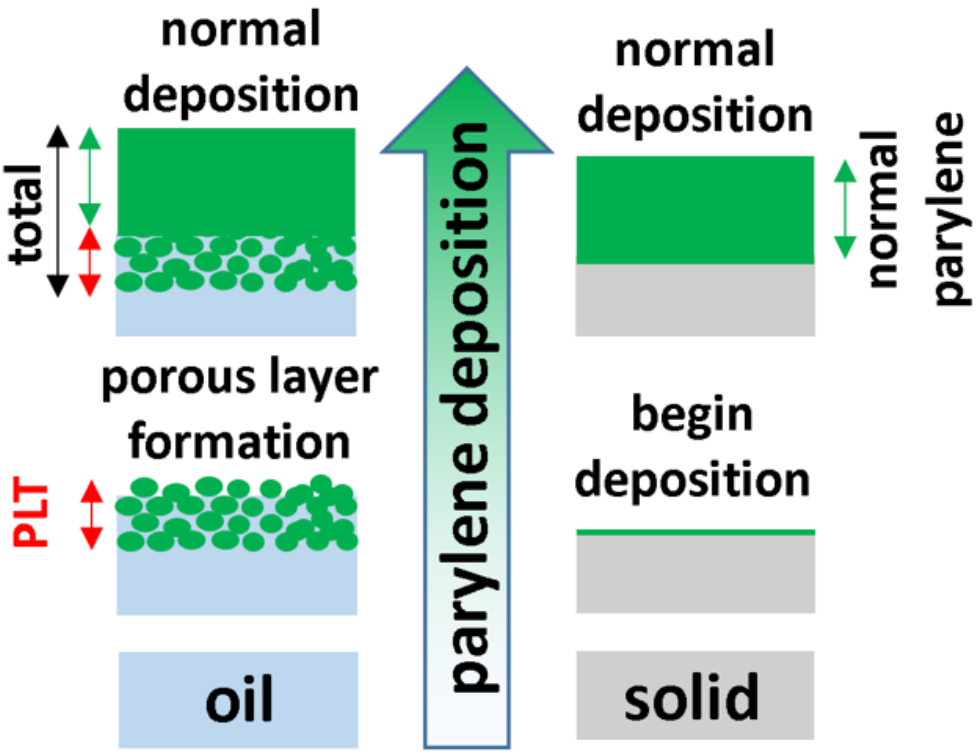

Figure 2.3: Parylene deposition on oils versus solids. The initial conditions is at the bottom of the image, and increased parylene deposition is seen moving upwards.

A plot of the deposition thickness versus nominal thickness with time indicators is shown time is shown in Figure 2.4 [75]. A scanning electron microscopy (SEM) image of the cross-section of the porous film is shown in Figure 2.5 [75].

We directly measured the film thickness with a profilometer. We coated parylene on silicone oil, cut out parylene films with a blade, washed away the oil in an acetone bath, and laid them flat on glass slides. Since parylene-on-oil deposition

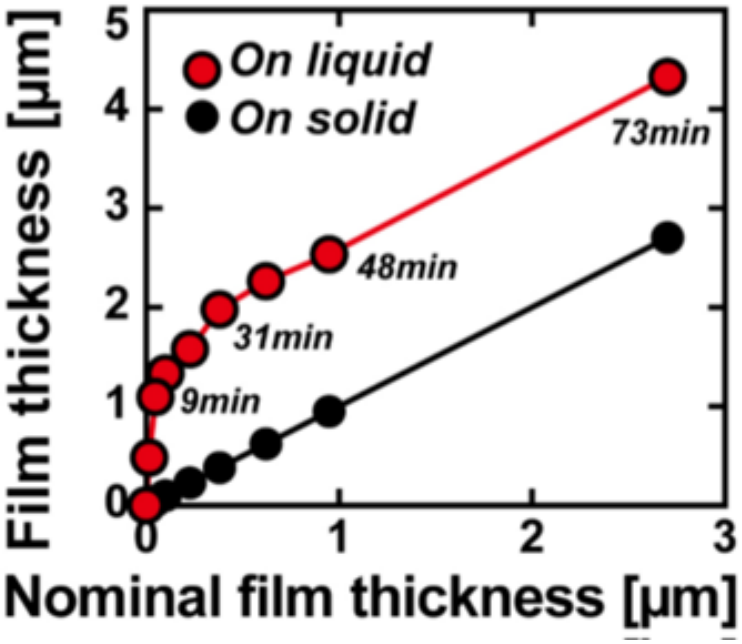

Figure 2.4: Parylene deposition on liquid versus solids with time indicators, where solid is considered the nominal thickness. Reprinted from [75].

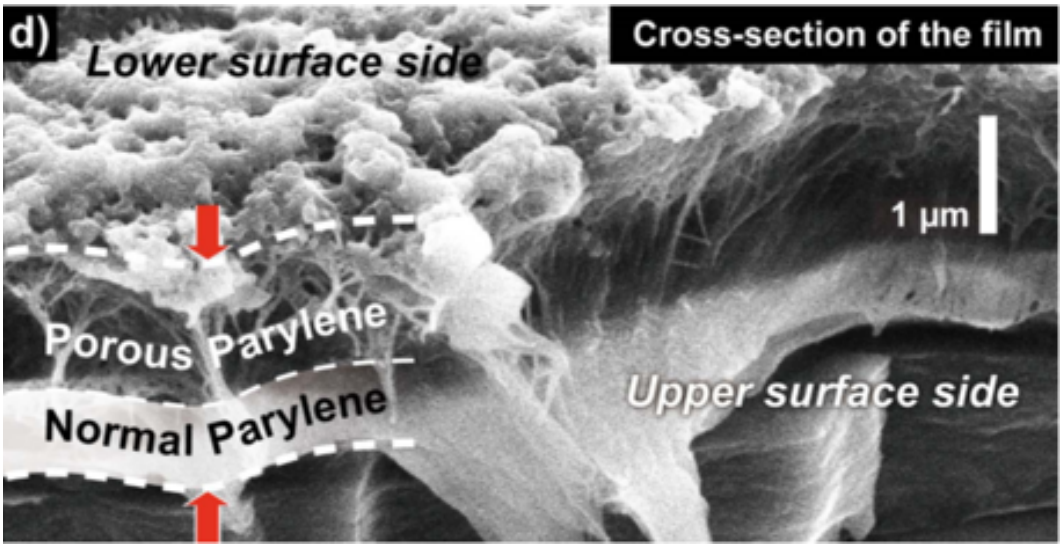

Figure 2.5: SEM cross-section of parylene coated onto a liquid. The lower side of the surface is in the top side of the image, and the porous quality of the parylene on the liquid side is evident. Reprinted from [75].

can result in a wrinkled film, attention and interpretation for flat, parylene-glass contacted segments using the profilometer data in conjunction with microscope visual confirmation was required. This method made extremely small dimer weights

difficult to measure, as the parylene film would rip if the non-porous parylene layer was too thin when trying to remove it from the oil. Figure 2.6 shows an example dish filled with silicone oil and coated with parylene, and the piece laid on a glass slide. The dotted line and arrow indicate the step and direction measured by the profilometer.

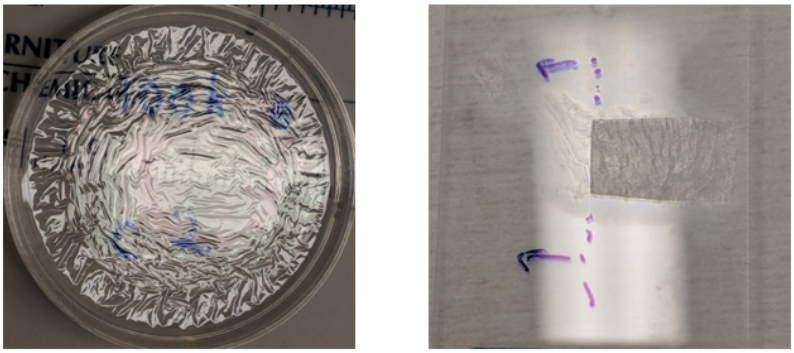

Figure 2.6: Samples to measure the porous layer thickness (PLT). Silicone oils of different molecular weights/viscosities were prepared in dishes as shown on the left. Then after parylene deposition, the films were excised with a razor blade, cleaned with acetone, and placed on glass slides as shown on the right.

The PLT is inferred as the extra anomalous thickness for films coated on silicone versus the thickness on a glass slide from the same run (Figure 2.7). We deposited parylene-C, and –HT (PA-C, PA-HT) on various viscosities of silicone oil.

Figure 2.8 shows the PLT versus molecular weights (MW), which was matched to the listed viscosity according to [78]. In agreement with a diffusion model for parylene penetration into liquid, the PLT is smaller with logarithmic increase in MW of the oil. The PLT varied from around 810 μm for 2k Da (= 20 cSt) silicone oil, and was around 1-2 μm for 139k Da (=100k cSt) silicone oil. Only PA-C and PA-HT PLT thicknesses were characterized, as opposed to also including PA-D, because PA-C and PA-HT are approved for implantation by the FDA, whereas PA-D is not presently approved.

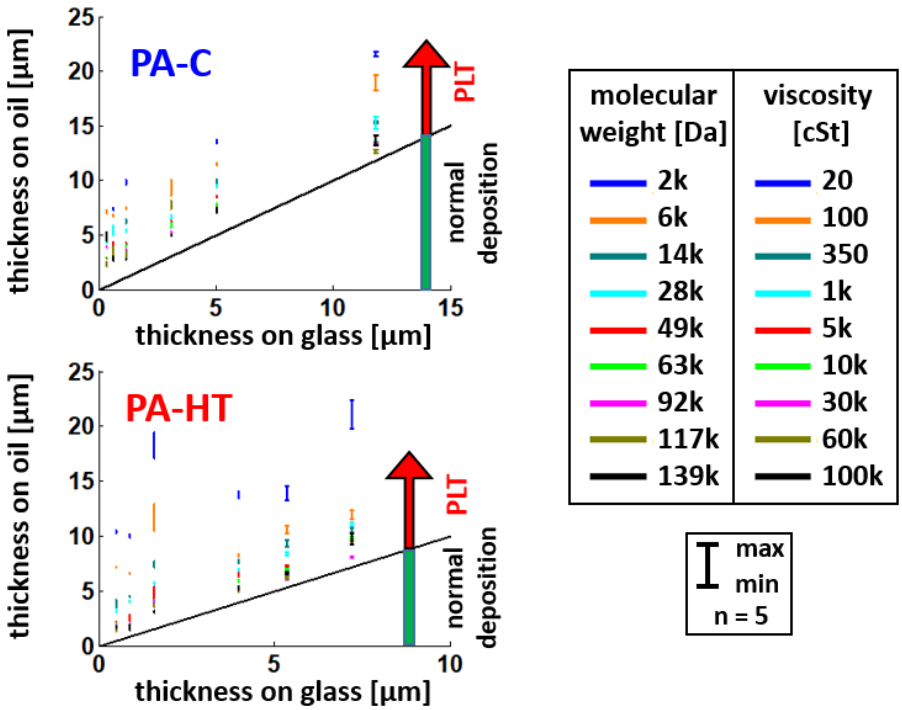

Figure 2.7: Raw thickness measurement data of parylene-C (PA-C) and parylene-HT (PA-HT) coated on silicone oils of different molecular weights. In the same runs, simultaneous depositions on glass slides define the nominal thickness.

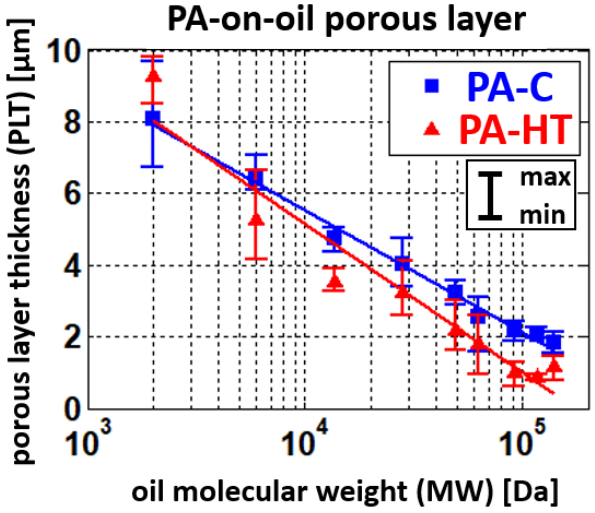

$$PLT_C[\mu m] = -3.42\log(MW\ [Da]) + 19.2$$

$$PLT_{HT}[\mu m] = -4.16\log(MW\ [Da]) + 21.8$$

Figure 2.8: Parylene porous layer thickness (PLT) versus molecular weight (MW).

2.4 As-deposited Stress of Parylene-on-Oil

The as-deposited stress of parylene-on-oil films can influence the pressure reading if encapsulating a pressure sensor. It was previously reported that parylene deposited on liquids produces zero or tensile stress, but that is based on incomplete experiments [79]. In fact, tensile and compressive stress states are possible, depending on the parylene type, thickness, and liquid type and molecular weight, as evidenced by the presence of wrinkles indicating compressive stress, or no wrinkles, indicating small or tensile stress. See Figures 2.9 and 2.10.

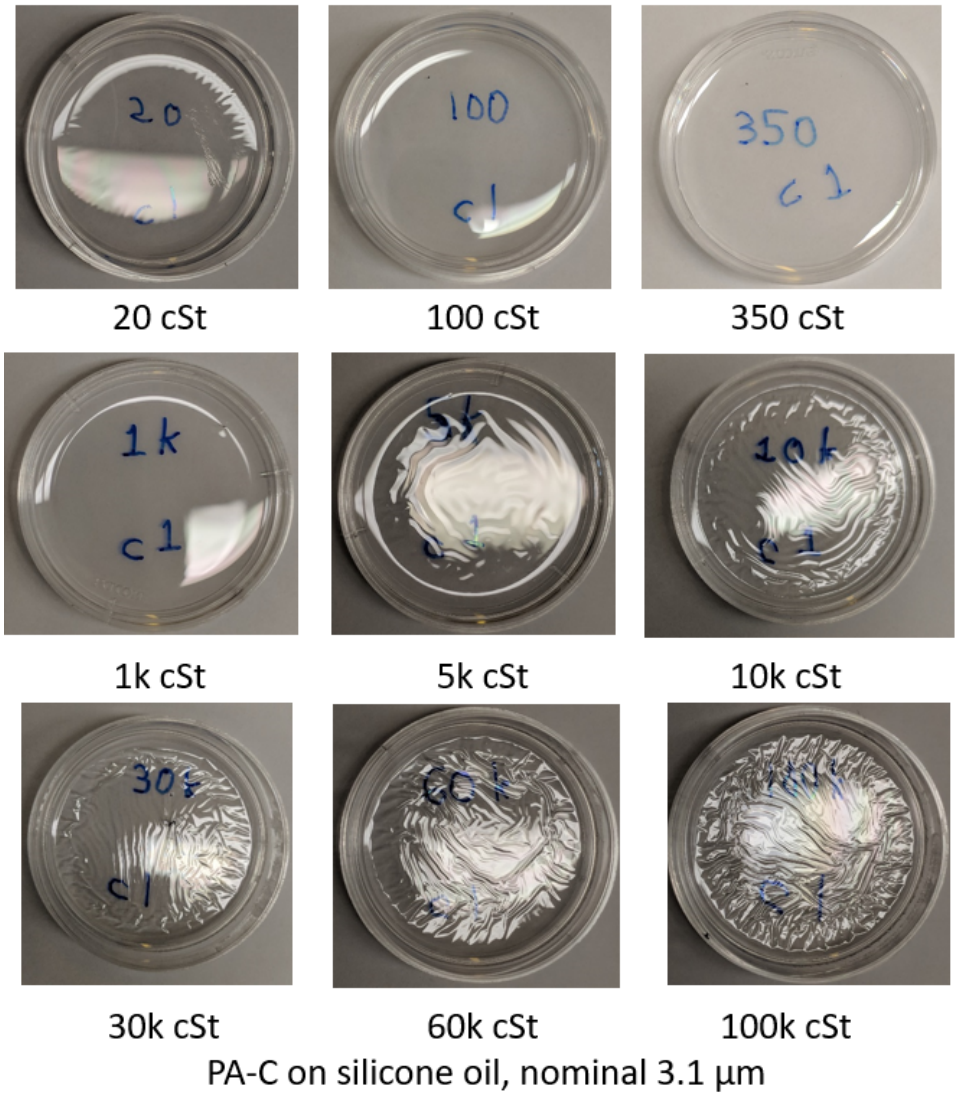

Figure 2.9: Parylene-C on silicone oils show increased wrinkling on higher viscosities/molecular weights. Dishes are 35 mm diameter.

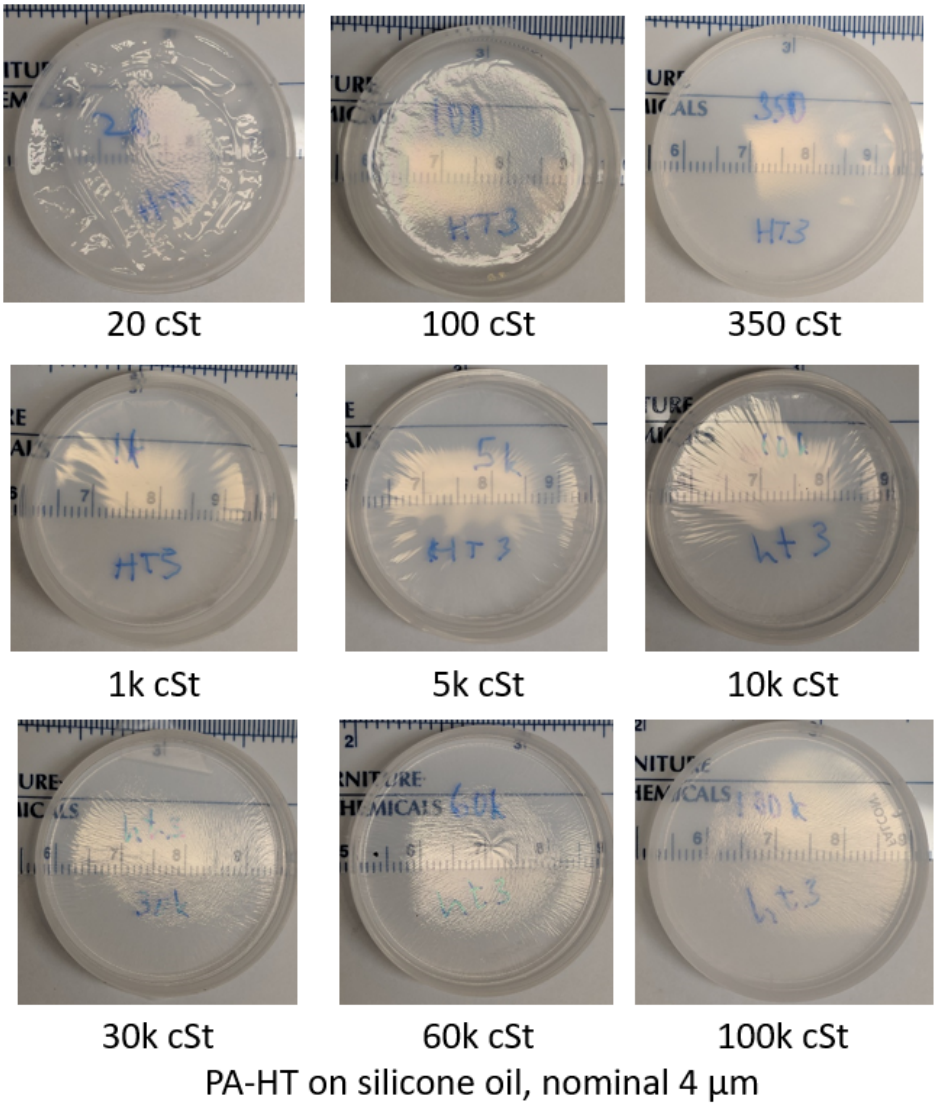

Figure 2.10: Parylene-HT on silicone oils show increased wrinkling on higher viscosities/molecular weights. Dishes are 35 mm diameter.

Notice that the PA-D samples in Figure 2.11 show smooth parylene films for all viscosities, rather than wrinkles as for parylene-C and parylene-HT films. Since early on I was using PA-D on oil, the wrinkling nature was not discovered immediately. Nonetheless, eventually PA-HT was used because of its superior FDA approval and higher glass transition temperature instead of PA-D.

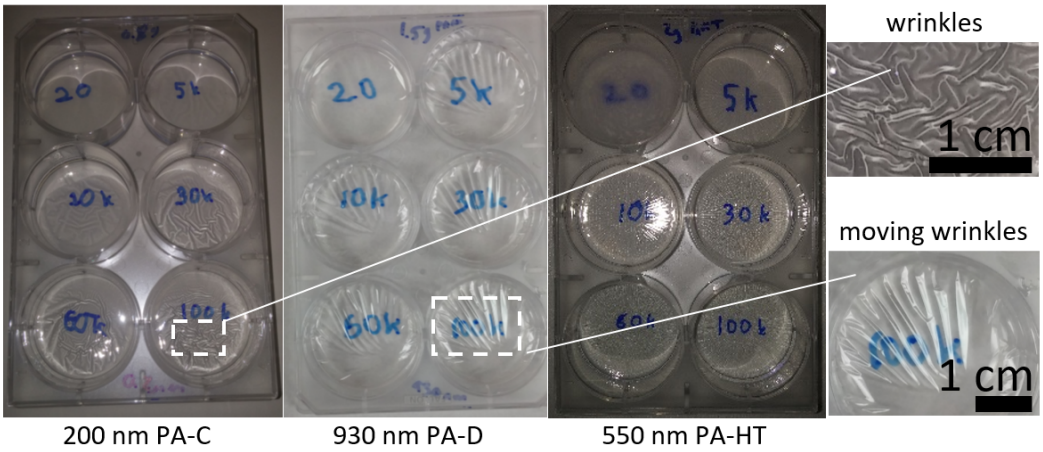

Figure 2.11: Stress of parylene-on-oil. Nominal 200 nm PA-C, 930 nm PA-D, and 550 nm PA-HT on silicone oil, ranging from 20 cSt to 100k cSt viscosity. Signs of stress of parylene on oil depends on parylene type and viscosity. For PA-C, smooth film on 20 cSt oil indicating tensile stress, progresses to a wrinkled surface on 100k cSt oil, indicating compressive stress. For PA-D, wrinkles are not seen at any viscosity, indicating tensile stress. PA-HT deposits as murky white film on 20 cSt, but is otherwise similar to PA-C. Note that the wrinkles, which do not shift during movement, have higher spatial frequency than the folds, which do shift during movement (see right).

2.5 Theoretical Error Expected Due to Drifts

First let us define the term relative sensitivity (see Figure 2.12).

$$S_{r_{state}} = \frac{\text{Signal in current state}}{\text{Signal before packaging}} \tag{2.1}$$

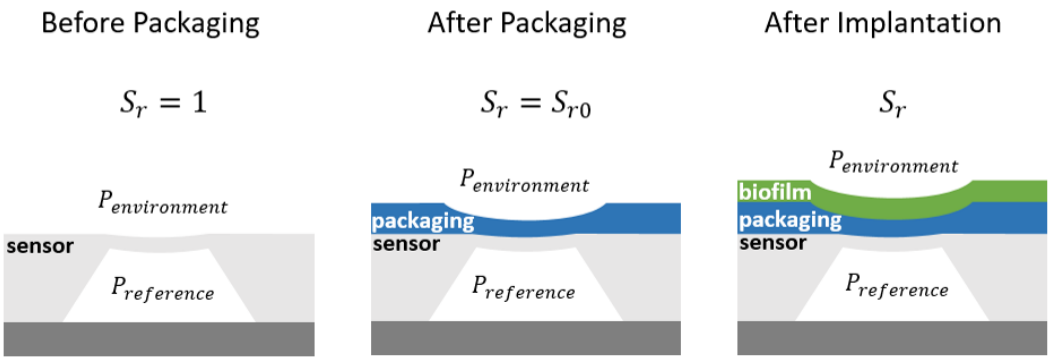

Figure 2.12: Definition of relative sensitivity S_r.

P_{env} - actual environment pressure (true absolute pressure)
$P_{env,calc}$ - estimated environment pressure
P_{error} - difference between $P_{env,calc}$ and P_{env}
P_{ref} - actual pressure inside chamber
P_{ref0} - reference pressure value in memory
$P_{reported}$ - signal from sensor + P_{ref0}
S_r - relative sensitivity
S_{r0} - relative sensitivity after packaging only
c_T - actual temperature coefficient for pressure
c_{T0} - temperature coefficient for pressure after packaging only
T - actual temperature
T_{error} - error in temperature reading
$T_{reported}$ - reported temperature by sensor
T_{bias} - arbitrary bias temperature value
$P_{offset,T_{bias}}$ - actual pressure offset at $T = T_{bias}$
$P_{offset,T_{bias},0}$ - pressure offset at $T = T_{bias}$ after packaging only
$\square_0$ - subscript denotes a calibrated value, or a value which could be composed from measurable values after packaging prior to implantation

Say we have a calibrated pressure reference so that P_{env} is known. Now let us discuss a pressure sensor. The signals reported by the sensor, in terms of pressure and temperature are

$$P_{reported} = (P_{env} - P_{ref})S_r + c_T(T - T_{bias}) + P_{offset,T_{bias}} + P_{ref0} \tag{2.2}$$

$$T_{reported} = T + T_{error} \tag{2.3}$$

At this point, P_{ref0} is set to equal a known P_{ref}. The first term uses P_{ref} because that is the actual pressure inside the chamber, and the last term is P_{ref0} because that is the amount to adjust according to a value in memory. Before packaging, $S_r = 1$ by definition, but other variables can have any value.

After packaging, there can be calibrations such that the true P_{env} is reproduced by $P_{env,calculated}$ without discrepancy at the time of calibrations.

$$P_{env,calculated} = \frac{(P_{reported} - P_{ref0}) - c_{T0}(T_{reported} - T_{bias}) - P_{offset,T_{bias},0})}{S_{r0}} + P_{ref0} \tag{2.4}$$

In transforming equation (2.2) to equation (2.4) by isolating P_{enc}, the term P_{ref} from the former equation now becomes P_{ref0} in the latter because the value of all non-reported quantities must be assumed. Therefore,

$$P_{error} = P_{env,calc} - P_{env} \tag{2.5}$$

$$= \frac{(P_{reported} - P_{ref0}) - c_{T0}(T + T_{error} - T_{bias}) - P_{offset,T_{bias},0}}{S_{r0}} + P_{ref0} - P_{env} \tag{2.6}$$

The next several equations are just algebra.

$$\begin{aligned} P_{error} = \frac{1}{S_{r0}}\Big[\Big((P_{env} - P_{ref})S_r + c_T(T - T_{bias}) + P_{offset,T_{bias}} + P_{ref0} - P_{ref0}\Big) \\ - c_{T0}(T + T_{error} - T_{bias}) - P_{offset,T_{bias},0}\Big] \\ + P_{ref0} - P_{env} \end{aligned} \tag{2.7}$$

$$\begin{aligned} P_{error} = \frac{1}{S_{r0}}\Big[\Big((P_{env} - P_{ref})S_r + c_T(T - T_{bias}) + P_{offset,T_{bias}}\Big) \\ - c_{T0}(T + T_{error} - T_{bias}) - P_{offset,T_{bias},0}\Big] \\ + P_{ref0} - P_{env} \end{aligned} \tag{2.8}$$

$$\begin{aligned} P_{error} = P_{env}\Big(\frac{S_r}{S_{r0}} - 1\Big) + \Big(P_{ref0} - \frac{S_r}{S_{r0}}P_{ref}\Big) \\ + \frac{(c_T - c_{T0})(T - T_{bias})}{S_{r0}} + \frac{(P_{offset,T_{bias}} - P_{offset,T_{bias},0})}{S_{r0}} + \frac{c_{T0}T_{error}}{S_{r0}} \end{aligned} \tag{2.9}$$

$$P_{error} = P_{env}\left(\frac{S_r - S_{r0}}{S_{r0}}\right) + \left(\frac{S_{r0}}{S_{r0}}P_{ref0} - \frac{S_r}{S_{r0}}(P_{ref0} + \Delta P_{ref})\right) + \frac{\Delta c_T(T - T_{bias})}{S_{r0}} + \frac{\Delta P_{offset,T_{bias}}}{S_{r0}} + \frac{c_{T0}T_{error}}{S_{r0}} \tag{2.10}$$

$$= P_{env}\left(\frac{\Delta S_r}{S_{r0}}\right) + \left(-\frac{\Delta S_r}{S_{r0}}P_{ref0} - \frac{S_r}{S_{r0}}\Delta P_{ref}\right) + \frac{\Delta c_T(T - T_{bias})}{S_{r0}} + \frac{\Delta P_{offset,T_{bias}}}{S_{r0}} + \frac{c_{T0}T_{error}}{S_{r0}} \tag{2.11}$$

$$= (P_{env} - P_{ref0})\left(\frac{\Delta S_r}{S_{r0}}\right) - \frac{S_r}{S_{r0}}\Delta P_{ref} + \frac{\Delta c_T(T - T_{bias})}{S_{r0}} + \frac{\Delta P_{offset,T_{bias}}}{S_{r0}} + \frac{c_{T0}T_{error}}{S_{r0}} \tag{2.12}$$

The next equation is full absolute pressure error expected due to drift.

$$P_{error} = \left(\frac{1}{S_{r0}}\right)\left[(P_{env} - P_{ref0})\Delta S_r + \Delta c_T(T - T_{bias}) + \Delta P_{offset,T_{bias}} + c_{T0}T_{error} - S_r\Delta P_{ref}\right] \tag{2.13}$$

ΔP_{ref},T_{error}, are internal issues only, and additional packaging has minimal effect on those terms. Assuming they are zero, (such that $P_{ref} = P_{ref0}$),

$$\boxed{P_{error} = \left(\frac{1}{S_{r0}}\right)\left[(P_{env} - P_{ref})\Delta S_r + \Delta c_T(T - T_{bias}) + \Delta P_{offset,T_{bias}}\right]} \tag{2.14}$$

Next, if $S_{r0} \approx 1$, then

$$P_{error} = (P_{env} - P_{ref})\Delta S_r + \Delta c_T(T - T_{bias}) + \Delta P_{offset,T_{bias}} \tag{2.15}$$

Notice that stiffening the additional packaging, even with calibration before implanting, necessarily makes the offset pressure drift and temperature-dependent pressure drift worse. The sensitivity drift is more complicated, but given that the sensitivity drift of packages with oil is nearly zero, as derived in the next section, there is clear motivation to maintain the original sensitivity.

2.6 Analytical Model of Relative Sensitivity

Here an analysis of the relative sensitivity after packaging with parylene-oil-encapsulation is provided. Relative sensitivity is defined as the interpreted unit change in pressure per unit change in environmental pressure. For example, if the pressure sensor is originally housed in a fluid and then packaged with parylene-oil-encapsulation, the relative sensitivity will be the change in pressure in the oil immediately adjacent to the electrically-active, deflecting membrane, divided by the change in pressure in the outer fluid. Theoretically, relative sensitivity should have a value between 0 and 1, with an ideal value of 1.

2.6.1 Parylene-Oil-Encapsulation Model, No Bubbles

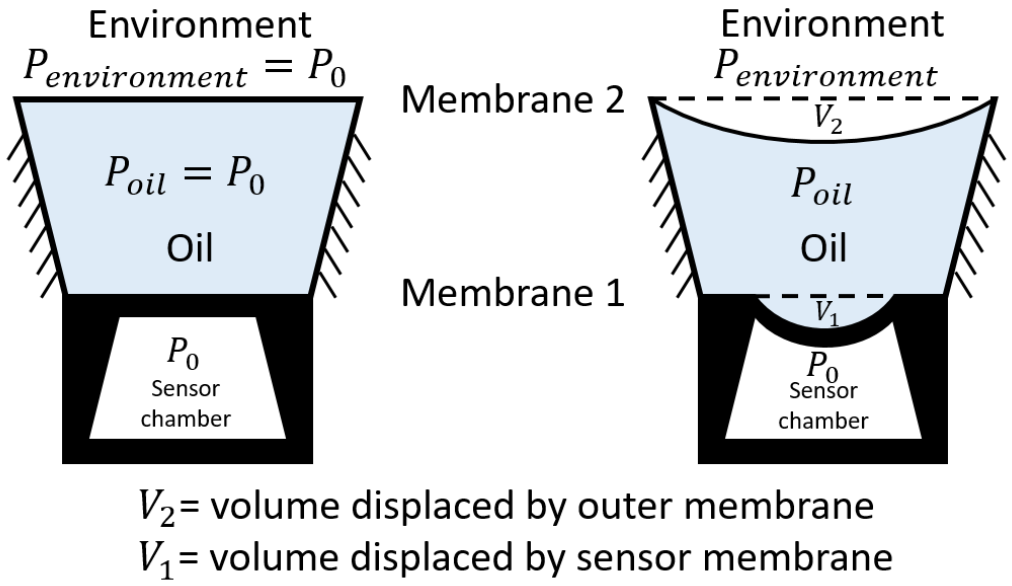

Figure 2.13: "Funnel model" to derive the relative sensitivity S_r.

In this model, other than the flexible membrane, the funnel walls are rigid and the oil has bulk modulus K. We assume a fixed value of P_0, the initial pressure inside the sensor chamber. The absolute sensitivity of a piezoresistive pressure sensor is reported in output voltage per supply voltage per unit pressure. Please follow starting Figure 2.13. P_{oil} refers to the absolute pressure in the oil. $P_{environment}$, or P_{env} for short, is the absolute pressure in the exterior environment. Since the pressure sensor is submerged in oil, by definition,

$$S_{sensor} \equiv \frac{dV_{sensor}/V_{supply}}{dP_{oil}} \tag{2.16}$$

The absolute sensitivity of the packaged sensor with respect to the environment of interest is

$$S_{package} \equiv \frac{dV_{sensor}/V_{supply}}{dP_{environment}} \tag{2.17}$$

Thus, relative sensitivity after packaging is

$$S_r \equiv \frac{S_{package}}{S_{sensor}} = \frac{dP_{oil}}{dP_{environment}} \tag{2.18}$$

because the relative voltage cancels out as the silicon membrane has not changed. We assume an initial condition $P_{env} = P_{oil} = P_0$, so we can rewrite (2.18) as

$$S_r = \frac{P_{oil} - P_0}{P_{environment} - P_0} \tag{2.19}$$

Equations (2.20)-(2.23) are straightforward:

$$dP_{oil} = -\frac{K}{V_oil} dV_{oil} \tag{2.20}$$

$$V_{oil} = V_1 - V_2 + V_{funnel} \tag{2.21}$$

$$dV_{oil} = V_1 - V_2 \tag{2.22}$$

$$dP_{oil} = P_{oil} - P_0 \tag{2.23}$$

Substituting (2.21), (2.22), and (2.23) into (2.20) yields

$$P_{oil} - P_0 = \frac{K}{V_1 - V_2 + V_{funnel}}(V_2 - V_1) \tag{2.24}$$

In most cases $V_{funnel} \gg V_1, V_2$, so we can simplify (2.24) as such,

$$P_{oil} - P_0 \approx \frac{K}{V_{funnel}}(V_2 - V_1) \tag{2.25}$$

Under the assumption of small deflections, the volume displaced by each membrane is linear with the pressure difference across the membrane. We then define the volume-pressure compliance c as such,

$$V = cp \tag{2.26}$$

Assuming a thick circular membrane, the deflection as a function of distance from the center $w(r)$ is [80],

$$w(r) = \frac{pa^4}{64D}\left(1 - \frac{r^2}{a^2}\right)^2 \tag{2.27}$$

where flexural rigidity D is,

$$D = \frac{Et^3}{12(1-\nu^2)}$$

p is the differential pressure across the membrane, a is the radius, E is Young's modulus, ν is the Poisson ratio,and t is the thickness of the membrane. It can then be shown that,

$$V = \int_0^a 2\pi r w(r) dr = \frac{pa^6\pi}{192D} = cp \tag{2.28}$$

for the volume-pressure compliance c, and the volume swept is indeed linear with pressure for small deflections. Similarly, the derivation can be done for square membranes of side length $2a$ [80],

$$w(x,y) = \frac{2pa^4}{99D}\left(1 - \frac{x^2}{a^2}\right)^2\left(1 - \frac{y^2}{a^2}\right)^2 \tag{2.29}$$

and

$$V = \int_a^a \int_a^a w(x,y) dx dy \approx \frac{pa^6}{43.5D} = cp \tag{2.30}$$

Applying (2.26) yields

$$V_1 = c_1(P_{oil} - P_0) \tag{2.31}$$

$$V_2 = c_2(P_{environment} - P_{oil}) \tag{2.32}$$

Substituting (2.31) and (2.32) into (2.25) results in

$$P_{oil} - P_0 = \frac{K}{V_{funnel}}\Big(c_2\big(P_{env} - P_{oil}\big) - c_1\big(P_{oil} - P_0\big)\Big) \tag{2.33}$$

Combine like terms for the intermediate equation

$$\left(c_1 + \frac{V_{funnel}}{K}\right)(P_{oil} - P_0) = c_2(P_{env} - P_{oil}) \tag{2.34}$$

to get the relative sensitivity

$$S_r = \frac{P_{oil} - P_0}{P_{environment} - P_0} = \frac{c_2}{c_1 + c_2 + \frac{V_{funnel}}{K}} \tag{2.35}$$

First of all, if the bulk modulus K is large, or the initial volume of the oil (V_{funnel}) is small, as are often the cases, then we can simplify (2.35) to

$$S_r = \frac{P_{oil} - P_0}{P_{environment} - P_0} = \frac{c_2}{c_1 + c_2} \tag{2.36}$$

We can now determine the expected error due to a change in the outer compliance $c_{2_0} \rightarrow c_2$ (c_1 remains unchanged). Starting from the relevant terms in equation (2.14),

$$P_{error|\Delta c_2} = \left(\frac{1}{S_{r0}}\right)\left[(P_{env} - P_{ref})\Delta S_{r|\Delta c_2}\right] \tag{2.37}$$

$$= (P_{env} - P_{ref})\left(\frac{c_1 + c_{2_0}}{c_{2_0}}\right)\left(\frac{c_2}{c_1 + c_2} - \frac{c_{2_0}}{c_1 + c_{2_0}}\right) \tag{2.38}$$

$$= (P_{env} - P_{ref})\left(\frac{c_1 + c_{2_0}}{c_{2_0}}\right)\left(\frac{c_2(c_1 + c_{2_0}) - c_{2_0}(c_1 + c_2)}{(c_1 + c_2)(c_1 + c_{2_0})}\right) \tag{2.39}$$

$$P_{error|\Delta c_2} = (P_{env} - P_{ref})\left(\frac{c_1}{c_{2_0}}\right)\left(\frac{c_2 - c_{2_0}}{c_1 + c_2}\right) \tag{2.40}$$

The absolute minimum c_2 can be is 0, which is equivalent to saying $S_r = 0$, the signal ignores pressure variation entirely. But consider the scenario where the outer compliance decreases many times, yet does not go to 0 such that $c_1 \ll c_2 \ll c_{2_0}$,

$$\left(\frac{c_1}{c_{2_0}}\right)\left(\frac{c_2 - c_{2_0}}{c_1 + c_2}\right) \rightarrow \left(\frac{c_1}{c_{2_0}}\right)\left(\frac{-c_{2_0}}{c_2}\right) = -\frac{c_1}{c_2} \tag{2.41}$$

So that

$$P_{error|\Delta c_2} = -(P_{env} - P_{ref})\left(\frac{c_1}{c_2}\right) \tag{2.42}$$

This tells us that as long as $c_1 \ll c_2$ including after biofouling, the sensitivity component of the pressure error will be small. This is easily achievable because $c \propto \frac{a^6}{Et^3}$. In other words, increasing the effective outer membrane's radius has a large impact on c_2. Before biofouling starts the LPS25H ©STMicroelectronics pressure sensor has a square footprint $(2.5\ \text{mm})^2$ and a square sensing membrane $(280\ \mu\text{m})^2$. Using 1.5 µm of parylene, and assuming a standard thickness (10 µm) for the silicon membrane, the estimated ratio of c_{2_0} to c_1 is larger than 10^9.

2.6.2 Relative Sensitivity of Oil versus No Oil, and Theoretical Motivation Even with Initial Calibration

As stated earlier, the larger exterior membrane means that, for the same thickness of biofouling, the effect on the reduction of sensitivity is less than if the pressure sensor was directly covered with parylene. In other words, the sensitivity drift is predicted to be negligible with the parylene-oil-encapsulation. It is imperative to understand that the sensitivity drift can be mistaken as a large offset drift if there is typically a large pressure difference across the piezoelectric membrane. One might try to recalibrate the device by updating the constant offset only, when it is appropriate to update the assumed sensitivity. However, estimating sensitivity drift over time is harder than for offset drift because it requires multiple point calibration. The problem with drift is that it is impossible to perfectly predict over time, inevitably leading to accuracy degradation. The larger the drift, the harder it is to estimate to the same absolute level of precision. Thus suppressing drift, especially sensitivity drift if possible, is a fruitful strategy.

To model the effect of parylene or other material deposited onto another membrane, the theory of multilayer plates is used. The funnel model is not appropriate is parylene deposits directly onto silicon without any gel or oil in between, since now all diaphragm layers must have the same curvature. Likewise, multilayer plate theory should be used to model material accumulation on the appropriate membrane.

Once the flexural rigidity D of a composite membrane is known, the bending of the membrane can be computed. There are two equivalent versions of writing the equation:

Version A, 'intuitive version': Say there are m layers, with thicknesses t_i. The bending moment M is

$$M = -\sum_{i=1}^{m} \int_{h_{i-1}}^{h_i} \sigma_{x_i}(z - \bar{h}) dz \tag{2.43}$$

where z is the transverse direction and

$$h_0 = 0, h_1 = t_1, h_i = h_{i-1} + t_i,$$

$$\sigma_{x_i} = E_i'(z - \bar{h}) \frac{d^2 y}{dx^2}$$

where

$$E_i' = \frac{E_i}{1 - \nu_i^2}$$

and center of rigidity $\bar{h}$ is

$$\bar{h} = \frac{\sum_{i=1}^{m} E_i' t_i Y_i}{\sum_{i=1}^{m} E_i' t_i}$$

where centers of layers

$$Y_i = \frac{h_{i-1} + h_i}{2} = h_{i-1} + \frac{t_i}{2} = h_i - \frac{t_i}{2}$$

After solving the integral:

$$M = -\sum_{i=1}^{m} \frac{E_i'}{3} \left[(h_i - \bar{h})^3 - (h_{i-1} - \bar{h})^3 \right] \frac{d^2 y}{dx^2} \tag{2.44}$$

Flexural rigidity D is

$$M = -D \frac{d^2 y}{dx^2} \tag{2.45}$$

So

$$\boxed{D = \sum_{i=1}^{m} \frac{E_i'}{3} \left[(h_i - \bar{h})^3 - (h_{i-1} - \bar{h})^3 \right]} \tag{2.46}$$

Version B, 'polynomials' version: An equivalent, but separately derived version of D is found in [81], which is a special case for small-deflections from the general derivation provided in [82].

$$\boxed{D = C - \frac{B^2}{A}} \tag{2.47}$$

where

$$A = \sum_i E_i' (h_i - h_{i-1})$$

$$B = \sum_i \frac{E_i'}{2} (h_i^2 - h_{i-1}^2)$$

$$C = \sum_i \frac{E_i'}{3} (h_i^3 - h_{i-1}^3)$$

A short proof of the equality of both versions is provided here.

$$D_1 = \sum_i \frac{E_i'}{3}\Big[(h_i - \bar{h})^3 - (h_{i-1} - \bar{h})^3\Big]$$

$$D_2 = C - \frac{B^2}{A}$$

Note that

$$\bar{h} = \frac{\sum_{i=1}^m E_i' t_i Y_i}{\sum_{i=1}^m E_i' t_i} = \frac{\sum_{i=1}^m E_i'(h_i - h_{i-1})(\frac{h_i + h_{i-1}}{2})}{\sum_{i=1}^m E_i'(h_i - h_{i-1})} = \frac{\sum_{i=1}^m \frac{E_i'}{2}(h_i^2 - h_{i-1}^2)}{\sum_{i=1}^m E_i'(h_i - h_{i-1})} = \boxed{\frac{B}{A}}$$

$$D_1 = \sum_i \frac{E_i'}{3}\Big[(h_i - \bar{h})^3 - (h_{i-1} - \bar{h})^3\Big]$$

$$= \sum_i \frac{E_i'}{3}\big[h_i^3 - 3h_i^2\bar{h} + 3h_i\bar{h}^2 - \bar{h}^3 - h_{i-1}^3 + 3h_{i-1}^2\bar{h} - 3h_{i-1}\bar{h}^2 + \bar{h}^3\big]$$

$$= \sum_i \frac{E_i'}{3}\big[h_i^3 - h_{i-1}^3 - 3h_i^2\bar{h} + 3h_i\bar{h}^2 + 3h_{i-1}^2\bar{h} - 3h_{i-1}\bar{h}^2\big]$$

$$= \sum_i \frac{E_i'}{3}[h_i^3 - h_{i-1}^3] + \sum_i \frac{E_i'}{3}[-3h_i^2\bar{h} + 3h_i\bar{h}^2 + 3h_{i-1}^2\bar{h} - 3h_{i-1}\bar{h}^2]$$

$$= C + \sum_i E_i'[-h_i^2\bar{h} + h_i\bar{h}^2 + h_{i-1}^2\bar{h} - h_{i-1}\bar{h}^2]$$

$$= C + \bar{h}\sum_i E_i'[-h_i^2 + h_i\bar{h} + h_{i-1}^2 - h_{i-1}\bar{h}]$$

$$= C + \bar{h}\sum_i E_i'[-h_i^2 + h_{i-1}^2 + \bar{h}(h_i - h_{i-1})]$$

$$= C + \bar{h}\Big[\sum_i E_i'[-h_i^2 + h_{i-1}^2] + \bar{h}\sum_i E_i'[h_i - h_{i-1}]\Big]$$

$$D_1 = C + \Big(\frac{B}{A}\Big)\Big[-2B + \Big(\frac{B}{A}\Big)A\Big] = C + \frac{B}{A}[-B] = C - \frac{B^2}{A} = D_2$$

$$D_1 = D_2 = D \quad \blacksquare.$$

Multilayered plate deflection is also discussed in [83].

Whereas for the parylene-oil-encapsulation relative sensitivity $S_r = \frac{c_2}{c_1+c_2}$, the relative sensitivity for the multilayer plate is derived here. Starting with $D_0 \rightarrow D_f$, then we get $c_0 \rightarrow c_f$, remembering that $c \propto \frac{1}{D}$. Since $V_0 = c_0 p \longrightarrow V_f = c_f p$, with p unchanged, the volume displaced will reduce with increased D with an inverse relationship. In the small deflections scenario applicable to most pressure sensors, the volume swept is linear with the maximum displacement in the center of the deflecting membrane, which is also linear to the amount of stretching of a piezoresistor which would be placed near the edge of the membrane as well. Simply, if the flexural rigidity D doubles, the interpreted pressure reported by the sensor will be halved.

Experiments with the system empirically found zero cross-terms between pressure sensitivity and temperature at the relatively small pressure and temperature range of interest. Again, only changes after calibration, like in an implanted environment contribute to error. A calculation of the normalized sensitivity drift is shown in Figure 2.14.

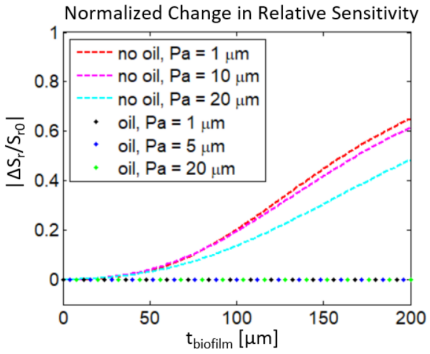

	Silicon	Parylene	Biofilm
E	130 GPa	3.2 GPa	6.5 MPa
v	0.3	0.4	0.4
t	10 μm	variable	variable
$a_{\text{no oil}}$	140 μm	140 μm	140 μm
a_{oil}	140 μm	1.25 mm	1.25 mm

Figure 2.14: Sensitivity calculations for hypothetical sensor packaged with and without oil with different thicknesses of parylene, then calibrated, and then subjected to different amount of biofilm accumulations.

Equation (2.14) explains why implanted sensors may show large absolute drift in units of pressure if all the different sources of drift are not considered. Figure 2.15 shows empirical data confirming the prediction that material buildup on a parylene-oil-encapsulated pressure sensor would not distort the relative sensitivity. Two pressure sensors were coated with parylene-on-oil process, and two parylene-alone as control. Performance was calibrated after parylene deposition and overnight heat treatment but before deposition of spray-coated photoresist to model the performance

after material accumulation *in vivo* without further recalibration. The thickness of the photoresist on the parylene-oil-encapsulated sensor is on the order of the width of the bubbles that appeared. It is hard to exactly quantify the thickness of the photoresist, but because of the wrinkling of parylene-on-oil deposition, the photoresist pooled in the wrinkles and resulted in much thicker coating than the parylene-only case. The bubbles were not fully open windows explaining the retained pressure, because otherwise the pressure offset would not have changed. Additionally, the other parylene-oil-encapsulated sensor (not shown) had small bubbles in the spray photoresist with similar quantitative performance.

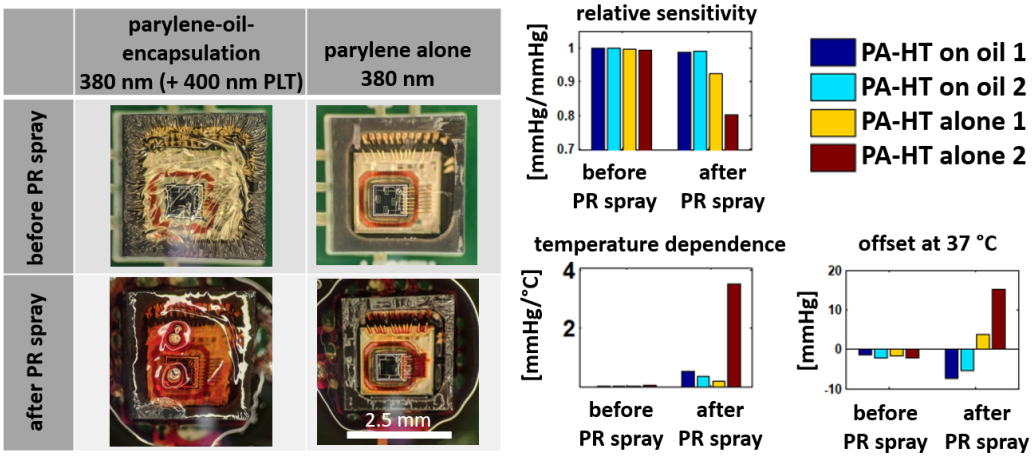

Figure 2.15: Sensitivity retention despite material buildup. Left: LPS25H sensors sprayed with photoresist and baked to model biofouling accumulation. PA-HT is coated on all samples (380 nm total deposition + 400 nm PLT on 100k cSt oil). Right: Despite visibly much thicker buildup, the parylene-oil-encapsulated sensors change sensitivity by less than 1%, whereas thinner buildup cause drops of 8% and 20% in the parylene-alone samples. However, changes of pressure offset and temperature dependence are possible.

2.6.3 Longevity Experiment (Including Parylene Only Package)

In the first generation of benchtop testing, to demonstrate and illustrate the packaging, miniature SPI digital barometer (©Freescale MPL115A1) sensors were chosen because of the convenience of their built-in temperature and linearity compensation. The sensors were dipped in incompressible 30,000 cSt silicone oil and then encapsulated by chemical vapor deposited (CVD) parylene. Parylene is used as an isolation barrier from biomolecules to avoid direct biofouling of the sensor, while biofouling on outer parylene is mitigated as described above. This results in an oil packaging that is conformally sealed by parylene without bubbles

in the oil. At this point in the project, PA-C and PA-D were inspected, because PA-C is FDA approved, but PA-D has higher glass transition temperature, but is not FDA approved. Eventually, the process was switched to using PA-HT on oil because PA-HT has the highest glass transition temperature of all and is also approved for implantation.

Silicone posts were epoxied to the PCB and sensor under the impression it would help alleviate offset, but I will not discuss further because we know that is not correct. But the posts did help hold the high viscosity in place while it was upside down and not fall for a sufficiently long time that parylene could be coated on the surface. The packaging process for a ©Freescale MPL115A1 pressure sensor is shown in Figure 2.16.

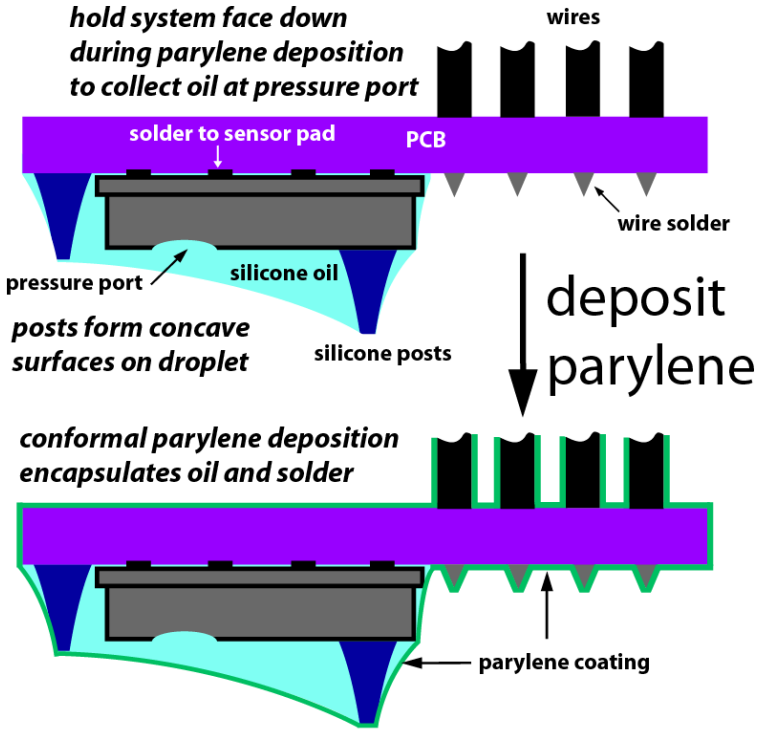

Figure 2.16: Early parylene-oil-encapsulation process. Pressure sensor and wires are first soldered onto a PCB, and then silicone posts are attached onto the sensor and PCB. Next, the sensor is dipped in hexane and then in 30,000 cSt silicone oil. Low-viscosity hexane works as a surfactant to fill the voids inside the pressure port, and then gets replaced by silicone oil later, which greatly accelerates the degassing process. After degassing, the sensor is held face down in a parylene deposition chamber (top). The high-viscosity oil does not fall for hours. A layer of CVD PA-C or PA-D is coated conformally on oil and on the rest of the apparatus (bottom).

A photograph of the final packaged device is shown in Figure 2.17.

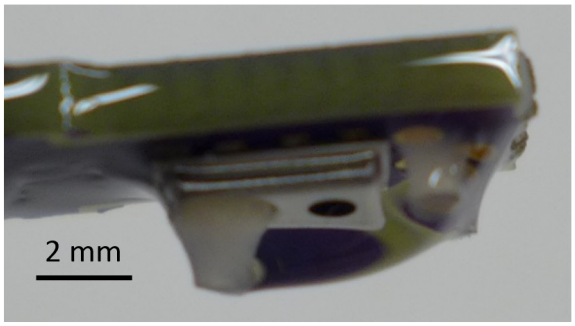

Figure 2.17: Photograph of a finished sensor (generation 1), which is made of a ©Freescale MPL115A1 pressure sensor on PCB with three silicone posts. The sensor inside is bathed in 30,000 cSt silicone oil, whose outer surface is later coated with 27 μm PA-D.

2.6.3.1 Experimental Setup with MPL115A1

Since the hull of the pressure was made of metal, the sensor was placed on a long, thin printed circuit board (PCB), and then dipped in high viscosity silicone oil, and hung upside to keep the oil around the sensor while in the parylene deposition chamber. Wires were soldered to the PCB with leads that would be easy for the parylene to be cleaned off for inspection with a microcontroller.

Silicone posts were added around the structure to give the oil shape more curvature, which was erroneously thought at the time to alleviate pressure offsets created by parylene. More likely, the silicone posts only helped keep the oil hanging with surface tension.

2.6.3.2 Pressure Sweep and Step Response

Figure 2.18 shows that a typical packaged sensor drifts very little over time. To separate stable offset induced by initial exposure to high temperature alone from offset drift caused by accelerated soaking in saline, the packaged sensor was thermally cycled between room temperature and 77 °C in air overnight. Calibration occurred after this thermal cycle, but before soaking in saline. Training set data was generated by recording the sensor's 10-bit pressure and temperature outputs during pressure sweeps at 21 °C, 37 °C, and 45 °C in air. After soaking in 77 °C saline for two days, the packaged sensor was compared to a control sensor in air at room temperature. The calibrated output has an error less than 1 mmHg, meeting the

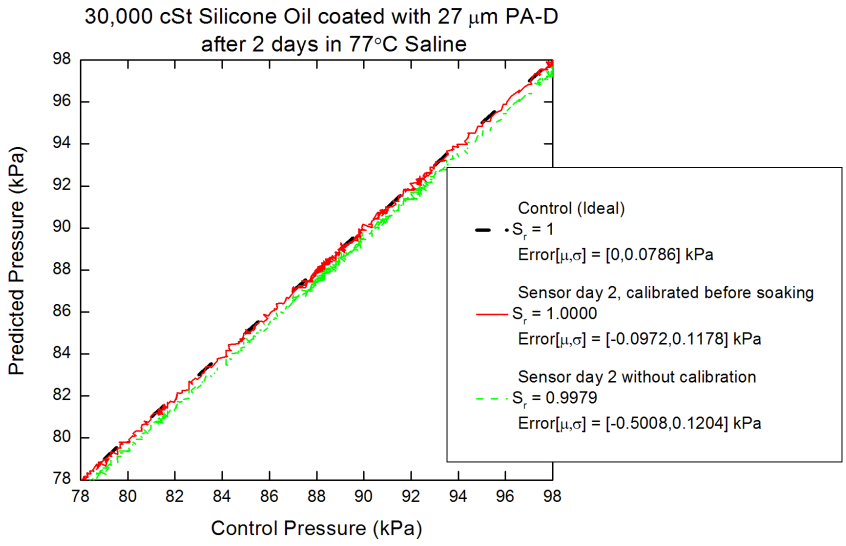

Figure 2.18: Room temperature characterization of a packaged sensor in 30,000 cSt silicone oil, coated with 27 μm PA-D. An unmodified device has natural standard deviation of .0786 kPa, but otherwise assumed to read correct pressure. Offset issues over time are studied in more depth in subsequent generations of tests.

accuracy requirement for most medical applications, with more in depth study in the second generation [4].

The pressure sensor packaged with oil and parylene was found to have a quick pressure step response. A typical device with parylene-on-oil packaging is shown in Figure 2.19. The pressure step response of the packaged sensor is as fast as that of the unpackaged sensor. Note that the temperature measurements are only for pressure calibration. As expected, the packaged pressure sensor experiences a different steady state temperature in partial vacuum and a tempered temperature step because the silicone oil has heat capacity. The strong correlation in the pressure step responses, which considers raw pressure and temperature data, indicates that the temperatures reported by both sensors are correct.

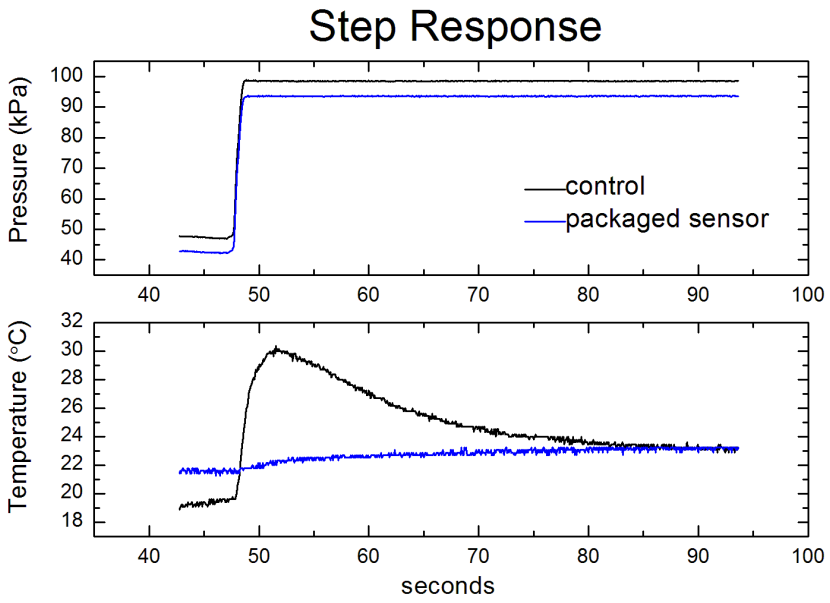

Figure 2.19: Pressure and temperature step response of a device with 30,000 cSt silicone oil and coated with 27 µm PA-D.

2.6.3.3 Generation 1 Longevity Results

Various pressure sensor packages using (MPL115A1) were investigated for accelerated soaking tests. A control sensor was uncoated and failed quickly as expected after 1 day in 67 °C saline. Some sensors were coated with PA-C or PA-D without oil, but still retaining a layer of gel as produced by the manufacturer. The remaining sensors were packaged with 30,000 cSt silicone oil and encapsulated with PA-C or PA-D. The results are summarized in table 2.1. With the exception of the one with "Oil +21 µm PA-C", all of the other devices were thermally baked in air overnight at the temperature which they were to be soaked to isolate sensitivity and offset drift due to elevated temperature versus soaking time in saline. The relative sensitivity and offset after thermal treatment, but before soaking in saline, are in the "Pre-Soak" column. One device was purposely not modified nor given a thermal regiment before soaking in 5000 cSt silicone oil at 97 °C, since the water saturation limit increases at elevated temperatures. At 97 °C, the saturation limit of water is extrapolated to be around 1000–1500 ppm [59]. After the first week a small offset was induced, presumably due to thermal treatment, but in the following weeks neither the sensitivity nor offset changed. This confirms that silicone oil is

not harmful to the pressure sensor.

Roughly every 10 °C increase in temperature doubles the soaking life-time acceleration factor according to the Arrhenius relationship [56]. It was found that thicker layers of PA-C would not survive higher temperatures in attempting to achieve faster acceleration factors so devices were instead packaged with PA-D due to its higher glass transition temperature so saline soaking tests at higher temperatures could more quickly and efficiently extrapolate lifetime at 37 °C. Experimentally, the longest soaked device while maintaining adequate sensitivity and minimal offset is the one with "Oil +27 μm PA-D", which lasted for 6 weeks at 77 °C, equivalent to 21 months at 37 °C. At this point a bubble was observed, due to the delamination of the parylene from the PCB, leading to a void volume during vacuum, which could be filled by air permeating through the membrane. However, a leak of oil was not observed.

The device with "Oil +25 μm PA-D" showed instability in getting a signal in week 3 when it was noticed that the wires used to connect the device to external electronics had fallen into the saline, leading to corrosion. These wires would not be present in a final wireless device so they were not supposed to be submerged in saline.

Recall that the sensors have a layer of gel on the membrane as delivered by the manufacturer. In all sensors, the gel has not been disturbed, so devices without oil still have a layer of gel between the silicon and parylene. Despite the presence of gel, two problems with direct deposition of parylene arise. First, even though the devices without oil but with "25 μm PA-D 1, 2" report output data up to week 4, 14 respectively, their offsets drift much more than 1 mmHg (0.13 kPa), which is the maximum tolerance for most medical applications, after just one week. Second, devices without oil and with parylene like "25 μm PA-D 1, 2" exhibit smaller relative sensitivity because membranes stiffen as material accumulates on them, as expected. Depositing 32 μm of PA-C in the deposition chamber directly onto two MPL115A1 pressure sensors gave them an initial relative sensitivity of 0.913 ± 0.063. The true thickness of parylene deposited on the sensor membrane is less than in the deposition chamber due to a pinhole effect caused by the pressure port of the original housing. Thus this result underestimates the severity of sensitivity degradation. For both reasons, parylene-on-oil packaging is superior to direct deposition of parylene without oil.

Table 2.1: Accelerated lifetime soaking test of packaging of gen 1 devices.

Package[c]	Temp.	Parameter	Pre-Soak	Week 1	2	3	4	5	6	7
No Package	67 °C	S_r	1.015	Electronics failure as expected with no protection in saline						
		Offset (kPa)	1.753	after one day.						
Oil +25 µm PA-D	77 °C	S_r	0.996	1.000	1.001	0.999	Failed due to wire corrosion on wk 4.			
		Offset (kPa)	-0.854	-0.574	-0.204	0.061				
Oil +21 µm PA-C	87 °C	S_r	1.050	1.026	1.073	1.023	0.996	0.248	Week 5 sensitivity	
		Offset (kPa)	0.423[a]	-19.4	-21.8	-21.3	-21.4	10.73	failure.	
25 µm PA-D 1	77°C	S_r	0.979	0.987	0.983	0.980	0.995	Delamination-induced cor-		
		Offset (kPa)	48.37	52.47	53.12	48.52	55.50	rosion signal failure at wk 5.		
5000 cSt Oil Bath	97 °C	S_r	0.998	0.997	0.998	0.998	0.996	0.997	0.997	0.9969
(no saline)		Offset (kPa)	-0.222	-0.468	-0.468	-.446	-0.410	-.443	-.420	-.433
25 µm PA-D 2	77 °C	S_r	0.971	0.974	0.978	0.955	0.972	0.969	0.986	0.976
		Offset (kPa)	49.96	53.68	54.51	51.04	54.67	55.60	56.13	55.82
Oil +27 µm PA-D	77 °C	S_r	1.001	1.000	0.993	1.001	0.999	0.994	0.997	0.973
		Offset (kPa)	-0.512	-0.119	-0.048	0.300	-0.155	-0.02	0.286	1.116

			8	9	10	11	12	13	14	15
25 µm PA-D 2	77 °C	S_r	0.990	1.000	0.978	0.996	0.986	0.983	0.987	[b]
		Offset (kPa)	55.51	57.6	56.43	56.44	55.71	53.47	36.00	
Oil +27 µm PA-D	77 °C	S_r	Delamination of parylene at wire/PCB junction caused bubble at wk 7.							
		Offset (kPa)	Electronics were intact on week 8.							

[a] The PA-C package was not thermally stressed before soaking, unlike the PA-D packages. Thus, an offset was created during the first week in 87 °C saline, whereas the others were thermally stressed beforehand.

[b] Corrosion-induced error on week 14, fail on week 15.

[c] The thickness of parylene is reported as that on a glass slide. Offset is defined as the error versus control at P_{env} = 75 kPa, midway between 1 atm and 50 kPa.

2.6.4 Behavior When Bubble is Present

Unsurprisingly the presence of bubbles inside the oil would be problematic for the parylene-oil-encapsulated package, or if constructed with a bag-first fabrication method. A rough model of the effect of the bubble is presented here, only to the degree of accuracy necessary to prove that bubbles are a problem, and should be avoided if possible. Luckily, the parylene-oil-encapsulation method is naturally bubble-free, so a dynamically accurate bubble-inclusive model of the relative sensitivity is not attempted.

2.6.4.1 Mathematical Model and Derivation

In this scenario, it is assumed that pressure is changing quickly relative to permeation and dilution in the liquid such that there is no mass changing in the bubble. Please refer to Figure 2.20.

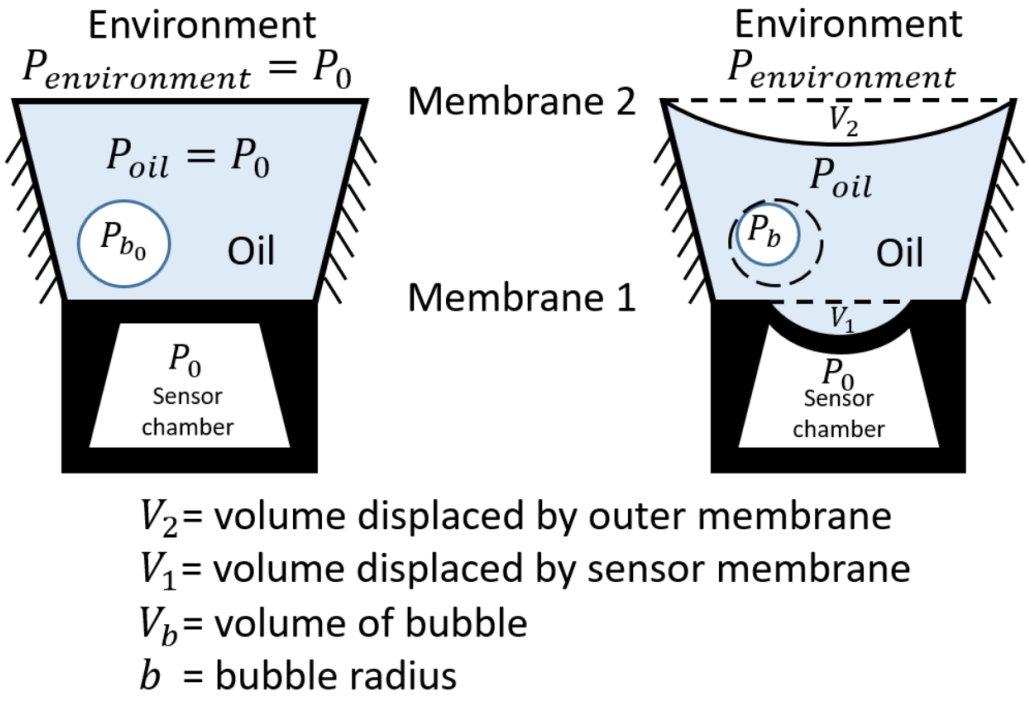

Figure 2.20: Bubble version of the "Funnel model" for deriving the sensed pressure as a function of environment pressure and bubble size and other factors.

When a bubble is present, the relative sensitivity S_r loses meaning as the slope of sensed pressure to control pressure is not constant. A numerical method to explain a bubble's effect on relative sensitivity is proposed. In Figure 2.20 the left is the starting condition, where the environmental pressure and the oil pressure

equal the sensor chamber pressure so that neither membrane deflects, and where the bubble size is measured by observation. Right, the environmental pressure increases so as to cause deflections in both membranes and shrinkage of the bubble.

We assume a spherical bubble for simplicity. Like before, we assume that the walls of the funnel and pressure sensor are rigid. Also, the liquid (oil) has bulk modulus K.

Let b = bubble radius.

Let b_0 = bubble radius when $P_{oil} = P_{env} = P_0$

Let $V_{b_0} = \frac{4}{3}\pi b_0^3$

Let V_{funnel} = volume of funnel (constant)

Visually we can add all the liquid volumes.

$$V_{oil} = V_1 - V_2 - V_b + V_{funnel} \tag{2.48}$$

Now we examine the change in oil volume for bulk modulus considerations.

$$dV_{oil} = V_1 - V_2 + (V_{funnel} - V_b) - (V_{funnel} - V_{b_0}) \tag{2.49}$$

which simplifies to

$$dV_{oil} = V_1 - V_2 - V_b + V_{b_0} \tag{2.50}$$

From first principles,

$$K = -V\frac{dP}{dV} \tag{2.51}$$

which rearranged can be written as

$$dP = -\frac{K}{V_{oil}}dV_{oil} \tag{2.52}$$

Remembering $dP = P_{oil} - P_0$, and substituting (2.48) and (2.50) into (2.52) produces

$$P_{oil} - P_0 = \frac{K}{V_{funnel} + V_1 - V_2 - V_b}\left(V_2 - V_1 + V_b - V_{b_0}\right) \tag{2.53}$$

Since typically $V_{funnel} \gg V_1, V_2, V_b$, we may simplify to

$$P_{oil} - P_0 \approx \frac{K}{V_{funnel}}\left(V_2 - V_1 + V_b - V_{b_0}\right) \tag{2.54}$$

Substituting the $V = cp$ terms yields

$$\frac{V_{funnel}}{K}(P_{oil} - P_0) = c_2(P_{env} - P_{oil}) - c_1(P_{oil} - P_0) + V_b - V_{b_0} \tag{2.55}$$

Combine like terms of pressure across each membrane

$$\left(c_1 + \frac{V_{funnel}}{K}\right)(P_{oil} - P_0) = c_2(P_{env} - P_{oil}) + V_b - V_{b_0} \tag{2.56}$$

Isolating V_{b_0} and substituting V_b in terms of b yields

$$\boxed{\frac{4}{3}\pi b^3 + c_2(P_{env} - P_{oil}) - \left(c_1 + \frac{V_{funnel}}{K}\right)(P_{oil} - P_0) = V_{b_0}} \tag{2.57}$$

Let us now consider the bubble laplace pressure.

$$P_b = P_{oil} + \frac{2\gamma}{b} \tag{2.58}$$

where P_b is the pressure inside the bubble and γ is the surface energy. Assuming a constant temperature, then

$$nRT = V_b P_b = V_{b_0} P_{b_0} = \left(\frac{4}{3}\pi b_0^3\right)\left(P_0 + \frac{2\gamma}{b_0}\right) \tag{2.59}$$

and thus

$$\boxed{\frac{4}{3}\pi b^3 = \frac{nRT}{P_{oil} + \frac{2\gamma}{b}}} \tag{2.60}$$

With a measured initial radius of the bubble b_0, and an assumed value for P_0, (still at constant temperature), P_{env} is swept and equations (2.57) and (2.60) are solved simultaneously with a numerical solver using the variables (b, P_{oil}), such as ©Matlab. Choice of P_0 in practice mostly only changes the constant offset of P_{oil} versus P_{env} for the range of values inspected. Another simplification is that the bulk modulus can be quite large, so the $\frac{V_{funnel}}{K}$ term in (2.60) may be ignored.

2.6.4.2 Experimental Results of Package with Bubble

One of the pressure sensor packages was found to have a bubble. The device's pressure response was examined at multiple times. Afterwards the package was sliced open, leaving the sensor in oil but otherwise exposed to air, and examined again. The bubble can be seen in Figure 2.21.

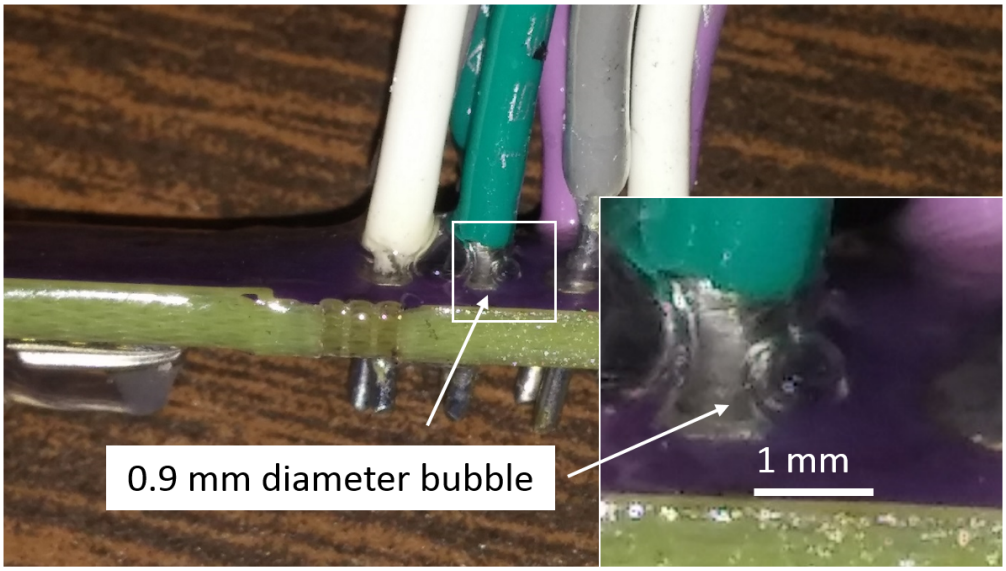

Figure 2.21: A packaged MPL115A1 sensor was observed to have a bubble presumable due to parylene delamination and gas permeation.

The results of the experiments are shown in Figure 2.22. For modeling purposes, P_0 is assumed to be 99 kPa. An effective circular outer membrane of 1.3 mm radius is assumed, which is approximately the area between the silicone posts used for this device. The square silicon membrane of the sensor is measured to be 9 µm thick and 375 µm wide. Packaging was 30,000 cSt silicone oil and PA-D thickness of 27 µm. The bubble radius at room pressure b_0 is measured to be 0.45 mm.

As shown in Figure 2.22, the qualitative non-linear behavior from the presence of a bubble is predicted by the model quite well. Although a hysteresis is observed, which cannot be replicated by this non-dynamical model, it is hypothesized that some mass exchange inside the bubble occurred. It is also found that repeated measurements of a sensor under vacuum would cause the bubble to increase in size and hence the offset, consistent with the hypothesis that the void induced by the vacuum would be filled by air when brought up to atmosphere.

After the bubble was observed, the parylene package was cut open to release the bubble (Figure 2.23). As expected, the following experiments without the bubble showed that the pressure sensor output was indistinguishable from that of an unmodified device. This proves that the bubble alone caused the loss of pressure transduction to the sensor. Thus, the silicone oil must be free of bubbles for accurate pressure sensing.

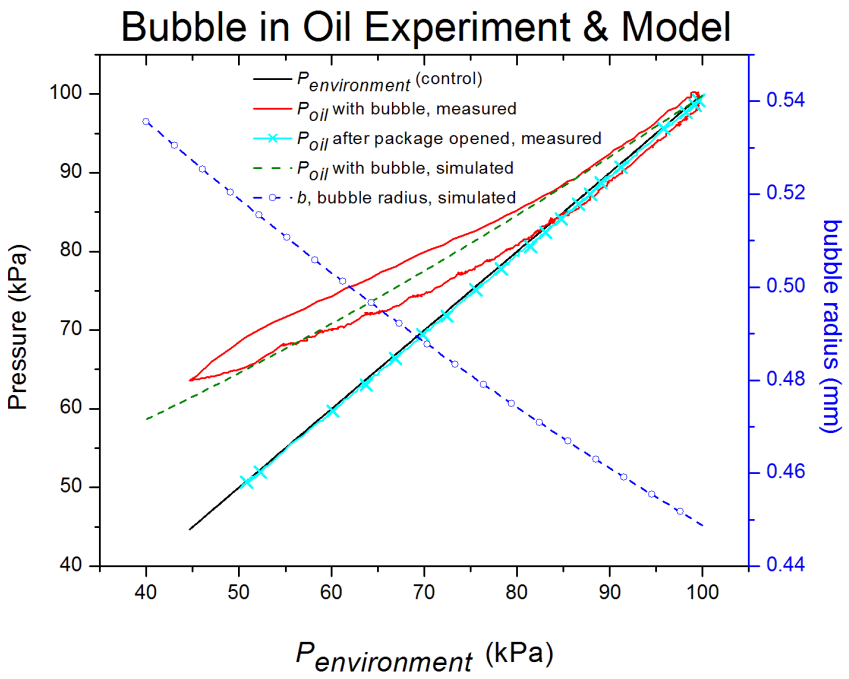

Figure 2.22: Data from packaged pressure sensor with a bubble, presumably due to parylene delamination and gas permeation. Pressure responses from before and after the packaging was opened are shown here. The theoretical pressure reading with a bubble is in good agreement with the measurements. After the package is cut open, the pressure sensor behaves as if unmodified, confirming that the nonlinearity is caused by the bubble alone.

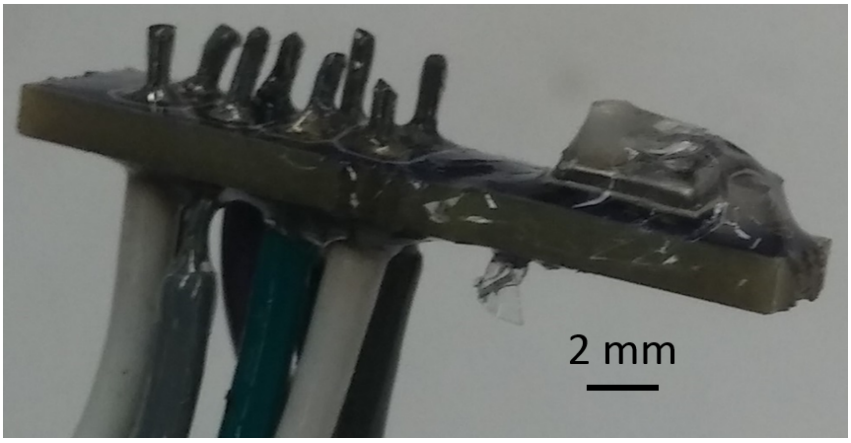

Figure 2.23: The package in Figure 2.21 was cut open to confirm the full functionality of the original pressure sensor.

2.7 Second Generation (LPS25H)

Since the first generation (MPL115A1) devices soaking test proved the feasibility of long term survival, improvements were made to the package. The first thing to review was the choice of commercial pressure sensor, since everything afterwards is potentially affected by that choice. Eventually it was found that the ©STMicroelectronics LPS25H digital barometer was the best possible choice. There were several reasons why this was the best choice to be used in a wireless implant. First, as a barometer, the absolute range of 280-1280 mbar and sub-mbar resolution meet the specification for biological applications. Next, it is a digital-output sensor with temperature compensation, and also can report the temperature if desired, just like the earlier device. A digital-output sensor, given it initially meets the accuracy, precision, and range requirements, is the best one can do from a noise perspective. If the output were analog (e.g. voltage), one would have to consider noise and distortion effects, and ultimately recreate the ADC to get a digital signal. So we just used the commercial part since it was available. Furthermore, the internal temperature compensation and temperature reporting are two separate issues. The pressure reported by the sensor already takes the temperature into account by the on-chip circuitry, producing better stability with respect to temperature. However, since the parylene-oil-encapsulation process can induce a temperature-dependent pressure offset, having the on-chip circuitry automatically compensate for the temperature effects that occur even in unmodified sensors, allowed me to isolate the temperature-depended pressure offset due to the parylene-on-oil structure itself.

Next, the LPS25H is actually one of a family of sensors offered by STM. In fact, I discovered the LPS331AP, a $3 \times 3 \times 1\text{mm}^3$ barometer, which was an older version of the same device. So some of the initial results used the LPS331AP, but quickly afterwards I discovered the newer, smaller LPS25H sensor which is essentially the same exact sensor except it is only $2.5 \times 2.5 \times 1\text{mm}^3$ in size. Additionally, STM offers two newer versions of the sensor which are unsuitable for my use with parylene-oil-encapsulation, the LPS25HB, and the LPS22HB, which are $2.5 \times 2.5 \times 1\text{mm}^3$ and $2 \times 2 \times 1\text{mm}^3$ in size. The "HB" sensors have a submerged pressure sensitive membrane that is called a "bastille" design, where the bending membrane is only accessible to fluids through tiny holes etched in the top, non-bending silicon section. As described below, I used high-viscosity silicone oil, and bubbles cause pressure sensing inaccuracy, so it is determined that it was better to use the LPS25H instead of the LPS22HB even though the LPS25H is slightly larger. It is appropriate to mention here that the LPS25H (and earlier LPS331AP) sensor packages are plastic,

where the top plate has a pressure port, but could be removed by slicing with a razor blade[1]. The result is like a pressure sensor inside its own bowl, without an increase in size from the original commercial package (Figure 2.24). This makes silicone posts and hanging droplet structures obsolete.

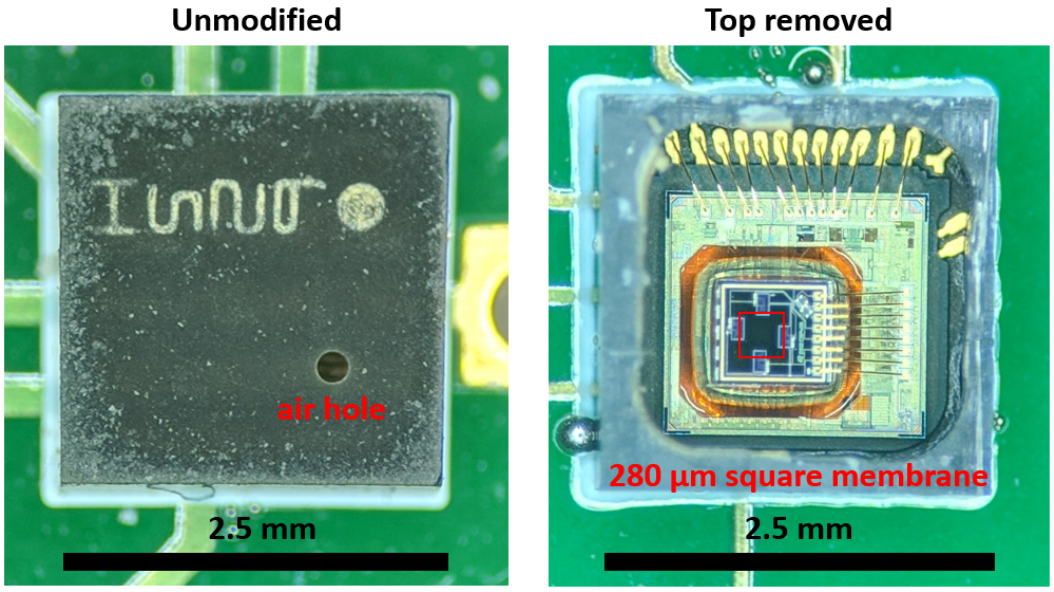

Figure 2.24: LPS25H sensor unmodified and with the top removed. The pressure sensitive membrane can be seen.

2.7.1 Construction Recipe

Digital-output barometers (i.e., ©STMicroelectronics LPS331AP ($3 \times 3 \times 1\text{mm}^3$), LPS25H ($2.5 \times 2.5 \times 1\text{mm}^3$)) were chosen with < 0.1 mmHg resolution and accuracy, and internal temperature compensation and temperature readout. This accuracy is within the tolerance to make clinical decisions for glaucoma monitoring (1-2 mmHg) [4].

Figure 2.25 shows a photograph of a parylene-oil-encapsulated pressure sensor. Wrinkling of the parylene-on-oil is observable.

A Laplace-pressure-based model motivates the packaging design.

$$\Delta P = \frac{2\sigma t}{r} \tag{2.61}$$

where ΔP is the pressure across the membrane, σ is stress, t is thickness, and r is the radius of curvature. Of course, with a chaotically wrinkled surface, the modeling of

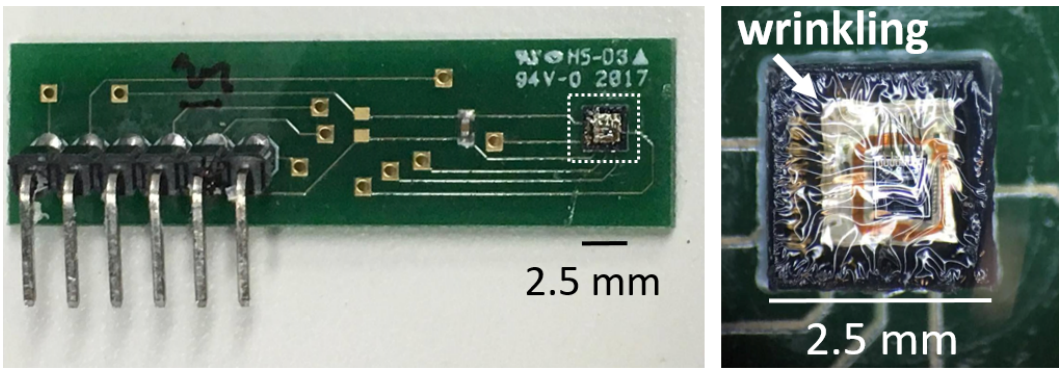

Figure 2.25: Photograph of parylene-oil-encapsulated pressure sensor (generation 2). Left, STMicroelectronics LPS25H digital barometer on PCB, packaged with nominal 11.6 µm and subsequent nominal 0.6 µm PA-C on 100k cSt silicone oil, total nominal 12.2 µm PA-C. Right, close up showing wrinkled parylene-on-oil indicates compressive film stress, which makes pressure offset small.

the surface radius of curvature becomes very complicated. So this equation is just used to make design decisions, which overall have been found to be valid.

We remove the top of the plastic housing with a razor blade to expose the sensing membrane. Biocompatible 100,000 cSt silicone oil is injected into the housing to separate the sensor membrane from the parylene which is coated using CVD. Parylene can induce sensitivity change, excessive pressure offset and offset drift if deposited directly on the sensor membrane due to mechanical load and intrinsic stress. This first parylene coating may be as thick as desired to sufficiently coat any other electronics or components. However, since the Laplace pressure offset is linear with membrane thickness, the recipe would cause too much offset if this was the last step. Instead, the first parylene-on-oil is cut and removed, re-exposing the oil to air, more silicone oil is re-injected into the plastic housing, and a razor blade is used make the oil flush with the top of the exposed container to minimize meniscus curvature. Viscosity of 100,000 cSt is used because it was the highest viscosity easily available, and thus had the flattest meniscus, which is optimal for reducing Laplace pressure offset. A second, “thin” (sub-micron) parylene coating is deposited on the oil window. The result is a same-sized pressure sensor with parylene-oil-encapsulation ready for implantation (Figure 2.26).

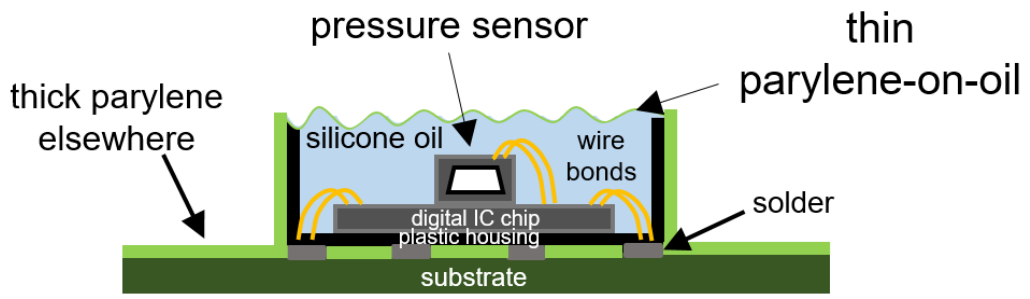

Figure 2.26: Schematic of parylene-oil-encapsulated pressure sensor. The top of the plastic housing is removed with a blade. Silicone oil is dispensed over the sensor to prevent direct deposition of parylene on the piezoresistive Si membrane. Thick parylene is coated everywhere by CVD. The thick parylene over the oil is removed with a razor blade and tweezers, and oil is redeposited. A syringe/spatula is used to add/remove oil to obtain a flat meniscus. Higher viscosity oil helps achieve flatness, further reducing Laplace-pressure-offset. A second, thin parylene deposition encapsulates the oil.

2.7.2 Parylene-Oil-Encapsulation Recipe Optimization

The goal of the packaging optimization is to develop a recipe which will result in the smallest amount of drift of all kinds (pressure sensitivity drift, absolute offset drift, and temperature dependency drift). It is observed that large initial pressure offset, large temperature dependence, and large hysteresis are all correlated with large drifts. There are several variables examined in the parylene-oil-encapsulation method, including parylene type (-C, -D, and –HT), thickness, and silicone oil viscosity. Parylene of all three types are investigated in longevity tests, but otherwise effects due to oil viscosity and parylene thickness are examined only with PA-C.

2.7.2.1 Dependence on Oil Viscosity, Film Thickness

Low versus high viscosity silicone oils have drastically different behavior in a temperature sweep test, held at constant pressure. It is found that higher viscosity is better because it results in flatter meniscus. Every sample was fabricated to have as small a meniscus as possible for fair comparison. Also, even though the Laplace pressure offset formula suggests that pressure offset is linear with thickness, there is a lower limit to the thickness below which pressure offsets start to grow again (Figure 2.32). This is because the actual thickness always includes the porous layer of a fixed thickness (PLT), despite reducing the dimer weight to make the nominal thickness approach zero.

Since this evidence proved that 100,000 cSt silicone oil was the best option (highest viscosity easily available), it became the oil of choice for achieving low-drift.

2.7.2.2 Parylene-Oil-Encapsulated Pressure Sensor Response When Exceeding the Parylene Glass Transition Temperature

As mentioned earlier, parylene undergoes plastic deformation when it exceeds its glass transition temperature. An experiment was carried out where the pressure was read continuously from a parylene-oil-encapsulated pressure sensor during a heat treatment hot enough to exceed the glass transition temperature of parylene.

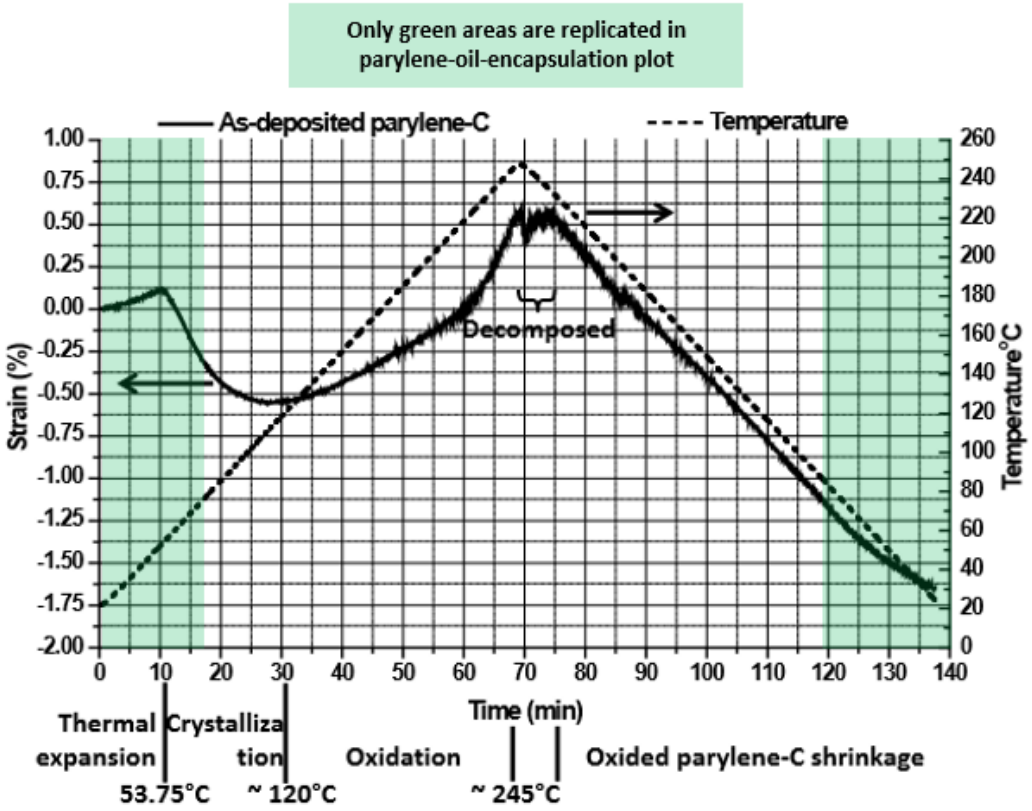

Figure 2.27: Length change of PA-C film annealed under the temperature ramping rate at 3.33 °C/min and its hypothesized phenomenon interpretation by dominant effect. Adapted from Jeffrey Lin Thesis, Caltech, 2012 [5].

Figure 2.27 shows the phases PA-C goes through at various temperatures. In a heat ramp up, the PA-C undergoes thermal expansion, then crystallization/shrinkage, then oxidation (growth again), and lastly decomposition. For the cool down, the already-oxidized PA-C shrinks [5]. The green shading is added to correspond to the

temperature range to which the device is exposed. The chart in Figure 2.28 shows the Young's modulus of PA-C decreases with increased temperature [5].

Parameter / As-deposited parylene-C testing temperature	Elastic modulus	Elastic modulus from 0 MPa and 0%
Symbol	E	E_0
Unit	GPa	GPa
SCS	2.758	
Spivack [235]*	2.354;2.746 (1% strain)	
Baker [195]	2.917	
Beach [101, 102]	3.2	
20°C	3.654	2.641
40°C	3.166	2.677
60°C	2.400	2.400
80°C	2.270	2.270
100°C	1.771	1.771
120°C	1.575	1.575
150°C	1.123	1.123

Figure 2.28: Young's modulus decreases with increased temperature. Adapted from [5].

The sample used for this experiment is shown in Figure 2.29.

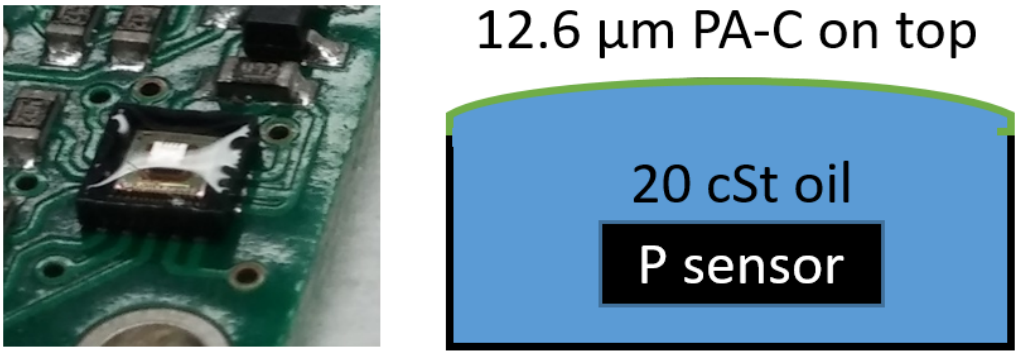

Figure 2.29: Non-ideal pressure package regarding pressure offset (LPS331AP). The package has convexity, and the parylene is thicker than necessary.

A temperature sweep from 18 to 78 °C and back is conducted over the course of an hour (Figure 2.30). The PLT of the PA-C on 20 cSt oil is 8 µm, meaning the sample with 12 µm nominal thickness has a total of about 20 µm. It is surmised that the temperature thresholds for the various states of the partially-porous parylene film on oil is similar to standard parylene. This sample also had a convex meniscus

with 20 cSt viscosity silicone oil. The parylene was not wrinkled as it would on high viscosity oils. Notice the initial pressure offset is around +15 mmHg, which is large compared to the accuracy threshold of 1-2 mmHg. Even if it can be calibrated, a large initial offset tends to drift over time in absolute larger terms than packages with smaller initial offsets. A larger initial offset is also due to the thickness of the film, which is partially due to the PLT, which is also determined by the parylene type and oil molecular weight.

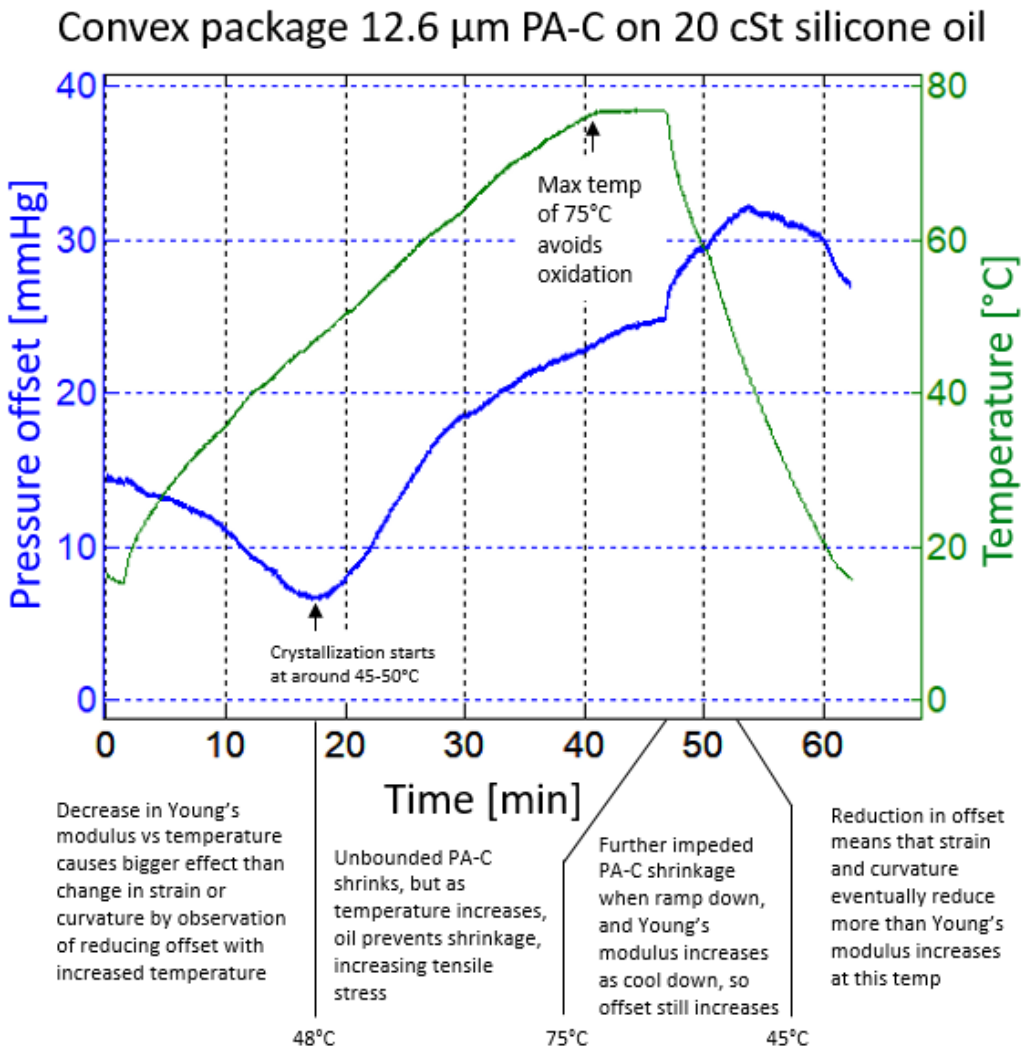

Figure 2.30: Pressure offset for parlyene-oil-encapsulated sensor shows plastic deformation if glass transition temperature of parylene is exceeded.

At the beginning, the pressure offset decreases with increased temperature. This can be explained by the change in Young's modulus over time. The change in Young's modulus of parylene with temperature causes a bigger effect than the

change in strain or curvature due to excess thermal expansion of the oil compared to the plastic housing.

At around the 18-minute mark, the pressure offset starts to rise again. This was around 48 °C, which corresponds to the crystallization point. Unrestrained PA-C would tend to shrink, but in this case, the oil prevents the oil from shrinking. Thus the tensile stress increases, and with the convex geometry, results in an increasing positive pressure offset. This continues until the max temperature of about 78 °C, in order to avoid oxidation.

When the temperature climbs down from the 78 °C point, the pressure offset further increases, because the unrestrained parylene would also tend to shrink if it has crystallized. This further increase in pressure offset only continues until the temperature sank below 45 °C, where the pressure offset started to decrease again. It is surmised that the reduction in offset suggests that the strain and curvature reductions from oil shrinkage eventually outpace the shrinkage of the parylene, at least at this moment.

However, the final pressure offset is now about 27 mmHg, when it started around 14 mmHg, a large change. In summary, exceeding the glass transition of the parylene causes large and permanent change in the pressure offset, meaning that low-drift is improbable if one exceeds the glass transition temperature T_g, which for the case of PA-C is about 45 °C [5]. This is the main reason to use PA-HT over PA-C for parylene-oil-encapsulation, as the T_g of PA-HT is much higher (continuous use of 350 °C compared to continuous use of PA-C of up to 80 °C, even though our own data suggests a T_g for PA-C of around 45 °C) [44]. Since the highest exposed temperature the system will be exposed to would be at most the temperature of autoclaving (132 °C) [84] or ethylene oxide sterilization (about 63 °C) [85], PA-HT has a high enough value of T_g with a large safety margin.

Plotting the data of offset versus temperature without time reiterates the hysteresis effect (Figure 2.31).

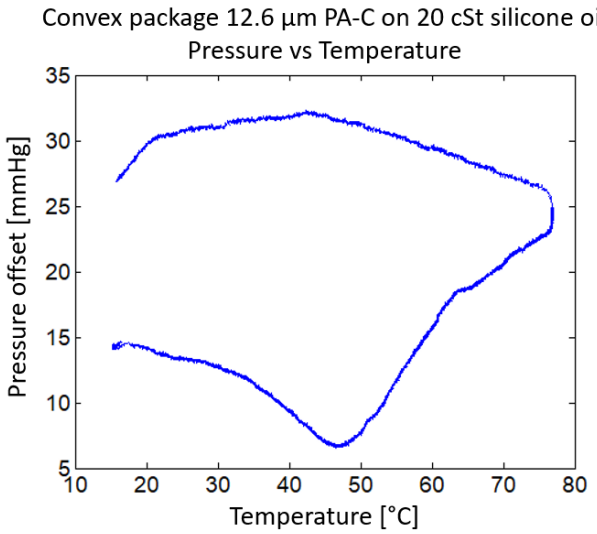

Figure 2.31: Pressure offset for parlyene-oil-encapsulated sensor shows plastic deformation if glass transition temperature of parylene is exceeded, and plotted Pressure versus Temperature directly shows huge hysteresis.

2.7.2.3 Offset and Temperature Dependence Below Glass Transition Temperature

An initial analysis of the effect of oil viscosity and thicknesses of parylene-on-oil is shown in Figure 2.32.

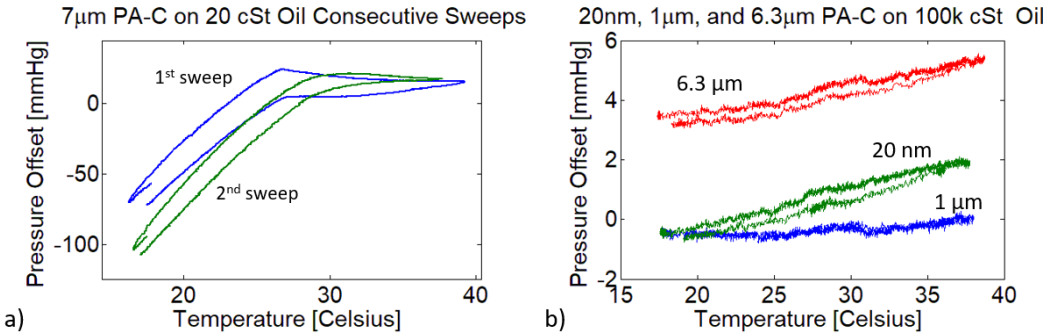

Figure 2.32: Oil viscosity and parylene thickness during thermal cycle. a) 7 µm PA-C on 20 cSt silicone oil LPS331AP had concavity due to surface tension. A temperature sweep shows hysteresis and plastic deformation. b) 3 LPS331AP sensors on 100k cSt oil show much flatter and linear temperature dependence. The 6.3 µm PA-C on 100k cSt oil shows much flatter temperature response than the 7 µm PA-C on 20 cSt oil. Also, the 1 µm thick PA-C on oil has flatter temperature dependence than the 20 nm thick PA-C on oil. All PA thicknesses quoted are nominal.

A detailed analysis of the effect on PA-C thickness on pressure offset, and temperature dependence, both immediately after deposition, and after an overnight bake in air at 37 °C is shown in Figure 2.33. Five LPS25H and five LPS331AP sensors were calibrated against an unmodified control sensor of the same model to eliminate inherent offset variability among the sensors and to analyze the offset due to packaging alone. The internal temperature compensation is assumed to eliminate all temperature effects except those due to packaging. Every pressure sensor was filled with silicone oil with a meniscus as flat as possible because it was both the most desirous and reproducible curvature for parylene-oil-encapsulation. Whether the parylene-on-oil appeared wrinkled was recorded at each thickness. The Laplace pressure equation is used only as a guideline in interpreting the data, because the curvature of wrinkled surfaces is hard to quantify.

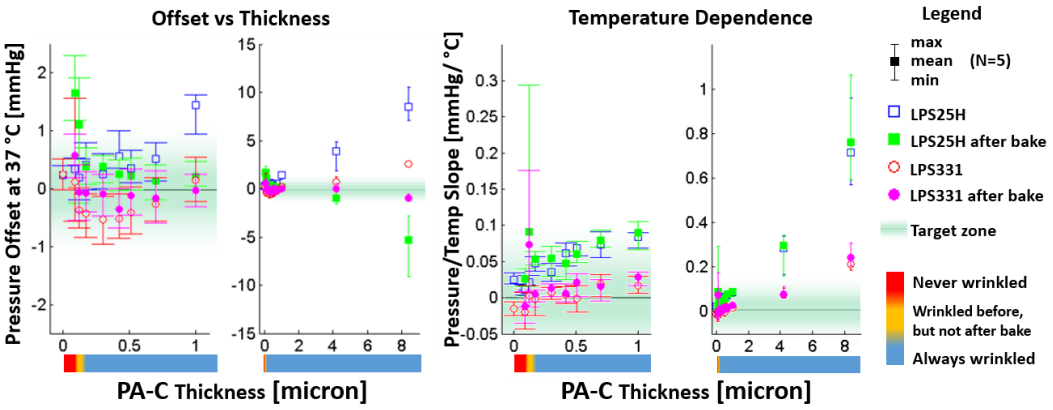

Figure 2.33: Optimization of PA-C package thickness. Nominal 170 nm to 1 µm PA-C has small initial offset & pressure/temp slope, correlating to small drift. Five LPS331AP/25H sensors each were packaged and examined before and after bake at 37 °C in air relative to an unmodified control device of the same model. Data are shown as mean and min/max. Only-oil data (0 µm) were not baked. Baking changed pressure offset proportionally to thickness and also when wrinkles were absent. Baking affects pressure/temperature slope only if wrinkling changes (nominal 120 nm).

A satisfactory thickness should have small initial offset, small offset after bake, and small, unchanging temperature dependence because they are correlated with small drift in absolute terms, in accordance with our observations. This method of investigation is quicker than waiting to examine the drift itself. Initial values can be calibrated, but the drift post implantation cannot be recalibrated in any practical, reliable implantable pressure sensor setup. An overnight bake in air at 37 °C progresses age-related effects with short time constants, so in a real setting,

the implant will be calibrated after this step, thus circumventing drift due to those effects post-implantation.

Several trends are clearly noticeable in Figure 2.33. First, the magnitude of the initial offset at 37 °C, both before and after an overnight bake in air at 37 °C, increases linearly with thickness. This effect is the dominant contributor to pressure offset at and above 1 μm thickness. The initial offset at these large thicknesses changes from positive to negative for all 10 sensors of both sizes.

For reference, the nominal thickness refers to the thickness as on a glass slide. At smaller nominal thicknesses of 120 nm and below and 90 nm and below, after-bake offset increased for LPS25H devices and LPS331AP devices respectively. For 90 nm nominal thickness and below across all devices, the parylene did not appear wrinkled ever. The non-wrinkles and increase of offset after bake are correlated, and it is surmised that the increased porosity of nearly-app porous parylene films explains the enhanced viscoplasticity effect after an overnight bake compared to the nominal 170 nm to 1 μm-thick films.

For most film thicknesses, the pressure offset dependence on temperature did not change after baking. However, for samples with nominal 120 nm PA-C, a large change in pressure/temperature slope was measured after baking. In addition, the 120 nm PA-C samples were the only ones to appear wrinkled before, but not after, the overnight bake. Otherwise, the pressure/temperature slope increases linearly with thickness.

The target zones for both pressure offset at body temperature (37 °C) and pressure/temperature dependence are chosen based on medical accuracy tolerance needs for IOP diagnosis. Nominal film thicknesses of 0.2-1 μm PA-C meet these criteria, and thus are expected to have acceptable drift in saline. We investigated packages with similar thicknesses of PA-D and PA-HT for the subsequent saline soaking tests.

2.7.3 Longevity Experiment

A large quantity of sensor long term reliability data with non-detectable sensitivity drift, minimal offset, offset slope versus temperature, and offset drift was collected.

2.7.3.1 Sample Setup

The LPS25H pressure sensors were assembled and parylene-oil-encapsulated, and then epoxied through a hole drilled into a bottle cap for longevity saline soaking tests (Figure 2.34). The pins are exposed to air on the PCB, and since they would not be exposed in a real, wireless system, they are placed outside the airtight bottle, to prevent circuit failure due to exposed solder joints.

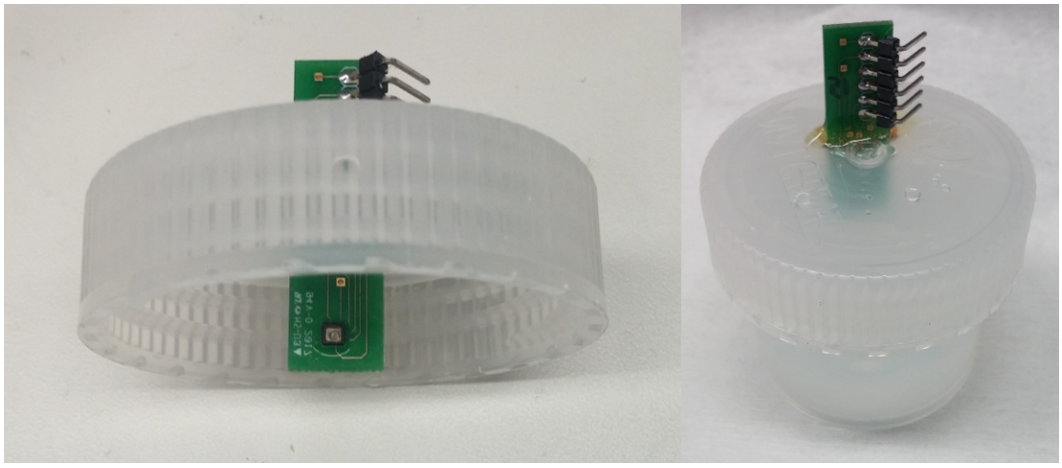

Figure 2.34: Saline Aging Test Sample Preparation. Parylene-oil-encapsulated LPS25H pressure sensor on PCB, inserted into a bottle cap and sealed with epoxy.

2.7.3.2 Disassociation of Pressure, Temperature, Light

To determine the pressure sensor package stability, first the original sensor was thoroughly investigated. Despite what the data sheet said, it was found that the LPS25H sensor had a pressure dependence on its supply voltage, which was not mentioned in the data sheet (Figure 2.35). So, the nominal 3.3V rail on the arduino was used as the supply voltage always for the unmodified LPS25H control sensor, especially after the initial long term test data had used the control sensor on that rail.

The pressure dependence on voltage became another specification for the voltage drop that could be tolerated by the wireless system that was later built around the LPS25H while still providing pressure data within a tolerable accuracy band. This is discussed in more detail in the next chapter, but the main source of voltage drop would be the current draw by the pressure sensor during the one-shot pressure measurement per digital measurement request, sent over SPI or I2C by the arduino (first using SPI, and then switched to I2C protocol) and the wireless ASIC chip (I2C only). It was also found that the chip could only use I2C below around

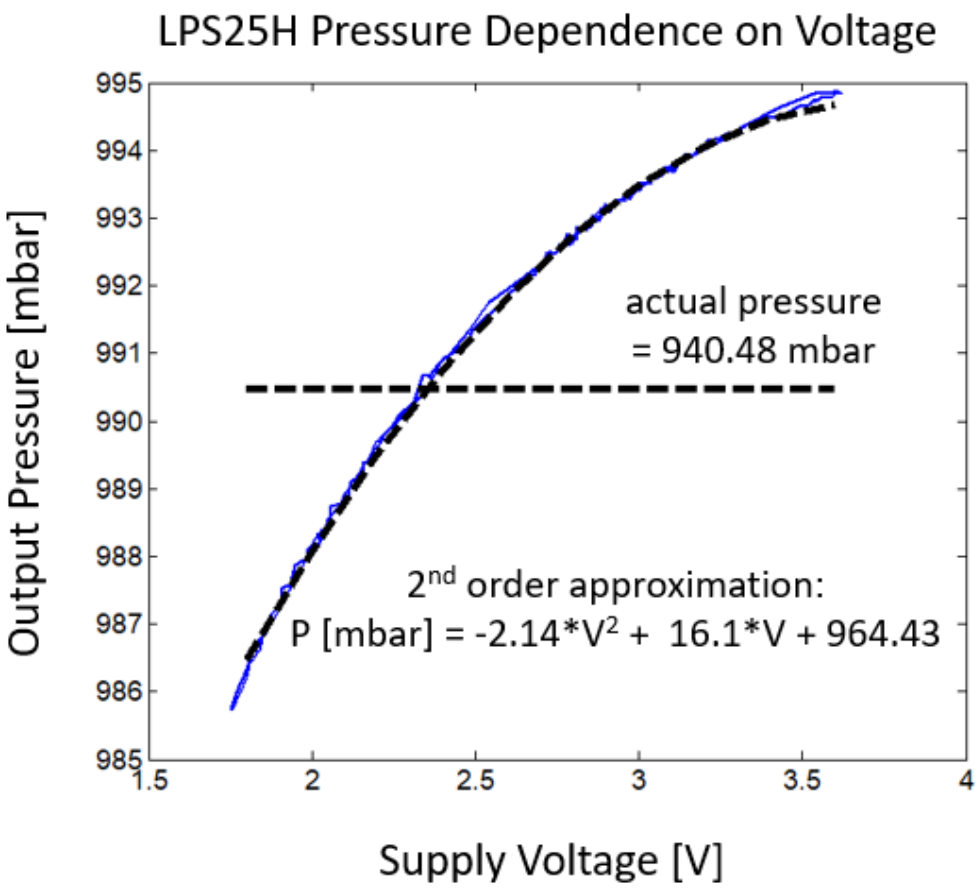

Figure 2.35: Non-ideal pressure dependence on supply voltage for the LPS25H pressure sensor.

2.6 V supply, despite the data sheet suggesting that both SPI and I2C could be used over the full supply voltage range of 1.8 V to 3.6 V. Of course for the wireless chip, we used as low voltage as possible to reduce the power consumption.

Also, the amount of light shown on a pressure sensor after the top had been removed, which also applies to parylene-oil-encapsulated sensors, it was found that the amount of light exposure affected the pressure measurement. The unmodified sensors had a black covering, so the engineers expected the light levels to be low enough to not noticeably affect measurement. In ambient light in the lab, it was found that the pressure reading was about 0.2 mbar less so than in full darkness. If a brighter light source was shined on the sensor, the digital pressure reading would reduce by up to 20 mbar. The longest longevity data was taken before noticing the light-exposure effect, but luckily it was a small enough effect in the lab space, and was taken under consistent conditions. But of course, the wireless sensors should be

calibrated in the dark for the best accuracy possible when implanted into the rabbit, as the light levels should be closer to full darkness rather than average room light conditions. This light dependence is easily explained by the photoconductor effect in semiconductors for the piezoresistors on the deflecting membrane, which could potentially be asymmetrically laid out, making it plausible for either a positive or negative correlation with increased light, depending on doping levels and geometry which are not known to me. In summary, it was not a problem once known.

2.7.3.3 Pressure Sweep

The vacuum test method for sweeping pressure is shown in Figure 2.36.

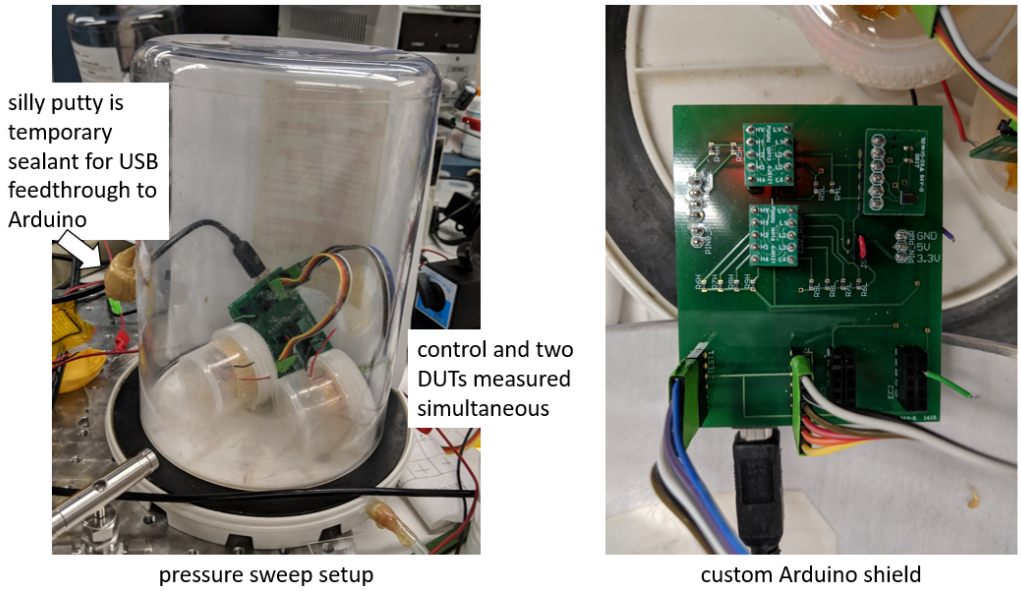

Figure 2.36: Pressure sweep setup for the longevity measurements. The control sensor is on the custom Arduino shield, and the two DUTs are connected by cables to the test jars. The jars have holes to let air through while shielding the sensor from potential puncturing during handling.

The commercial package has internal linearity and temperature compensation, so the reported data from the sensor before modification is reliable enough to use an unmodified one as my control sensor. However, after parylene-oil-encapsulation, the linearity and temperature dependence and pressure response were examined. The pressure test range of interest was 900-1000 mbar, as vacuum was easier to test for pressure sensitivity than adding positive pressure from a gas line every time after the positive gas pressure method was verified to agree with the vacuum method.

2.7.3.4 Temperature Sweep

The temperature range of interest in an animal would be near body temperature of 37 °C, but it is imperative that the temperature is actually measured by the sensor for temperature compensation. In fact [86] and other implantable pressure sensors failed to meet accuracy tolerances in part due to the lack of temperature sensing/compensation, despite being an implant. Nonetheless, since the commercial sensor reports temperature as well, that data was plotted to investigate the pressure dependence on temperature of the parylene-on-oil films. In fact, coating pressure sensors with parylene-on-oil is the most direct way to measure pressure offsets across the film. So, it was decided to cover a temperature range of 27-38 °C to ensure we cover any range that could be encountered.

It was also confirmed that for the pressure and temperature ranges inspected, that there were no pressure × temperature cross terms, and just linear terms for pressure and temperature in determining pressure. Likewise, the voltage dependence of pressure did not have any cross terms with pressure sensitivity, temperature, etc., over the range of pressure and temperature and environmental conditions of interest. In other words, if the calibration used higher powers of pressure, temperature, or any cross terms, it would result in over-fitting. The temperature was varied by using heating pads (Figure 2.37).

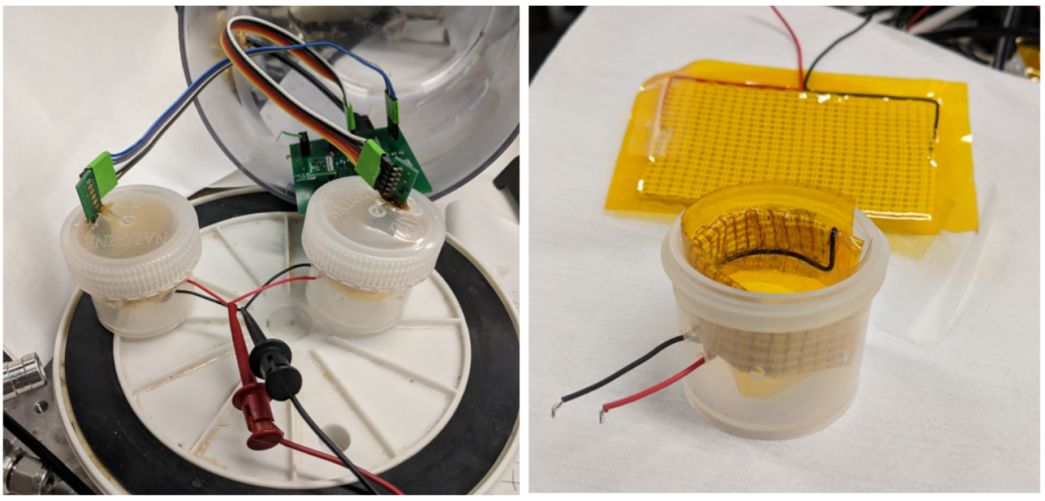

temperature sweep setup heat pad and holed-bucket

Figure 2.37: Temperature sweep setup for the longevity measurements. The test jars have folded heat pads inside.

2.7.3.5 Ideal Pressure Step Response

An ideal pressure sensitivity and step response are recorded for a packaged pressure sensor with 1 µm PA-C on silicone oil, proving the packaging is also suitable for applications which require high sampling rates (Figure 2.38)

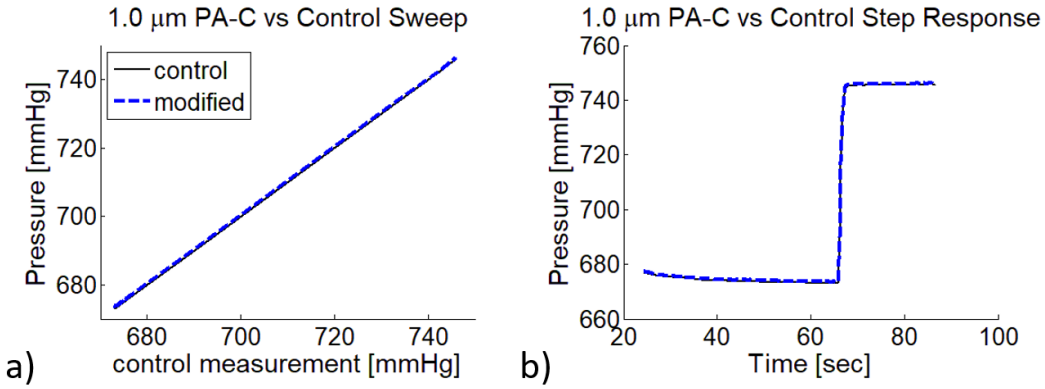

Figure 2.38: Ideal Relative Sensitivity and Step Response of LPS25H device with nominal 1 µm PA-C on 100k cSt silicone oil packaging maintains original relative sensitivity (a) and has ideal pressure step response (b).

2.7.4 Experimental Results

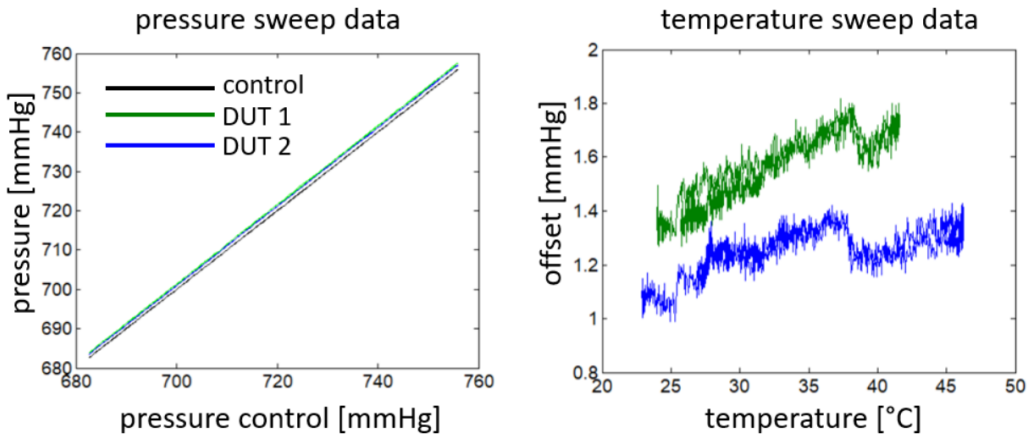

Figure 2.39: Raw pressure sweep and temperature sweep data taken usually once a week. The pressure sweep shows very nearly identical slope to the control device. The temperature sweep shows the pressure offset versus each sensors' own temperature measurement, relative to the control sensor which was in the same atmosphere, but not heated. "dark sensors 1 and 2, day 22, 77 °C saline".

Packaged sensors are examined at least once every seven days. Data is collected in the form shown in Figure 2.39. A one-dimensional fit is used to

calculate the relative sensitivity, and a one-dimensional fit is also used to characterize the temperature dependence. Although there is a distinctive jump around 37 °C in Figure 2.39, it is consistent both on heat-up ramp and cool-down ramp. The exact temperature at which the shift occurs can shift a couple degrees °C over time. Additionally, since the shift is small, a one-dimensional fit is used to avoid overfitting as well as being convenient to only report one number. The offset at 37 °C is quoted as the average pressure offset for all measurements within 37 ± 0.1 °C.

The following three plots measure LPS25H pressure sensors all using 100k cSt silicone oil and sub-micron nominal thickness of parylene (Figures 2.40-2.43). There are devices with PA-C, PA-D, and PA-HT. The PA-C packaged devices were soaked in saline at 37 °C (body temperature) to avoid exceeding the glass transition temperature, which affected the offset stability. The PA-D and PA-HT packaged devices were soaked in saline at 77 °C for high-temperature accelerated aging test. As stated earlier, the aging factor roughly doubles every 10 °C in parylene due to the Arrhenius relationship [56]. Thus 77 °C ages at about a rate of 16 times the rate for 37 °C. The number after each device is just a label for bookkeeping.

The offset is compared to an unmodified control device (Figure 2.40). Although the value at day 0 (before soaking, after heat treatment) is quoted as non-zero in this plot, that offset can also be calibrated so that only drift from the initial value creates error.

The pressure sensitivity is calibrated against a control device (Figure 2.41). Although the value at day 0 (before soaking, after heat treatment) is quoted as non-unity in this plot, that sensitivity can also be calibrated so that only drift from the initial value creates error.

The pressure dependence on temperature is approximated to the best one-degree fit (constant slope) over the a range of 20 to 40 °C (Figure 2.42). Although the value at day 0 (before soaking, after heat treatment) is quoted as non-zero in this plot, that slope can also be calibrated so that only drift from the initial value creates error.

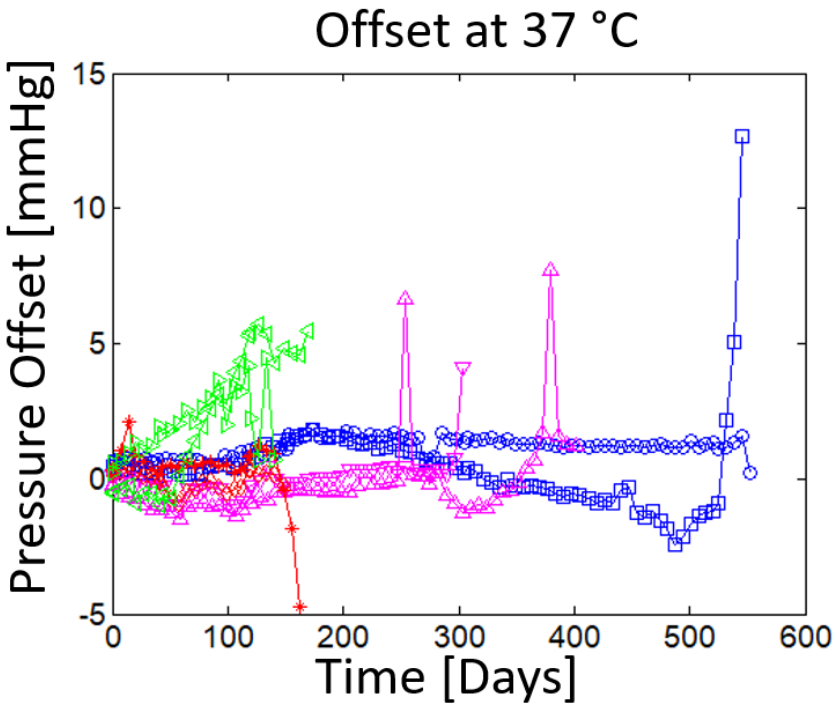

Figure 2.40: LPS25H wired saline soaking data, offset at 37 °C.

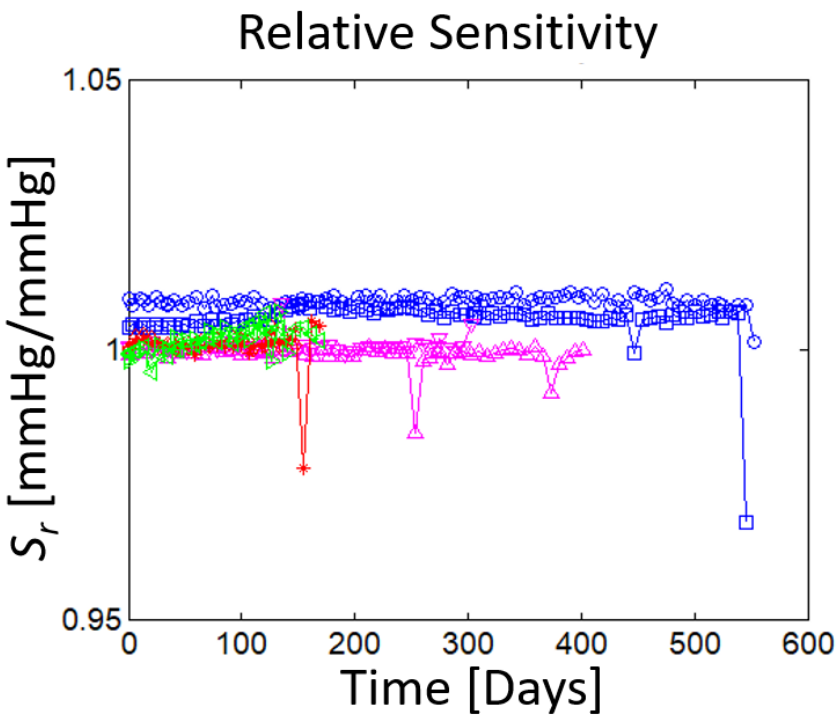

Figure 2.41: LPS25H wired saline soaking data, relative sensitivity.

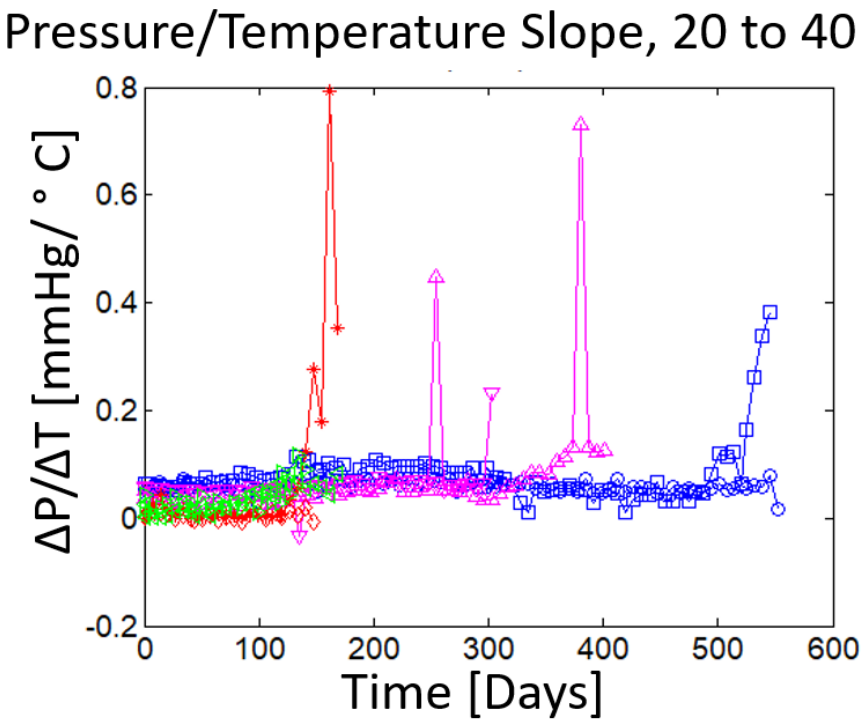

Figure 2.42: LPS25H pressure dependence on temperature, one-degree approximation over a temperature range of 20 to 40 °C.

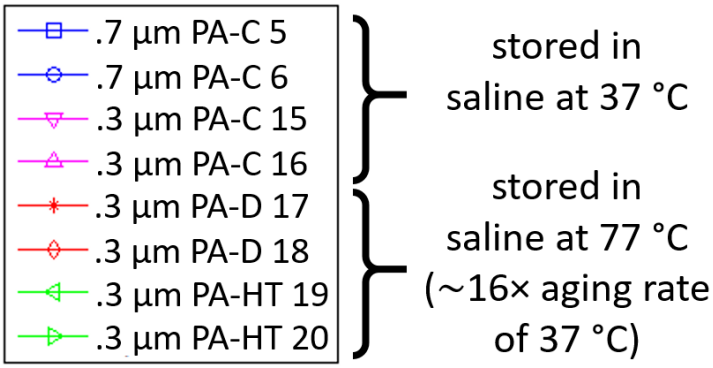

Figure 2.43: Legend for the wired saline soaking longevity plots with the LPS25H pressure sensors.

Additional comments for each sample are provided below: notice that some samples still reported data even after exceeding accuracy thresholds. For example, if I saw a bubble in the oil after a long time, I would know it would not yield reliable information. But it was still interesting to see how long the sensor could survive in a situation where most of the oil was still around the pressure sensor, but not fully encapsulated anymore. Also note that these samples were measured before the

light dependence was discovered. However, the difference between the light level conditions these sensors were exposed to and full darkness was about 0.2 mmHg, and additionally, the error introduced by the light should be much less than that because the lighting conditions were similar for every measurement (albeit not fully dark conditions).

Sample 5) 0.7 μm nominal PA-C. Stored in 37 °C. The offset drift magnitude at 37 °C was under 1 mmHg for 151 days and was under 2 mmHg for 468 days. On day 447, the relative sensitivity dipped from its normally stable value of 1.006 to 0.9997 for just one measurement. It recovered back to normal the next week, so I believe this was experimental error, as each measurement was done by hand. The pressure-temperature slope magnitude and drift were small (magnitude < 0.1 mmHg/°C and drift < 0.05 mmHg/°C) for at least as long as the offset was stable (468+ days). On day 521, this sample had a strange temperature sweep response, so it was not considered reliable from then on. Although it turned out not to be a problem, on day 34, this sensor reached up to 43 °C due to inattention. The sensor jumped up to larger offset on the way cooling down. It seemed to be fine by the next week, and was the one of the longest living sensor with stable readings in the end.

Sample 6) 0.7 μm nominal PA-C. Stored in 37 °C. The offset drift magnitude at 37 °C was under 1 mmHg for 167 days and was under 2 mmHg for 545 days. Sensitivity and temperature dependence were also stable for this time. On day 552 a bubble was observed in this sensor's package, leading to the offset, sensitivity, and temperature dependence shifts for the last recorded data point. Being the longest living and only remaining valid sensor at the time of this measurement, the experiment was concluded. This sample is used for the pressure-versus-temperature over time plot (Figure 2.44).

Sample 15) 0.3 μm nominal PA-C. Stored in 37 °C. The offset drift magnitude at 37 °C was under 1 mmHg for 45 days and was under 2 mmHg for 296 days. There was large hysteresis with temperature on day 303, with complete failure on day 310. There were two large bubbles observed in the oil on day 310, although it seems likely a failure event occurred before day 303. The sensitivity was stable for just as long. The temperature dependence was also stable for just as long, except for one measurement on day 135 where the temperature dependence was smaller than normal, but recovered to the typical value the following week. This is also attributed to human error in experimental procedure.

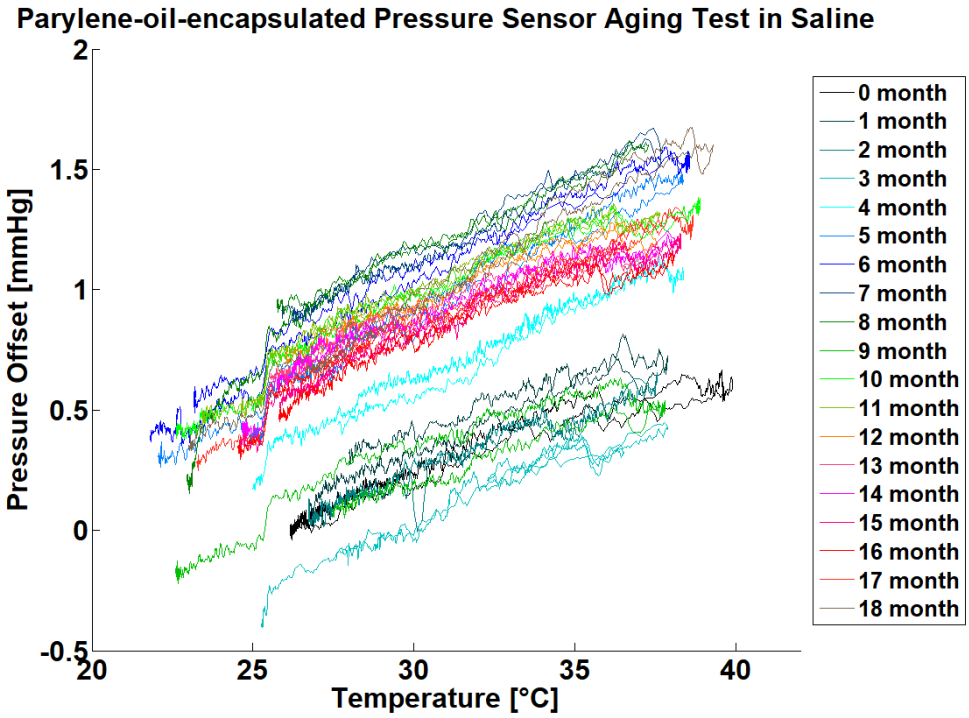

Figure 2.44: Sample PA-C 6. Pressure versus temperature plots over time. Assuming the temperature is known, the error should be less than 2 mmHg over the entire pressure range because the temperature dependence is stable.

Sample 16) 0.3 µm nominal PA-C. Stored in 37 °C. The offset drift magnitude at 37 °C was under 1 mmHg for 45 days and was under 2 mmHg for 247 days. On day 254, a bubble and a large hysteresis with temperature was observed. Data is still plotted afterwards, signifying data was still retrieved, but data is not necessarily meaningful from day 254 onward. Sensitivity and temperature dependence were stable until day 254, all explained by the presence of the bubble.

Sample 17) 0.3 µm nominal PA-D. Stored in 77 °C. The offset drift magnitude at 37 °C was under 1 mmHg for 7 days and was under 2 mmHg for 148 days, albeit on day 14 the offset change was over 1.9 mmHg. The device survived normally until day 155 when it seemed to warm up to 35 °C on its own, which was not normal. The sensitivity dipped on day 155 as well, unsurprisingly. It exceeded accuracy thresholds by the following week, although the temperature dependence seemed to grow starting on day 141. Using the day 148 point at 16 times aging factor, this corresponds to an extrapolated lifetime of nearly 6.5 years.

Sample 18) 0.3 µm nominal PA-D. Stored in 77 °C. The offset drift magnitude at 37 °C was under 1 mmHg for 44 days and was under 2 mmHg for 148 days. It

started to heat up on its own, which is not normal, on day 148. It failed entirely on day 155. Sensitivity and temperature dependence measurements were good until the device failed electronically. It survived the exact same number of days as sample 17, or extrapolated lifetime of nearly 6.5 years.

Sample 19) 0.3 μm nominal PA-HT. Stored in 77 °C. The offset drift magnitude at 37 °C was under 1 mmHg for 58 days and was under 2 mmHg for 71 days. The sensitivity and temperature dependence were good for at least as long. Measurements were still taken until day 162, when a large temperature dependence and hysteresis were observed. A lifetime of 71 days makes an extrapolated lifetime of over 3 years.

Sample 20) 0.3 μm nominal PA-HT. Stored in 77 °C. The offset drift magnitude at 37 °C was under 1 mmHg for 14 days and was under 2 mmHg for 58 days. The sensitivity and temperature dependence were good for at least as long. The device failed entirely on day 148, which was not surprising given the rapid positive and negative change in offset the previous two weeks. A lifetime of 58 days mames an extrapolated lifetime of over 2.5 years.

Note that the Arrhenius relationship of parylene is used as the accelerated aging factor of 16 is used for soaking tests in saline conducted at 77 °C to extrapolate the lifetime for devices at 37 °C, rather than a factor of 3 as the saturation age curve for the oil would suggest according to Figure 1.20. This is appropriate if we assume the failure mode for these devices are from delamination between the parylene and the solid substrate, which could leave voids to be filled by water (Figure 2.45), rather than the corrosion due to the presence of the water in the oil before voids were created. However, temperature cycling may have be an important factor as well. During the experiment, the samples were taken out of the oven and were exposed to room temperature to sweep pressure, and for the short-duration temperature sweep. An alternative hypothesis is that water vapor or other gases become super-saturated when the temperature drops so quickly, thus causing the formation of liquid. This seemed to be more prominent in earlier, lower 20 cSt viscosity oil packaged sample. It was obvious because the oil would become cloudy when taken out of the oven, then gradually become transparent again. This visual cue was not apparent for the 100k cSt viscosity oil. However, I cannot rule out that this effect is occurring, just at a much smaller magnitude in the higher viscosity case. The good news is that this is an artifact of the longevity setup, as the temperature varies much less than is necessary for this effect to occur inside the body. The temperature cycles were hard

to avoid because it would require a dedicated setup to store pressure sensors in saline at higher temperature, while also periodically sweeping pressure and temperature with an accurate reference pressure. In other words, testing under liquid would require extremely stable and accurately measured liquid column height.

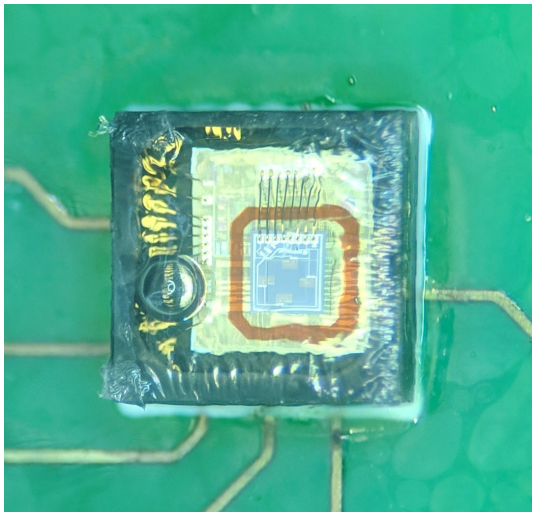

Figure 2.45: Bubble appears as a failure mode for some devices. It is surmised that parylene delamination over the plastic housing allows a void to be filled by saline. "dark 1 77 °C saline, day 36".

Far into the longest-duration wired longevity test, it was noticed that the pressure sensors had some sensitivity to light, since the top of the plastic housing was removed. While the maximum pressure dependence between the lighting conditions so far and total darkness was about 0.2 mmHg, uncoupled to pressure sensitivity, the longevity experiment was repeated with new sensors while measuring in total darkness. By this I mean all the overhead lights were off, but residual equipment monitor LEDs might be on. The results are summarized in Figures 2.46-2.49. There were three LPS25H sensors, packaged with 100k cSt silicone oil and nominal 0.53 µm PA-HT on oil, with additional 12.0 µm PA-C underneath. The sensors were stored in up to 100 °C oven temporarily for faster acceleration factor, but since the oven being used was found to be inconsistent in temperature by up to 10 °C, they were moved to a consistent 77 °C oven for the majority of the experiment. The failure mode of all three devices is hypothesized to be delamination of PA-HT from the package. This problem was plausible, as when packaging the sample an overflow of the oil was dispensed temporarily. So this resulted in a little oil touching the upper part of the outer side walls, giving greater risk of delamination. By day 43-44 for

the three samples, it was found all three samples had bubbles, so the experiment was ended.

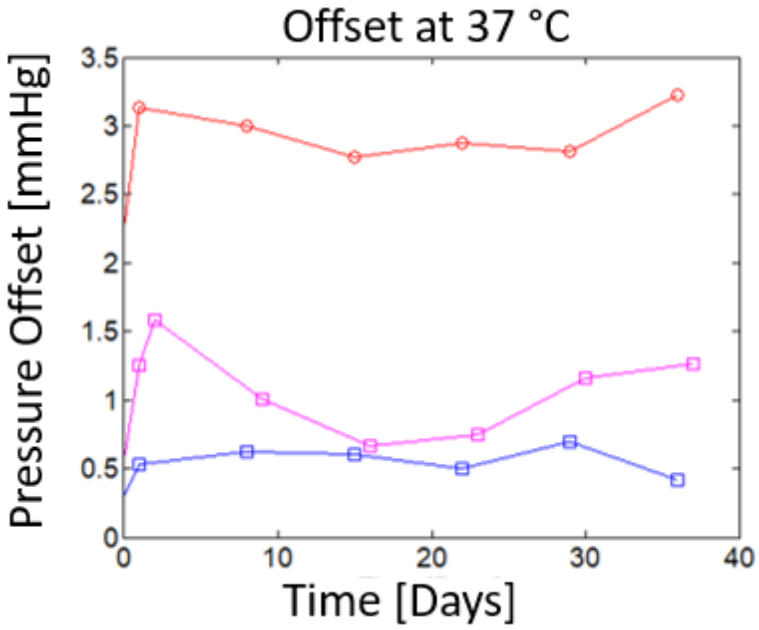

Figure 2.46: LPS25H wired saline soaking data, offset at 37 °C, measured only in the dark.

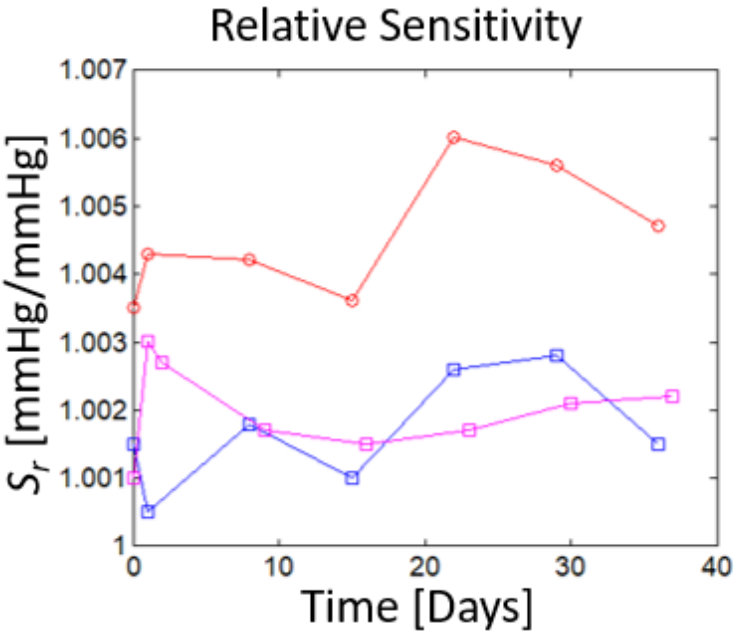

Figure 2.47: LPS25H wired saline soaking data, relative sensitivity, measured only in the dark.

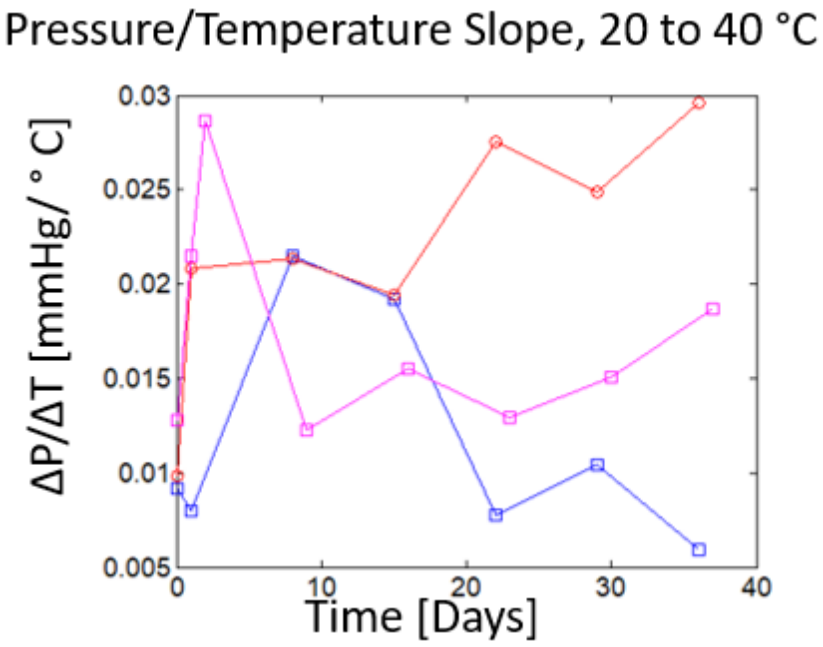

Figure 2.48: LPS25H pressure dependence on temperature, one-degree approximation over a temperature range of 20 to 40 °C, measured only in the dark.

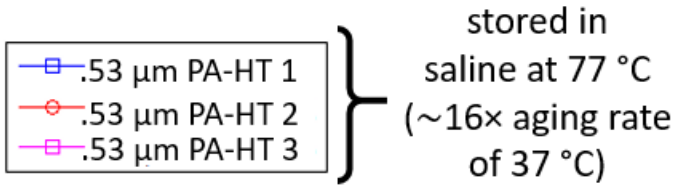

Figure 2.49: Legend for the wired saline soaking longevity plots with the LPS25H pressure sensors, measured only in the dark.

Sample Dark 1) 0.53 µm nominal PA-HT. Stored in 77 °C, with minor exceptions. It was stored at 84 °C in air overnight, and then in 95 °C saline for the first day. Afterwards it was stored in 77 °C. Up to day 27, the sensor was found to have less than 1 mmHg offset drift, and low sensitivity and pressure dependence on temperature drift. On day 36, it was found to have a bubble, probably from delamination of the PA-HT. This yields an extrapolated lifetime of over 13 months.

Sample Dark 2) 0.53 µm nominal PA-HT. Stored in 77 °C, with minor exceptions. It was stored at 84 °C in air overnight, and then in 95 °C saline for the first day. Afterwards it was stored in 77 °C. Up to day 36, the sensor was found

to have less than 1 mmHg offset drift, and low sensitivity and pressure dependence on temperature drift. On day 43, it was found to have a small bubble, and oil had visibly leaked out. This yields an extrapolated lifetime of over 18 months.

Sample Dark 3) 0.53 μm nominal PA-HT. Stored in 77 °C, with minor exceptions. It was stored at 100 °C in air overnight, and then in 84 °C saline for the first day, and then 95 °C saline for the second day. Afterwards it was stored in 77 °C. Up to day 37, the sensor was found to have less than 1 mmHg offset drift, and low sensitivity and pressure dependence on temperature drift. On day 44, it was found to have a large bubble. This yields an extrapolated lifetime of over 18 months.

In summary, the dark sensor data looks very similar to the first LPS25H longevity data, except that these sensors failed a little earlier, probably due to delamination issue described above. However, it is seen that the light-dependence is negligible.

2.8 Summary

In this chapter, the fundamental pressure sensor packaging scheme for implantable applications was proposed, discussed and analyzed. The packaging method, which is called parylene-oil-encapsulation, or parylene-on-oil packaging, is designed to protect an implantable sensors functionality and pressure sensing accuracy for a long time. Silicone oil surrounds the electronic pressure sensor, and the liquid is encapsulated by *in situ* parylene. Starting with a commercial, digital-output pressure with on-chip temperature reporting allowed for the analysis of the parylene-on-oil film stress itself as well. Wired, benchtop saline soaking tests were carried out as well as benchtop mock-up material accumulation tests. In short, this chapter covered all the fundamentals of the packaging method itself. Ideally, sub-micron nominal thicknesses of parylene-HT on high viscosity (100k cSt) silicone oil are suitable for packaging pressure sensors for implantable applications.

Chapter 3

WIRELESS, LOW-DRIFT IMPLANTABLE INTRAOCULAR PRESSURE SENSOR WITH PARYLENE-OIL-ENCAPSULATION

Towards proving the pressure sensor packaging scheme works in an animal, a full implant was developed with the idea of incorporating parylene-oil-encapsulation (Figure 3.1). This implant is only the first effort with the parylene-oil-encapsulation in mind, with the understanding that if the packaging concept is validated, future efforts could minimize the overall system size. For example, the ASIC and MEMS pressure sensor could be combined onto a single chip, thus reducing off-chip communications and capacitor, and perhaps also allowing for the removal of the charge storage capacitor. However, this requires a large effort, with less research value, as this type of work is well established within industry already. So, a commercial pressure sensor with parylene-oil-encapsulation formed the kernel of the implant architecture.

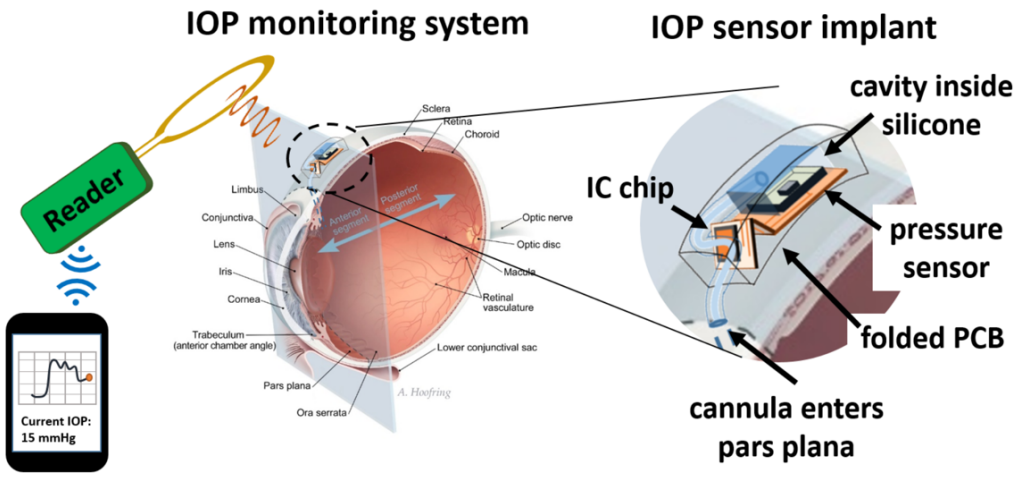

Figure 3.1: IOP monitoring system. An external reader powers the implant at 915 MHz, and receives RF backscattered data. The IC chip with on-chip coil receives the power, delivers it to the pressure sensor, retrieves the data over I2C, and transmits it back wirelessly.

3.1 System Architecture

The system is implanted in the superotemporal quadrant of the eye between the sclera and conjunctiva. It consists of a commercial pressure sensor (STMicroelectronics LPS25H) with digital readout, a 65 nm CMOS chip that supports wireless power/data telemetry and the I2C serial communication interface with the pressure sensor (3.2). The chip and pressure sensor are assembled on a flexible polyimide PCB. The implant uses an on-chip integrated RF coil to receive power from near-field RF coupling at 915 MHz and transmit measurement bits via RF-backscattering to an external reader. A 2 mm x 1.2 mm chip is fabricated in TSMC 65 nm CMOS process. The IOP implant achieves a pressure sensitivity of 0.17 mmHg with a total power consumption of 9.7 µW.

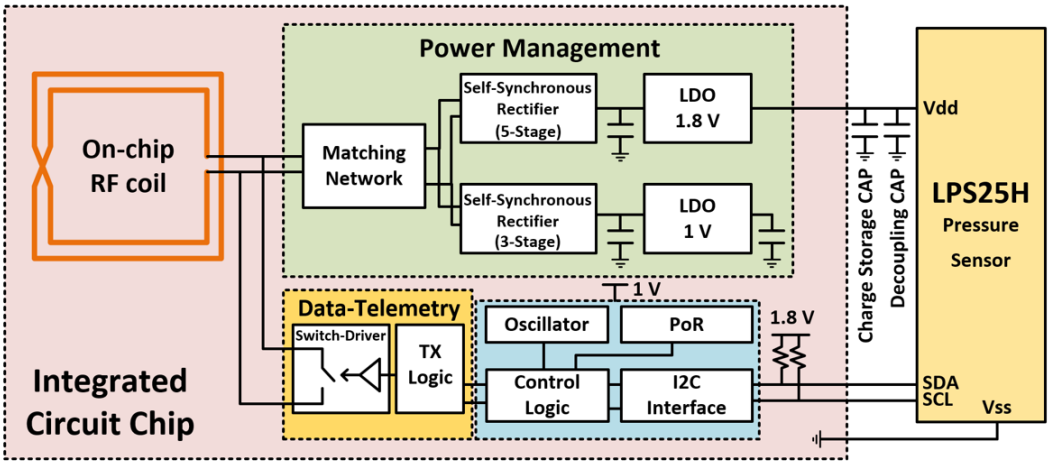

Figure 3.2: Electronic system architecture of the implant. The architecture at this level of the detail was decided jointly by A. Shapero and A. Agarwal.

The RF coil and analog circuitry was designed and laid out by A. Agarwal [87]. The digital logic on-chip could be run as low as 1 V, but the minimum voltage for the pressure sensor was 1.8 V, so there were two low-dropout regulators to minimize power consumption. A 100 nF capacitor is for decoupling the I2C lines for smooth I2C interaction. In parallel is a 22 µF charge storage capacitor. A die photo is shown in Figure 3.3.

3.1.1 Electrical Design and Verification

To test whether the electrical circuitry would be compatible with the LPS25H pressure sensor, we put the digital code on an FPGA and supplied the pressure sensor with a conservatively current-limited voltage supply, in order to mimic worst case power limited scenario (Figure 3.4). The various features we tested and debugged

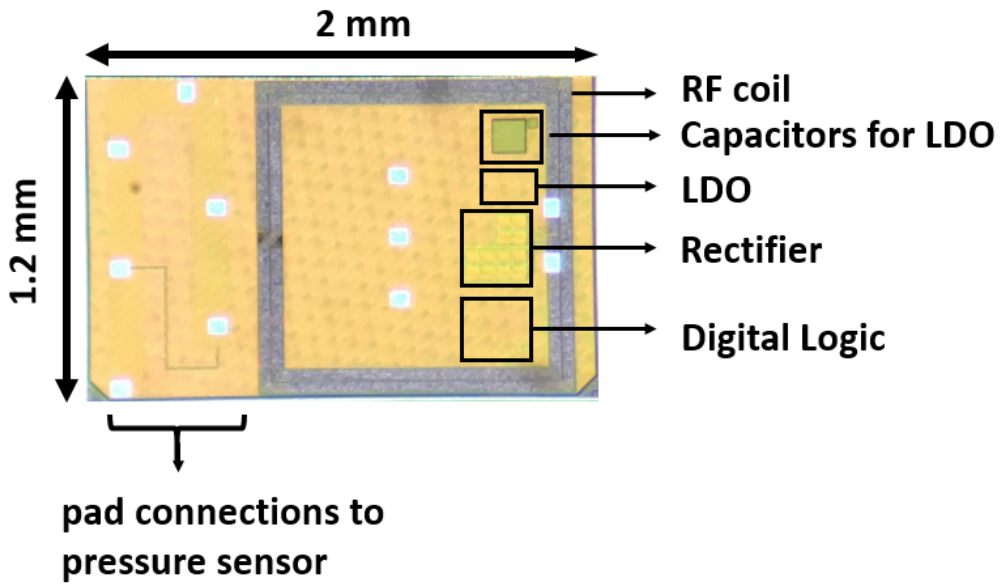

Figure 3.3: Die photo of IOP implant IC chip with on-chip coil. Designed jointly by A. Shapero and A. Agarwal.

were the choice of capacitors, the voltage supplies, the pressure over-sampling options, the pull-down resistors' values, the communication frequency, and the digital code on-chip. We could also measure the current consumption of the pressure sensor with the various options. Besides the fact that modelsim files are not provided by the company, it was safer to verify with actual parts since we could. We verified that pull-down resistor values of 47 kΩ and a bus frequency of 50 kHz worked, and was a good balance between achievable communication speed and low energy consumed during communication over I2C.

3.1.1.1 External Capacitors

It is worth noting that the 100 nF capacitor in parallel with the 22 µF capacitor is not negligible when considering parasitic effects that better model real capacitors. The equivalent series resistance (ESR) is small in our case and is ignored, but included here for completeness. Much more important are the equivalent series inductance (ESL) and internal resistance (IR). The ESL goes up with increased capacitance, and the IR goes down with increased capacitance. Since IR is in parallel, it is equivalent to saying the parallel conductance goes up with increased capacitance (Figure 3.5). For I2C communication, the 100 nF decoupling capacitor prevents additional ripples upon logic rises and falls from bouncing signals, but a

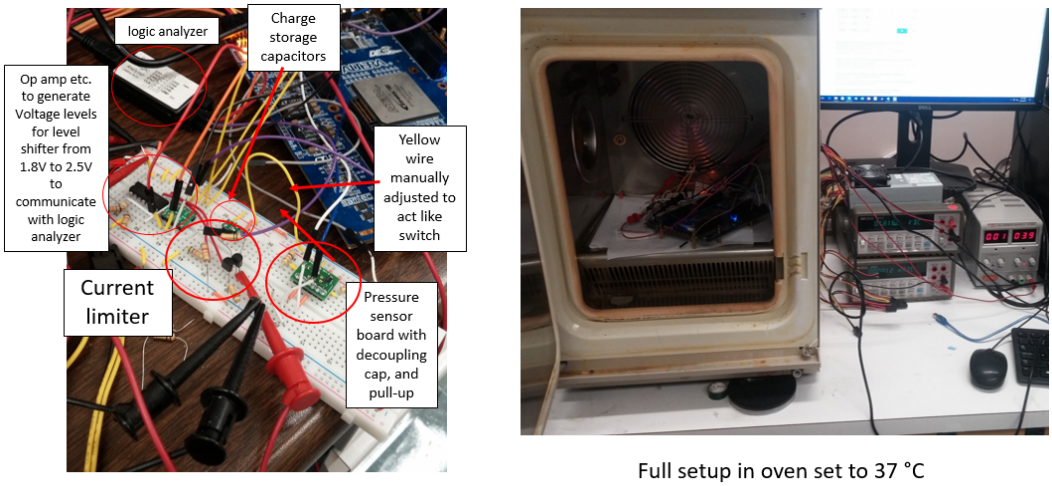

Figure 3.4: FPGA test setup to verify digital code, components, frequency, and supply voltage, and pull-down resistor values. Setup put in oven to verify components were valid at body temperature, with the oven door open for photograph only.

large inductance exacerbates ringing. Thus, since the two physical capacitors are in parallel, the small ESL of the 100 nF capacitor nullifies the larger ESL from the 22 µF capacitor.

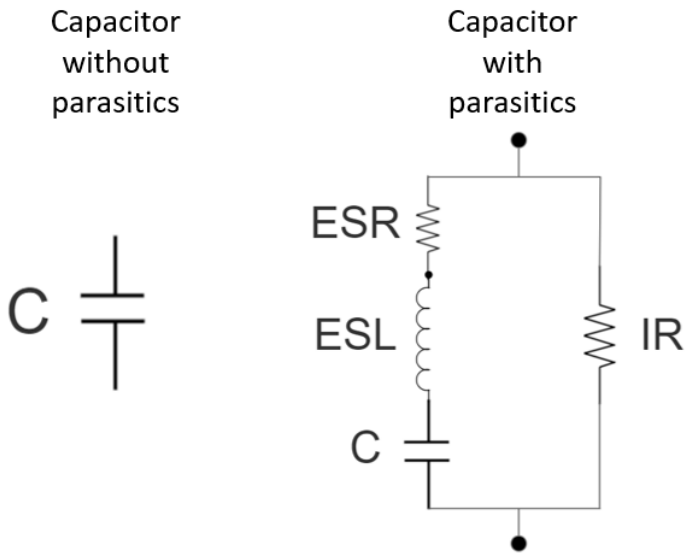

Figure 3.5: Capacitor model without and with parasitic effects of equivalent series inductance (ESL), equivalent series resistance (ESR), and internal resistance (IR).

Unlike pulsing signals where the smaller of the two capacitors dominates the inductance, the leakage current will be dominated by the lower IR of the two

capacitors, which is the charge storage capacitor . I discovered that the IR of the charge storage capacitors for all 0402 (1 mm × 0.5 mm) capacitors with 22 µF were too small for the assumed constant current supply of 5 µA, which was constructed with two transistors. The smallest volume 22 µF capacitor I found with sufficient IR was 0508 (1.25 mm × 2 mm) in size. Note that the charge-storage capacitor is wider than than it is long.

The charge-storage capacitance value was chosen to be the smallest value for quickest charging and smallest value that was large enough such that the voltage would not drop more than tolerable during a pressure measurement activity. As seen in Figure 2.35, there is a voltage dependence of roughly 6.3 mmHg/V at a supply voltage of 1.8 V. So, a voltage droop of 80 mV as seen in 3.6 yields a pressure error between half to the full droop amount of between 0.25 mmHg and 0.5 mmHg, since the temperature measurements are made first, and the pressure measurements are averaged throughout the multiple samples for each measurement. This was done assuming a maximum current source of 5 µA, which is worse than worst-case as the regulator on-chip supplies more current from the charge stored at the rectifier capacitors on the IC chip, shown in Figure 3.7. Since the oscillator in the fabricated chip was a little slower than predicted, the data rates come once every 1.3 seconds.

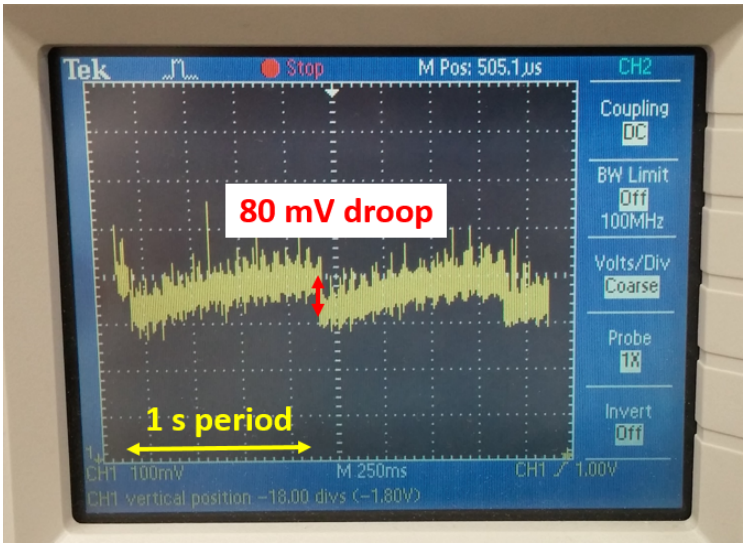

Figure 3.6: Voltage droop by sensor measurement. Every 1 second, a measurement is taken by the pressure sensor. The voltage drops by 80 mV, and recharges back to the original value.

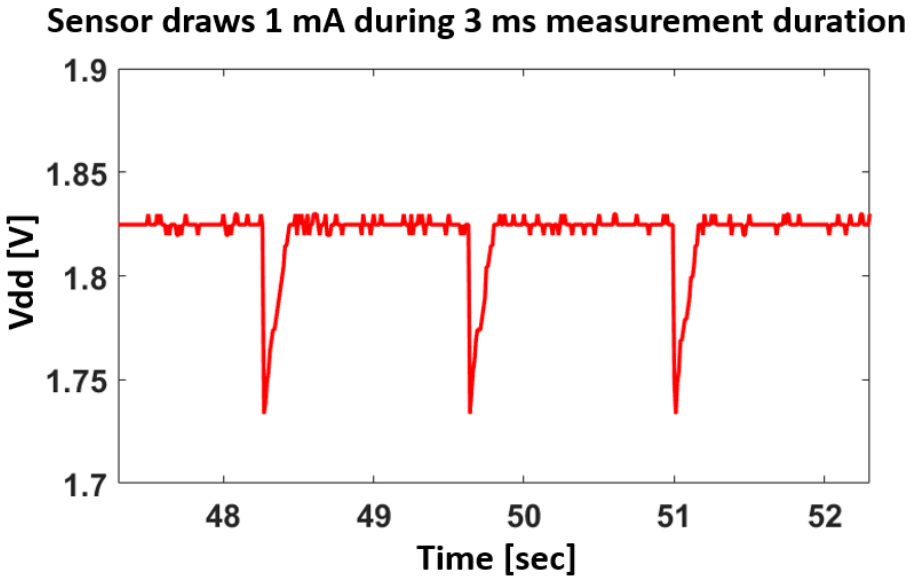

Figure 3.7: Measured wireless IOP with IC chip. Voltage drop is only 100 mV for 3 ms each measurement. All analog circuits, including coil, rectifier, and regulator on IC chip designed by A. Agarwal.

3.1.1.2 Current Limited Operation

A target sampling rate of 1 sample per second was chosen as a balance between enough data rate, but less demanding power consumption overall. Given that 1 mA × 3 ms = 3 µC, assuming worst case current source of 5 µA, then 1 sample per second gives almost a safety margin factor of 2. Figure 3.8 shows the current profile for a one-shot measurement by the LPS25H sensors. The current draw was seen to be consistent over 1.8 to 3.6 V supply.

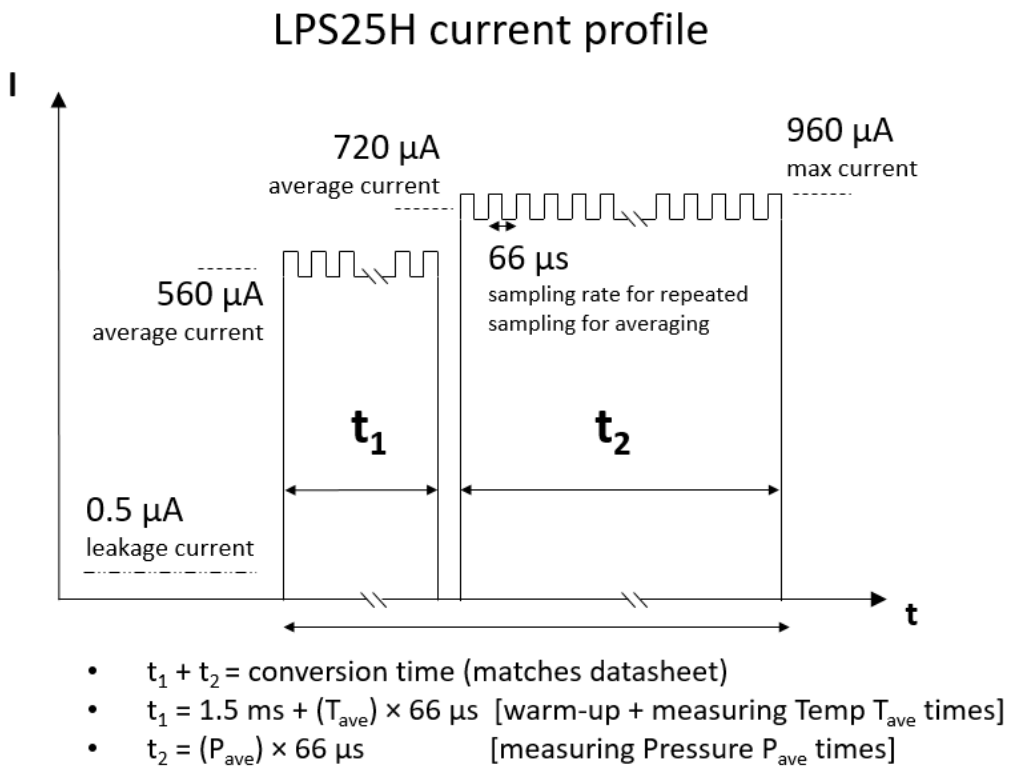

Figure 3.8: Current profile for one-shot measurement by the LPS25H pressure sensor.

Even though the final sensor used was the LPS25H and not the LPS331AP, an interesting experiment was conducted with the LPS331AP. The two sensors are very similar, where the 25H is newer and smaller. One difference is that for the one-shot measurements, the minimum pressure oversampling for the 331AP can go as low as one pressure sample per measurement. However, the minimum sampling available to the 25H is 8P, 8T samples. Figure 3.9 shows that sampling beyond about 8 pressure samples is not efficient, as the standard deviation diverges from what would be iid measurements. For that reason, the design was chosen that the IC chip that would run the LPS25H sensor on the implant would only call for the minimum oversampling.

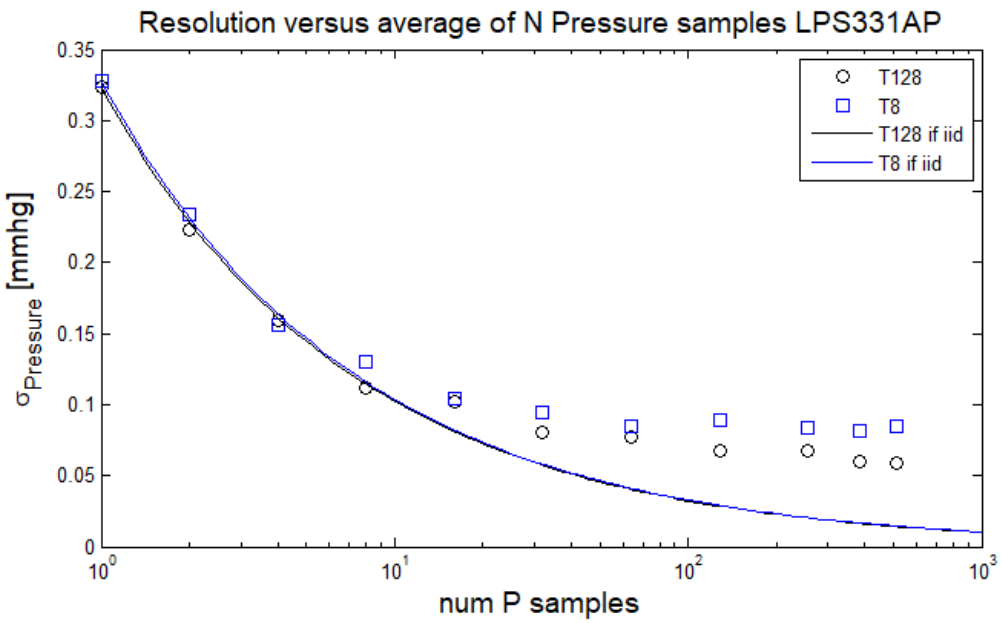

Figure 3.9: Efficiency of oversampling for LPS331AP pressure sensor.

A current limiter circuit with 2N3906 PNP transistors was used. There was about 0.6 V drop-off with this circuit (Figure 3.10). This circuit was sufficient for testing, and is not claimed to be the best performing current-limited voltage source.

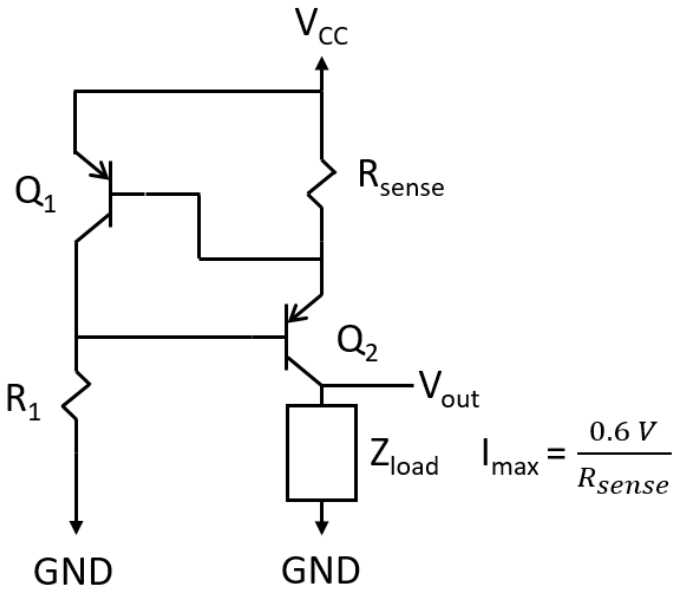

Figure 3.10: Current limiter circuit with pnp transistors for prototyping component viability and compatibility and debugging verilog code on the ASIC using an FPGA [88].

3.1.2 System State Behavior and Verilog Code

Upon power-on-reset, a start-up clock is initiated. This is a pre-programmed delay to let the charge-storage capacitor charge up. Then the ASIC gives one-time option selection commands. The default values are chosen, called one-shot, and the smallest over-sampling option in order to save on the energy needed for a single measurement event. Then the IC chip requests a "one-shot" measurement over the I2C lines. This means the pressure sensor makes an averaged pressure and and averaged temperature measurement, and stores the values in registers. Then the IC chip retrieves serializes the constant 8-bit identifier word, the 24-bit pressure and 16-bit temperature values stored in the registers. Then it uses a switch to wirelessly transmit that data to the external antenna. A reading is done every 1 second. The chip also has programmed delays between the above-mentioned sub-steps. In this manner, the chip is deaf, as it does not listen for external commands. This design was chosen as the first generation of a chip to read a pressure sensor to maximize chance of success by minimizing the complexity of the system.

3.1.2.1 Data Packet Overview

The data packet sent by the IC chip is thus, 5-bit prefix ‘10101’ as pre-programmed into the IC chip, then the identifier word that is stored in the pressure sensor, but not the IC chip, which should read ‘10111101’ if successful, then the 24-bit pressure, MSB first, then the 16-bit temperature, also MSB first, then a 5-bit suffix ‘10101’ also pre-programmed into the IC chip. So each packet is 5+8+24+16+5 = 58 bits long. Fat and skinny pulses represent 1’s and 0’s respectively. Figure 3.11 shows an example data packet and interpretation.

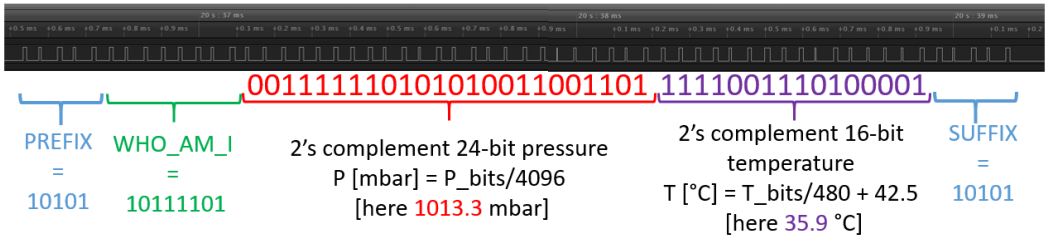

Figure 3.11: Data packet from the wireless device and overlaid interpretation.

3.1.2.2 Troubleshooting Wireless Operation by Viewing Data Packet

Thorough investigation of the electric system of the wireless implant, before attempting to package it was very helpful for debugging problems later on. Listed

are some of the observations and problems/solutions.

1. The first thing to check is whether the prefix and suffix are correct (both should read '10101'). The IC chip should be able to correctly report the prefix and suffix even if it is not connected to anything. If the prefix and suffix are not displaying, either the chip is damaged, or the chip is not receiving any power, or too little power. Or simply, the chip is not there. The next most useful thing about the prefix and suffix is for defining the threshold thicknesses for a 1 and 0, which changed slightly depending on my external circuitry.

2. If the prefix and suffix are correct, but all the bits in between are 1's, then the chip is receiving at least enough energy to power itself, but either the connections to the pressure sensor is broken, or there is not enough power for the commercial sensor. All 1's means that every byte that the pressure sensor should send over the I2C line is left blank, because it is a pull-down system.

3. Sometimes the prefix and suffix are correct, and the identifier word, also referred to on its data sheet as the 'WHO AM I' bits, is correctly showing '10111101', but the rest of the bits are incorrect. Since the 'WHO AM I' bits are stored only on the pressure sensor and not the IC chip, this would prove that the IC chip is talking to the pressure sensor correctly, but something has prevented an actual valid measurement event by the sensor. This could be multiple reasons. If the data bits are all 1's, all 0's, it is probably because the pressure sensor is not getting quite enough power, despite it getting more power than the scenario if 'WHO AM I' is blank. Another possibility is that the pressure sensor was turned off due to lack of power, and then turned on again too quickly. Since the IC chip does not reboot the pressure sensor except during the IC chip's own power-on-reset, this can put the commercial chip into a weird state. Given the rest of the system's configuration, it was advisable to turn off the RF power for at least 120 seconds if the RF power is ever turned off at all to let the power discharge in the capacitors. This is a side effect of choosing capacitors with the best possible internal resistance for the smallest leakage current during operation.

4. The implant should be stable for long periods of time if left on powered by RF with a clean start up. If the pressure and/or temperature values starts to wander up and down at an amplitude of up to 10 mbar over the course of minutes, then this was found to be evidence of ESD. Additionally, even though the IC

chip is 1.2 mm × 2 mm, it was made on a 2 mm × 2 mm die with another circuit on there. Several chips were diced by two different companies, and every functioning diced chip showed this wandering behavior. Whether the true cause is ESD or not, the IC chip cannot be fixed and needs to be replaced.

5. If sporadic bits are present and missing throughout the entire data packet, try realigning the coil and/or re-tuning the frequency and capacitor on the antenna.

3.1.3 Operation Protocol

Given the IC chip was not re-configurable, and had some quirks, such as a preset wait time to charge up, which may or may not have been necessary, and a long discharge time, and only resetting the pressure sensor upon the IC chip's own power-on-reset, the following operation protocol was developed.

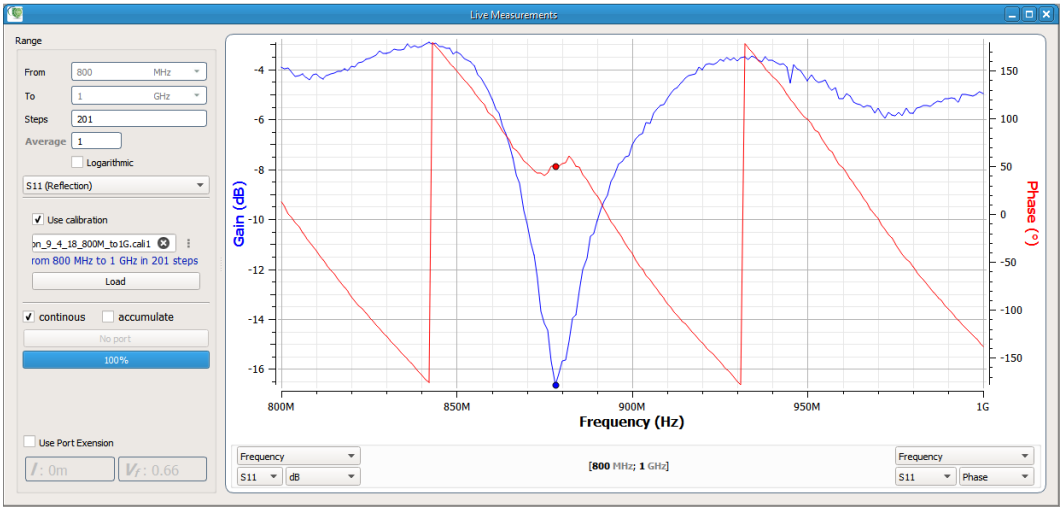

Figure 3.12: Reflection coefficient (s11) sweep for rabbit IOP *in vivo* measurement. At 878 MHz, the s11 is -16.25 dB.

1. First, make sure the antenna coil is dry. This applies more when the align the primary antenna coil as best as possible to the secondary coil on the implant. The positions of the antenna coil and implant need to be fixed in space, otherwise, restart from here.

2. Then, a vector network analyzer is connected to the antenna coil (disconnect the antenna from the RF circulator if necessary). See Figure 3.12. Sweep the frequency, and look for the frequency that has reflection below ideally

below -20 dB. If a narrow minimum below -20 dB is not present, re-tune the capacitor on the antenna coil and sweep the frequency again. If after sweeping the capacitor it is not possible to get a sharp minimum below -20 dB in air, or at least below -16 dB in a rabbit, recheck the position (go back to 1).

3. Note the optimum frequency and set the RF generator to the that frequency and select the power level not exceeding -18 dB.

4. Wait for at least 120 seconds in between turning off the vector network analyzer and turning on the RF generator. Reconnect the antenna coil to port 2 of the RF circulator and turn on when appropriate. The data reports in at around 23 seconds. Record with the logic capture simultaneously.

5. Confirm the data looks clean in the oscilloscope. If it is good, record for as long as desired. Recheck the oscilloscope for continued correct functionality as desired. When data collection is completed, export the file as a .mat file and process it with Matlab.

3.1.4 Plotting the Measurement from the Raw Logic Analyzer Data

A Matlab script is used to interpret the data and plot it. The raw data is a list of transition times. Bit 1's are wider than bit 0's. Threshold values, and optionally various sets of threshold values are used to interpret the data. This is only an artifact of the external circuitry, and not any effect internal to the implant itself. It was found that for some *in vivo* IOP measurements, the 0's pulses were not triggering. But luckily the signal was noise free in these scenarios, so it was feasible to interpret where the 0's should have been given the blank spaces within a data packet. Of course, this did not give reasonable results for every data packet, but since the implant measures roughly once a second, we could get a reading if at least a fraction of the data packets could be interpreted correctly, which was fortunately the case. See Figure 3.13.

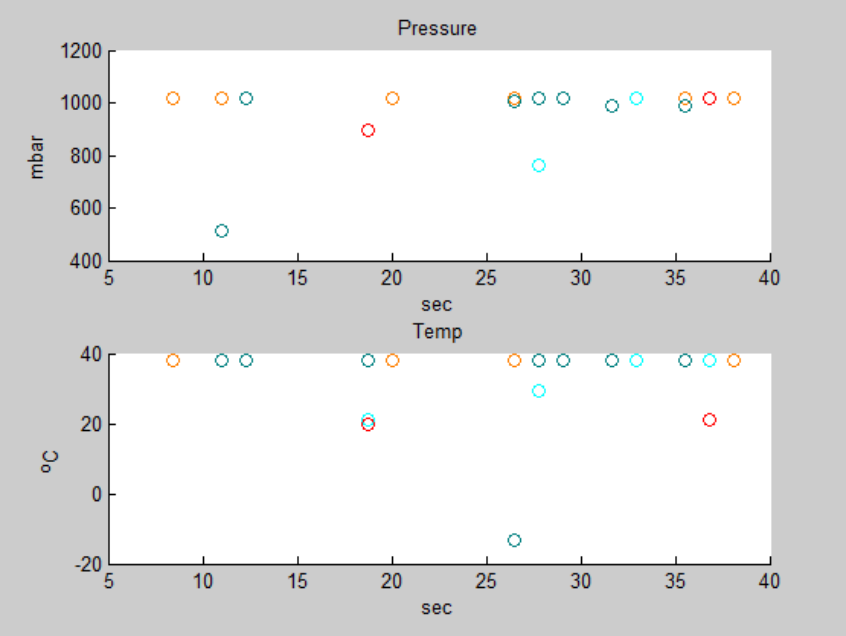

Figure 3.13: Rabbit *in vivo* raw absolute pressure and temperature data as plotted by the Matlab script. Various colors are different thresholds for interpreting 1's and 0's, and nonsensical values can be ignored.

3.2 External Circuit

The external RF powering and data telemetry circuit is standard, and is shown in Figure 3.14. A function generator generates nominal 915 MHz signal, which is amplified by an RF power amplifier. The power signal going into port 1 of the RF circulator goes out of port 2 and to the antenna coil, where it wirelessly powers the implant. During RF backscatter telemetry, a switch in the IC chip closes the on-chip coil (the same coil used for power), which changes the impedance and reflection wave. The reflected wave goes back into port 2 of the RF circulator and comes out of port 3, where it goes into the reader circuit. The reader circuit transfers the pulses in the envelope into 0-2.4 V logic to be interpreted by the logic analyzer and stored on the PC. Figure 3.15 shows the setup in the operating room.

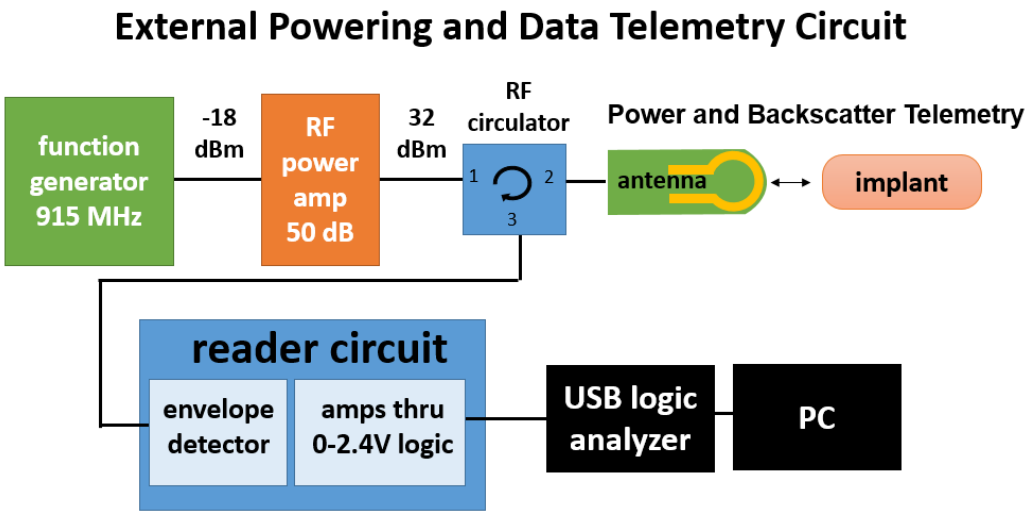

Figure 3.14: External wireless RF powering and data telemetry circuit.

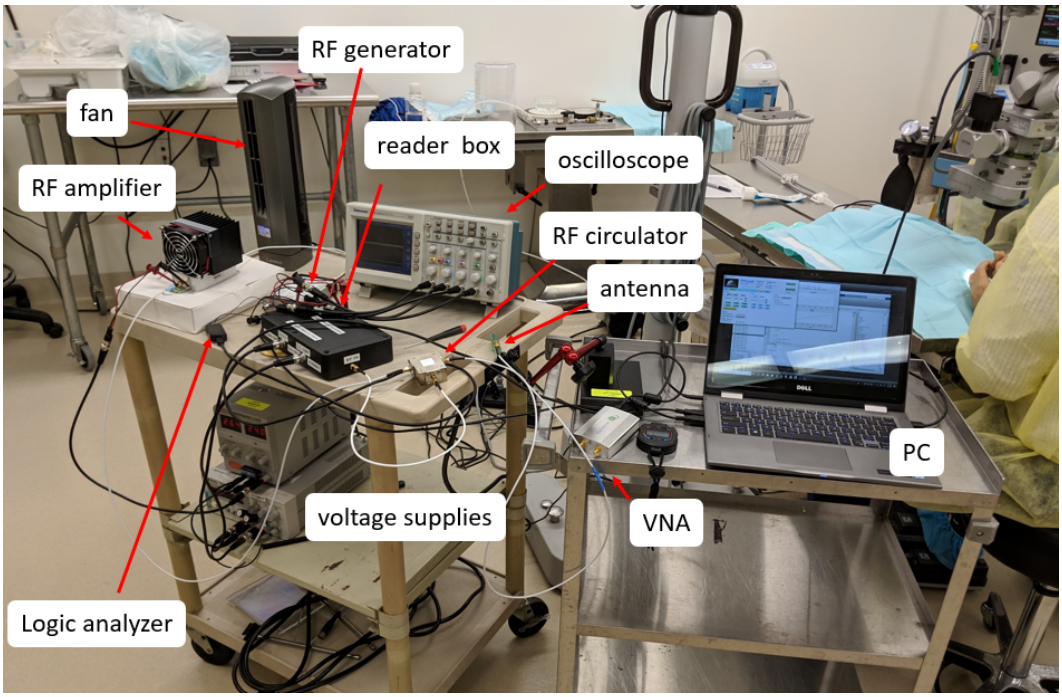

Figure 3.15: Electrical setup for wireless measurements.

3.2.1 Reader Box

The reader box converts the incoming RF reflection signal into 0-2.4 V logic (Figure 3.16). It consists of an ADL5511 RF envelope detector, and a custom board. Besides power supplies connections, there are debug pins to view in the oscilloscope and the output pin, with multiple leads for convenient viewing in the oscilloscope

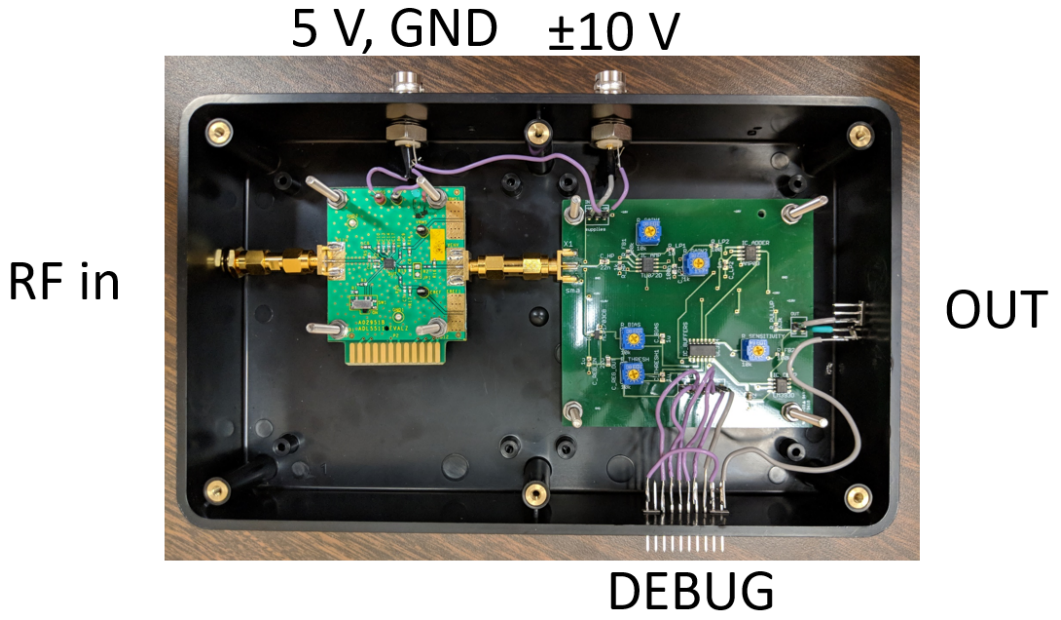

Figure 3.16: Wireless packet reader box.

while the data is being collected.

The reader box requires 3 voltages, plus GND line. The 5 V is to supply the envelope detector, and the ±10 V is to supply the remainder of the circuit. Figure 3.17 shows the circuit schematic. It is noteworthy to mention the four potentiometers on the circuit. One is to adjust the gain of the signal. Another is to adjust the sensitivity of the Schmitt trigger, and the last two are to adjust the bias levels of the positive terminal (where the AC signal is added) and a negative terminal, as the output needs to be 0-2.4 V logic to be read by the logic analyzer.

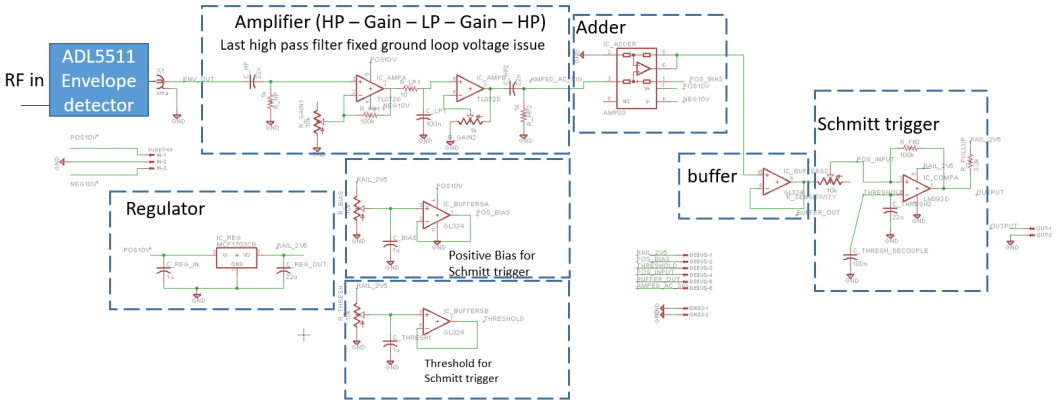

Figure 3.17: Wireless packet reader circuit schematic.

There are many pins to view and debug the circuit during operation, but it was found that these four lines were sufficient most of the time inside the oscilloscope: the AC signal, the two input signals to the Schmidt trigger, and the output signal (Figure 3.18). The potentiometers could be adjusted in the following way. First the amplitude of the AC signal is tuned, then the bias levels are fixed, and last, the sensitivity of the feedback for the Schmitt trigger is adjusted.

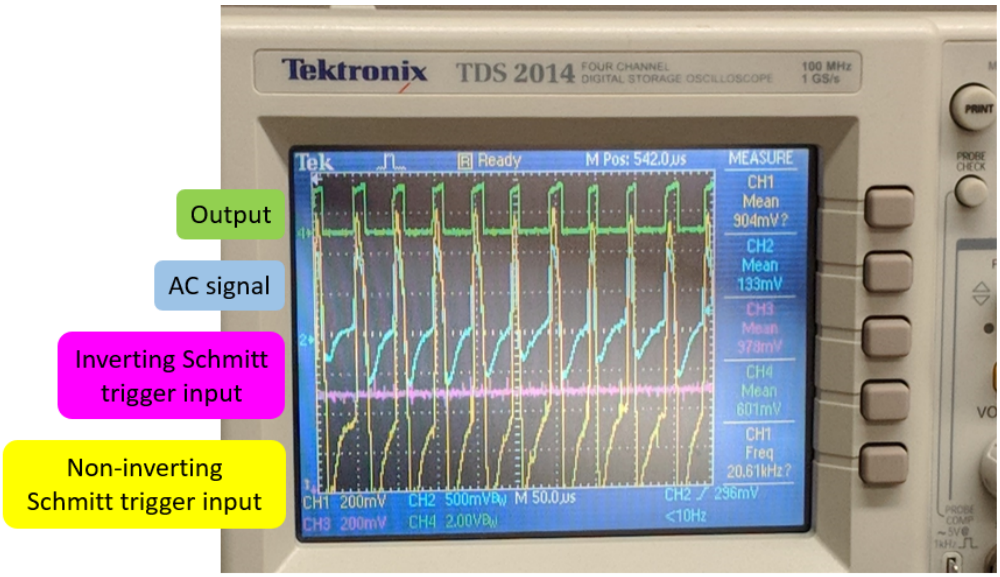

Figure 3.18: Typical capture of oscilloscope for debugging and verification during operation.

3.2.2 Reader Antenna

The coil is single turn, 16 mm OD coil, with one shunt capacitor and two series capacitors, where one is fixed and the other is a variable capacitor for manual tuning[2]. See Figure 3.19.

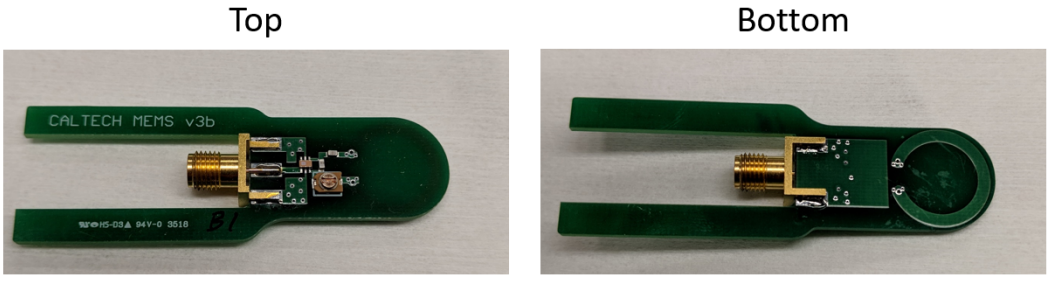

Figure 3.19: Reader antenna for power delivery and data reception.

Some additional notes are as follows. Earlier designs had a right-angle SMA cable connector, but the stiffness of the cable itself made the surface-mount solder connections break too easily, so ultimately a design with a side-mounting SMA cable connector was used. Two legs in the FR4 board were drawn as handles to clamp with the magnetic holder. The final design was robust.

The maximum range of the implant in air at the maximum power that the reader antenna could handle (32 dBm) was 9 mm (Figure 3.20). Computer controlled, multi-DOF (X, Y, Θ) motorized stage built by Siva Gangavarapu aided in this measurement (Figure 3.21) [89].

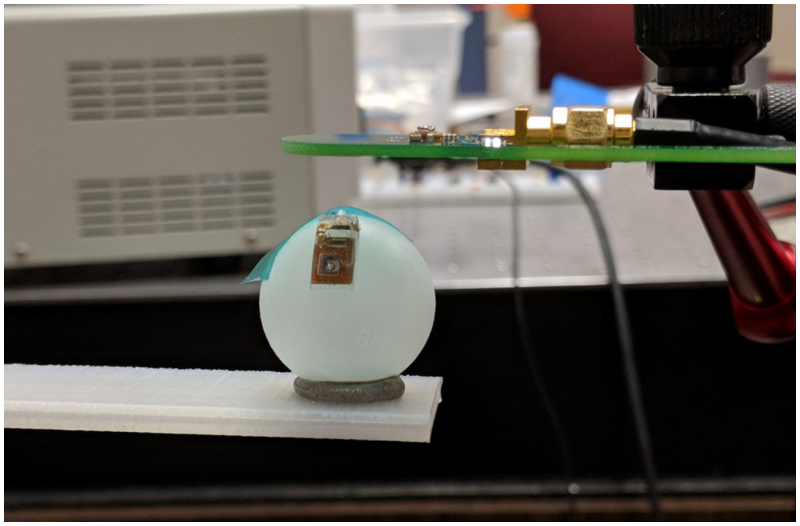

Figure 3.20: Maximum distance of powering implant in air was 9 mm.

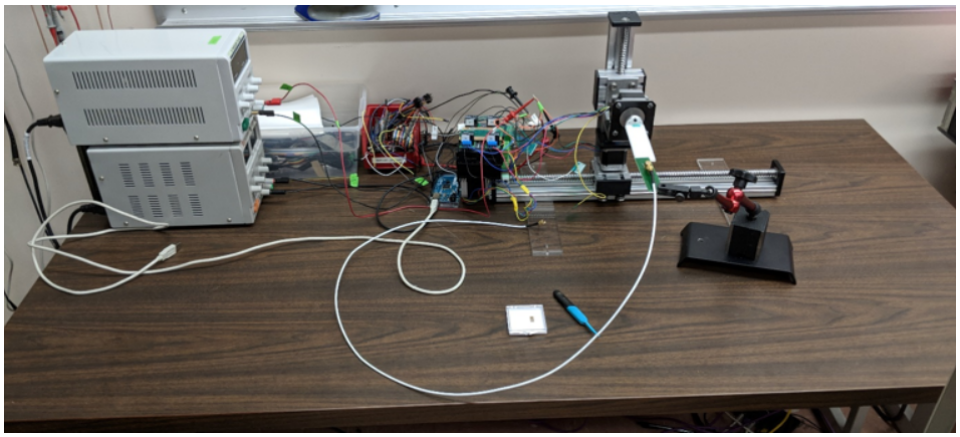

Figure 3.21: Custom computer controlled multi-stage positioner for coil characterization (courtesy of Siva Gangavarapu).

3.3 Silicone Chamber

To isolate the pressure sensor from its immediate and to sense the pressure at a remote location, say for an extraorbital device sensing intraocular pressure, a silicone chamber and tube structure was devised. Silicone Med-6219 by Nusil was used for the chamber, for its superior hardness and stiffness compared to Med-4210. To create the chamber, a positive 3D printed mold was made. Then, a negative mold is cast with a softer silicone such as Med-4210. Then, the final shape is cast with Med-6219. Parylene is coated on the 3D printed mold and the silicone mold to release the silicone mold and the final 3D printed part respectively. Figure 3.22 shows the 3D printed mold to make the stiffer chambers. The roof thickness was swept from 0.2 mm to 0.6 mm in this mold. The tab is to make it easier to grab out of the mold without fear of damaging the part. The tab can be sliced off if desired, but often isn't necessary, since the final form factor is the same shape anyways.

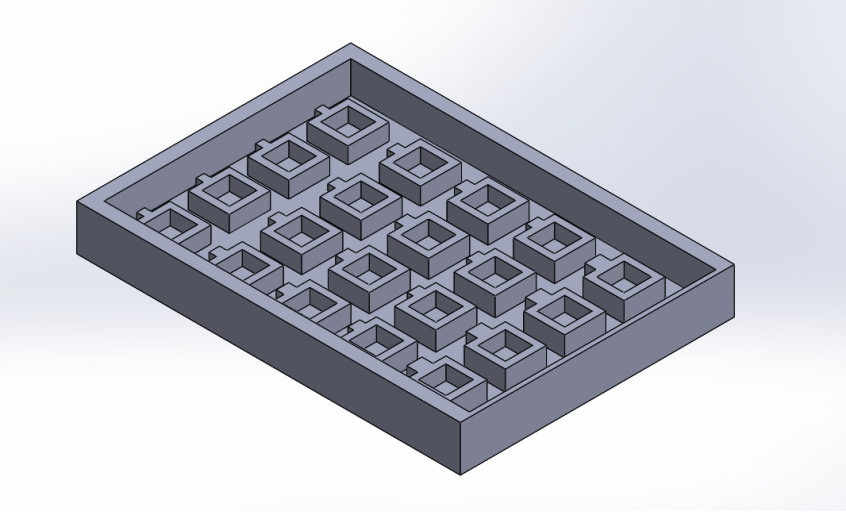

Figure 3.22: Positive mold for Med-6219 silicone chambers.

Earlier versions of the chamber used the Med-4210 and a smaller chamber, but it was found that after putting the implant in the rabbit, a too soft and too small inner chamber would compact enough such that the inner silicone surface would touch the parylene-on-oil film, which would cause a pressure offset. So, the final shape for the silicone chamber is inner chamber of $1.6 \times 3 \times 3$ mm^3, and outer hull of $2.0 \times 4.5 \times 4.5$ mm^3.

Next, a hole is made in the side of the chamber with a 1 mm diameter punch, and a silicone tube is threaded through, as shown in Figure 3.23. Then, Med-4210 is used to seal the outside of the tube to the wall. After the additional silicone

is cured, the tube is cut to be flush with the inside of the chamber. The silicone tube is not implantable grade, as that was difficult to find. The tube used is from McMaster-Carr[3], and is rated suitable for handling food and pharmaceuticals by the FDA. It is 0.63 mm OD, 0.31 mm ID.

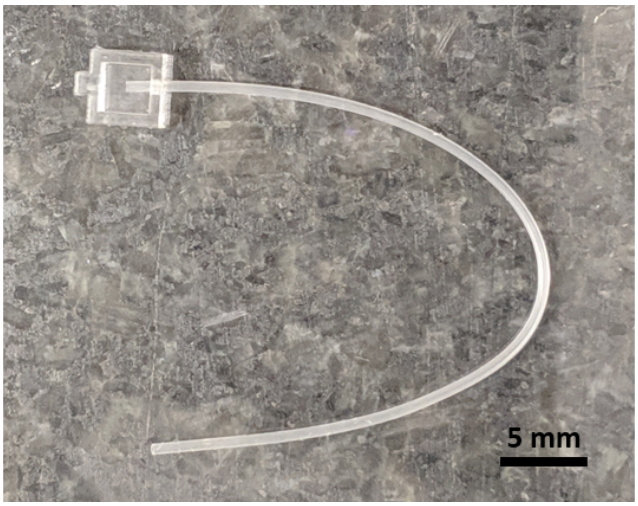

Figure 3.23: Underside of chamber and tube before sealing and cutting excess tube length on inside.

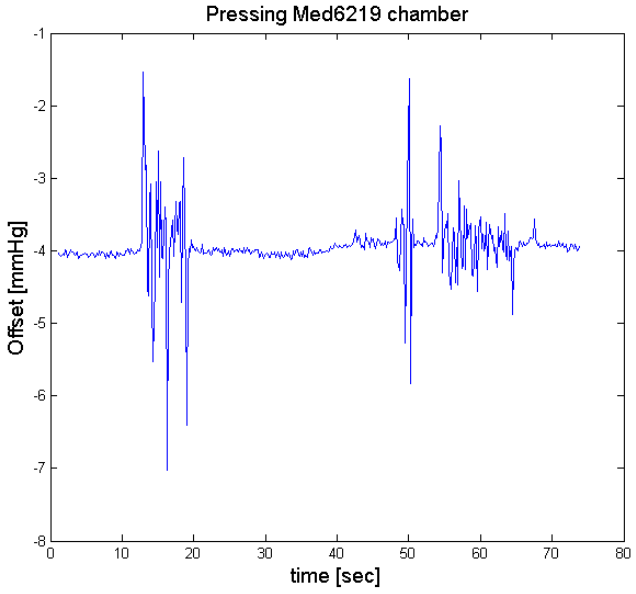

Figure 3.24: Pressing and holding Med-6219 silicone chamber only shows impulse disturbances, without a constant pressure offset from a softer Med-4210 silicone chamber.

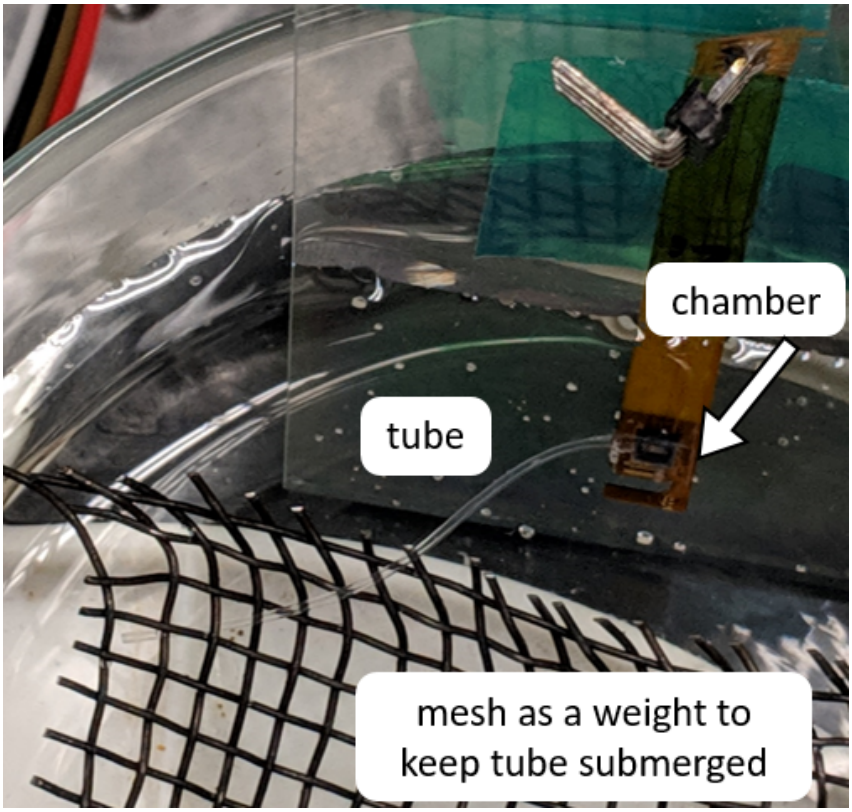

Figure 3.25: Med-6219 silicone chamber push test was conducted underwater.

Figure 3.24 shows the data of an experiment to verify that the chamber is sturdy enough. The presses seen roughly between 10-20 and 45-70 second ranges show transient pulses, but not constant shifts from constant presses like softer chamber would show. The experiment was done underwater (Figure 3.25).

3.4 Packaging and Assembly

Our system uses the LPS25H, a digital output pressure sensor with internal temperature calibration. It is also low power, $2.5 \times 2.5 \times 0.8$ mm^3 in size, requires a minimum supply voltage of 1.7 V. The pressure sensor and capacitors are first soldered onto the flexible polyimide PCB. At this point, the pressure sensor and solder are verified using a wired Arduino setup. If it is good, then an ASIC can be committed to the sample.

3.4.1 Assembly Before Silicone

As mentioned earlier, whenever we had the chips diced to try to isolate the 1.2 $\times$ 2 mm^2 IOP circuit, the pressure reported would not be stable. So in the end, it was decided that since the IC chip was small relative to the total volume, we would use

the full 2×2 mm^2 die. For the polyimide PCB used, the area section was intended for a diced version, and we kept using it even after residing to use un-diced chips. So in the interim and fully through the first successful *in vivo* tests, the chips were epoxied onto a piece of polyimide cut out from a spare PCB which was previously epoxied onto the region of the full PCB where the ASIC should reside. This was to provide a base larger than the whole base of the ASIC. This was a temporary fix so that we did not have to send out a new polyimide PCB and wait for the turnover time.

The IC chip is then epoxied and wire bonded to the PCB. During wire bonding, it important that the PCB is taped securely to a glass slide substrate. The PCB is taped in sections so that it could be gently removed without breaking the wire bonds, as shown in Figure 3.26. Masterbond UV10TKMed UV-curable epoxy is dispensed over the wire bonds to secure them. The polyimide PCB has a narrower midsection between the ASIC and other components, which is then doubly folded with tweezers to angle the chip 30° forward (see ahead, Figures 3.28, 3.71). This is so that the high-viscosity epoxy will stay in the vicinity of the ASIC and the wire bonds, rather than spread outward, which would prevent bending.

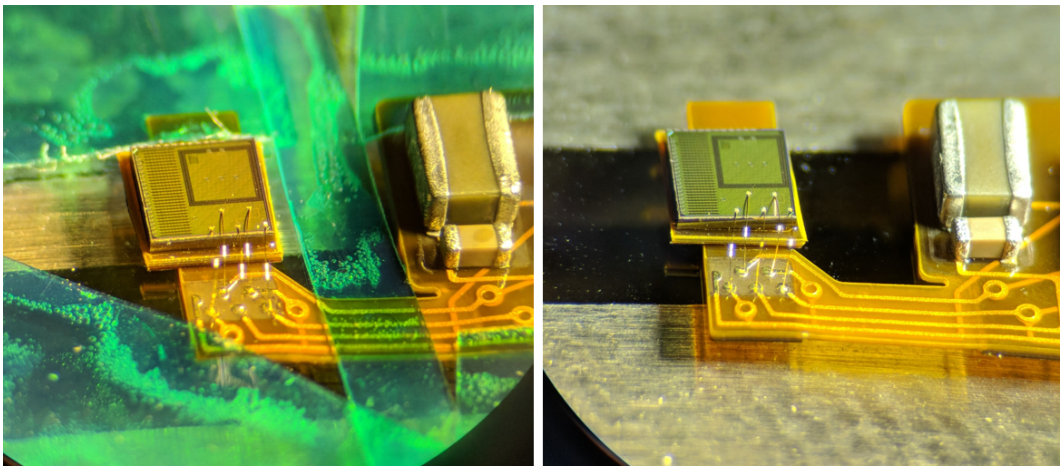

Figure 3.26: Sample that is wire bonded and stabilized with tape and after removal of tape.

Next, the sensor is packaged using the parylene-on-oil method: First, the top of the plastic housing for the LPS25H is removed with a razor blade so that the pressure sensor chamber resides in an open-faced box. Biocompatible, 100,000 cSt silicone oil is dispensed onto the sensor. Then, two runs of Parylene-C (>10 µm) is deposited on the components, where the samples are moved between the two runs

so that pin holes remaining after the first run could be coated by the second run. A special holder was made to hold the samples during fabrication. It was constructed out of a poster tube cap with holes punched into it and tape around it. The rough, holed surface enabled the samples to touch only at a few points, and also lay nearly flat so that the oil did not spill out while inside the parylene deposition machine (Figure 3.27).

Figure 3.27: Holder for folded-PCB implants while in the parylene deposition machine.

Thick parylene induces excessive drift, so the parylene over the pressure sensor is cut with a blade and removed with tweezers. More oil is dispensed with a syringe, and a flat edge is used to level the oil inside the plastic housing. A second, nominally sub-micron layer of parylene-HT is deposited in vacuum (≈23 mTorr), encapsulating the silicone oil bubble-free. The silicone oil prevents corrosion because of its low liquid water and water vapor solubility. In contrast, silicone gel has higher water vapor solubility. The silicone oil is deposited before the first parylene deposition to prevent parylene from directly touching the membrane, which would distort the device's sensitivity. Figure 3.28 shows the sensor at this point in the fabrication process.

3.4.2 Polyimide PCB Features

The polyimide PCB has two layers of copper traces with ENIG surface, with a stiffener section made of an additional layer of polyimide at some sections. The bond pads of the PCB match the orientation of the IC chip, as shown in Figure 3.26. The PCB has probes to the right which can be investigated to verify the components are attached before attaching the wire bonds. Samples intended for wireless implants were not investigated with wires after wire bonding the IC chip to reduce the risk of ESD. When ready, the extra length of the PCB to the debug pads was cut off. Of the six pads, one was a debug pad to probe the rectifier voltage, which was helpful

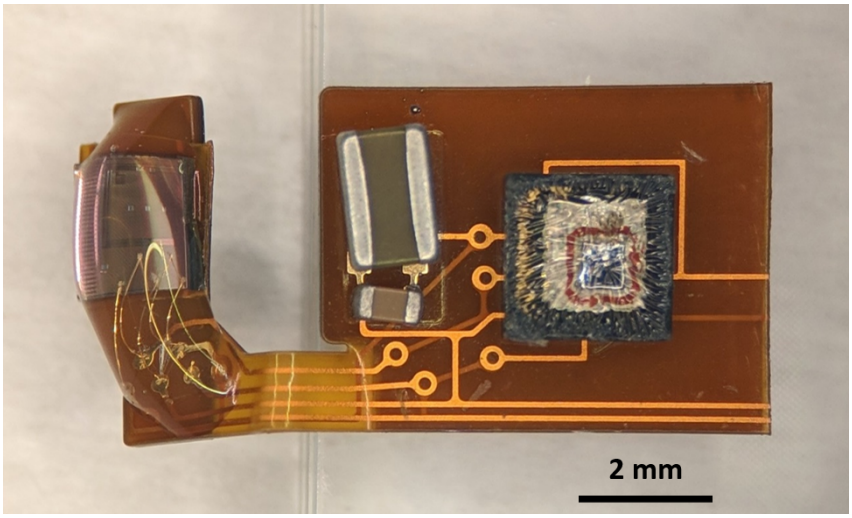

Figure 3.28: Implant after the bending the PCB and subsequent parylene-on-oil deposition but before the silicone steps.

for initial verification. Then there is the clock and data I2C lines, and there are two power lines. There was a switch for which was intended to allow for charging the capacitor to high voltage and quickly expose the pressure to intended supply voltage rather than ramp slowly because it was found that at an intermediate supply of around 1 V the LPS25H would consume a lot of leakage current and prevent initialization. However, the switch on the IC chip turned out to leak too much current, so the bypass supply pad from before the internal switch was wire bonded as well. So we wire bonded two supply voltage pads when a future design would only require one. In practice, the wireless chip charges up quick enough if within range.

It is convenient here to point out two features of the polyimide PCB itself, also to be seen in Figure 3.28. First, the PCB has stiffener sections below the IC chip and the electronic components. The stiffener section below the IC chip is so that the wire bonding was easier, and the stiffener section below the other components was so that they would be more resilient to the bending process. The bending process is described here. The sample is placed on a glass slide, where the narrower cable section and IC chip are hanging off the edge, away from the person assembling it. At the point where the cable section meets the larger portion, in other words, the empty space near the capacitors, the sample is pressed down with closed tweezers to pin it in place, with the right hand. Then, the cable section is pinched with tweezers by the left hand and rotated up and away from the assembly person while lifted up and towards the person to create a double bend. See Figure 3.29.

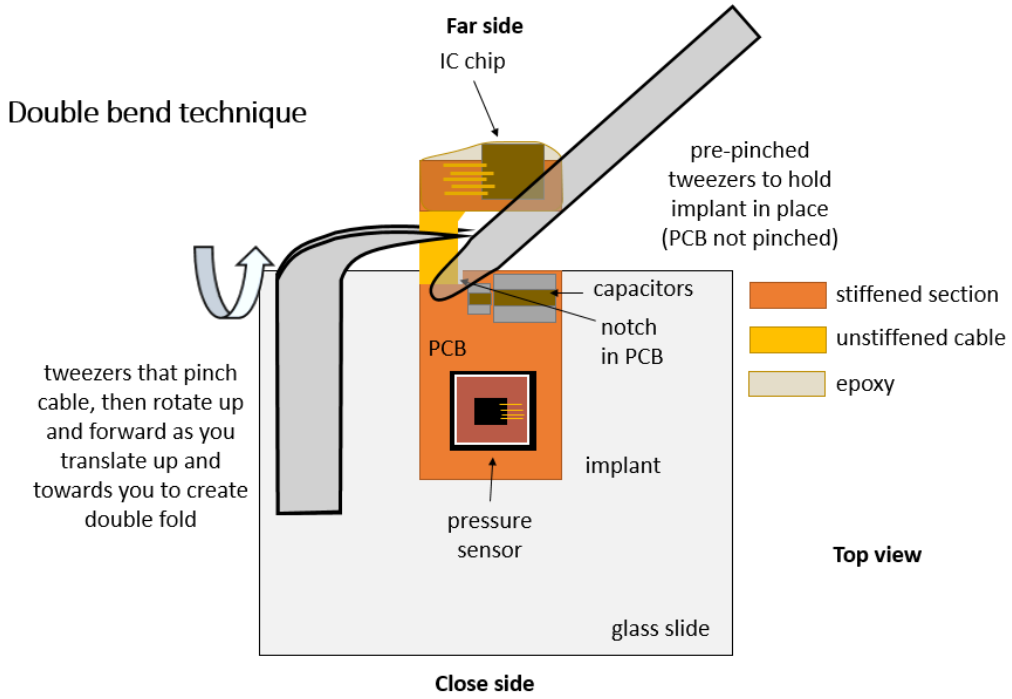

Figure 3.29: Manual method for bending the PCB with tweezers.

The notch at this same spot where the closed tweezers pinned the PCB during the bending has more features. There is a notch with rounded end that protrudes into the larger section of the PCB and the stiffener does not extend fully to the beginning of the cable section proper. This is to alleviate stress during the bending so that the copper trace within the PCB does not crack during bending. This indeed occurred in an earlier version without the notch and with the stiffener flush to end end. These features are also noticeable in figure 3.28.

3.4.3 Assembly of Silicone Components

Next, the silicone chamber with flexible 23-gauge silicone tube, prepared separately, are adhered to the PCB over the pressure sensor (Figure 3.30). Before this and all subsequent silicone on parylene fabrication steps, the implant is exposed to oxygen plasma (50W, 200 mT O_2, 30 sec each side) to roughen the surface for better adhesion. Note that previously, parylene coatings without plasma treatment are specifically used to suppress silicone adhesion to surfaces. Ideally, Med160 silicone adhesion promoter should also be used (but was not in the case of the working *in vivo* implant). After the chamber is cured on by using fresh Med4210 as an adhesive, the chamber integrity is tested by submerging the opening of the

tube in de-ionized water (DI), and pressing gently on the chamber. If the chamber is sealed from the outside and not blocked, you would be able to see a bubble or suck up water into the tube. Before continuing, remove all water remaining in this tube from the sample by baking and/or squeezing onto a texwipe.

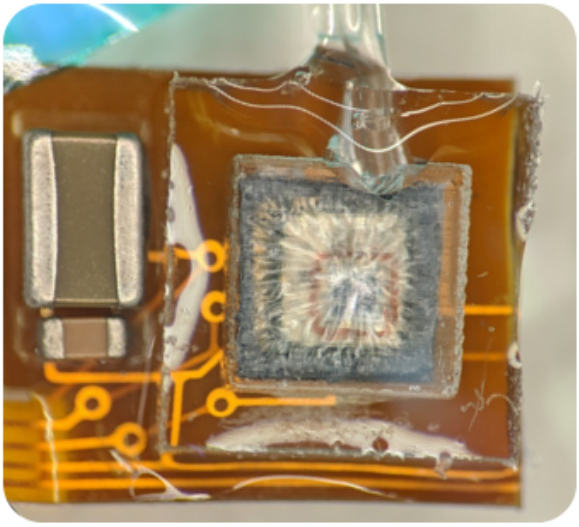

Figure 3.30: Silicone chamber and tube attached to implant.

Next, a droplet of med4210 silicone is added at the fold of the polyimide to hold that in place and cured. Then, the tube may be anchored onto a portion of the implant internally to hold the tube in place so it can fit inside the final form factor mold without stress and risk of popping out (see Figure 3.31).

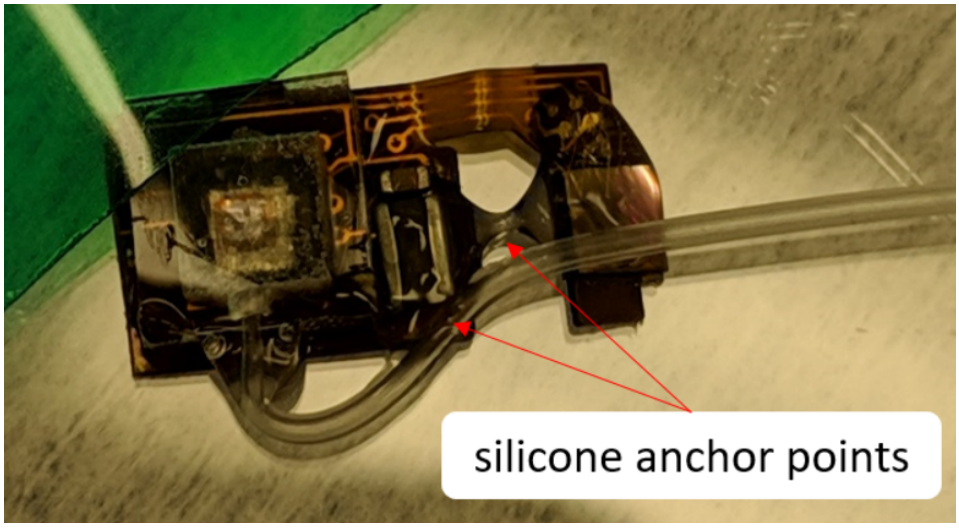

Figure 3.31: Silicone anchors for tube and fold in PCB.

The final cast mold is shaped to be rounded and thus more comfortable in a rabbit. A 25 mm diameter ball is used to cast the underside of the implant. There are notches in the mold so that one or more of the notches could fit the sensing tube, and potentially later also a drainage tube (Figure 3.32).

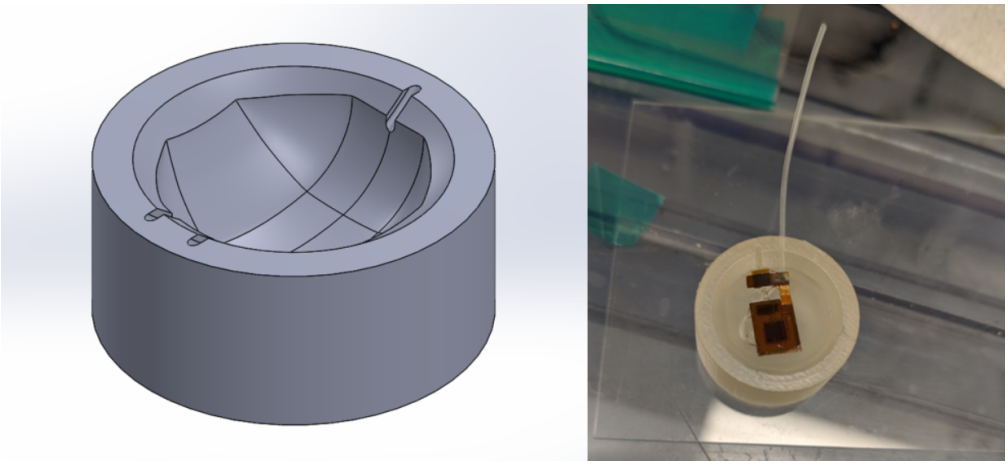

Figure 3.32: Mold to cast the final form factor. Notches are spaces for the tube to come out. A stainless steel ball goes on top to shape the inner side of the implant.

Silicone Med4210 forms the body of the implant. It is degassed and poured into the mold and degassed again. Then the implant was roughened with O_2 plasma and 10k cSt silicone oil is painted over the tube. This is to prevent new mixed silicone from sticking to the tube. Then the tube is submerged in the silicone in the mold. A custom weight was built to hold the implant down so it would not pop out of the mold while degassing (Figure 3.33).

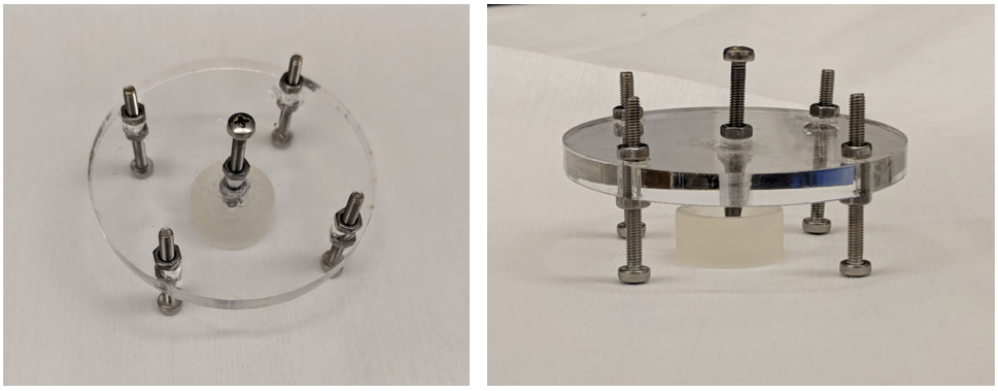

Figure 3.33: Weight to hold down implant during degassing so it does not come out of the mold. The screws allow for adjustable depth.

After the bubbles are removed in the vacuum, the steel ball is placed over the mold (Figure 3.34). Then a paintbrush is used to remove excess silicone that gets squeezed from the outside.

Figure 3.34: Steel ball on mold with tube sticking out through the notch.

Next, the paintbrush is dipped in isopropyl alcohol (IPA) to further clean the rim of the cast and the tube. If the tube gets silicone on it, it would be harder to insert into the eye. If too much IPA is squirted in between the mold and the ball, large cavities would form in the casting (Figure 3.35).

Figure 3.35: Cavity induced by excess IPA during removal of excess silicone.

The implant looks like Figure 3.36 immediately after separating the ball from the 3D printed mold. It is rough because the 3D printed molds have finite pixel resolution.

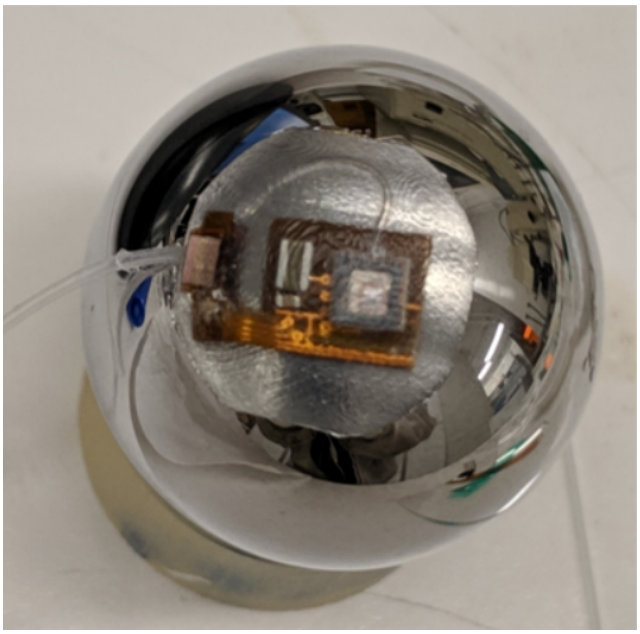

Figure 3.36: Silicone surface is rough after separating from the mold.

3.4.4 Smoothing Exterior of Silicone

The silicone surface was smoothed by a painting silicone diluted with hexane over the implant. The paint procedure is described here. (Thanks to Nicholas Scianmarello for guidance).

1. Mix Med4210, **Do not degas**
2. Pour small amount of hexane. It evaporates quickly, so you have to play around with how much is needed given the size of the container and how fast you are.
3. Mix in Med4210 silicone into hexane. Mix vigorously until solution looks a little hazy, and most of the silicone looks mixed in.
4. Add small amounts of hexane as needed.
5. Dip paint brush and let it drip/dab the top of the implant. If the result is not smooth, more hexane is needed. If does not spread efficiently, more silicone

is needed. Keep reapplying to wet all of surface if necessary. NOTE: this is not suitable for retaining small feature sizes! Instead use much more hexane versus silicone and dip coat. See Figure 3.37.

6. Let air-dry for about 3+ hours at room temperature to let hexane evaporate, then bake at higher temperature to fully cure.

7. Cut and remove implant. It is now smooth. See Figure 3.38.

8. Keep glassware dedicated for silicone and hexane mixture as it is more difficult than it is worth to try to clean well enough to use for any other purpose again.

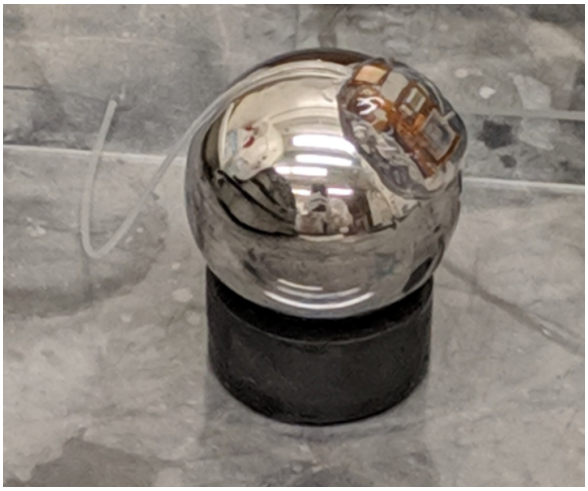

Figure 3.37: The implant is oriented vertically so that diluted silicone can be painted onto it and drip down the implant but not drip onto the tube.

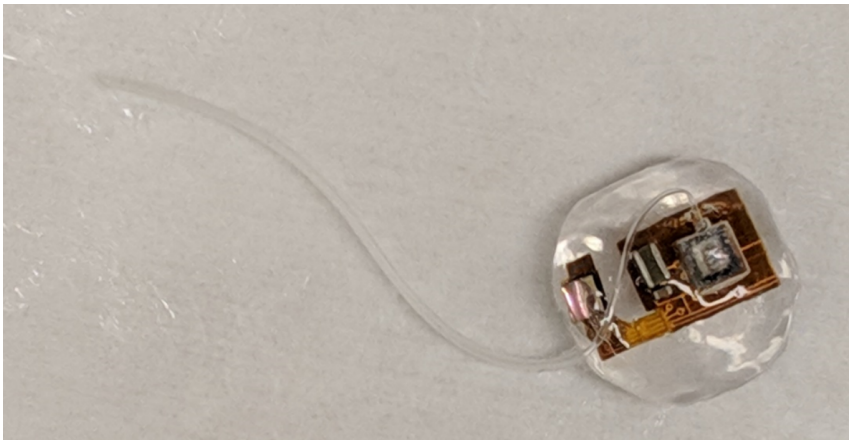

Figure 3.38: Final IOP implant is round and smooth.

3.4.5 Condensed Summary of Packaging and Assembly

There were many steps in packaging and assembly, so a summary of the steps is provided here.

1. Base electronics steps
    a) Cut off top of LPS25H pressure sensor
    b) Use solder paste to put pressure sensor and capacitors on polyimide PCB
    c) Solder pins onto PCB. Check pressure sensor with Arduino
    d) Epoxy IC chip to PCB
    e) Wire bond IC chip. Check wire bonds wirelessly.
    f) Add UV-curing epoxy around wire bonds. Cut off debug pads and pins
    g) Fold PCB
2. Parylene-oil-encapsulation steps
    a) Fill sensor with silicone oil
    b) Coat thick parylene. Shift position. Coat thick parylene a second time. This is to protect the electronics
    c) Re-open parylene-on-oil and re-fill the sensor with silicone oil until exactly flush
    d) Coat thin parylene for the optimal pressure sensing properties
3. Silicone steps
    a) Prepare silicone chamber and tube (can be done at any time)
    b) Add chamber and tube to implant
    c) Anchor the tube and fold with drops of silicone
    d) Cast the final form factor
    e) Paint diluted silicone to smooth outer surface

3.4.6 Earlier Unsuccessful Assembly Method

Before resorting to wire bonding, we attempted to connect the components using only conductive epoxy. Some initial tests worked, but it was deemed too difficult to align the IC chip without shorting the pads together, as the IC was designed before verifying the assembly method. This strategy involved putting components on a glass slide with a a droplet of low viscosity silicone oil and coating parylene. The oil prevented parylene from coating the electric pads on the bottom while also making a continuous film to the flap portion. The parylene could be cut and peeled off to create a parylene carrier for each component. The carrier flap made of parylene would be epoxied using UV curing epoxy to align, and then conductive epoxy would be used to connect the pads to the PCB. The small pitch and area on the IC chip and difficulty of getting the carrier flap extremely flat and close to the polyimide PCB led to the abandonment of this strategy at this time for this particular ASIC (Figure 3.39).

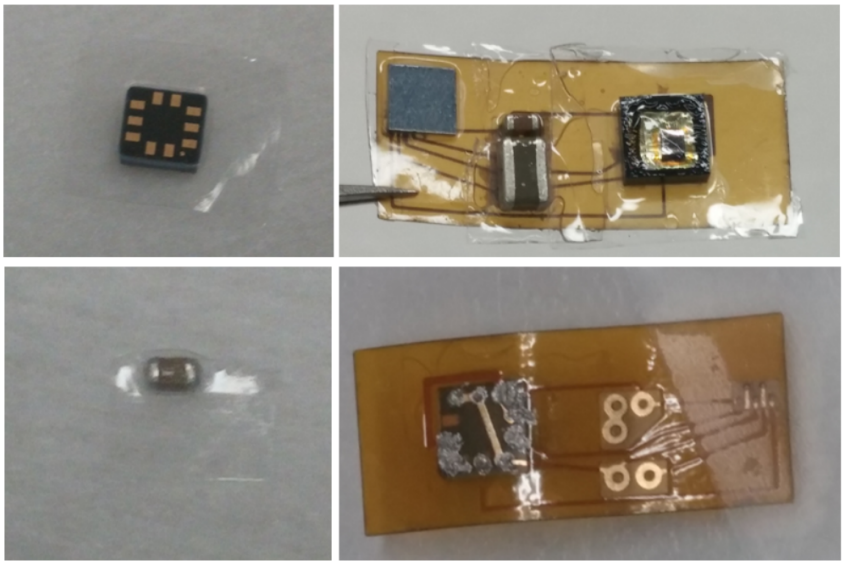

Figure 3.39: Early unsuccessful component assembly method with manual aligning with parylene carriers, shown left. Components would be attached with conductive epoxy from the other side.

In another test, the device was soaked in IPA in an effort to extract uncured silicone. A completed device was placed in IPA for one day at up to 40 °C, and it was found that the silicone delaminated from the parylene. The parylene in this case was treated with O_2 plasma (50 W, 200 mT O_2, 30 sec) only. The silicone extraction was abandoned, and the lack of irritation from the implantation *in vivo* justifies this decision.

3.5 Benchtop Results

Before going to *ex vivo* tests in animals, the implant with chamber and tube structure was verified wirelessly in air and with an enucleated porcine eye.

3.5.1 In-Air Calibration

Given the voltage dependence and small but non-zero temperature dependence, the implants are calibrated in air, over a pressure range of 0-70 mmHg vacuum gauge and temperature covering 27-40 °C. The implants are calibrated in air rather than in liquid, because bubble and meniscus effects can be avoided, and one-point calibration must be done right after implantation in the animal anyways because of hydrostatic pressure through the tube. The setup for calibration in air is shown in Figure 3.40. Calibration for devices that went in animals were heated up to 40 °C. The implant is taped to the inside of a vacuum chamber wall with a resistor heat pad in front of it. The implant is powered wirelessly through the chamber wall. An unmodified reference LPS25H pressure sensor is placed inside the chamber as well. The reference sensor is previously calibrated against a scientifically certified pressure sensor as good practice. Voltage is applied to the heat pad to heat up, and turned off to cool down. Also, a trigger signal synchronizes the wireless sensor and the wired Arduino data. As a note, the temperature of the reference sensor is not varied, as its temperature would not be the same as the temperature of the DUT. This is why the internal temperature sensor is convenient, as even an external temperature sensor would not be as accurate as an internal one.

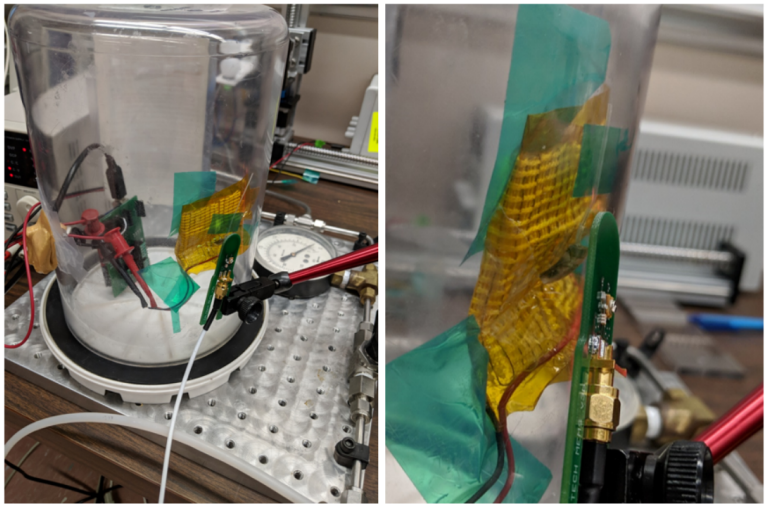

Figure 3.40: Calibration of the implant in air across pressure and temperature. The implant is investigated wirelessly through the chamber wall. A reference pressure is inside the vacuum chamber.

After calibrating in air, the results of testing the accuracy from a new set of data are shown in Figure 3.41. After calibration, the mean error is 0.022 mmHg, and the standard deviation is 0.17 mmHg.

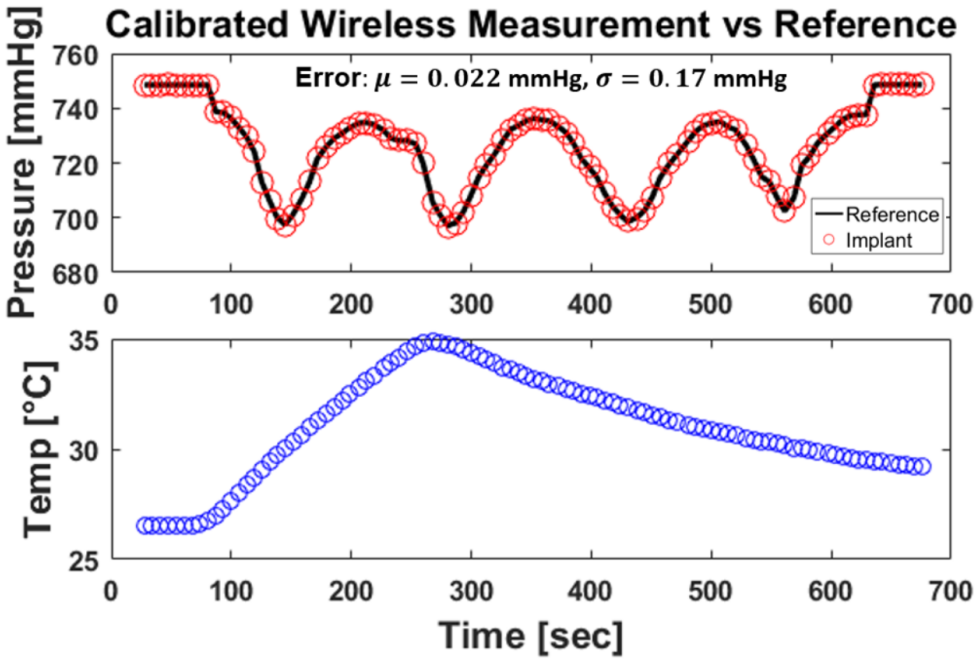

Figure 3.41: The accuracy of the wireless implant after calibration in air during simultaneous temperature and pressure sweeps. Only some samples are plotted for clarity. The true sampling period is 1 second.

3.5.2 Enucleated Porcine Eye Experiment

An earlier, larger, flat PCB version of the implant was used to test if the wireless data could be read from an enucleated porcine eye (Figure 3.42).

Before implantation, the silicone chamber and flexible tube are filled with saline, as bubbles may distort the sensed pressure. Post-implantation, a syringe is used to puncture the silicone chamber to flush any bubbles in the line that may have appeared from handling the tube during implantation. Anticipating the need to flush out bubbles was why the pressure sensor and chamber were placed in front of the implant. Later we found that bubble flushing post-implantation was not necessary, allowing the IC chip to be placed in front.

The porcine eye is vitrectomized using a Stellaris PC vitrector (Bausch and Lomb, Inc.) using a standard 3-port technique and 23 gauge instrumentation, with the infusion line placed inferiorly. The vitrector is then removed and the 23-

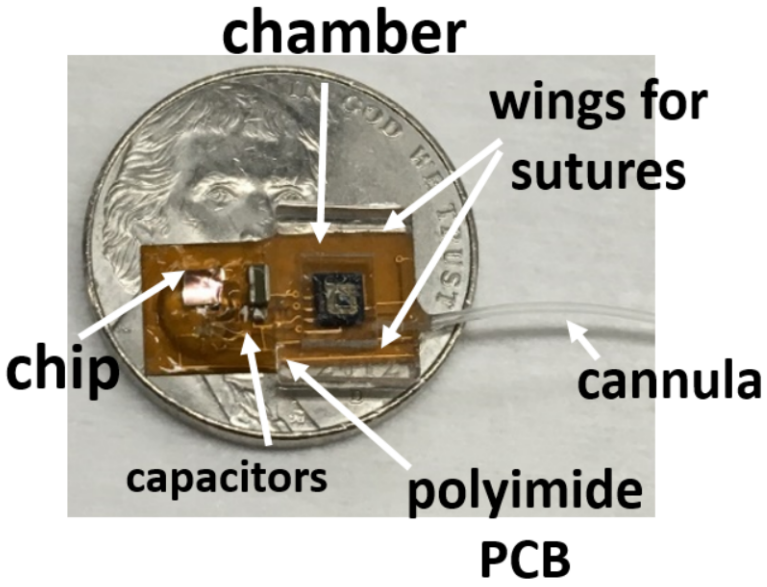

Figure 3.42: First version of the implant on a flat polyimide PCB for the enucleated porcine eye test.

gauge flexible tube is inserted through this port. IOP is modified by adjusting the hydrostatic pressure of the infusion line using the IOP setting on the machine (Figure 3.43). The sensor had to be placed on top of the reader antenna to collect data in this experiment (Figure 3.44).

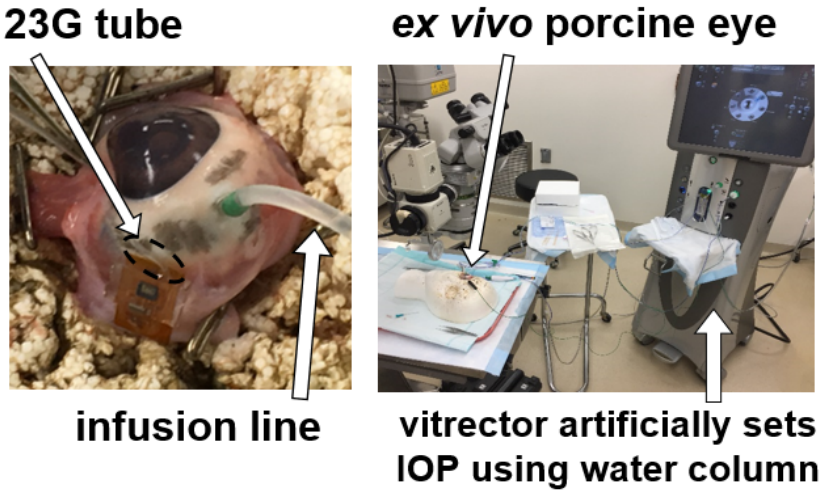

Figure 3.43: Enucleated porcine eye IOP experiment setup, including infusion line and vitrector for adjusting pressure. The reader coil and implant on the eye are representational, and actually achieved in later experiments in full animals.

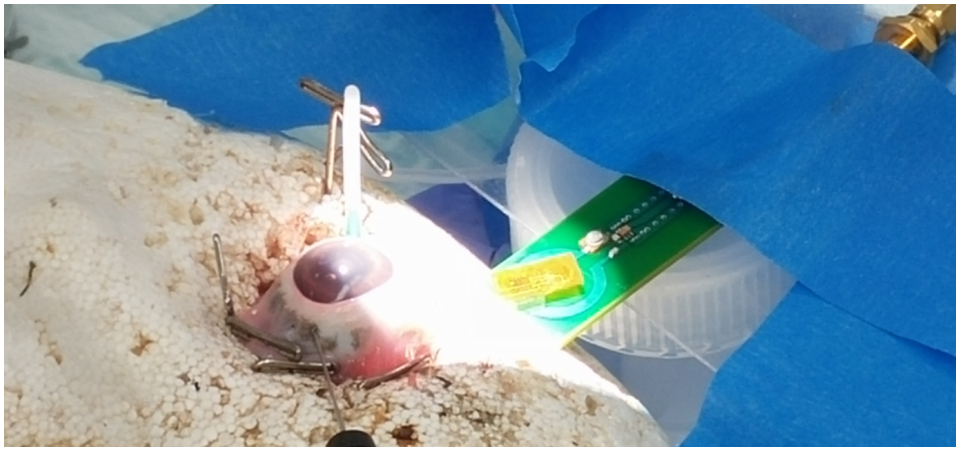

Figure 3.44: The implant is intended to be positioned on the eye as in Figure 3.43, but the readings were done with the implant body away from the eyeball laying flat on the reader coil. Earlier benchtop tests with the tube not inside the eyeball could get readings, but not in this particular experiment.

The IOP in the porcine eye was swept between 5 and 34 mmHg in steps of 1 mmHg every 30 seconds (Figure 3.45).

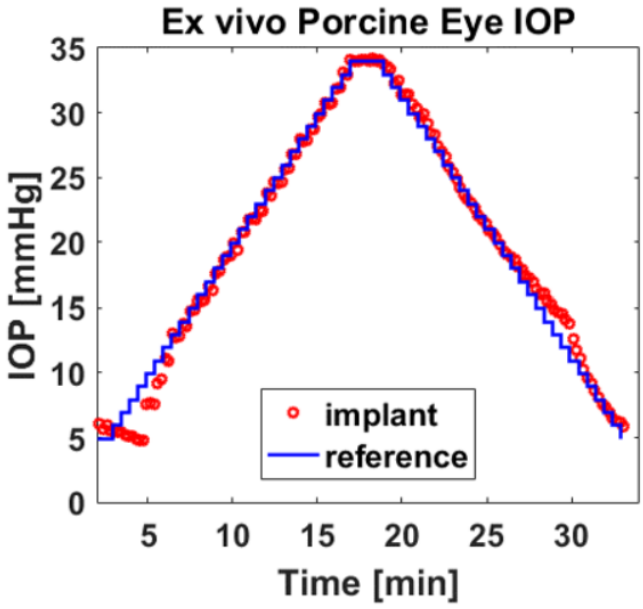

Figure 3.45: Wireless IOP versus reference in *ex vivo* porcine eye. Irregularities at low IOP are attributed to inaccuracy by the vitrector itself, as clarified in Figure 3.46.

A small mismatch in the *ex vivo* data at IOP levels below 10 mmHg (Figure 3.45) are not attributed to implant measurement error, because the implant shows

ideal performance in the same regime in a water column benchtop test (Figure 3.46). Thus, we hypothesize that the mismatch is attributed to reference error by the vitrector. Additionally, this was after adjusting for a constant +13 mmHg offset that we could not explain entirely by hydrostatic pressure. The hydrostatic pressure mismatch problem reduced in magnitude steadily as the tube length decreased for the various experiments.

The water column experiment shown in Figure 3.46 shows ideal performance even at low IOP measurements, suggesting the error in Figure 3.45 is indeed due to the vitrector instrument. However, the water column data is after removing a +1.67 mmHg offset compared to the height expected from water. The implant coupled to custom silicone bucket with a silicone tube. The wider silicone bucket is to lessen any meniscus pressure, but perhaps it is still present. The jar was cast with Med4210 by inserting one jar into another and curing. The weight and viscosity of the silicone prevented the jar from sinking too quickly.

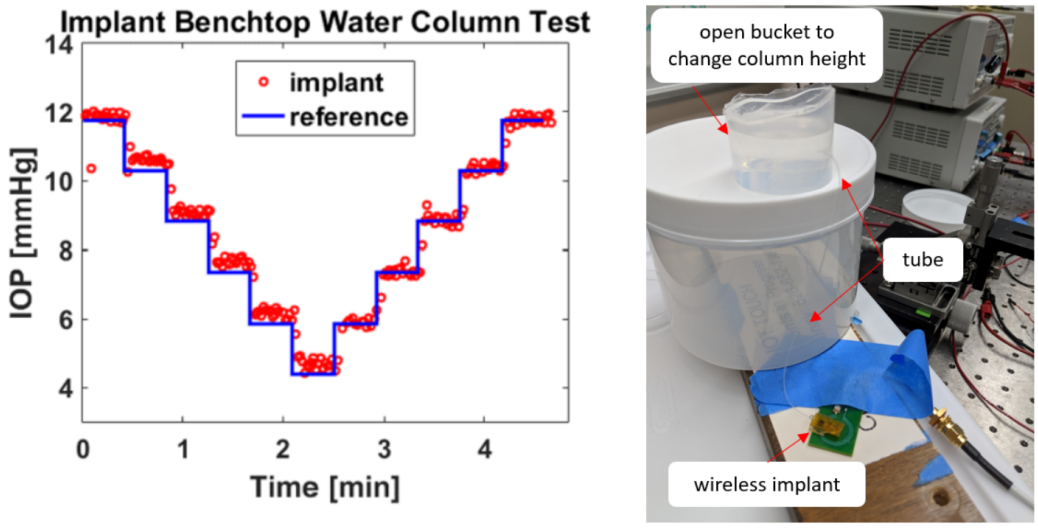

Figure 3.46: Water column test with wireless implant on benchtop shows ideal IOP sensitivity, with sharp step response.

3.6 Saline Longevity Results

This section contains various experiments, but common to all is that a polyimide PCB would be soaking in saline at body temperature or hotter. Some had pressure sensors, and others did not. Some also had other components such as dummy chips to test wire bonds in saline.

3.6.1 Polyimide with Sensor

Besides saline soaking tests on the FR4 PCB material, soaking tests on polyimide PCBs were conducted to test the long term viability of the polyimide PCB with copper traces, which was available for manufacturing through a website.

3.6.1.1 Wired Test with Polyimide

Wired soaking tests like those in Figures 2.40-2.43 except on a polyimide PCB were conducted. Figure 3.47 shows a typical sample, where the pins are outside the jar so they won't get corroded.

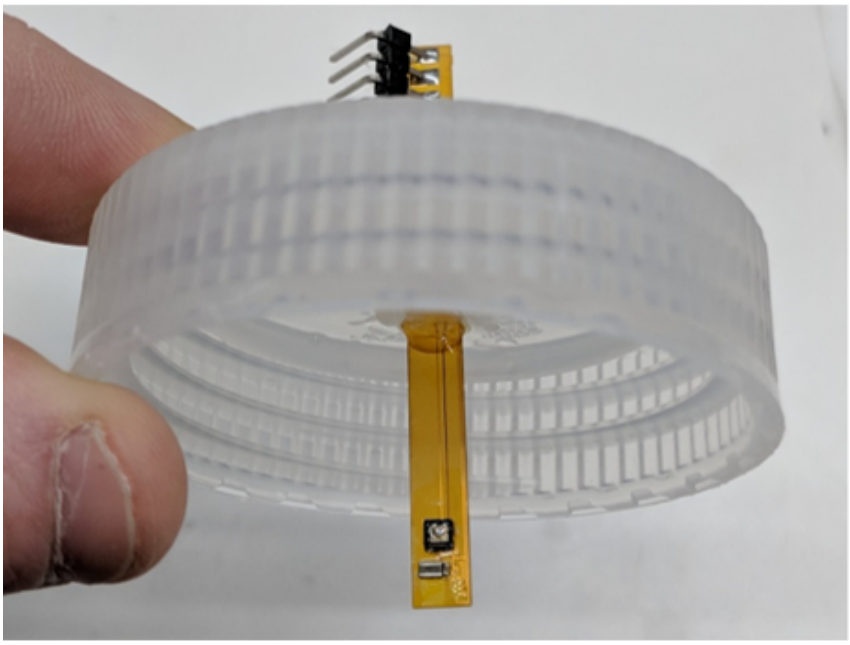

Figure 3.47: Polyimide PCB packaged LPS25H and epoxied through jar for saline soaking test.

The experimental results of the wire polyimide PCB experiment is described here. The following three plots measure LPS25H pressure sensors all using 100k cSt silicone oil and sub-micron nominal thickness of parylene. There are devices with PA-C and PA-HT. The PA-C packaged devices were soaked in saline at 37°C (body temperature) to avoid exceeding the glass transition temperature, which affected the offset stability. One PA-HT packaged device was also soaked at body temperature out of curiosity, and another PA-HT packaged device was soaked in saline at 77 °C for high-temperature accelerated aging test. The number after each device is just a label for bookkeeping. See Figures 3.48-3.51.

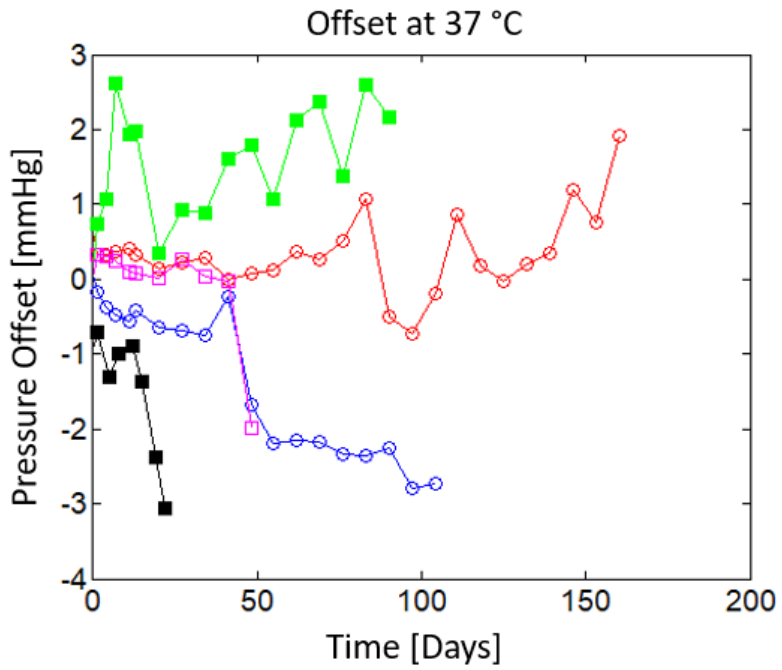

Figure 3.48: Polyimide PCB LPS25H wired saline soaking data, offset at 37 °C.

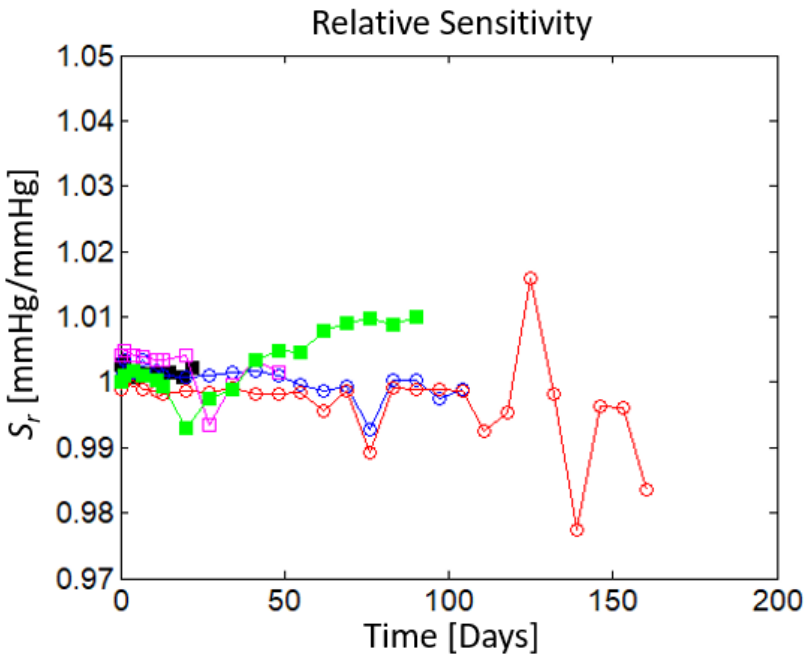

Figure 3.49: Polyimide PCB LPS25H wired saline soaking data, relative sensitivity.

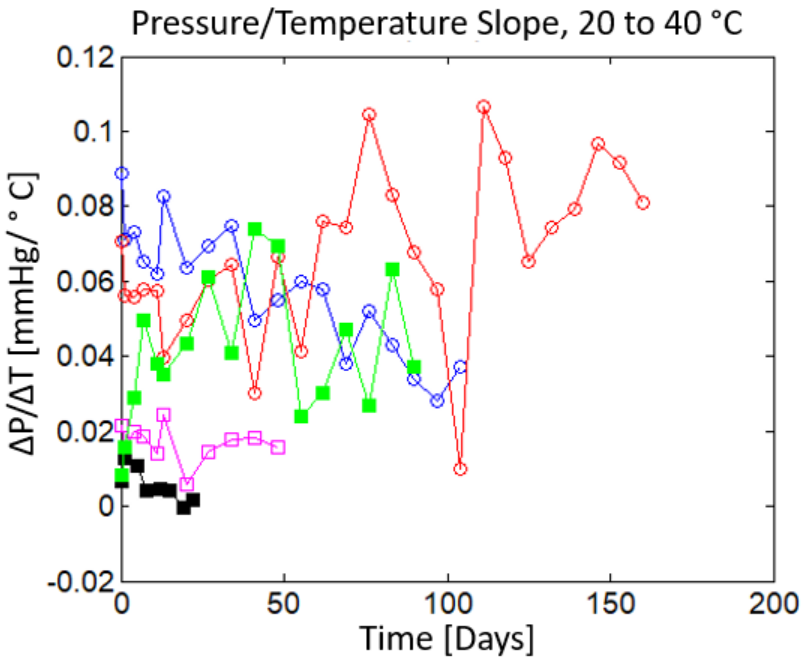

Figure 3.50: Polyimide PCB LPS25H pressure dependence on temperature, one-degree approximation over a temperature range of 20 to 40 °C.

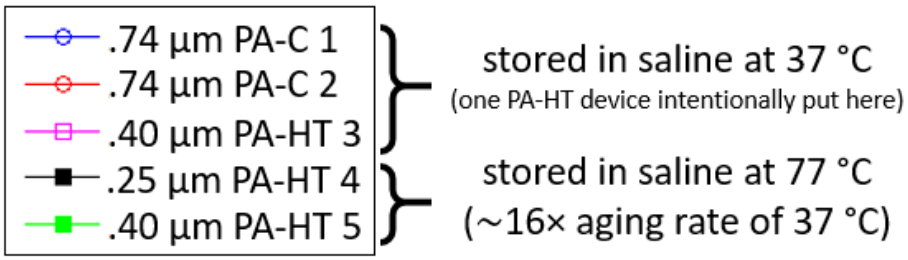

Figure 3.51: Legend for the polyimide PCB saline soaking longevity plots.

In all other ways this test was conducted exactly as previously described for the wired tests. The overall conclusions and observations are that the polyimide PCB, after coating with about 20 µm PA-C can last up to about 1-2 months reliably, but no more. Given the earlier benchtop test with longer lifetimes, the failure mode is likely to be what was different from that previous test, which was the polyimide PCB.

Additional comments for each sample are provided below.

Sample 1) 0.74 µm PA-C. The polyimide was covered by a coating of 11.5 µm + 11.3 µm of PA-C before the final sub-micron coating. Stored in 37 °C. The offset

drift magnitude at 37°C was under 1 mmHg for 41 days and was under 2 mmHg for 48 days. It failed entirely (no or nonsensical data) on day 111.

Sample 2) 0.74 µm PA-C. The polyimide was covered by a coating of 11.5 µm + 11.3 µm of PA-C before the final sub-micron coating. Stored in 37 °C. The offset drift magnitude at 37°C was under 1 mmHg for 83 days and was under 2 mmHg for 160 days. It failed entirely (no communication) on day 167.

Sample 3) 0.40 µm PA-HT. The polyimide was covered by a coating of 11.5 µm + 11.3 µm of PA-C before the final sub-micron coating. Stored in 37 °C. The offset drift magnitude at 37°C was under 1 mmHg for 41 days and under 2 mmHg for 48 days. It failed entirely (no communication) on day 55.

Sample 4) 0.25 µm PA-HT. The polyimide was covered by a coating of 8.2 µm + 8.2 µm of PA-C before the final sub-micron coating. Stored in 77 °C. The offset drift magnitude at 37°C was under 1 mmHg for 15 days and under 2 mmHg for 19 days. The last data point was day 22, though that may have been caused by human error. Using the day 19 point at 16 times aging factor, this corresponds to an extrapolated lifetime of 10 months.

Sample 5) 0.40 µm PA-HT. The polyimide was covered by a coating of 11.5 µm + 11.3 µm of PA-C before the final sub-micron coating. Stored in 77 °C. The offset drift magnitude at 37°C was under 1 and 2 mmHg for 4 days (crossed the threshold at the same time). On day 34, I saw a large bubble. Using the day 4 point at 16 times aging factor, this corresponds to an extrapolated lifetime of 2 months.

Pictures were taken every time the pressure was measured for sample 1 and sample 2 (Figures 3.52 and 3.53). Some significant pictures are shown for both devices. The corrosion spread correlates to the timing of the device failures.

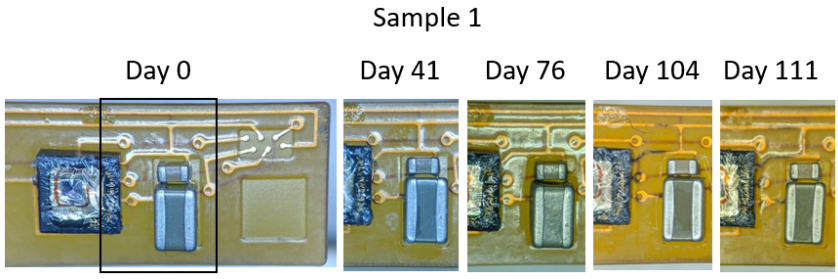

Figure 3.52: Corrosion pictures for polyimide PCB sample 1. Day 41 was the last day of less than 1 mmHg error. Day 104 was the last day with regular communication, and day 111 it failed entirely. The corrosion visibly spreads from day 76 to day 111.

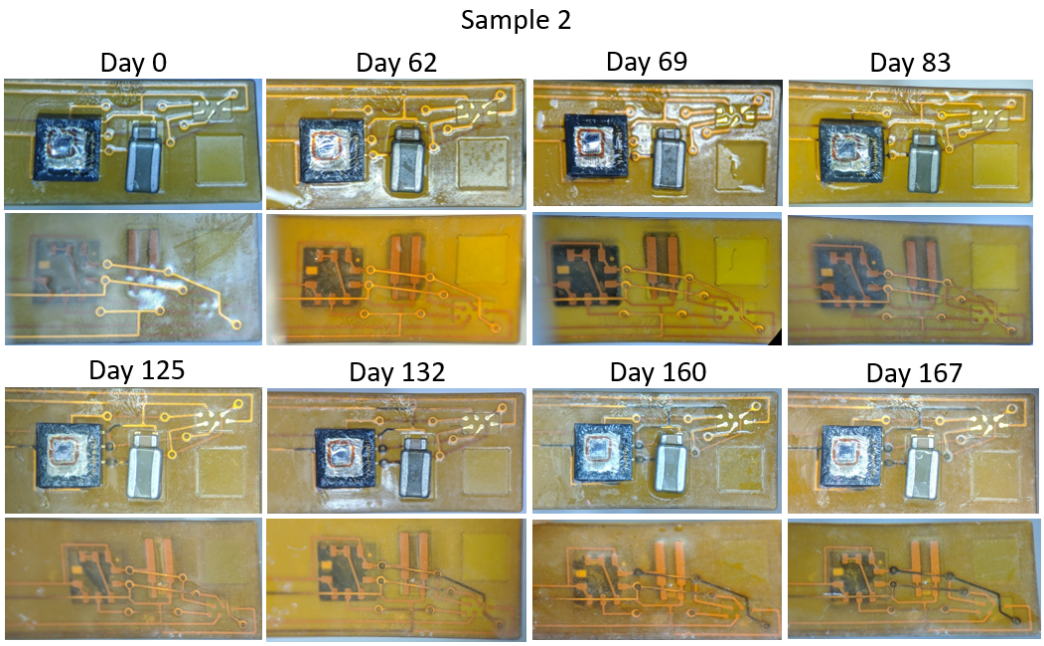

Figure 3.53: Corrosion pictures for polyimide PCB sample 2. Day 83 was the last day of less than 1 mmHg error. Day 160 was the last day of regular communication, and had less than 2 mmHg error by that point, and day 167 it failed entirely. The corrosion visibly spreads from day 69 to day 167.

3.6.1.2 Wireless Device with Polyimide

The Version 1 pressure sensor was left in saline at 37 °C for 2 months, but unfortunately, was not examined until after 2 months had gone by. At that time, there were some interesting results. Additional details were a 3.7 µm PA-C coating, with 400 nm PA-C parylene-on-oil (nominal) coating. At the end of the two months, the data was corrupted, but packets are sent. Additionally, the period between packets was initially 1.3 sec, but then turned to 3.5 sec.

I hypothesize that oscillator and other blocks are corroded, leading to less conductance, reducing clock frequency. Thicker coatings of PA-C might by help it survive longer. A parylene PCB seems necessary for longevity to the years range. The implant from underneath is visibly corroded (Figure 3.54).

Late in the process, a saline soaking test at 37 °C was conducted for a fully wireless implant. The implant gave data on day 1, but not by day 2. The accuracy of the data on day 1 was not verifiable easily, but given that the device failed quickly was cause for concern. It is suspected the wire bonds or epoxy was the failure mode, as the IC chip responded as if there was no pressure in communication with it (all

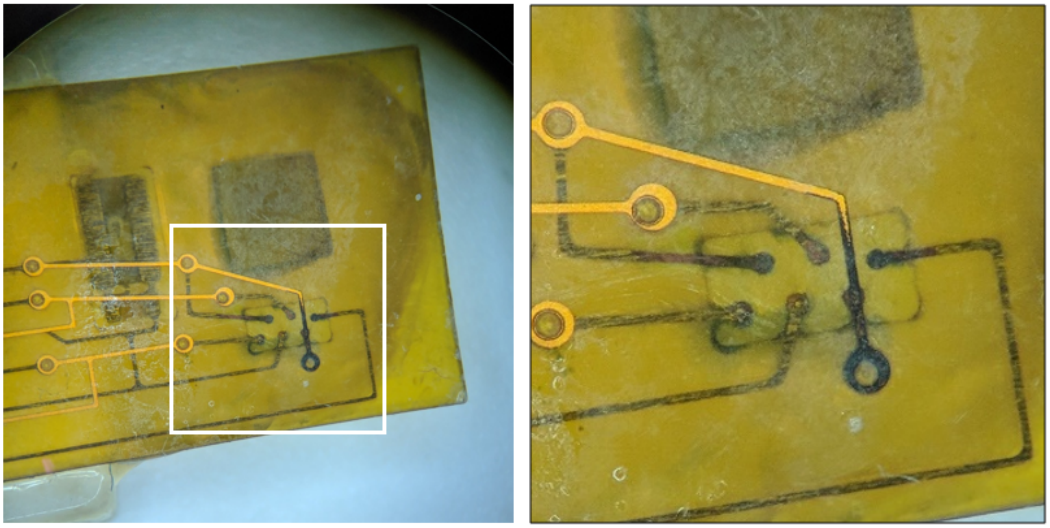

Figure 3.54: Corrosion in the polyimide PCB after two months in body temperature saline on a wireless implant.

1's during the data portion, but prefix and suffix were normal).

3.6.2 Polyimide without Sensor

Various tests were examined without the IC chip or pressure sensor. The IC chips were in limited supply, so they were not consumed if alternative methods could be found. It was also seen if epoxy or silicone may accelerate or inhibit corrosion of traces or wire bonds. In addition, it was also of interest to see if the oil could extend the lifetime of polyimide beyond 1-2 months anyways.

3.6.2.1 Epoxy versus Silicone Corrosion Acceleration or Inhibition

An experiment was conducted where 8 polyimide PCBs with different potting materials were soaked in 77 °C saline. Pictures for each type are shown in Figures 3.55-3.58. The traces are copper with ENIG surface (electroless nickel immersion gold). The observations are presented in Table 3.1. The silicone and parylene only coated polyimide PCBs corrode at the same rate, while the pads near the epoxy seem to corrode quicker.

Table 3.1: Polyimide PCB corrosion test without oil in 77 °C saline.

Sample	PA-C thickness	A174	Potting	Comments
Control	none	No	none	Discoloration visible after 3 days (no earlier data). Pads fall off by day 17.
C	24.5 µm	No	none	Universal trace darkening from days 8 to 15.
1	24.5 µm	Yes	none	Universal trace darkening between day 8 and day 12.
2	24.5 µm	Yes	none	Universal trace darkening from day 8 to day 15.
ns1	21.9 µm	No	Silicone	Universal trace darkening from days 6 to 16. No discernible difference for traces under/near silicone.
as1	21.9 µm	Yes	Silicone	Universal trace darkening from days 6 to 19. No discernible difference for traces under/near silicone.
ne1	21.9 µm	No	Epoxy	Universal trace darkening from day 6 to day 19. Traces darken faster under/near epoxy.
ae1	21.9 µm	Yes	Epoxy	Universal trace darkening from day 6 to day 19. Traces darken faster under/near epoxy.

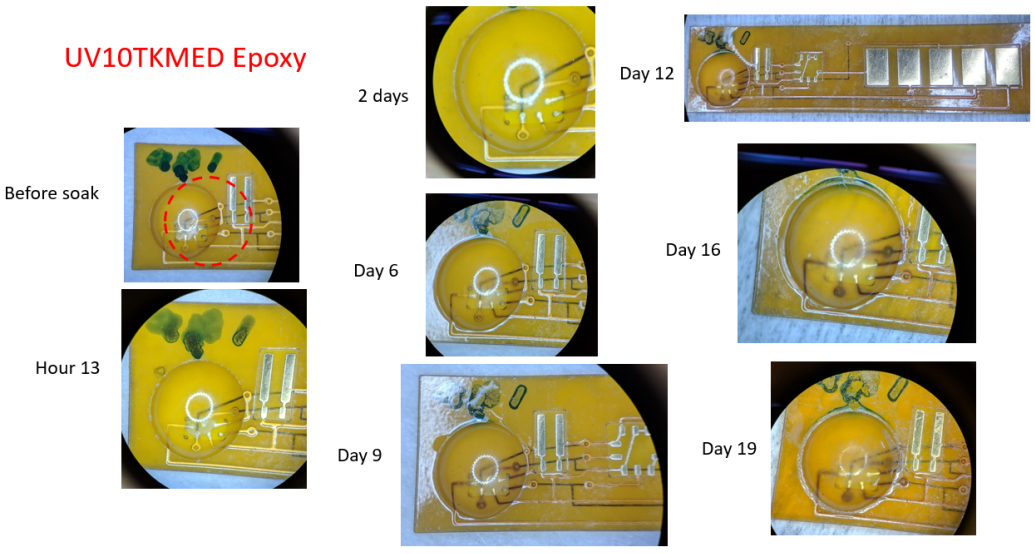

Figure 3.55: Epoxy as potting material (sample ae1, no wire bonds).

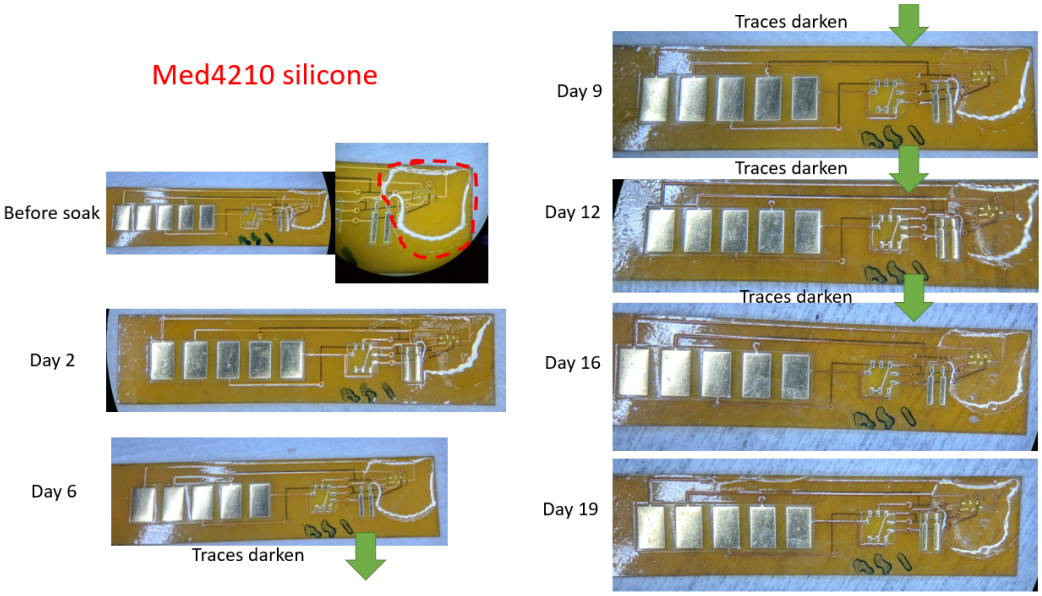

Figure 3.56: Med4210 as potting material (sample ns1, no wire bonds).

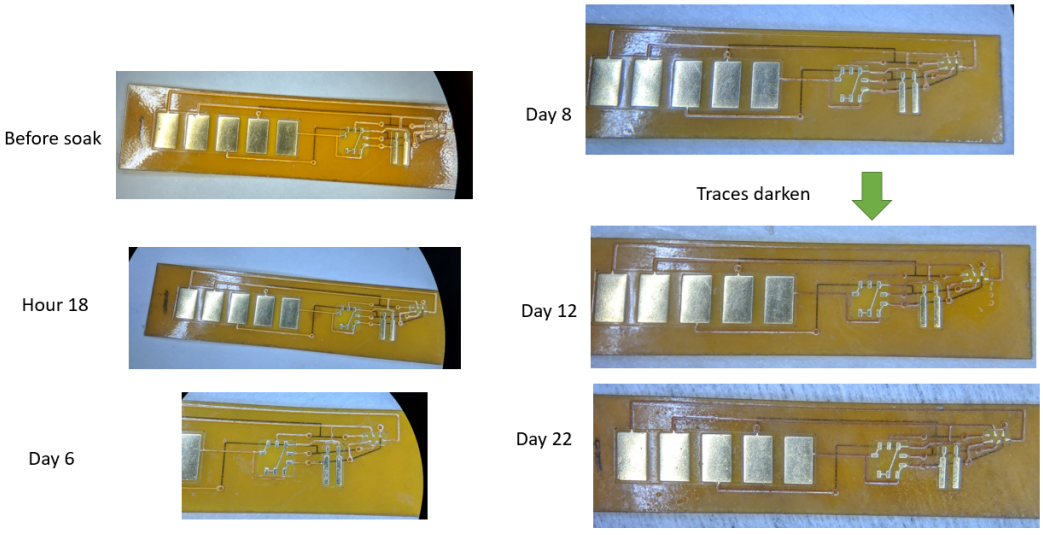

Figure 3.57: Sample 1, 24.5 µm PA-C only.

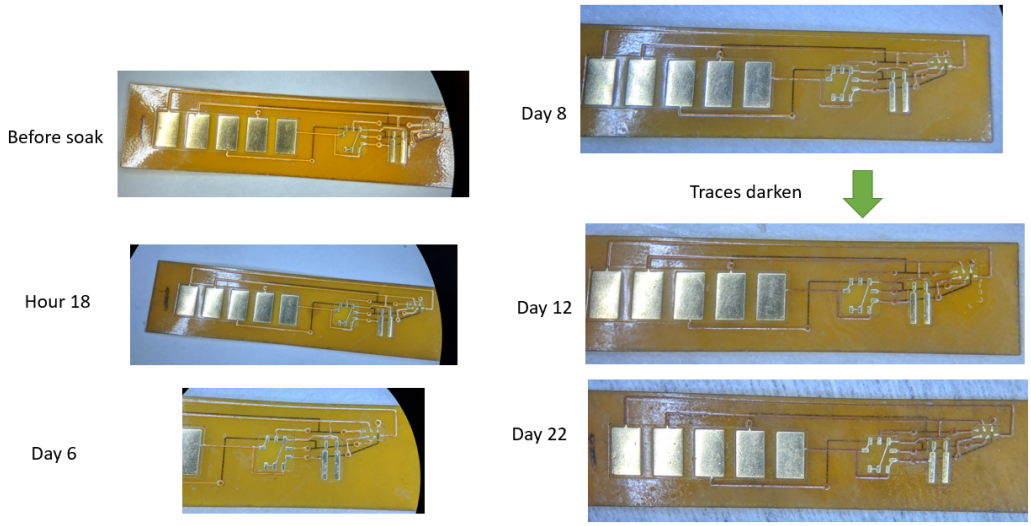

Figure 3.58: Control, no parylene coating.

3.6.2.2 Polyimide Encapsulated with Parylene and Oil vs Parylene vs Bare

A saline soaking test at 37 °C was conducted with two samples each of unmodified polyimide PCB, with 6 µm PA-C, and with 100k cSt silicone oil and 6 µm PA-C (nominal). So far, the unprotected sample corroded quickly as expected. Significant corrosion can be seen at the day 15 point. By day 54, no visible corrosion can be seen in the oil plus parylene packaging, but the parylene only coating has a spot of corrosion which is growing. A higher temperature test could speed this up. See Figure 3.59.

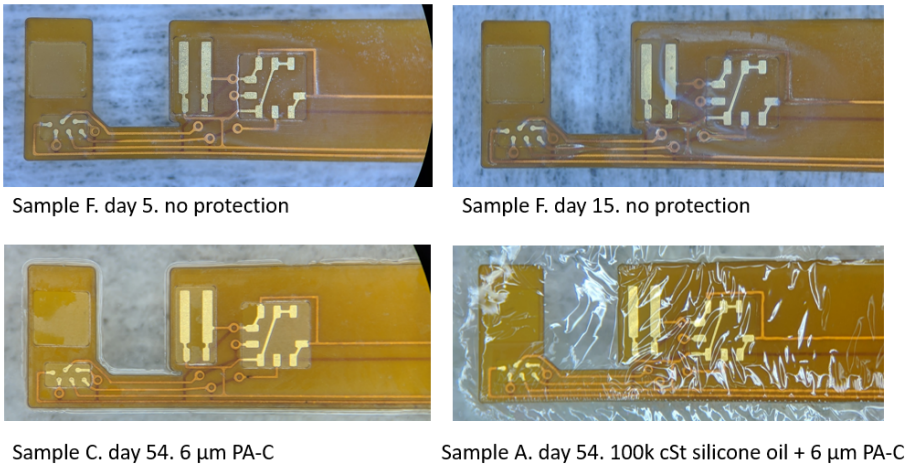

Figure 3.59: Polyimide PCB protection test with control, parylene only, and parylene-oil-encapsulation.

A close up of the spot of corrosion in the parylene only protected sample is shown in Figure 3.60.

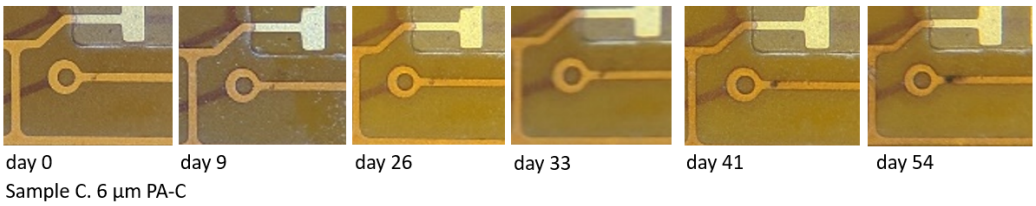

Figure 3.60: Spot corrosion in polyimide PCB with parylene coating. The discoloration is growing steadily.

3.6.2.3 Potted Wire Bonds

After the unexpectedly short life time of the wireless implant in 37 °C saline, a test was conducted to see if the wire bonds were related to the failure. Dummy chips with traces and bonding pads were placed onto the polyimide PCB and wire bonded. In this way, the resistance could be probed externally through the wire bonds, which could indicated their bond integrity. Three types of samples were made: 1) UV-curing epoxy potting with parylene coating, 2) UV-curing epoxy potting with parylene coating and silicone coating, and 3) silicone potting (Figure 3.61).

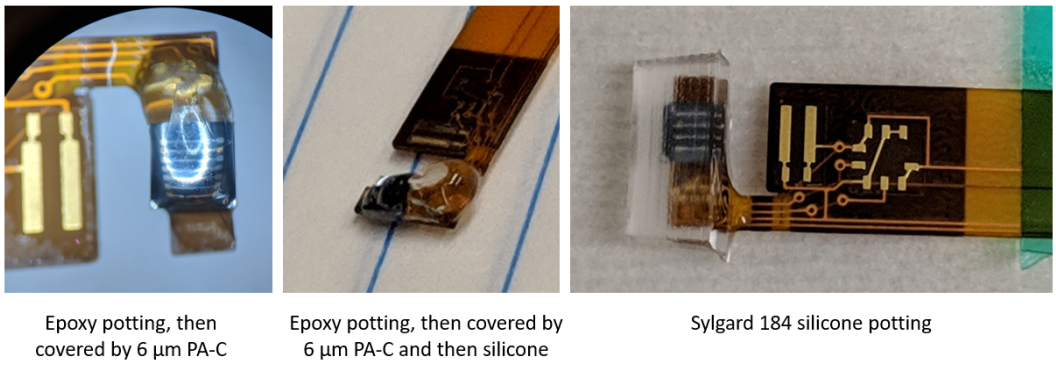

Figure 3.61: Wire bond potting and encapsulation test samples.

Silane A174 adhesion promoter was used before the parylene coatings, and O_2 plasma (50 W, 200 mT O_2, 30 sec) plus Med160 silicone adhesion promoter was used for the epoxy-parylene-silicone example. And med160 alone was used for the silicone potted example. They were then soaked in 37 °C saline. Different epoxy-parylene-silicone samples were coated with either Med4210 or Sylgard 184

silicone. The silicone potted sample was with Sylgard 184, as that is the softer of the two variants. Figure 3.62 shows the assembly method for silicone potting. The PCB was taped to a glass slide which was gently and methodically placed into the mold with fresh silicone and left to cure in room temperature to avoid mishandling, despite the longer cure time.

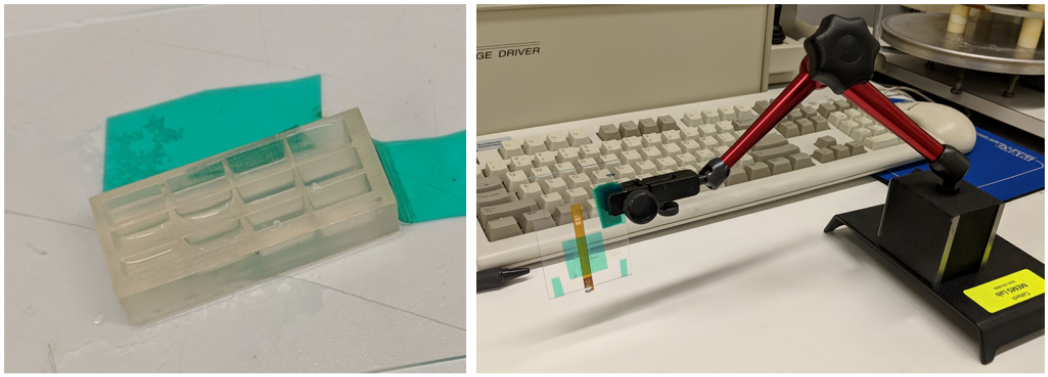

mold for potting wire bonds with silicone

holder arrangement for dipping into mold (mold shown left)

Figure 3.62: Silicone potting mold and holder.

The observations so far were surprising. To be explicit, the resistance (< 30 Ω) was confirmed for each sample before starting the soaking test. All samples that failed before this step have not been and will not be mentioned outside this statement. There were two types of UV-curing epoxy tested, the UV10TKMed and UV15X-6Med-2, but there was no observable difference between the two in the data. Interestingly, it seemed the most significant factor was the type and amount of coating of silicone, either as potting or as a surrounding material.

There were two samples with UV-curing epoxy and 6 µm PA-C only that lasted the longest. One of those samples survived until day 20, and the other is still functional as of the latest sampling date, day 36. The resistance creeping up is not concerning, since that is expected due to corrosion in the polyimide PCB itself. Rather the fact that the resistance shows a value at all rather than an open load is the significant metric. See Figure 3.63. The UV-curing epoxy potting with parylene and silicone failed by the day 1 measurement for the Med4210 dip coat, and by the day 2 measurement for the Sylgard 184 dip coat. The Sylgard 184 silicone potted sample failed by the day 1 measurement. Interestingly, for some of the samples at failure, such as the silicone potted sample and one of the samples with epoxy, parylene, and silicone, for a very brief moment, the multimeter could read a resistance when

initially probing on the day of failure, but then it read an open load. Re-probing the sample immediately or within minutes after still read as an open load, as if the current from the resistance measurement itself triggered the breaking of the wire bond. Despite checking under a microscope, no visual change was apparent for samples with newly broken wire bonds, so no pictures of that are included.

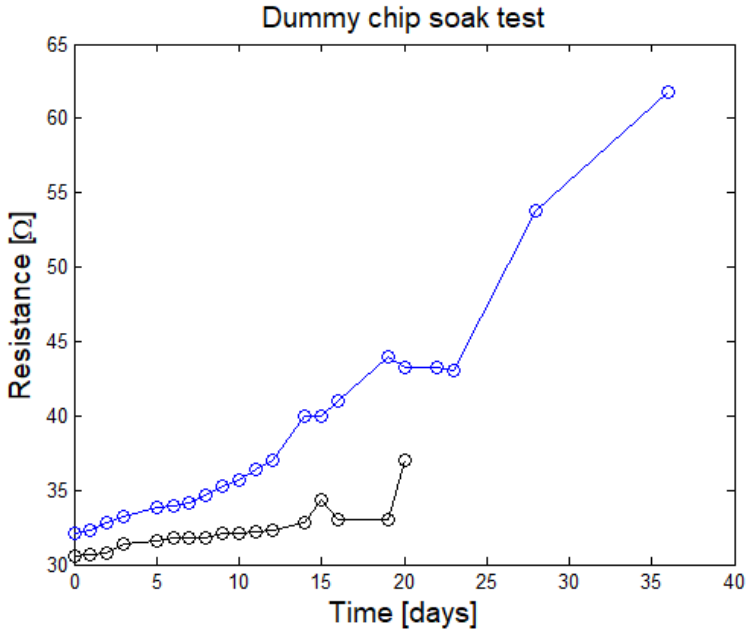

Figure 3.63: UV-curing epoxy potting with 6 µm PA-C wire bond longevity saline soaking test at 37 °C.

Although more study is necessary, the tentative hypothesis is that the silicone is somehow causing stress to the wire bonds when in saline. Storing in air hasn't been a problem, as the fully wireless implant from the *ex vivo* rabbit test in September 2018 is still functional as of April 2019, seven months later, and that has UV10TKMed UV-curing epoxy, 22 µm PA-C, and Med4210 silicone around the wire bonds.

Nonetheless, it is clear that any ways to avoid or better protect wire bonds in long term implanted devices should be investigated. An interesting point is that the LPS25H pressure sensors had wire bonds internally, and the encapsulation by oil and parylene has shown them to last much longer than these dummy chip tests. So protecting the wire bonds with oil and parylene might be an avenue of interest.

3.7 Full Animal Tests

Rabbits were used as the animal model because they have relatively large eyes for their size (18 mm diameter), similar to humans (24 mm diameter), which makes

them cheaper to use than other animals with comparable eye size to humans [90], [91]. Although other animals have more similar physiology to humans than rabbits, such as pigs, the principles and lessons learned from making an IOP implant for rabbits will translate to humans well.

3.7.1 Degassing the Implant Before Implantation

For the full animal tests, it was necessary to degas the implant, specifically the chamber and tube around the pressure sensor before implantation. It was found that the method of flushing the bubble post-implantation, as done for in the enucleated eye benchtop test, was not necessary.

The implant is submerged in sterile saline in a sterile dish and put under vacuum for 15 minutes. A sterile metal mesh is placed in the dish to keep the implant submerged when the vacuuming with cause bubbles to grow and even lift the implant. If the mesh was not there to weigh it down, the opening of the tube could reach the air, and saline would not fill the chamber after vacuum is broken, which is the opposite of the desired result (Figure 3.64). After vacuum is broken, there will be small bubbles apparent in the chamber, but they will dissolve after a few minutes. The tube is left to have extra length while removing the bubbles so that if there is any evaporation before the implant is ready to be implanted, the tube can be cut to the desired length and be as full with saline as possible before handling it.

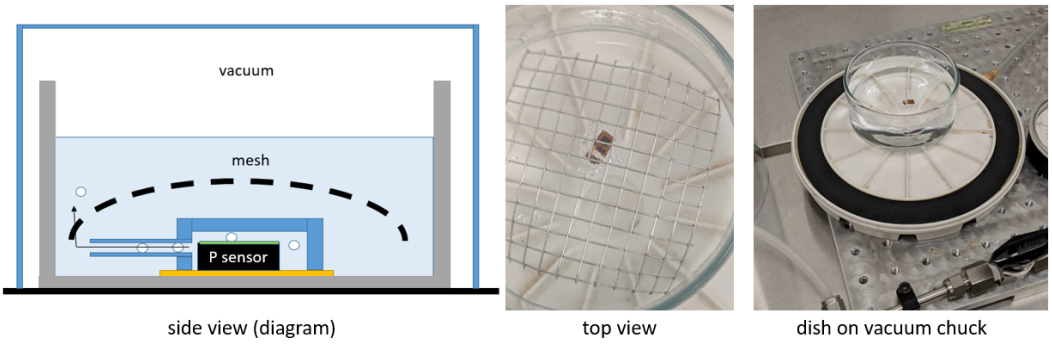

Figure 3.64: The implant is submerged in saline and put under vacuum to fill chamber and tube completely. Left: Diagram. Middle: Top view. Right: After degassing is complete.

3.7.2 *Ex vivo* Rabbit Experiments

There were three stages of differing amounts of progress, described below.

3.7.2.1 Large Implant (Version 1)

Immediately after the porcine eye experiment as shown in Figure 3.44, it was attempted to put the implant into a rabbit *ex vivo* (Figure 3.65). This experiment made it obvious that the implant needed to be smaller, be rounded, and have the coil be as far forward as possible. No data was successfully retrieved from this attempt.

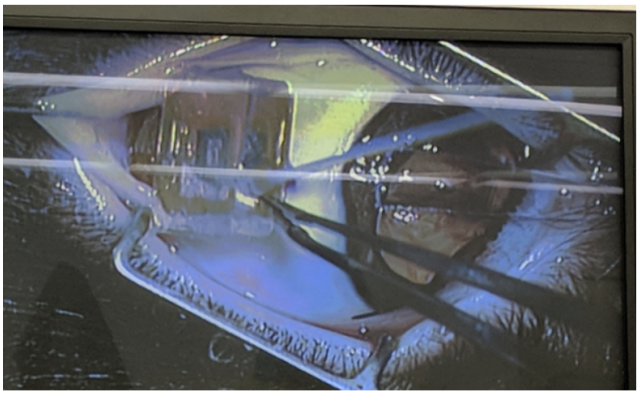

Figure 3.65: Early wireless implant is too large.

3.7.2.2 Small Flat-PCB Implant (Version 2)

Given the observations from the previous attempt in a rabbit, a new implant design was made. Also, the silicone form factor was made rounded. The pressure sensing tube was redirected from the opposite direction from before so that the IC chip with on-chip coil would be at the front (Figure 3.66).

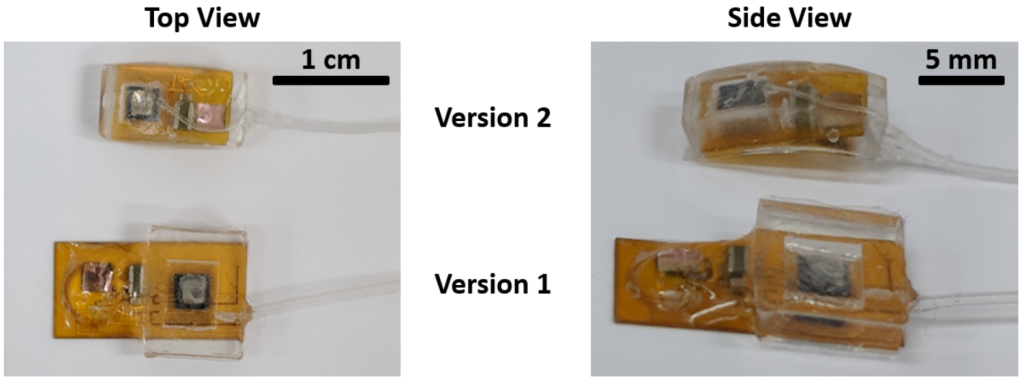

Figure 3.66: First two versions of the IOP sensor implant. Both are flat. Version 2 is smaller, fully encapsulated with silicone, and rounded to fit around the eye compared to version 1.

Since the pressure sensor and chamber are now in the back of the implant, it would not be possible to flush out any bubbles if they appeared in the tube. Luckily, small air bubbles that would get introduced at the opening of the tube dissolved after implantation, as can be seen in Figure 3.67.

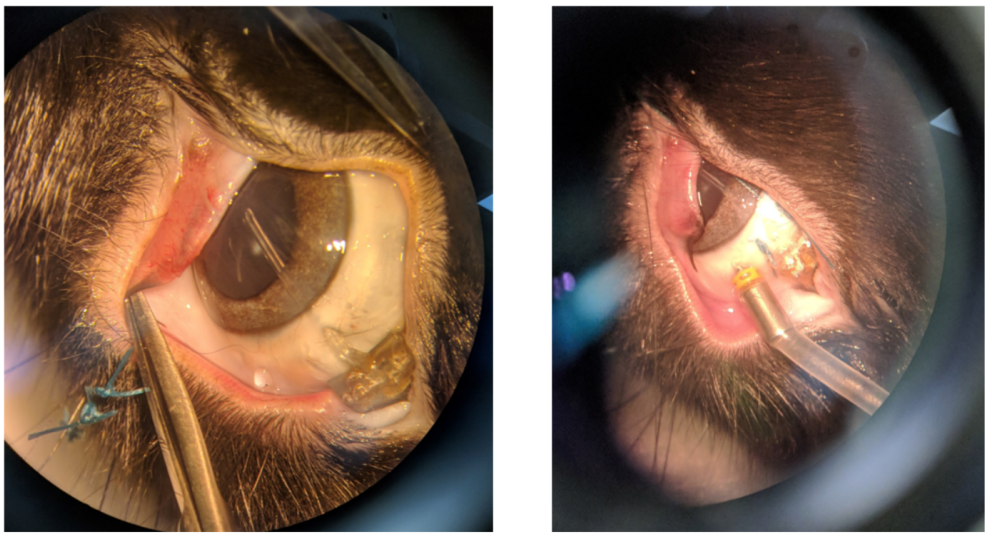

implant with tube inserted

infusion line added to vary IOP

Figure 3.67: Small flat-PCB in rabbit. There is no bubble in the tube line. The infusion line is added to vary the IOP.

The implant could only be powered if sutures were used and the eye was unnaturally tugged forward (Figure 3.68). However, this experiment proved that the implant could be powered in the vicinity of the eyeball tissue if the angle of the coil itself could be improved.

suture and forceps necessary to align coil to retrieve data

Figure 3.68: Rabbit eye needed to be pulled forward to power implant version 2.

The data in Figure 3.69 was after accounting for a constant offset of -1.95 mmHg. Error is attributed to several things: The vitrector is not very accurate, there is a column height offset, and the falling time constant is known to be long in vitrector setup, as fluid can enter easier than it can leave.

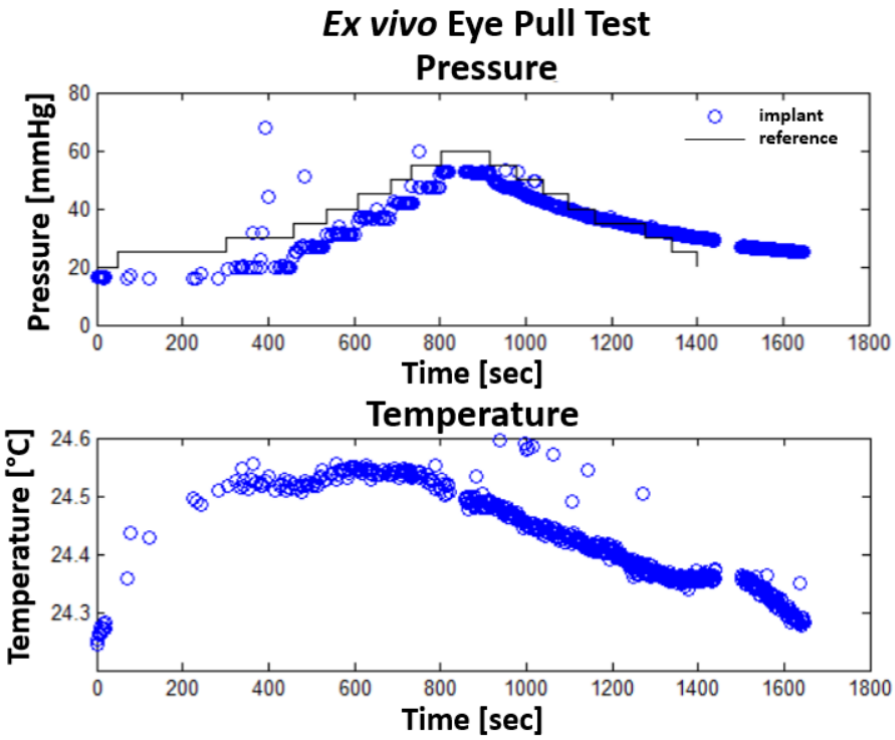

Figure 3.69: Wireless IOP Data from the *ex vivo* test with the eye pulled forward. The IOP was artificially adjusted through the infusion line and the vitrector like in Figure 3.43.

3.7.2.3 Folded PCB Implant (Version 3)

After Version 2, it was apparent that not enough power could reach the implant. Without changing much of the overall structure of the implant, we tried a folded PCB to orient the RF, on-chip coil in the optimal direction, directly to the surface. See Figure 3.70. With the flat PCB, close enough proximity and satisfactory alignment could not be achieved simultaneously, but with a folded PCB, it was achievable.

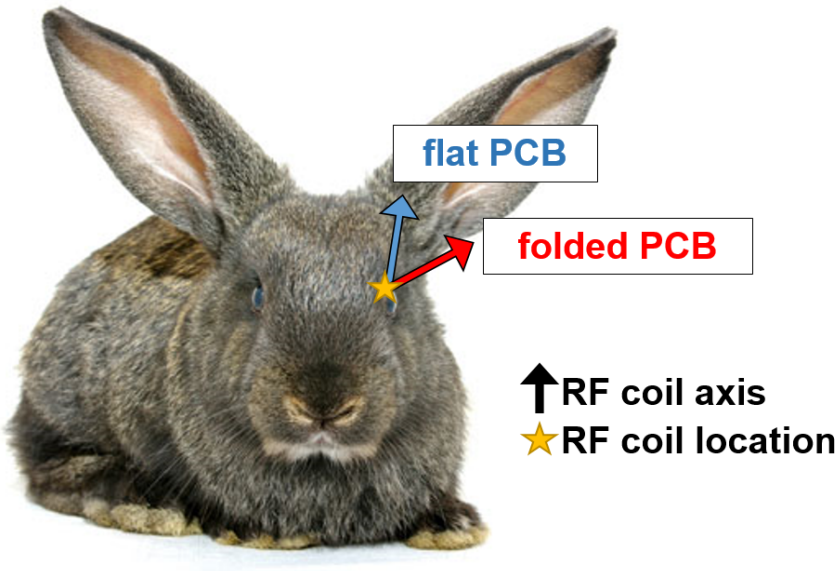

Figure 3.70: RF coil orientation in rabbit model motivating diagram. The flat PCB has the coil axis point through the brow, whereas the optimal direction should point directly to the outside, achievable by folding the PCB.

We achieved an angle improvement of 34 ° (Figure 3.71).

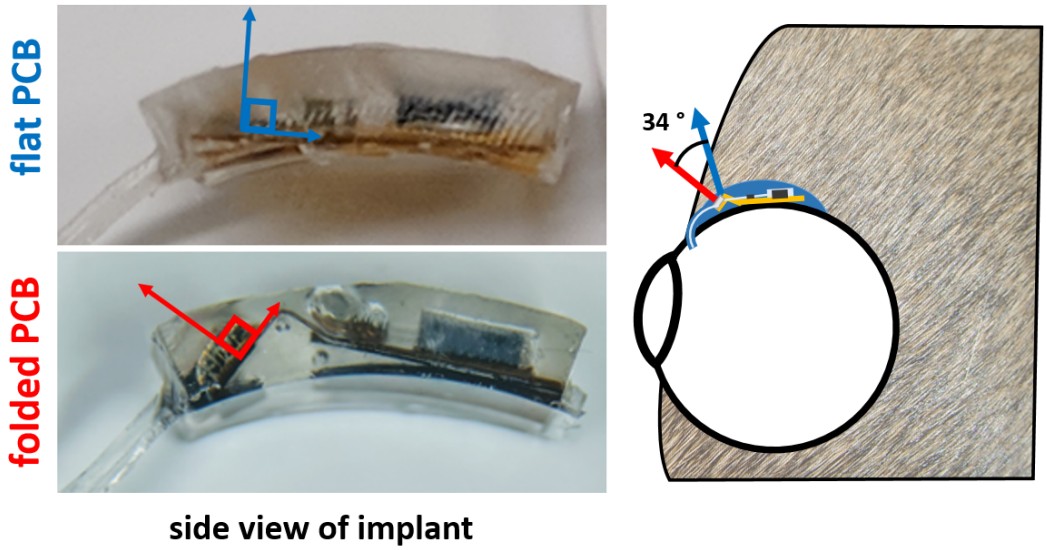

Figure 3.71: Angle improvement was 34 ° by folding the PCB.

The implant for the *ex vivo* folded PCB test is shown in Figure 3.72. The bubbles seen in the top view were imperfections in the silicone casting process, but it did not effect the acute measurement with this device. After the weight in Figure 3.33 was used, the bubbles in the silicone were gone, as seen in Figure 3.38.

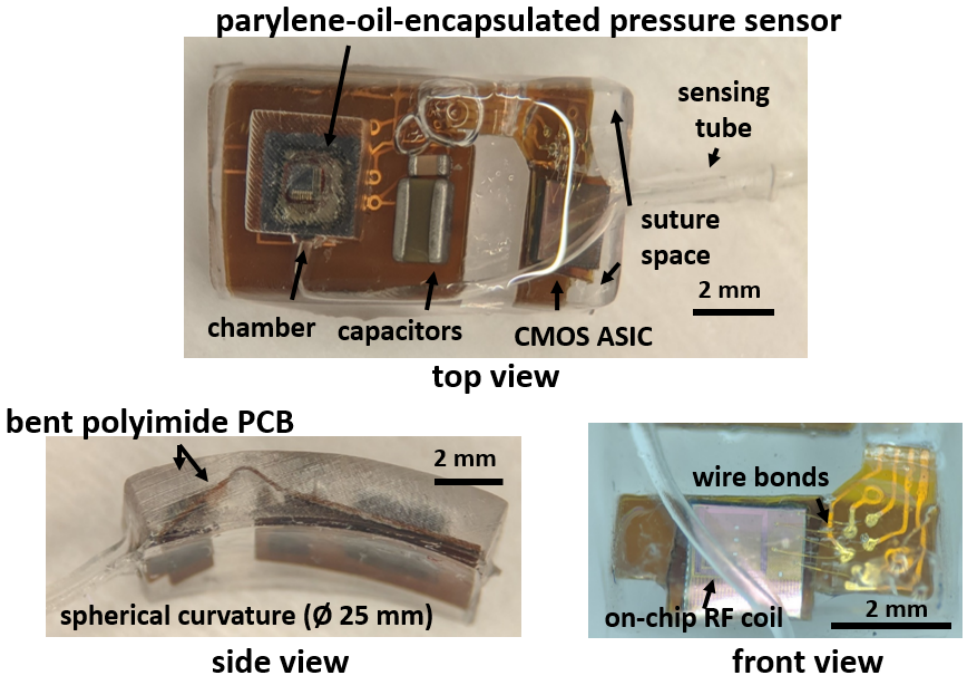

Figure 3.72: Implant with bent polyimide PCB for efficient RF coupling.

A side view diagram of the folded PCB version of the implant is shown in Figure 3.73.

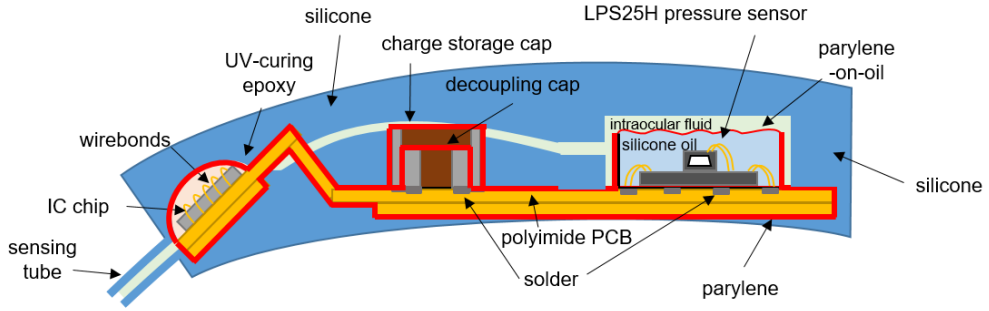

Figure 3.73: Folded PCB implant diagram.

The implant was inserted *ex vivo* (Figure 3.74).

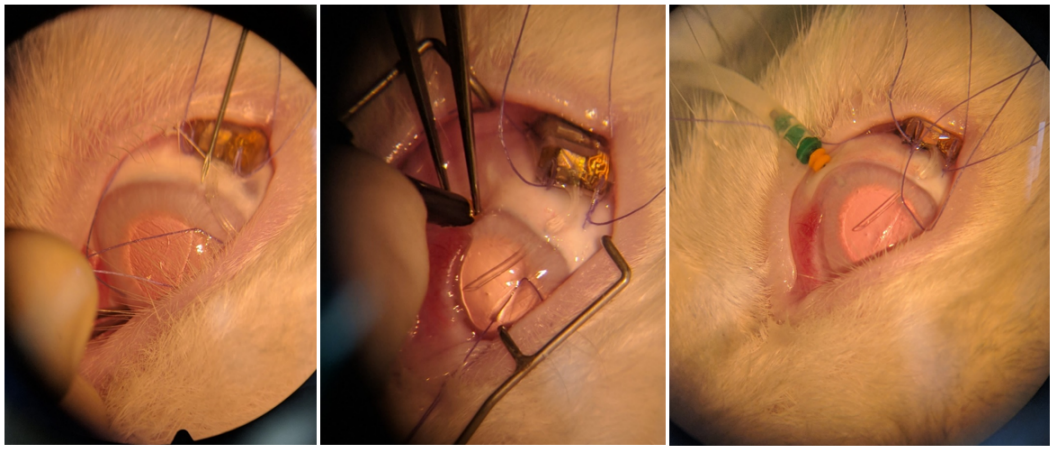

Figure 3.74: Implantation of the folded PCB implant *ex vivo*. Left: Implant is already implanted and needle is about to make a hole in pars plana. Middle: Sensing tube in anterior chamber, and infusion line is introduced. Right: Final picture.

The RF coil of the implant is facing the camera, and the end of the tube is in the anterior chamber, and free of bubbles (Figure 3.75). The implant could be powered at up to a 5 mm air gap at 32 dBm input power. It could also be operated when the implant was covered by the eyelid. Figure 3.76 shows a top view of the reader antenna on the rabbit.

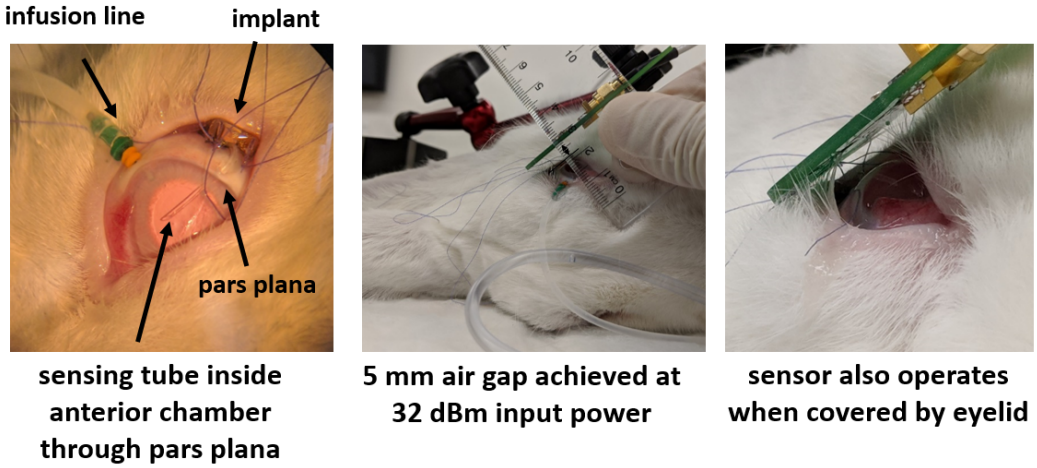

Figure 3.75: Operation of the folded PCB implant *ex vivo*.

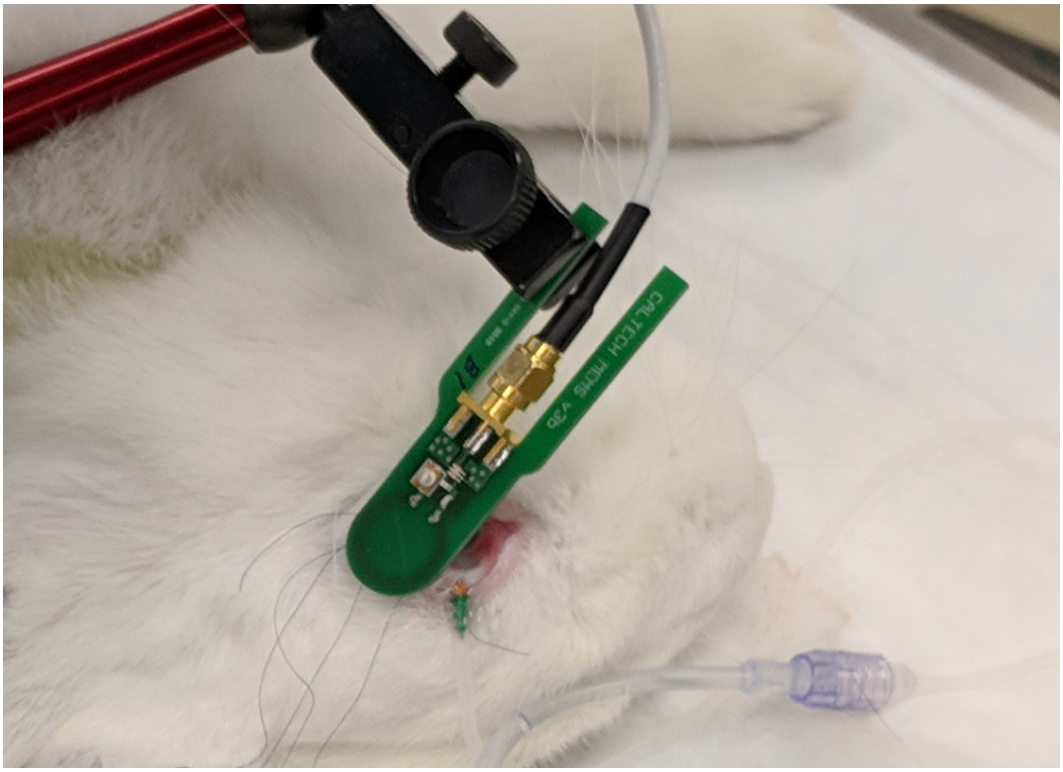

Figure 3.76: Reader antenna on rabbit *ex vivo*.

The IOP of the rabbit was then modulated by changing the height of a water column manually. The intended pressure is from the height of a water column which was manually adjusted, explaining the time constants and under and overshoot. The intended pressure could be set to 1 mm H2O differential, with a bulk precision of 1 cm H2O. See figure 3.77. Like the other *ex vivo* experiments, an anomalous constant offset was observed, this time +10 mmHg. Temperature data was recorded simultaneously and calibrated for that, but is not shown in the figure.

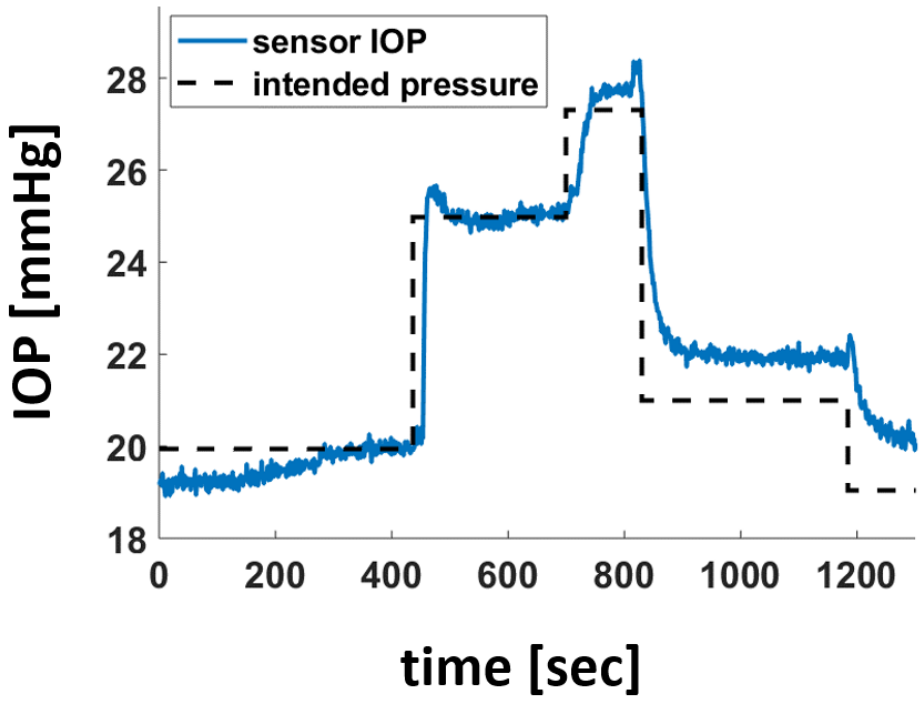

Figure 3.77: *Ex vivo* IOP data with bent PCB, after adjusting for extra +10 mmHg constant offset after implantation.

3.7.3 *In vivo* Rabbit Experiment

The IOP sensor implant for the *in vivo* experiment was rounded, smooth, and about 2.6 mm thick. No antibiotics were added to the sterile saline during degassing, but the dish, the implant, and the metal mesh to weigh down the implant during degassing went through EtO sterilization.

Figure 3.78 shows the implantation procedure for the *in vivo* experiment. A pocket in between the sclera and conjunctiva is made, and the implant is inserted. Then the implant is sutured into the sclera, and a hole is made to fit the sensing tube through the pars plana into the anterior chamber and the tube is inserted. Then the conjunctiva is stitched.

Although earlier experiments clearly showed the absence of bubbles in the tube during operation, since the conjunctiva is sewed over the tube, visual confirmation is not possible. In addition, during this trial, the sutures of the body were drawn tight before trying to insert the tube the first time, which was unsuccessful. So the sutures were loosened, the tube was inserted, and then the sutures were re-tightened. However, during the unsuccessful earlier attempts, more saline escaped the tube than previously, so a visible bubble was seen in the tube. However in the roughly

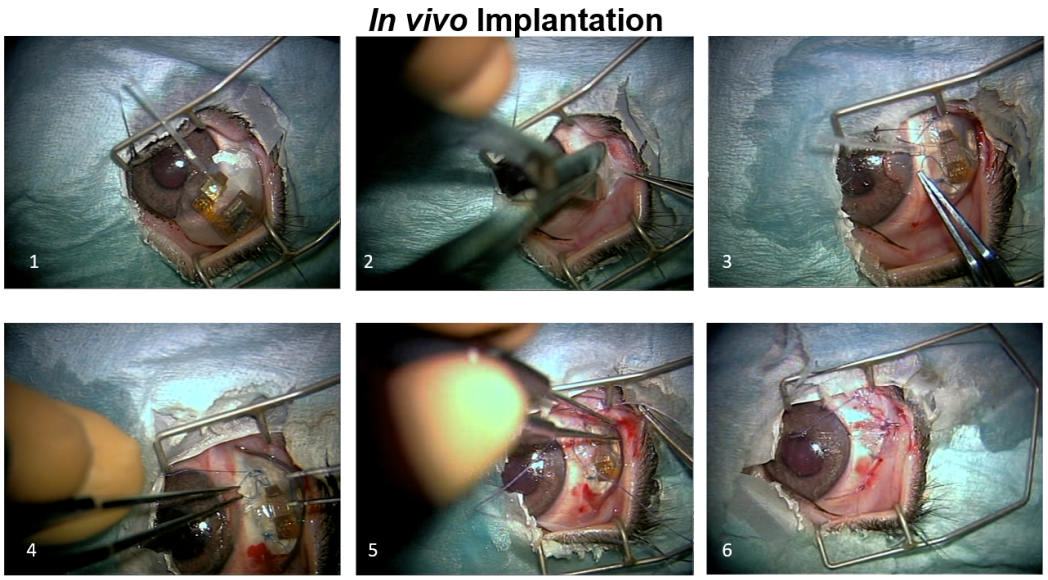

Figure 3.78: Implantation procedure for the IOP sensor implant *in vivo*.

30 minute long implantation procedure, the bubble was visibly shrinking, although it was not confirmed to be completely gone before the conjunctiva was sutured over it. However, the stable 7-day suggests the bubble did indeed dissolve by the time measurements were taken. The eye right after the surgery is completed is shown in Figure 3.79. The bubbles in the anterior chamber are seen, but are gone by the time of the day 4 measurement. The tube in the anterior chamber is also seen. The segment of the tube where the shrinking bubble was seen is occluded in the photo.

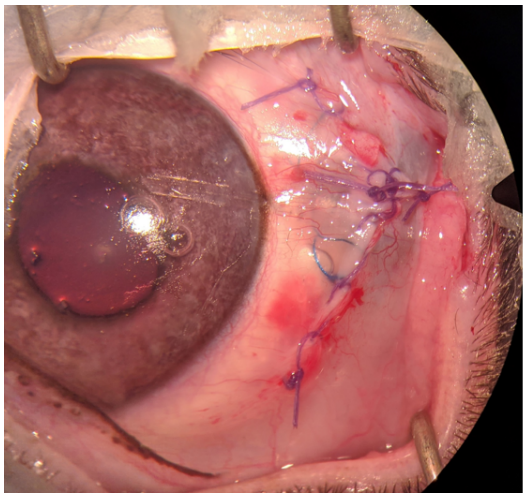

Figure 3.79: Close up of implant in eye after surgery *in vivo*.

3.7.3.1 7-Day IOP Data

IOP data from the implant and a tonovet tool was taken on days 0 (just after implantation), and day 4 and day 7, and attempted on day 10 (failure mode discussed later). Since the rabbit is anesthetized for each measurement because long and stable alignment is required due to how the ASIC was designed, a measurement is only possible once every 3 days three due to regulations. The measurement techniques are shown in Figure 3.80.

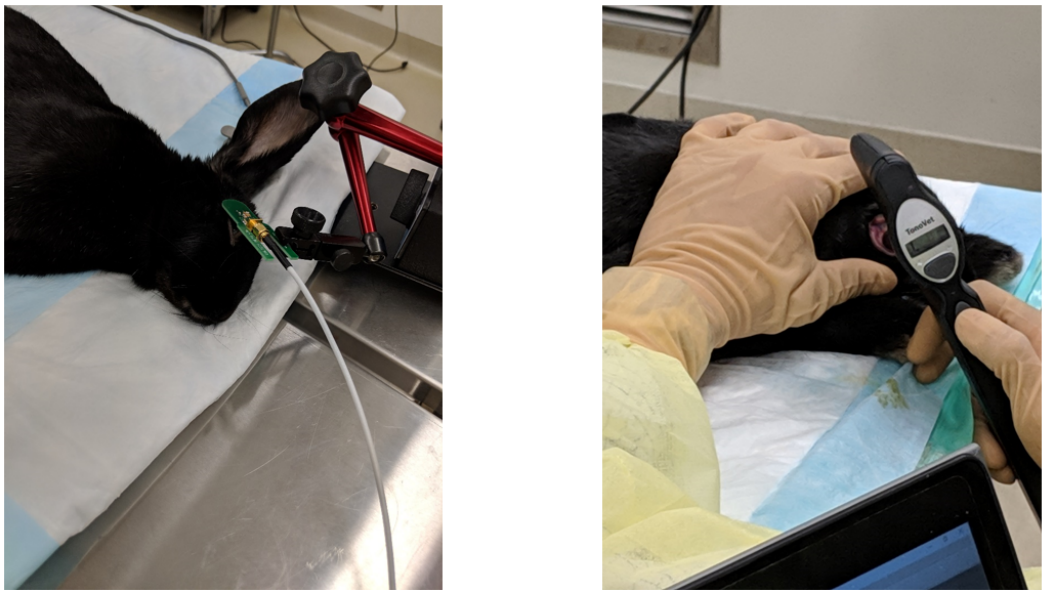

Figure 3.80: Pictures of reading IOP wirelessly with the implant and the tonovet as the reference IOP reading *in vivo*.

The IOP data is shown in Figure 3.81. The error bar is one standard deviation. Like the *ex vivo* plots, the data is adjusted for one-point calibration for this *in vivo* plot. The ability to do one-point calibration immediately after implantation is assumed, since the patient would be at the hospital anyways. Even though the initial pressure offset of +4.5 mmHg did not match the predicted hydrostatic pressure offset of +0.7 mmHg by nature of sensing through a tube with a small elevation drop, the error on day 0 is 0 mmHg by definition anyways after negating the measured offset. Note that the IOP data reported by the implant, including in the plot, is after calibrating in air and with temperature compensation. Thus the error is summarized in table 3.2 where the same constant offset measured on day 0 is assumed forever afterwards.

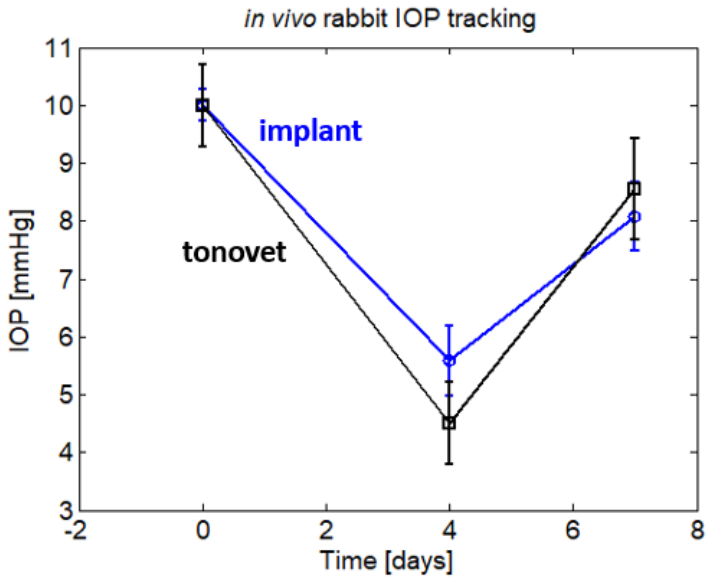

Figure 3.81: IOP in rabbit *in vivo* for 7 days with the wireless sensor versus the tonovet as the reference.

Table 3.2: IOP error of 7-day *in vivo* experiment.

Day	IOP Error [mmHg]
0	0
4	+1.1
7	-0.5

The clinical accuracy target for IOP is about 2 mmHg. For 7 days, the IOP was at most 1.1 mmHg off from the tonovet, which is recognized as the standard manual measurement technique. The IOP in the rabbit fluctuated throughout the measurement due to the different timings of the anesthesia to measurements on different days. It is known that anesthesia affects the measurements, and the longer the wait the more the IOP will drop. Efforts were made to take tonovet measurements as close in time to the wireless sensor inputs, so the two lines should correlate. The higher IOP on day 0 is unsurprising given the trauma and stress of a surgery, according to the surgeon. Even though the lines are not constant, the good agreement between our device and the tonovet is convincing evidence that both independent methods measured real pressure variation.

On day 10, the IOP data retrieval was unsuccessful. The IC chip reported back data packets of all 1's, as if the connection to the pressure sensor was broken. Given the other benchtop test with saline with the pressure sensor and the dummy chip with wire bonds, this failure mode was expected. Interestingly, it lasted longer

(7 days) in the rabbit than a similar sample did in 37 °C saline (less than 2 days). The implant was left in the rabbit to complete a safety assessment for up to 1 month, since the rabbit eye appeared healthy as of day 7.

On day 29, the implant was extracted. The eye and the implant look healthy. The bubble was not seen immediately after the conjunctiva was cut open, meaning that the bubble must have dissolved just as we presumed (Figure 3.82). The biofouling response is minor, as there is no discoloration visible to the naked eye. In fact, the only indication it was in the eye is that the exterior surface now scatters some light, just like the an implant would after casting with the 3D printed mold, before painting with dilute silicone, so there must something on the surface. The inner surfaces look clean too, which was made visible by adding a droplet of IPA to remove the scattering of light at the exterior surface. However, we expect the inner surfaces may have some material accumulation too small to see.

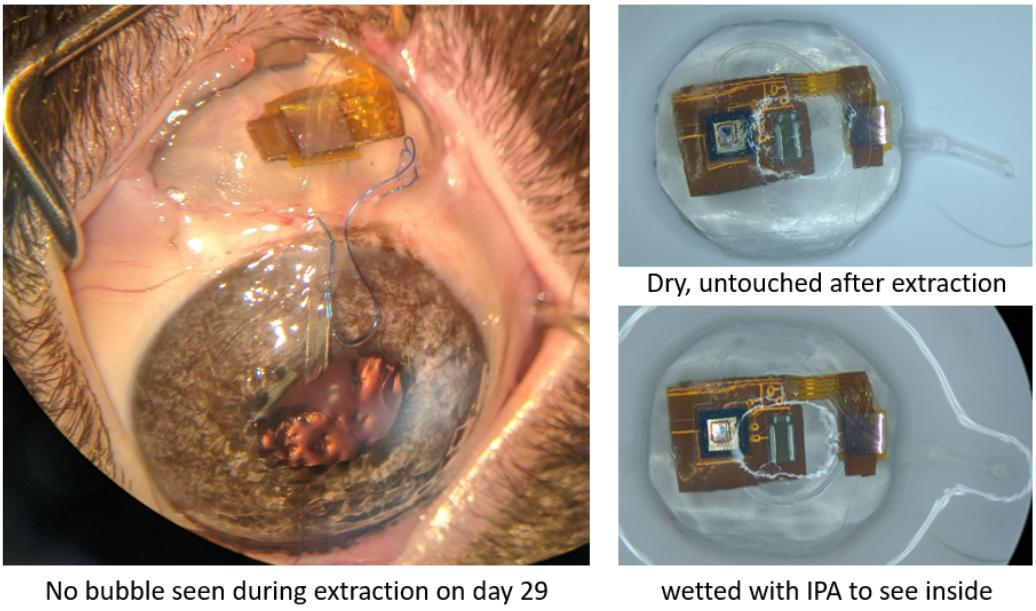

Figure 3.82: Implant after extraction on day 29.

After explantation, IOP readings were attempted once again. As expected based off the failure to collect data on day 10 *in vivo*, the prefix and suffix were normal, but all the other data were 1's. However, the sampling period was the original 1.27 seconds, suggesting that the IC had not corroded at all after one month inside the rabbit. This is in contrast to an earlier test where the 1.3 sec sampling period degraded to 3.5 sec sampling period after 2 months in saline at body temperature.

3.7.3.2 Safety Experiment

The implant did not seem to harm the rabbit from day 0 through day 29, the last day of the experiment. There is no clouding or other irritation visible near the tube (Figure 3.83). The rabbit wore a collar for 3 days, then it was taken off, but the rabbit has not been observed to be trying to scratch it either, so we conclude the implant is not causing a lot of discomfort for the rabbit. The eye appears healthy, including the sclera underneath where the device was located after it was extracted.

Figure 3.83: Implant tolerance photos. Implant does not cause irritation or discomfort for 29 days.

The tonovet was used to measure the IOP of the rabbit eyes. The right eye had the device, so the left eye was used as a control. Anesthesia was administered and can cause the IOP to change depending on how long ago was it administered [92]. Measuring the IOP with the tonovet before applying anesthesia was not conducted until day 16. The earlier days all included measurements with the tonovet after retrieving or attempting to retrieve IOP data from my sensor, so that was over 10 minutes after applying anesthesia. Later, the sensor was ignored because it failed, so IOP was measured quicker after anesthesia. On day 16, IOP before, and 5 minutes after anesthesia and 35 minutes after anesthesia for both eyes was measured. In summary, the IOP values were within expected range. The left eye, which did not have an implant, even seemed to have larger variance in IOP than the right eye with

the device, so we conclude that the IOP sensor implant did not negatively affect the IOP of the right eye (see Figure 3.84).

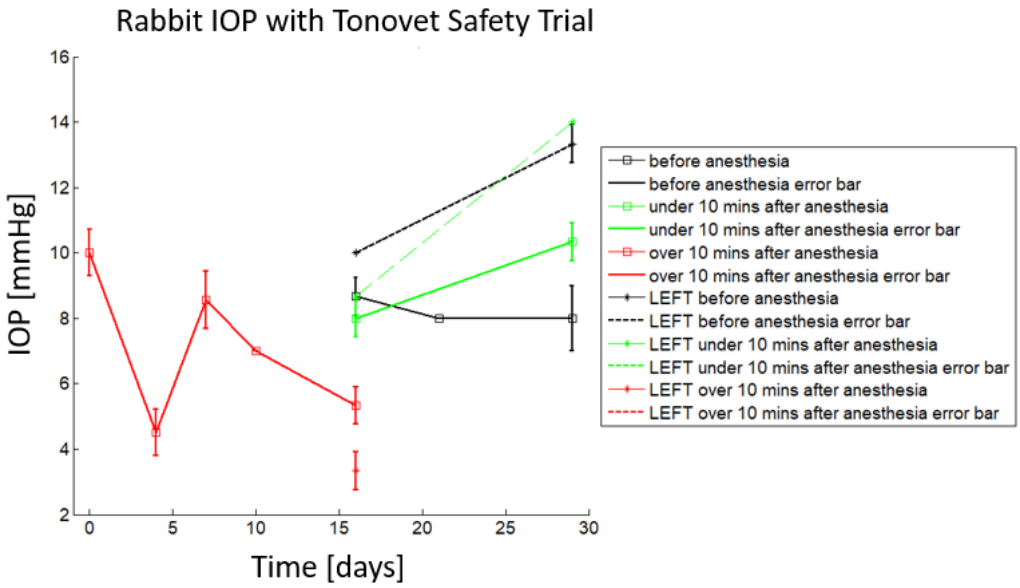

Figure 3.84: Rabbit IOP is normal when sensor is present.

3.8 Future improvements

Although the 7-day *in vivo* lifetime is a good first step, clearly it is not the final desired age, but the benchtop data implies that the failure point was not the pressure packaging itself. Improving the wire bonds and switching the PCB from polyimide to parylene could also extend the lifetime. Further, circuit improvements could be made such that the powering can occur quicker rather than wait for the fixed amount of time. This would make aligning the implant easier or at least more tolerable to momentary misalignments. Also, a system that would restart the pressure sensor for each measurement would avoid the need for a hard reset whenever power is lost. Last, another way to automatically sweep the frequency and re-tune the antenna coil would make the measurement process more convenient. Given that the *in vivo* experiment lasted for seven days.

3.9 Summary

This chapter covered the efforts to put the implantable pressure sensor packaging into practice in an intraocular pressure sensor. Polyimide benchtop data suggest that a polyimide PCB would be able to survive for months, but unlikely to last for years. The intraocular pressure sensor implant was built and verified to work *in vivo*

for at least 7 days, and the failure point is suspected to be the assembly/wire bonds, but luckily that is not fundamental to the pressure sensor packaging, but rather a consequence of the limitations and scope of a thesis project. Also, the implant is verified to be safe and seemingly not irritating the rabbit to the point where it tries to scratch it. Nonetheless, the data shown here suggests that the bottleneck in IOP monitoring with parylene-oil-encapsulation is not the packaging itself, but other factors which are known how to solve, although they take time and resources. Of course, the only way to prove that the pressure packaging survives *in vivo* for long term is to make an implant that survives for long term, which is still future work at this point. But the overall architecture is valid basis from which future designs can build. Indeed, the system is designed to be easily modified without a change to one block necessitating a complete re-work of another block, especially now that the approach is proved to be safe.

Chapter 4

CONCLUSIONS

Long term implantable pressure sensing with an active sensor would be very useful in the clinic for monitoring many diseases. Hermetic materials like glass and metal are intractable for general active implantable pressure sensors, since the fabrication with acceptable pressure sensing resolution is hard. Instead a packaging approach is taken made from non-hermetic materials. The key insight is that since diffusion properties are not low enough anyways, to limit corrosion, a material with low water saturation limit is favorable. This is achieved by submerging the pressure sensor in silicone oil.

An implantable pressure sensing scheme called parylene-oil-encapsulation is conceived and proven to work on benchtop. The parylene deposition on the surface of the oil traps the oil around the pressure sensor bubble free. Saline soaking tests at elevated temperature suggest a lifetime of up to 4.5 years at body temperature while maintaining stable sensitivity and <2 mmHg offset drift, which is the clinically relevant accuracy for glaucoma monitoring. Theoretical results were conceived and verified on benchtop. The packaging scheme was modelled to predict the relative sensitivity of the pressure sensor after packaging compared to the original value. The packaging of parylene around the oil can be thought of an "area-gain" effect, such that the accumulation of any biofouling is felt by the sensor like a much thinner film than it would if an equal sized film was deposited on the active deflecting membrane of MEMS pressure sensor itself. In other words, the entire footprint of the pressure sensor can used to sense the pressure to the environment, not just the deflecting area in the MEMS sensor alone. Additionally, the intuitive notion that a bubble in the oil would cause pressure sensing error is modelled and replicated on benchtop. This demonstrated the importance of reliable, easy bubble-free packaging that parylene-oil-encapsulation achieves.

While an argument is presented that maintaining stable sensitivity is most important, a stable offset is also important. The parylene-oil-encapsulation recipe was optimized to start with minimized initial offset with a recipe of nominal 0.5-1 μm of PA-HT on 100k cSt silicone oil. Meanwhile, a newly documented phenomenon of wrinkling of parylene as deposited on higher viscosity/molecular weight silicone

oils, demonstrating compressive stress is shown. Also, the thickness of films is characterized by an additional porous layer thickness of a value that is determined by the species of parylene and molecular weight of the oil, but not the amount of parylene dimer.

While the pressure sensor packaging scheme was conceived as a general method, a wireless intraocular pressure sensor was built towards proving the method *in vivo*. A custom IC chip was designed in collaboration and built for this implant to receive RF power, run a commercial digital barometer which was packaged, and send the data out. The IOP sensor architecture is entirely new, where the implant is large and therefore resides outside the sclera, but a silicone tube enters the anterior chamber through the pars plana. A construction method on polyimide was conceived to verify the *in vivo* performance for one week in a rabbit with <1.1 mmHg offset error drift compared to tonometry, which is the gold standard in the clinic. The wire bond failure mode is hypothesized and replicated on benchtop, which needs to be fixed. Luckily, that is not related to the pressure sensor packaging scheme at all.

Future work towards achieving a long term active implantable pressure sensor is clear. This overall pressure sensor packaging and assembly of such an implant with that could exploit the packaging scheme is shown to be safe and practical. The approach in general distributes the components to circumvent size limitations. For example, the pressure sensor is large and resides outside the eye, so it exists further back in the implant, but a small on-chip coil made the performance of the coil repeatable, predictable, and independent of the total shape of the implant in a way that a large, flexible coil cannot. The flexible coil could even have better performance, but it requires co-design with the overall shape of the implant, which is difficult. In fact, the separation of the design process along with the small on-chip coil anticipated the need to re-orient the IC chip without changing the rest of the implant during *ex vivo* tests in a rabbit. So this is a promising engineering approach towards developing a real implant by uncoupling the design of the various components.

More work should be done on the lifetime of parylene-oil-encapsulated pressure sensors, both *in vitro* and *in vivo*, especially in regards to possible delamination of parylene at the boundary of the contained oil, but the bottleneck in long term implantable pressure sensing when using the packaging scheme seems to be no longer the packaging of the pressure sensor itself. However, stable long term *in vivo* data is needed to rigorously prove that conjecture.

Last, the parylene-oil-encapsulation scheme may have applications in protecting implantable electronics in general. It is especially interesting because most electronics applications can ignore pressure effects anyways, making it potentially simpler than packaging pressure sensors.

Appendix A

PARYLENE-OIL-ENCAPSULATED BATTERY

Although the wireless implant did not use a battery in the end, the option to use a battery was investigated for functionality, longevity, and safety. Some batteries were packaged with parylene-oil-encapsulation, and decent longevity results were achieved. However in the end, using a battery was deemed not worth the difficulty of assembling the battery into the whole implant nor the increased safety risk, as the main goal was to prove the longevity of the pressure sensor. So anything that could threaten the longevity, despite other benefits, such as a battery and memory system allowing pressure reading passively was put aside for the first generation implant, with the understanding that they might be included in future versions.

A.1 Commercial Bare Die Battery

We found bare die rechargeable batteries from Cymbet. In fact, this battery was used in a previous IOP sensor paper [86]. The model we found is the Cymbet005 5 µAh, 4 V battery (Figure A.1). The bare die is $2.2 \times 1.8 \times 0.2$ mm^3 [93]. Battery could allow IOP measurements for 12-24 hours if sampled every 10-20 minutes, depending on the standby current of the implant.

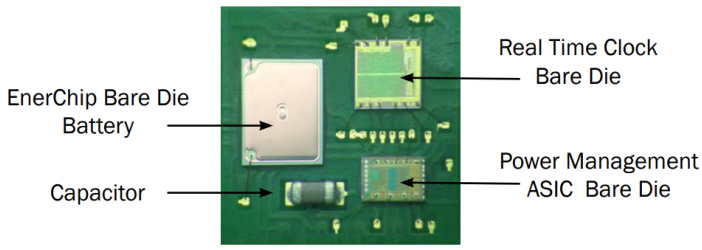

Figure 4: EnerChip RTC multiple bare die in single package

Figure A.1: Cymbet005 battery. Reprinted from [93].

A.2 Charging the Battery

Batteries are charged from initially uncharged bare die at 57 °C and at room temperature (Figure A.2). The cell resistance decreases with increased temperature, agreeing with decreased charged time at higher temperature (Figure A.3).

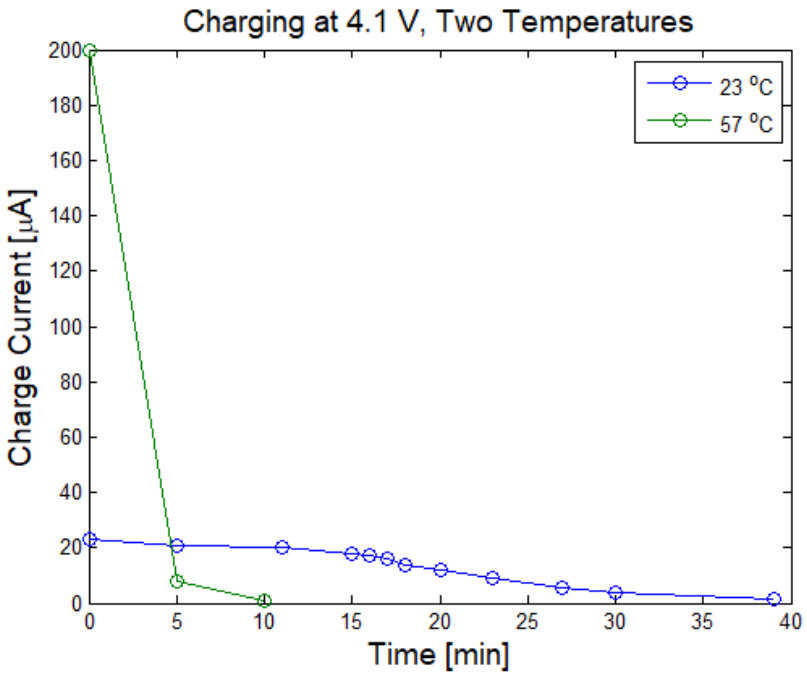

Figure A.2: Battery charging experiment.

Here are some early observations.

1. At room temperature, no leakage is observed (<0.1 μV over 20 minutes, open load).

2. With an open load, the output voltage changes slightly with temperature. The Output voltage increased with time as temperature decreased from 57 to 37 °C.

3. At 37°C, the discharge leakage is <9.1 μV/min, possibly 0, and the temperature may have been settling from when I set oven from 37 °C to 39 °C so that the mercury thermometer read 37 °C. Assuming a worst case of 9.1 μV/min, the battery would last over 22 days above 3.8 V with an open load at 37 °C.

4. At 57 °C, the discharge leakage varied device to device, but was about 18 mV/hour, which is not usable.

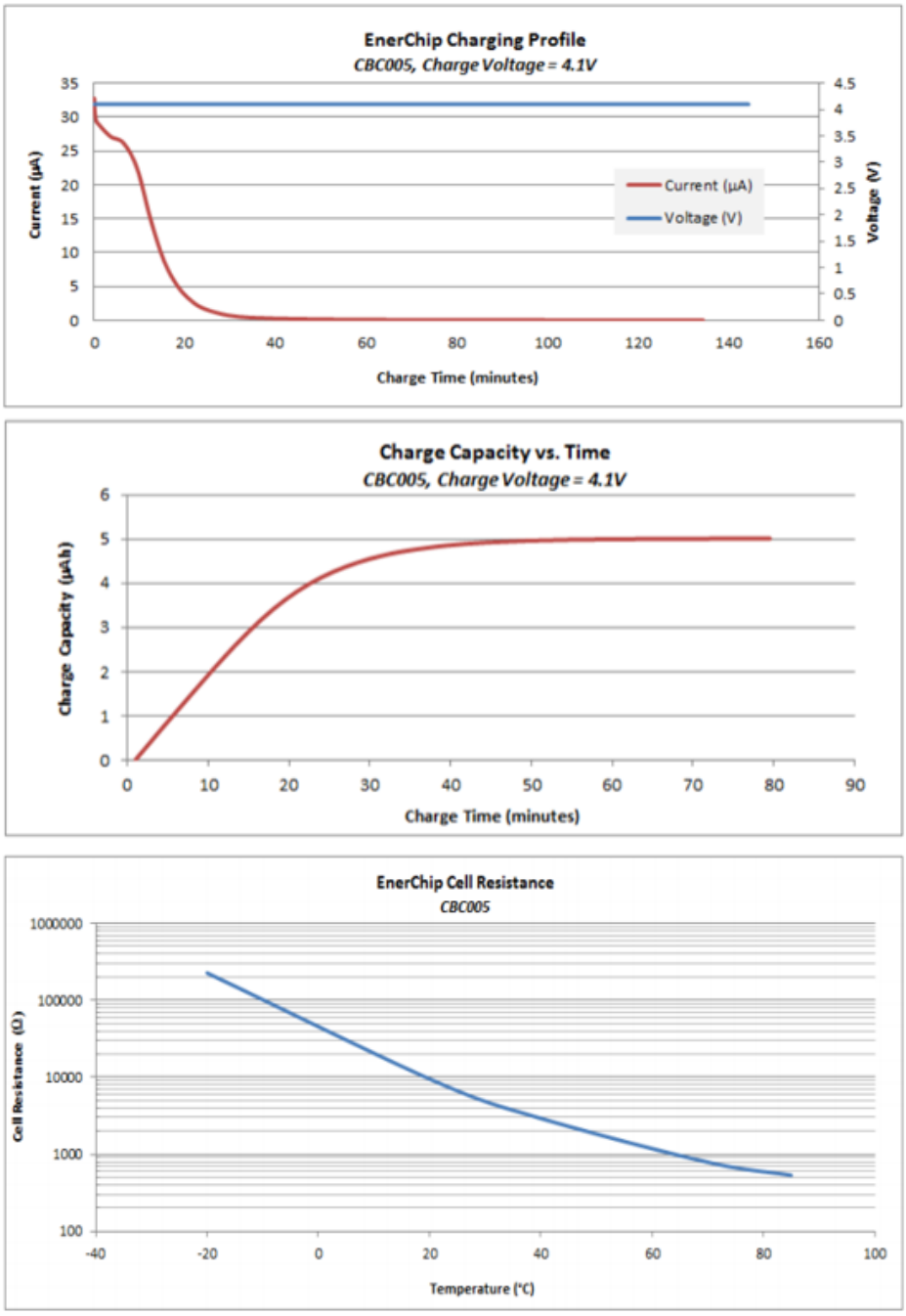

Figure A.3: Battery charging plots. Reprinted from [93].

A.3 Packaging and Connecting to the Battery

You cannot touch the sides and/or top of the silicon, because this shorts the anode. The diced bare die sides are not insulated. See Figures A.4 and A.5.

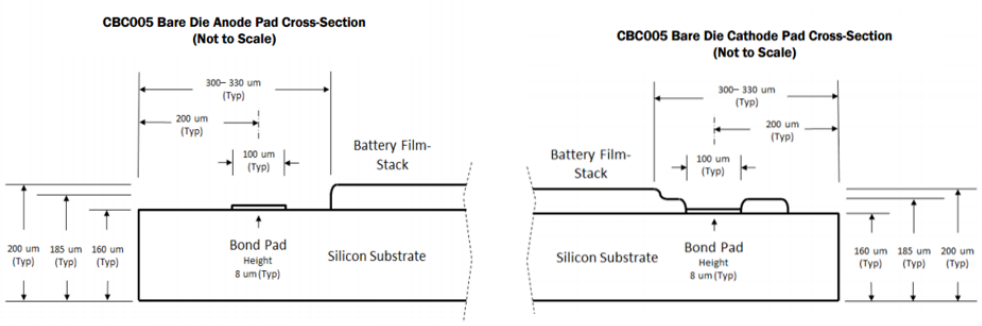

Figure A.4: Cross-section of the battery. Reprinted from [93].

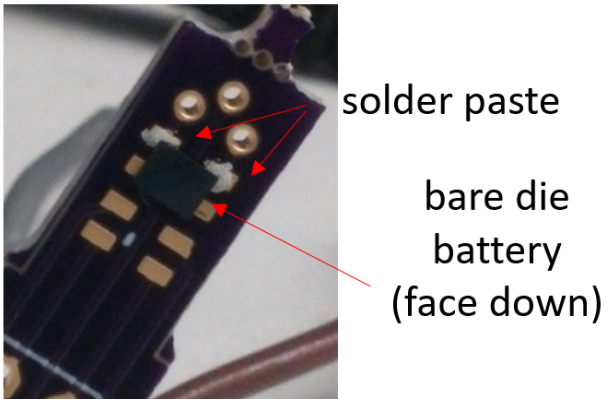

Figure A.5: Battery face down with solder paste is shorted.

Wire bonding was found to be the simplest way to connect to the bare die battery without damaging it. Figure A.6 shows the control sensor with only wire bonds, and the battery after packaging with silicone oil and parylene-C. Also, a sample with only parylene coating was prepared.

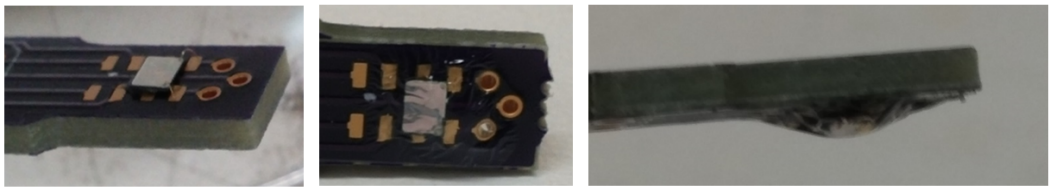

Figure A.6: Bare die wire bonded to the PCB. Control sensor left as is, and other batteries protected by 100k cSt silicone oil and 11 packaged with 11 µm PA-C.

A.4 Battery Packaging Saline Soak Test

Batteries were packaged to see how well the packaging scheme devised to protect pressure sensors would also protect the battery.

A.4.1 Sample Preparation

The bare dies were prepared in jars much like the pressure sensors from the first generation samples (MPL115A1 sensors). Here, the wires went through the jar lid, rather the PCB itself as in later versions. As can be seen. this results in the wire-PCB connection being inside the jar above the saline level, buts exposed to humidity. The joints would be protected by parylene only. Presumably oil at the joins could help, or even better, putting the joints outside the jar by using a longer test PCB template. This was not done as the battery approach was abandoned by the time I optimized the template PCB for wired soaking tests. See Figure A.7.

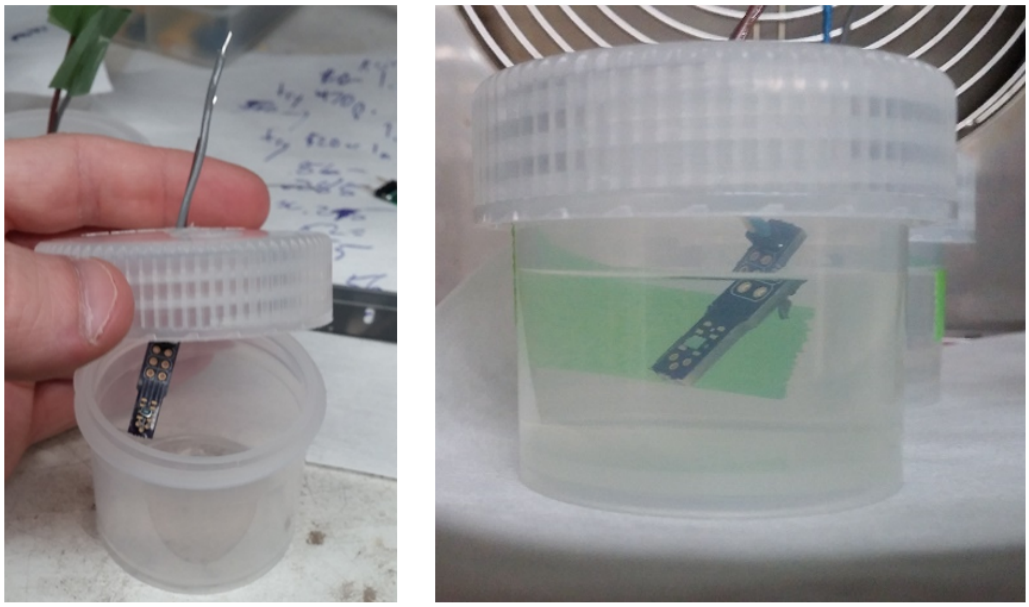

Figure A.7: Bare die battery in jar for saline soak test.

A.4.2 Battery Saline Soak Experiment Setup

Before charging the batteries, the batteries were exposed to the maximum heat they would be exposed to, per the data sheet. Charging the batteries before heating up to a higher temperature than they experienced previously will cause battery failure. The batteries were placed in saline and heated to 57 °C for a factor of 4 times accelerated aging compared to body temperature of 37 °C. See Figure A.8.

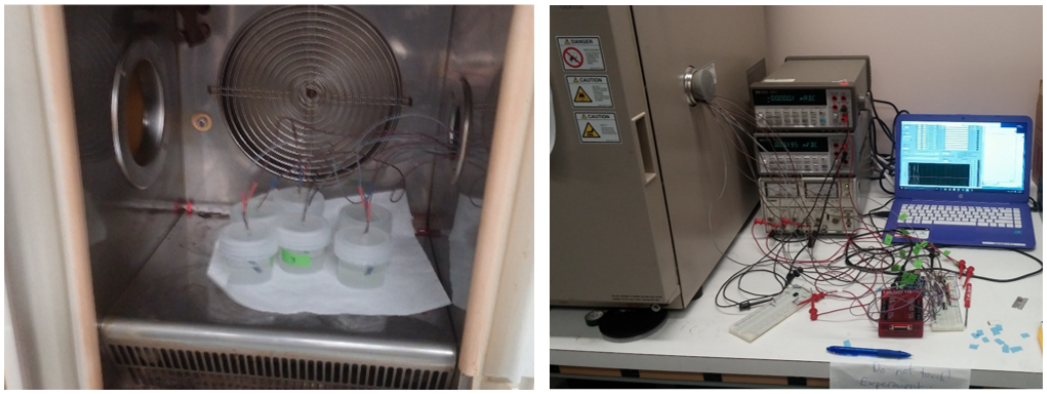

Figure A.8: Accelerated saline soak test setup, at 57 °C.

The batteries were then charged and discharged and their voltage was continuously measured and logged a circuit. The circuit topology is seen in Figure A.9.

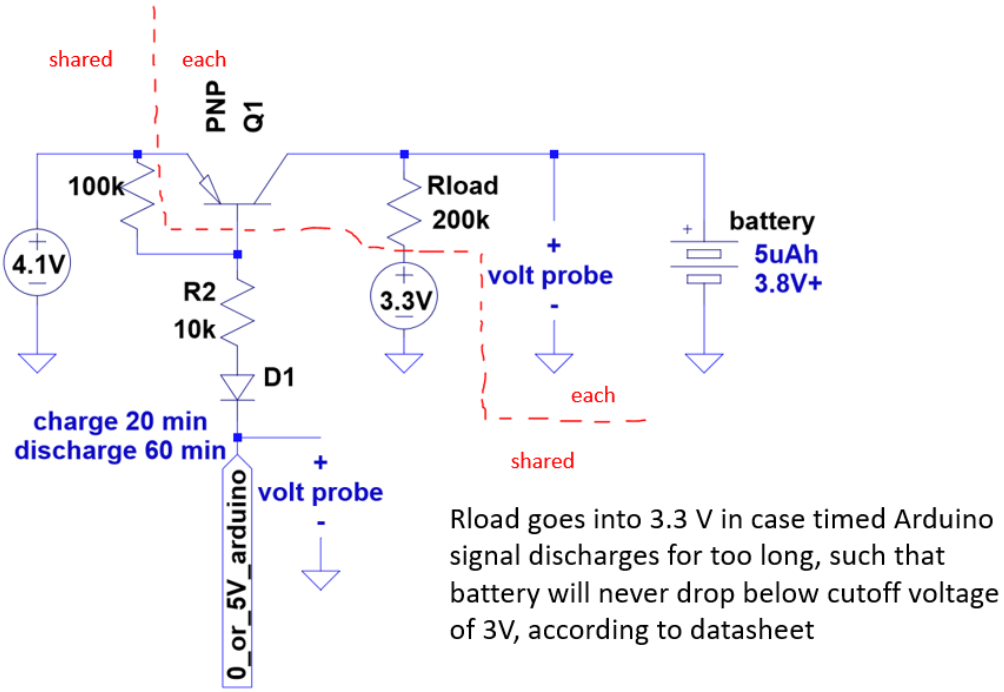

Figure A.9: Battery experiment switching circuitry.

The Arduino controls the voltage at the transistors to switch from 20 minute charge or 60 minute discharge states. In the charging state, the voltages logged are just the power source voltages, but during the discharging state, the voltages logged are the voltages from the batteries. A labjack U3 was used as the data

acquisition box. A safety 3.3 V supply was used to prevent catastrophic failure due to excessive discharging, in the case that the charge storage decreased enough such that 60 minutes would fully discharge the battery. The point of the test is to see how long the batteries could survive in a hostile environment with our packaging, rather than other failure modes that in principle could be avoided with smarter battery handling circuitry than the board-level circuit I made for the longevity test. Typical data of a few cycles is shown in Figure A.10.

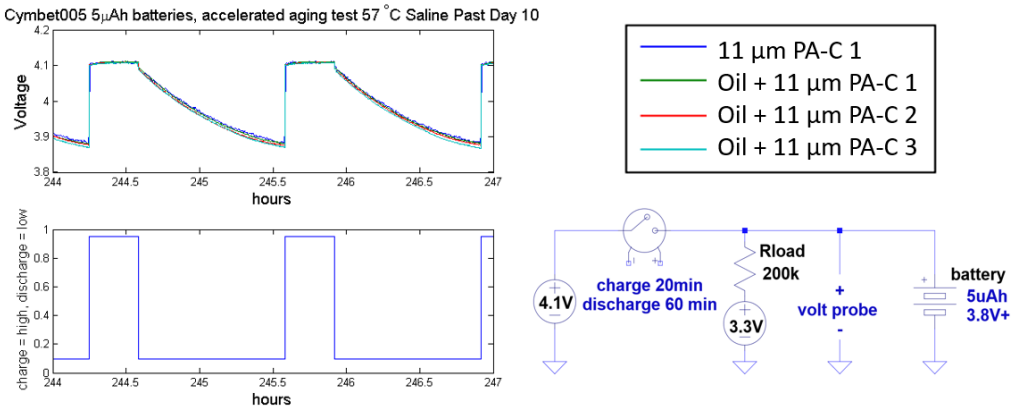

Figure A.10: Accelerated saline soak test experiment.

A.4.3 Battery Saline Soak Experiment Results

There was an unpackaged battery which failed instantly when put in saline, as expected. Besides that sample, the results are summarized here.

- 6 batteries: Each in 57°C Saline, charged for 20 mins, discharged for 60 mins at 4 μA (supposedly 5 μAh capacity per battery
- 1,2,3: no oil, 11 μm PA-C
- 4,5,6: 100k cSt silicone oil, + 11 μm PA-C
- **Summary: Parylene-on-oil packaged sensors do better than parylene-only sensors. Parylene-on-oil sensors do not fail catastrophically, capacity degrades over time as predicted by data sheet.**
- Should redo experiment with batteries in air as control to determine natural aging at 57 °C.
- All wire bonds (except for battery 3) intact.

- Battery 1 failed before start of experiment due to human error.
- Battery 2 failed at hour 540 (almost no charge capacity anymore).
- Battery 3 failed at hour 16. Bubble seen on battery, wire bond probably broke.
- Battery 4 failed at hour 455.
- Battery 5 (best) retains roughly half-original capacity at hour 806 = 590th charge cycle. Fails by hour 852.
- Battery 6 failed at hour 338.

The devices after failure are shown in Figure A.11.

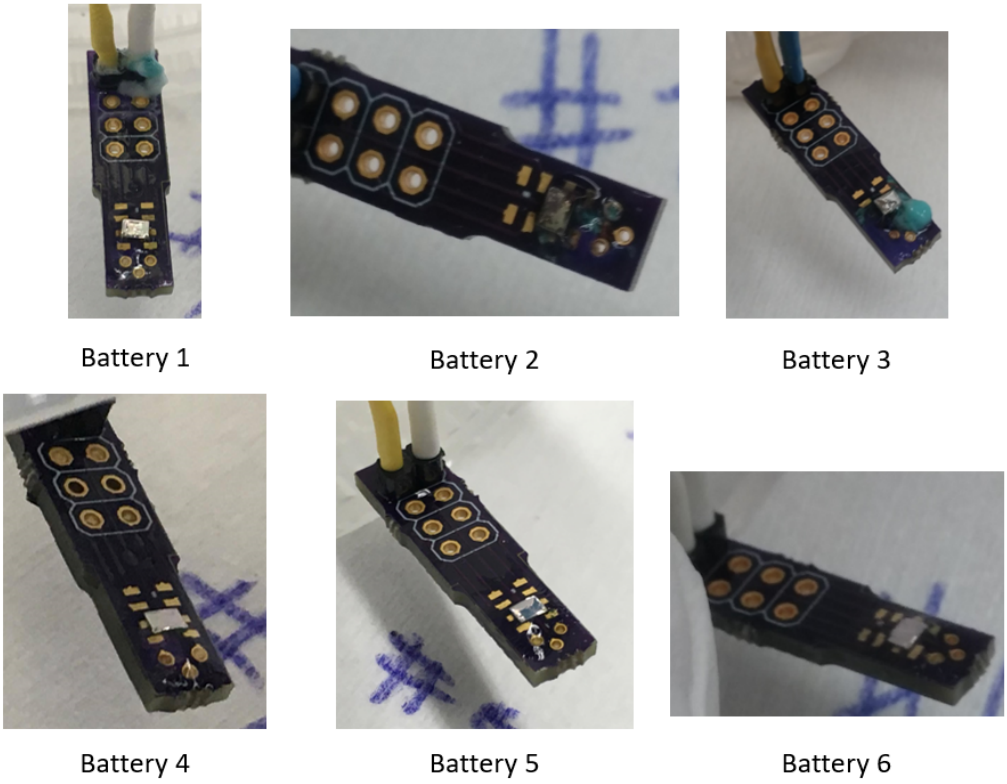

Figure A.11: Packaged batteries after failure from the long term saline soaking test at elevated temperature.

- Batteries 1, 2, 3 (no oil) show teal corrosion. Liquid saved in 6 separate containers for future analysis.
- Batteries 4, 5, 6 (with oil) do not show teal corrosion

The sample that survived the longest (sample 5) is analyzed in more depth below (Figure A.12). The first plot shows the full 852-hour lifetime. Being zoomed out so far, the information in this plot is in the bottom of the blue curve. This is the minimum voltage the battery reaches after the fixed 60-minute discharge phase. The top of the blue is flat because that always would read the 4.1 V charge voltage for the 20-minute charge phase. It can be seen at hour 80 the initial discharge voltage is about 4.1 V, and it steadily decreases to 3.9 V over 60 minutes, which is still a valid voltage. At hour 80, the initial discharge voltage drops to 3.9 V instantly, then about after 30 minutes, the charge runs out entirely, so the voltage drops to the 3.3 V of the safety voltage supply. Then at about hour 850, the charge does not hold for practically any time at all before dropping to 3.3 V. Full failure is considered to be the first entirely anomalous voltage dip below 3.3 V as seen at hour 852. Similar anomalous dips were seen for the other samples earlier, and was used to designate failure events for those samples. Other well-behaving samples looked much the same as this sample, but aged faster.

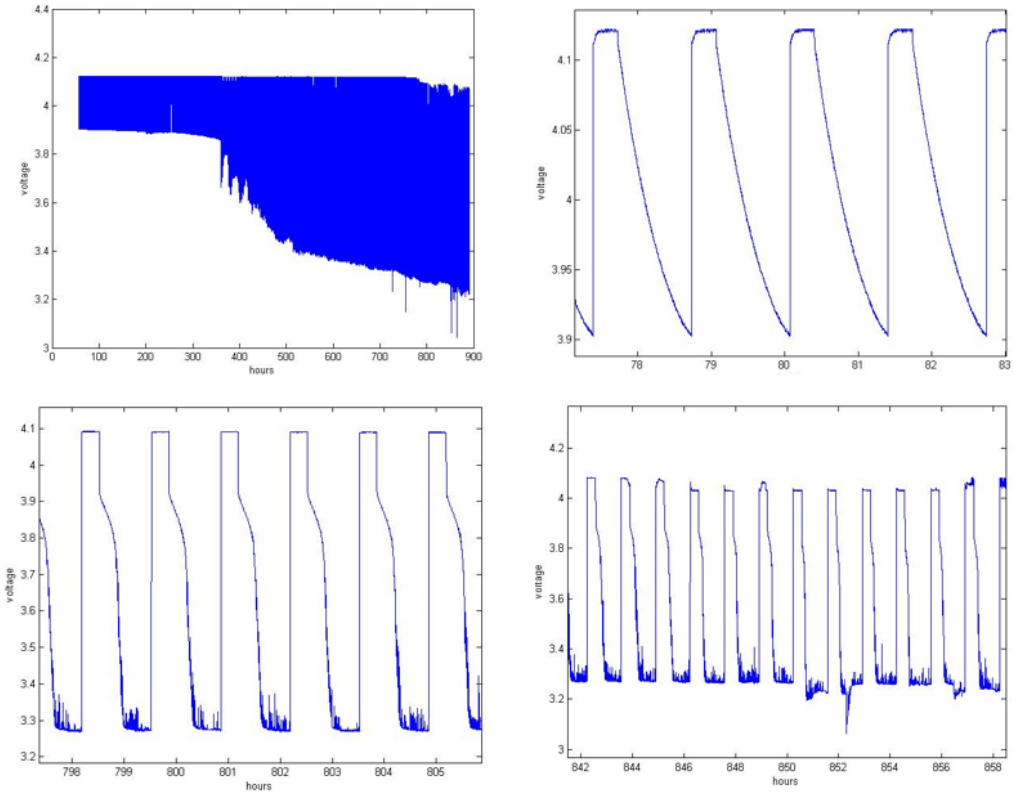

Figure A.12: Battery 5 plot over time. Clockwise, starting top left: Full plot, zoomed in at 80 hours, 800 hours, and 850 hours.

A.5 Summary

Bare die chip batteries were packaged with parylene-oil-encapsulation and tested in saline soak test. It was found that the parylene-oil-encapsulated batteries survived longer than those coated with parylene only. The results are promising enough to warrant further exploration. Last, even if a rechargeable battery is used, it is important to remember that they have a maximum amount of total charge, in coulombs, that they can dispense, even if it is over many charge-discharge cycles. The saline soak test shows that the parylene-oil-encapsulation was good enough to make a battery survive until its maximum charge dispensing limit. However, for a more complete understanding of the effect of the packaging, further experiments of battery longevity with samples also left in air at the equivalent temperatures should be conducted.

Appendix B

MICRO-SCALE INNER DIAMETER SILICONE DRAINAGE TUBE FOR GLAUCOMA DRAINAGE

The proposed IOP sensing implant is large, and may seem silly to assume that it would ever be implanted inside a person if the only feature is measuring pressure. However, since the the form factor is already similar to other glaucoma drainage devices (GDDs) [94], and a drainage tube could be mated with the implant. Compared to the Ahmed valve or Baerveldt valve, the space filled up by the plastic plate to hold in place should now be filled up by electronics that can measure IOP so that one may think of it as a self-aware drainage tube that can be inspected if the drainage part ever gets clogged, as is known to be the case. The clogging in the long term due to biofouling is known to be an unsolved problem, and is especially problematic for check-valve type devices such that they have not been proven to be more efficacious than simple tubes of ideal dimensions [95]. Some of these procedures are described as minimally invasive glaucoma surgery [15].

B.1 Comparably Dimensioned Glaucoma Drainage Devices

For comparison, several glaucoma drainage devices are shown here (Figures B.1, B.2, B.3, B.4). There is a lot of literature available that describes these in depth [94].

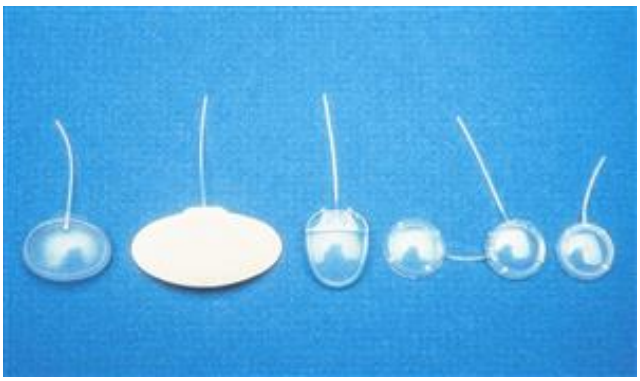

Figure B.1: Commercial glaucoma drainage devices. Shown are Ahmed valve, Baerveldt, Krupin shunt. Reprinted from [94].

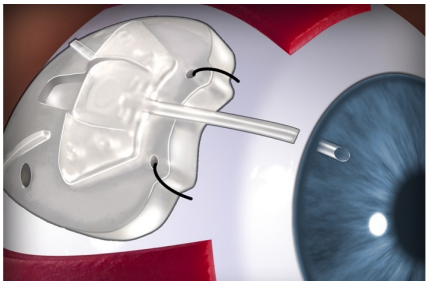

Figure B.2: Cartoon of device implanted onto the eye on the superotemporal quadrant. Reprinted from [96].

Table 1
XEN®45 Gel Stent Dimensions

XEN®45 Gel Stent Measurements	Dry Dimensions
Length	6 mm
Inner Diameter	45 µm
Outer Diameter	150 µm

Figure B.3: Xen gel shunt. Reprinted from [97].

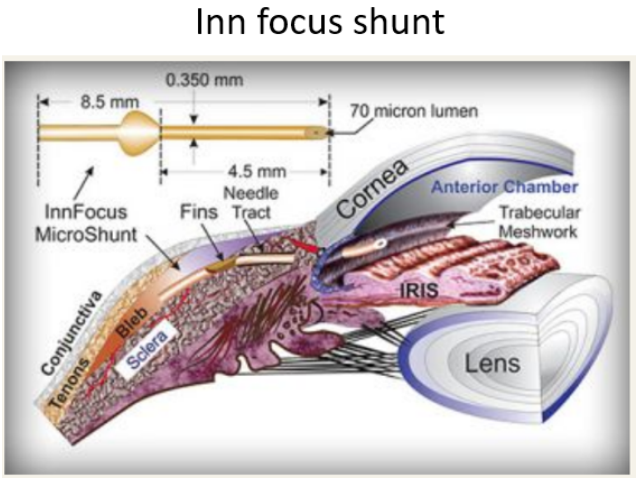

Figure B.4: Innfocus microshunt. Reprinted from [98].

B.2 Tube Construction Method

Here is described a method of fabricating a tube with selected inner diameter. First a metal wire with equal or less than the final desired inner diameter is found. Parylene could be coated on it to get the desired tube inner diameter. Separately, find a tube with the final desired outer diameter, but any larger inner diameter is

acceptable. Then the wire is strung inside tube and syringe, and tied to washers to hold in place from both ends. Then pull out at the ends.

Then load the syringe with uncured silicone, push it through for some distance, and then cure it. After curing, the tube can be cut and the wire can be pulled out of it (Figures B.5, B.6).

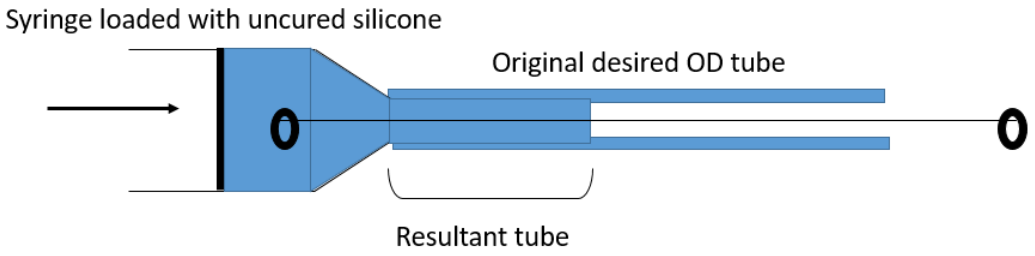

Figure B.5: Diagram of micro-scale inner diameter silicone tube fabrication.

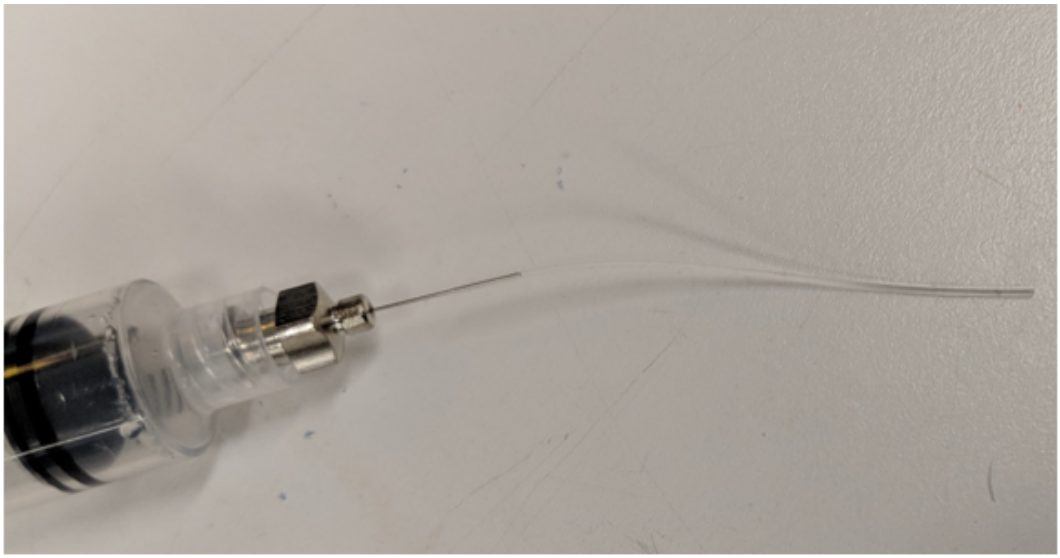

Figure B.6: Photograph of tube fabrication technique.

An example tube is shown in Figure B.7. The tube was verified to be able to not have any leaks or blockages; in other words, it was functionally a tube.

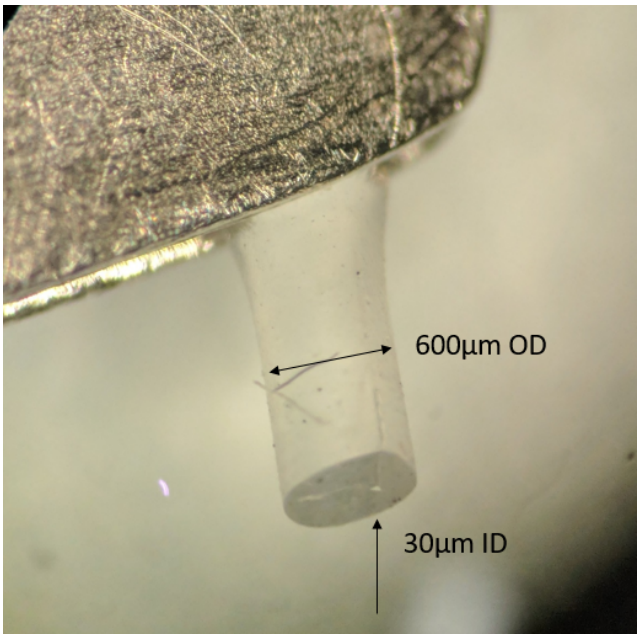

Figure B.7: Close up of micron-scale inner diameter silicone tube.

B.3 Integration of Drainage Tube into Full Implant

A drainage tube can be integrated with the rest of the intraocular implant shown in Chapter 3. A diagram of the additional drainage tube is shown in Figure B.8. This is possible because the drainage tube is not coupled to the rest of the implant, and can be its own inner channel, even if it is mated with the sensing tube so that there would be one hole for insertion into the pars plana.

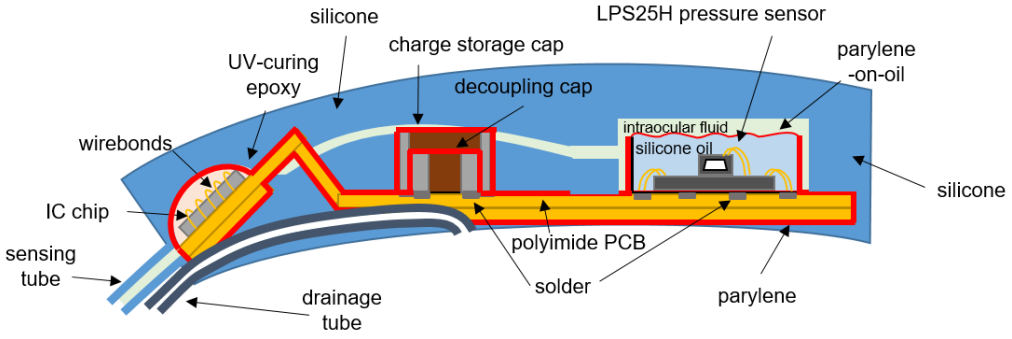

Figure B.8: Diagram of proposed integration of glaucoma drainage tube with rest of implant.

B.4 Summary

Glaucoma drainage devices are commercially available, but are passive. Nonetheless, the implant in chapter 3 is intentionally inspired in size and shape by the working drainage devices. However, these implants are known to clog at a rate that it would be good to have convenient IOP monitoring in such an implant. A fabrication method for creating a drainage tube and a prototype with the right dimensions is shown, as well as a conceptual diagram of how the drainage tube could be easily integrated with the rest of the intraocular implant shown in Chapter 3. This is especially significant because the goal at the end of the day in the clinic is to deliver therapy, not solely monitor, even though that helps. This shows that the implant shown in this thesis progresses towards both therapy and monitoring in one combined device, albeit with much more focus on making the pressure sensor last long term than improving the drainage tube over what is the state-of-the-art drainage tube.

BIBLIOGRAPHY

[1] *Pressure conversion chart*, 2019. [Online]. Available: http://www.semicore.com/reference/pressure-conversion-reference (visited on 2019).

[2] G. T. A. Kovacs, *Micromachined transducers sourcebook*. Boston, Ma: WCB, 1998, 911 pp.

[3] O. Akar, T. Akin, and K. Najafi, "A wireless batch sealed absolute capacitive pressure sensor," *Sensors and Actuators A: Physical*, vol. 95, no. 1, pp. 29–38, Dec. 2001. (visited on 04/25/2019).

[4] L. Yu, B. Kim, and E. Meng, "Chronically implanted pressure sensors: Challenges and state of the field," *Sensors*, vol. 14, no. 12, pp. 20 620–20 644, Oct. 31, 2014. (visited on 02/21/2018).

[5] J. C.-H. Lin, "MEMS for glaucoma," PhD thesis, California Institute of Technology, Feb. 6, 2012.

[6] L. Vijaya, R. George, R. Asokan, L. Velumuri, and S. Ramesh, "Prevalence and causes of low vision and blindness in an urban population: The chennai glaucoma study," *Indian Journal of Ophthalmology*, vol. 62, no. 4, p. 477, 2014. (visited on 04/27/2019).

[7] *Glaucoma facts*, 2019. [Online]. Available: https://nei.nih.gov/health/glaucoma/glaucoma_facts (visited on 2015).

[8] H. A. Quigley, "The number of people with glaucoma worldwide in 2010 and 2020," *British Journal of Ophthalmology*, vol. 90, no. 3, pp. 262–267, Mar. 1, 2006. (visited on 04/26/2019).

[9] Y. Barkana, "Clinical utility of intraocular pressure monitoring outside of normal office hours in patients with glaucoma," *Archives of Ophthalmology*, vol. 124, no. 6, p. 793, Jun. 1, 2006. (visited on 04/27/2019).

[10] J. H. K. Liu, K. Mansouri, and R. N. Weinreb, "Estimation of 24-hour intraocular pressure peak timing and variation using a contact lens sensor," *PLOS ONE*, vol. 10, no. 6, M. G. Anderson, Ed., e0129529, Jun. 15, 2015. (visited on 04/26/2019).

[11] M. Jody Piltz-Seymour and M. Tak Yee Tania Tai, *Trabeculectomy*, 2019. [Online]. Available: https://eyewiki.aao.org/Trabeculectomy (visited on 2015).

[12] C. Jiang, Y. Li, D. Huang, and B. A. Francis, "Study of anterior chamber aqueous tube shunt by fourier-domain optical coherence tomography," *Journal of Ophthalmology*, vol. 2012, pp. 1–5, 2012. (visited on 04/27/2019).

[13] S. S. MD, *Trabeculectomy*, 2019. [Online]. Available: https://eyewiki.aao.org/Glaucoma_Drainage_Devices (visited on 2015).

[14] R. A. Moses, "The goldmann applanation tonometer*," *American Journal of Ophthalmology*, vol. 46, no. 6, pp. 865–869, Dec. 1958. (visited on 04/26/2019).

[15] H. B. Dick, T. Schultz, and R. D. Gerste, "Miniaturization in glaucoma monitoring and treatment: A review of new technologies that require a minimal surgical approach," *Ophthalmology and Therapy*, vol. 8, no. 1, pp. 19–30, Mar. 2019. (visited on 05/01/2019).

[16] G. Jóhannesson, P. Hallberg, A. Eklund, A. Behndig, and C. Lindén, "Effects of topical anaesthetics and repeated tonometry on intraocular pressure," *Acta Ophthalmologica*, vol. 92, no. 2, pp. 111–115, Mar. 2014. (visited on 04/27/2019).

[17] *Tonovet*, 2019. [Online]. Available: https://www.jorvet.com/product/tonovet-plus-tonometer/ (visited on 2019).

[18] A. J. Sit, "Continuous monitoring of intraocular pressure: Rationale and progress toward a clinical device," *Journal of Glaucoma*, vol. 18, no. 4, pp. 272–279, Apr. 2009. (visited on 04/27/2019).

[19] *Goldmann applanation tonometry*, 2019. [Online]. Available: https://ophthalmiatroscyprus.com/en/equipment/goldmann-applanation-tonometry (visited on 2019).

[20] *Tonopen*, 2019. [Online]. Available: http://premierop.com/reichert-avia-tonopen-starter-kit/ (visited on 2019).

[21] M. Czosnyka, "Monitoring and interpretation of intracranial pressure," *Journal of Neurology, Neurosurgery & Psychiatry*, vol. 75, no. 6, pp. 813–821, Jun. 1, 2004. (visited on 04/24/2019).

[22] *Pulmonary arterial pressure*, 2019. [Online]. Available: https://www.heart.org/en/health-topics/high-blood-pressure/the-facts-about-high-blood-pressure/pulmonary-hypertension-high-blood-pressure-in-the-heart-to-lung-system (visited on 2019).

[23] *Paraplegia effects*, 2019. [Online]. Available: https://www.christopherreeve.org/living-with-paralysis/health/secondary-conditions/bladder-management (visited on 2019).

[24] *Electrochemcial corrosion*, 2019. [Online]. Available: https://chem.libretexts.org/Bookshelves/General_Chemistry/Book%5C%3A_Chem1_(Lower)/16%5C%3A_Electrochemistry/24.08%5C%3A_Electrochemical_Corrosion (visited on 2019).

[25] N. Tsuchida and M. Ueda, "Ionic behaviours in silicone oil," *Journal of Physics D: Applied Physics*, vol. 13, no. 9, Apr. 1980.

[26] J. M. Anderson, A. Rodriguez, and D. T. Chang, "Foreign body reaction to biomaterials," *Seminars in Immunology*, vol. 20, no. 2, pp. 86–100, Apr. 2008. (visited on 04/30/2019).

[27] V. Quaglini, S. Mantero, and T. Villa, "Mechanical properties of breast periprosthetic capsules and the correlation to capsule contracture," *J Appl Biomater Biomech*, vol. 3, no. 3, pp. 184–191, Dec. 2005.

[28] S. P. Nichols, A. Koh, W. L. Storm, J. H. Shin, and M. H. Schoenfisch, "Biocompatible materials for continuous glucose monitoring devices," *Chem. Rev.*, vol. 113, no. 4, pp. 2528–2549, Apr. 10, 2013.

[29] K. L. Helton, B. D. Ratner, and N. A. Wisniewski, "Biomechanics of the sensor-tissue interface—effects of motion, pressure, and design on sensor performance and the foreign body response—part i: Theoretical framework," *Journal of Diabetes Science and Technology*, vol. 5, no. 3, pp. 632–646, May 2011. (visited on 02/21/2018).

[30] R. Zhou and R. R. Caspi, "Ocular immune privilege," *F1000 Biology Reports*, Jan. 18, 2010. (visited on 04/30/2019).

[31] P.-J. Chen, S. Saati, R. Varma, M. S. Humayun, and Y.-C. Tai, "Wireless intraocular pressure sensing using microfabricated minimally invasive flexible-coiled LC sensor implant," *Journal of Microelectromechanical Systems*, vol. 19, no. 4, pp. 721–734, Aug. 2010. (visited on 05/01/2019).

[32] *Cardiomems hf system for pulmonary pressure monitoring in heart failure patients approved by fda*, 2014. [Online]. Available: `https://www.medgadget.com/2014/05/cardiomems-hf-system-for-pulmonary-pressure-monitoring-in-heart-failure-patients-approved-by-fda-video.html` (visited on 2014).

[33] J. O. Lee, V. Narasimhan, J. Du, B. Ndjamen, D. Sretavan, and H. Choo, "Biocompatible multifunctional black-silicon for implantable intraocular sensor," *Advanced Healthcare Materials*, vol. 6, no. 4, p. 1 601 356, Feb. 2017. (visited on 10/07/2018).

[34] J. O. Lee, H. Park, J. Du, A. Balakrishna, O. Chen, D. Sretavan, and H. Choo, "A microscale optical implant for continuous in vivo monitoring of intraocular pressure," *Microsystems & Nanoengineering*, vol. 3, p. 17 057, Dec. 18, 2017. (visited on 10/07/2018).

[35] K. H. Kim, J. O. Lee, J. Du, D. Sretavan, and H. Choo, "Real-time in vivo intraocular pressure monitoring using an optomechanical implant and an artificial neural network," *IEEE Sensors Journal*, vol. 17, no. 22, pp. 7394–7404, Nov. 15, 2017. (visited on 05/01/2019).

[36] P. Enders, J. Hall, M. Bornhauser, K. Mansouri, L. Altay, S. Schrader, T. S. Dietlein, B. O. Bachmann, T. Neuhann, and C. Cursiefen, "Telemetric intraocular pressure monitoring after boston keratoprosthesis surgery with the eyemate-IO sensor: Dynamics in the first year," *American Journal of Ophthalmology*, Mar. 2019. (visited on 05/02/2019).

[37] S. Mariacher, M. Ebner, K. Januschowski, J. Hurst, S. Schnichels, and P. Szurman, "Investigation of a novel implantable suprachoroidal pressure transducer for telemetric intraocular pressure monitoring," *Experimental Eye Research*, vol. 151, pp. 54–60, Oct. 2016. (visited on 02/21/2018).

[38] *Argos io iop sensor*, 2018. [Online]. Available: https://implandata.com/EN/pdf/2018-10%5C%20Enders%5C%20et%5C%20al,%5C%20Telemetric%5C%20Intraocular%5C%20Pressure%5C%20Monitoring%5C%20after%5C%20Boston%5C%20Keratoprosthesis%5C%20Surgery.pdf (visited on 2018).

[39] G. E. Dunbar, B. Y. Shen, and A. A. Aref, "The sensimed triggerfish contact lens sensor: Efficacy, safety, and patient perspectives," *Clin Ophthalmol*, vol. 11, pp. 875–882, 2017.

[40] A. Kim, C. R. Powell, and B. Ziaie, "An universal packaging technique for low-drift implantable pressure sensors," *Biomedical Microdevices*, vol. 18, no. 2, Apr. 2016. (visited on 02/21/2018).

[41] P. Wang, S. Majerus, R. Karam, B. Hanzlicek, D. Lin, H. Zhu, J. Anderson, M. Damaser, C. Zorman, and W. Ko, "Long-term evaluation of a non-hermetic micropackage technology for MEMS-based, implantable pressure sensors," presented at the Transducers, IEEE, Jun. 2015, pp. 484–487. (visited on 02/21/2018).

[42] M. H. Ghaed, G. Chen, R.-u. Haque, M. Wieckowski, Y. Kim, G. Kim, Y. Lee, I. Lee, D. Fick, D. Kim, M. Seok, K. D. Wise, D. Blaauw, and D. Sylvester, "Circuits for a cubic-millimeter energy-autonomous wireless intraocular pressure monitor," *IEEE Transactions on Circuits and Systems I: Regular Papers*, vol. 60, no. 12, pp. 3152–3162, Dec. 2013. (visited on 02/21/2018).

[43] M. Shafahi and K. Vafai, "Human eye response to thermal disturbances," *Journal of Heat Transfer*, vol. 133, no. 1, p. 011 009, 2011. (visited on 02/21/2018).

[44] *SCS parylene properties*, 2007. [Online]. Available: https://scscoatings.com/wp-content/uploads/2017/09/02-SCS-Parylene-Properties-1016.pdf.

[45] W. F. Gorham, "A new, general synthetic method for the preparation of linear poly-p-xylylenes," *Journal of Polymer Science Part A-1: Polymer Chemistry*, vol. 4, no. 12, pp. 3027–3039, Dec. 1966.

[46] J. B. Fortin and T.-M. Lu, "A model for the chemical vapor deposition of poly(*para* -xylylene) (parylene) thin films," *Chemistry of Materials*, vol. 14, no. 5, pp. 1945–1949, May 2002. (visited on 04/24/2019).

[47] P. Kramer, "Polymerization of para-xylylene derivatives (parylene polymerization). i. deposition kinetics for parylene n and parylene c," *Journal of Polymer Science: Polymer Chemistry Edition*, vol. 22, no. 2, pp. 475–491, 1984.

[48] J. H.-C. Chang, "Wireless parylene-based retinal implant," PhD thesis, California Institute of Technology, 2013.

[49] O. Oluwatosin Abegunde, E. Titilayo Akinlabi, O. Philip Oladijo, S. Akinlabi, A. Uchenna Ude, 1 Department of Mechanical Engineering Science, University of Johannesburg, Johannesburg 2006, South Africa, and 2 Department of Chemical, Material and Metallurgical Engineering, Botswana International University of Science and Technology, Palapye, Botswana, "Overview of thin film deposition techniques," *AIMS Materials Science*, vol. 6, no. 2, pp. 174–199, 2019. (visited on 04/24/2019).

[50] J. Ortigoza-Diaz, K. Scholten, C. Larson, A. Cobo, T. Hudson, J. Yoo, A. Baldwin, A. Weltman Hirschberg, and E. Meng, "Techniques and considerations in the microfabrication of parylene c microelectromechanical systems," *Micromachines*, vol. 9, no. 9, p. 422, Aug. 22, 2018. (visited on 08/28/2018).

[51] X.-P. Bi, N. L. Ward, B. P. Crum, and W. Li, "Plasma-treated switchable wettability of parylene-c surface," in *2012 7th IEEE International Conference on Nano/Micro Engineered and Molecular Systems (NEMS)*, Kyoto, Japan: IEEE, Mar. 2012, pp. 222–225. (visited on 04/24/2019).

[52] J. H.-C. Chang, B. Lu, and Y.-C. Tai, "Adhesion-enhancing surface treatments for parylene deposition," in *2011 16th International Solid-State Sensors, Actuators and Microsystems Conference*, Beijing, China: IEEE, Jun. 2011, pp. 390–393. (visited on 04/24/2019).

[53] J. Ortigoza-Diaz, K. Scholten, and E. Meng, "Characterization and modification of adhesion in dry and wet environments in thin-film parylene systems," *Journal of Microelectromechanical Systems*, vol. 27, no. 5, pp. 874–885, Oct. 2018. (visited on 04/24/2019).

[54] F. Schamberger, A. Ziegler, and G. Franz, "Influence of film thickness and deposition rate on surface quality of polyparylene coatings," *Journal of Vacuum Science & Technology B, Nanotechnology and Microelectronics: Materials, Processing, Measurement, and Phenomena*, vol. 30, no. 5, p. 051 801, Sep. 2012. (visited on 04/24/2019).

[55] S. Dabral, J. Van Etten, X. Zhang, C. Apblett, G.-R. Yang, P. Ficalora, and J. F. McDonald, "Stress in thermally annealed parylene films," *Journal of Electronic Materials*, vol. 21, no. 10, pp. 989–994, Oct. 1992. (visited on 04/24/2019).

[56] J. H.-C. Chang, Y. Liu, D. Kang, and Y.-C. Tai, "Reliable packaging for parylene-based flexible retinal implant," in *2013 Transducers & Eurosensors XXVII: The 17th International Conference on Solid-State Sensors, Actuators and Microsystems (TRANSDUCERS & EUROSENSORS XXVII)*, Barcelona, Spain: IEEE, Jun. 2013, pp. 2612–2615. (visited on 03/07/2019).

[57] K. P. Menard, *Dynamic mechanical analysis: A practical introduction*. Boca Raton, Fla: CRC Press, 1999, 208 pp.

[58] C. Hassler, R. P. von Metzen, P. Ruther, and T. Stieglitz, "Characterization of parylene c as an encapsulation material for implanted neural prostheses," *Journal of Biomedical Materials Research Part B: Applied Biomaterials*, vol. 9999B, NA–NA, 2010. (visited on 12/02/2018).

[59] K. Liland, K. Eidnes, K. Bjorneklett, and S. Hvidsten, "Measurement of solubility and water content of insulating oils for HV XLPE cable terminations," presented at the International Symposium on Electrical Insulation, IEEE, Jun. 2008, pp. 7–10. (visited on 02/21/2018).

[60] A. Hogg, T. Aellen, S. Uhl, B. Graf, H. Keppner, Y. Tardy, and J. Burger, "Ultra-thin layer packaging for implantable electronic devices," *Journal of Micromechanics and Microengineering*, vol. 23, no. 7, p. 075 001, Jul. 1, 2013. (visited on 04/30/2019).

[61] B. Lutz, Z. Guan, L. Wang, F. Zhang, and Z. Lu, "Water absorption and water vapor permeation characteristics of HTV silicone rubber material," presented at the International Symposium on Electrical Insulation, IEEE, Jun. 2012, pp. 478–482. (visited on 02/21/2018).

[62] *Kapton properties*, 2019. [Online]. Available: `https://www.dupont.com/content/dam/dupont/products-and-services/membranes-and-films/polyimde-films/documents/DEC-Kapton-summary-of-properties.pdf` (visited on 2019).

[63] S. Kirsten, M. Schubert, M. Braunschweig, G. Woldt, T. Voitsekhivska, and K.-J. Wolter, "Biocompatible packaging for implantable miniaturized pressure sensor device used for stent grafts: Concept and choice of materials," presented at the Electronics Packaging Technology Conference (EPTC), IEEE, Dec. 2014, pp. 719–724. (visited on 02/21/2018).

[64] G. Jiang and D. D. Zhou, "Technology advances and challenges in hermetic packaging for implantable medical devices," in *Implantable Neural Prostheses 2*, D. Zhou and E. Greenbaum, Eds., New York, NY: Springer New York, 2009, pp. 27–61. (visited on 02/21/2018).

[65] A. Hogg, S. Uhl, F. Feuvrier, Y. Girardet, B. Graf, T. Aellen, H. Keppner, Y. Tardy, and J. Burger, "Protective multilayer packaging for long-term implantable medical devices," *Surface and Coatings Technology*, vol. 255, pp. 124–129, Sep. 2014. (visited on 04/30/2019).

[66] J. Moales, "Evaluating biocompatible barrier films as encapsulants of medical micro devices," PhD thesis, L'UNIVERSITÉ GRENOBLE ALPES, 2015.

[67] I. Clausen and T. Glott, "Development of clinically relevant implantable pressure sensors: Perspectives and challenges," *Sensors*, vol. 14, no. 12, pp. 17 686–17 702, Sep. 22, 2014. (visited on 02/21/2018).

[68] A. Koutsonas, P. Walter, G. Roessler, and N. Plange, "Long-term follow-up after implantation of a telemetric intraocular pressure sensor in patients with glaucoma: A safety report: Long-term ocular pressure sensor follow-up," *Clinical & Experimental Ophthalmology*, vol. 46, no. 5, pp. 473–479, Jul. 2018. (visited on 09/28/2018).

[69] W. Wessel, "Fluid pressure sensor, particularly diesel engine injection pump pressure sensor," U.S. Patent 4430899A. [Online]. Available: https://patentimages.storage.googleapis.com/6c/a3/b4/e5797d1515e9a5/US4430899.pdf.

[70] S. J. A. Majerus, P. C. Fletter, M. S. Damaser, and S. L. Garverick, "Low-power wireless micromanometer system for acute and chronic bladder-pressure monitoring," *IEEE Transactions on Biomedical Engineering*, vol. 58, no. 3, pp. 763–767, Mar. 2011. (visited on 02/21/2018).

[71] P. Cong, W. H. Ko, and D. J. Young, "Wireless batteryless implantable blood pressure monitoring microsystem for small laboratory animals," *IEEE Sensors Journal*, vol. 10, no. 2, pp. 243–254, Feb. 2010. [Online]. Available: http://ieeexplore.ieee.org/document/5361367/ (visited on 03/04/2019).

[72] T. Kan, H. Aoki, N. Binh-Khiem, K. Matsumoto, and I. Shimoyama, "Ratiometric optical temperature sensor using two fluorescent dyes dissolved in an ionic liquid encapsulated by parylene film," *Sensors*, vol. 13, no. 4, pp. 4138–4145, Mar. 27, 2013. (visited on 03/04/2019).

[73] Binh-Khiem Nguyen, Eiji Iwase, Kiyoshi Matsumoto, and Isao Shimoyama, "Electrically driven varifocal micro lens fabricated by depositing parylene directly on liquid," presented at the MEMS, IEEE, Jan. 2007, pp. 305–308. (visited on 02/21/2018).

[74] H. Keppner and M. Benkhaira, "Method for producing a plastic membrane device and the thus obtained device," pat. [Online]. Available: https://patentscope.wipo.int/search/en/detail.jsf?docId=WO2006063955&tab=PCTBIBLIO&maxRec=1000.

[75] N. Binh-Khiem, K. Matsumoto, and I. Shimoyama, "Porous parylene and effects of liquid on parylene films deposited on liquid," presented at the MEMS, IEEE, Jan. 2011, pp. 111–114. (visited on 02/21/2018).

[76] A. Homsy, E. Laux, L. Jeandupeux, J. Charmet, R. Bitterli, C. Botta, Y. Rebetez, O. Banakh, and H. Keppner, "Solid on liquid deposition, a review of technological solutions," *Microelectronic Engineering*, vol. 141, pp. 267–279, Jun. 2015. (visited on 02/21/2018).

[77] *Medtronic pacemaker*, 2017. [Online]. Available: medtronic.com/us-en/healthcare-professionals/products/neurological/spinal-cord-stimulation-systems/restoresensor-surescan-mri-neurostimulator.html (visited on 2017).

[78] *Silicone fluids property profile guide*, 2012. [Online]. Available: https://www.gelest.com/wp-content/uploads/Goods-PDF-brochures-inert_silicones_2013.pdf.

[79] N. Binh-Khiem, K. Matsumoto, and I. Shimoyama, "Tensile film stress of parylene deposited on liquid," *Langmuir*, vol. 26, no. 24, pp. 18 771–18 775, Dec. 21, 2010. (visited on 02/21/2018).

[80] W. K. Schomburg, "Membranes," in *Introduction to Microsystem Design*. Berlin, Heidelberg: Springer Berlin Heidelberg, 2011, vol. 1, pp. 29–52. (visited on 02/21/2018).

[81] E. Ventsel and T. Krauthammer, *Thin plates and shells: Theory, analysis, and applications*. New York: Marcel Dekker, 2001, p. 231-2.

[82] K. S. Pister and S. B. Dong, "Elastic bending of layered plates," *Journal of the Engineering Mechanics Division, Proceedings of the American Society of Civil Engineers*, vol. 85, EM 4 Oct. 1959.

[83] S. R. Choi, J. W. Hutchinson, and A. Evans, "Delamination of multilayer thermal barrier coatings," *Mechanics of Materials*, vol. 31, no. 7, pp. 431–447, Jul. 1999. (visited on 02/21/2018).

[84] *Steam sterilization*, 2008. [Online]. Available: https://www.cdc.gov/infectioncontrol/guidelines/disinfection/sterilization/steam.html (visited on 03/27/2019).

[85] *Ethylene oxide "gas" sterilization*, 2008. [Online]. Available: https://www.cdc.gov/infectioncontrol/guidelines/disinfection/sterilization/ethylene-oxide.html (visited on 03/27/2019).

[86] G. Chen, H. Ghaed, R.-u. Haque, M. Wieckowski, Y. Kim, G. Kim, D. Fick, D. Kim, M. Seok, K. Wise, D. Blaauw, and D. Sylvester, "A cubic-millimeter energy-autonomous wireless intraocular pressure monitor," presented at the International Solid-State Circuits Conference, IEEE, Feb. 2011, pp. 310–312. (visited on 02/21/2018).

[87] A. Agarwal, A. Shapero, D. Rodger, M. Humayun, Y.-C. Tai, and A. Emami, "A wireless, low-drift, implantable intraocular pressure sensor with parylene-on-oil encapsulation," in *2018 IEEE Custom Integrated Circuits Conference (CICC)*, San Diego, CA: IEEE, Apr. 2018, pp. 1–4, ISBN: 978-1-5386-2483-8. DOI: 10.1109/CICC.2018.8357049. [Online]. Available: https://ieeexplore.ieee.org/document/8357049/ (visited on 03/20/2019),

[88] *Current limiting*, 2018. [Online]. Available: https://en.wikipedia.org/wiki/Current_limiting (visited on 03/28/2019).

[89] S. Gangavarapu, "Development of a three-axis motorized system for coil characterization in applications involving intraocular pressure sensing," senior thesis, California Institute of Technology, Jun. 2018, 22 pp.

[90] A. Hughes, "A schematic eye for the rabbit," *Vision Research*, vol. 12, no. 1, 123–IN6, Jan. 1972. (visited on 04/17/2019).

[91] M. F. Deering, "A photon accurate model of the human eye," *ACM Transactions on Graphics*, vol. 24, no. 3, p. 649, Jul. 1, 2005. (visited on 04/17/2019).

[92] D. L. Holve, G. G. Gum, and S. L. Pritt, "Effect of sedation with xylazine and ketamine on intraocular pressure in new zealand white rabbits," *J. Am. Assoc. Lab. Anim. Sci.*, vol. 52, no. 4, pp. 488–490, Jul. 2013.

[93] *Cymbet005*, 2017. [Online]. Available: https://www.cymbet.com/wp-content/uploads/2019/02/DS-72-41.pdf (visited on 2017).

[94] *Glaucoma drainage devices*, 2018. [Online]. Available: https://eyewiki.aao.org/Glaucoma_Drainage_Devices (visited on 03/09/2018).

[95] V. Pathak Ray and D. P. Rao, "Surgical outcomes of a new affordable non-valved glaucoma drainage device and ahmed glaucoma valve: Comparison in the first year," *British Journal of Ophthalmology*, 2018.

[96] *Glaucoma drainage cartoon*, 2019. [Online]. Available: https://iristech.co/glaucoma-treatment/ (visited on 2019).

[97] *Xengel2017*, 2017. [Online]. Available: https://allergan-web-cdn-prod.azureedge.net/actavis/actavis/media/allergan-pdf-documents/labeling/xen/dfu_xen_glaucoma_treatment_system_us_feb2017.pdf (visited on 2017).

[98] *Innfocus2012*, 2018. [Online]. Available: https://innfocusinc.com/index.php/microshunt/innfocus-microshunt/ (visited on 2012).

[1]The top of the LPS25H being removable was a fortuitous accidental discovery.

[2]antenna design and parts list courtesy of Samson Chen and Abhinav Agarwal

[3]product no: 51845k65, https://www.mcmaster.com/51845k65